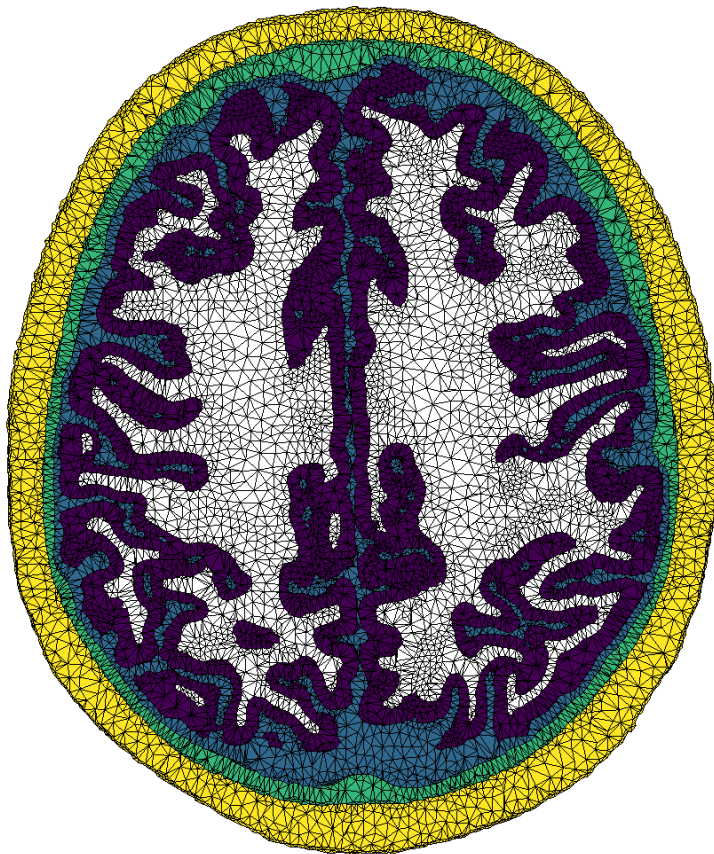# Studying experimental variability in EEG and tDCS through uncertainty and sensitivity analyses

Thesis submitted in partial fulfillment of the requirements for
the degree of Doctor of Philosophy (PhD) in Engineering Science
College of Electricity, Electronics and Informatics

Martin Grignard
Supervisors
Christophe Phillips, Christophe Geuzaine
– September 2022 –

LIÈGE université
Sciences Appliquées

Studying experimental variability in EEG and tDCS through uncertainty and sensitivity analyses

Martin Grignard
Master of Industrial Engineering, HELMo Gramme, 2018

Thesis submitted in partial fulfilment of the requirements
for the degree of
Doctor of Philosophy (PhD) in Engineering Science
In the Faculty of Applied Sciences, College of Electricity, Electronics and
Informatics

Supervisors

Christophe Phillips, PhD, GIGA CRC In-Vivo Imaging
Christophe Geuzaine, PhD, Department of Electrical Engineering
and Computer Science

Examining board

Steve Majerus, PhD, Department of Psychology
Benoît Vanderheyden, PhD, Department of Electrical Engineering and Computer Science
Guillaume Drion, PhD, Department of Electrical Engineering and Computer Science

External examiners

Dante Mantini, PhD, Movement Control and Neuroplasticity Research Group, Catholic University of Leuven
Alexandre Gramfort, HdR, MIND team, University of Paris-Saclay

UNIVERSITY OF LIÈGE
September 2022

Abstract

In neuroscience, simulating electric current in the head of a subject is of main interest for both *electroencephalography (EEG)* and *transcranial direct current stimulation (tDCS)*. EEG is used to reconstruct the electric activity of the brain based on the measured electric potential on the scalp. On the other hand, tDCS consists in injecting a small electric current through the head of a subject to modulate the activity of a specific brain region.

Such simulations rely heavily on the electric conductivity of the biological tissues composing the head. Unfortunately, there is currently no effective and non-invasive method to measure it accurately for each individual. Consequently, researchers and practitioners have to set arbitrary values chosen from the literature, despite the fact that this property has been shown to vary widely both inter- and intra-subject. The simulations also depend on the geometry of the tissues and on how they are modelled.

In this thesis, we studied the influence of different skull models and of the electrical conductivity of the tissues on the EEG forward problem. We also analysed the effect of the uncertainty in the conductivity on the electric field induced in different regions of the brain by several stimulating electrode montages in tDCS.

To support these experiments, we developed a python package named *Shamo* which provides the user with tools to perform mesh generation, current simulation, surrogate modelling and sensitivity and uncertainty analyses with a user-friendly API. It interfaces with industrial grade software to perform the computationally intensive tasks and is easy to use on distributed architectures.

The present work describes both *Shamo* and the results that it helped to obtain for the different experiments.

Résumé

Dans le domaine des neurosciences, la simulation du courant électrique dans la tête d'un sujet est d'un intérêt majeur, tant pour l'*électroencéphalographie (EEG)* que pour la *stimulation transcrânienne à courant continu (tDCS)*. L'EEG est utilisée pour reconstruire l'activité électrique du cerveau à partir du potentiel électrique mesuré sur le cuir chevelu. D'autre part, la tDCS consiste à injecter un petit courant électrique dans la tête d'un sujet pour moduler l'activité d'une région spécifique du cerveau.

De telles simulations dépendent de la conductivité électrique des tissus biologiques composant la tête. Malheureusement, il n'existe actuellement aucune méthode efficace et non invasive pour la mesurer avec précision pour chaque individu. Par conséquent, les chercheurs et les praticiens doivent fixer des valeurs arbitraires choisies dans la littérature, malgré le fait qu'il a été démontré que cette propriété varie considérablement entre les sujets et à l'intérieur d'un même sujet. Les simulations dépendent également de la géométrie des tissus et de la façon dont ils sont modélisés.

Dans cette thèse, nous avons étudié l'influence de différents modèles de crâne et de la conductivité électrique des tissus sur le problème direct de l'EEG. Nous avons également analysé l'effet de la conductivité sur le champ électrique induit dans différentes régions du cerveau par plusieurs montages d'électrodes en tDCS.

Pour soutenir ces expériences, nous avons développé un package python nommé *Shamo* qui fournit à l'utilisateur des outils pour effectuer la génération de maillage, la simulation de courant, la génération de modèles de substitution et les analyses de sensibilité et d'incertitude avec une API simple. Il s'interface avec des logiciels de qualité industrielle pour effectuer les tâches de calcul intensif et est facile à utiliser sur des architectures distribuées.

Ce travail décrit à la fois *Shamo* et les résultats que cet outil a permis d'obtenir pour les différentes expériences.

Table of Contents

Appendix

List of Symbols

Here are the notations used throughout the thesis. Due to the presence of both deterministic and random variables, the main specificity is that deterministic and random variables are respectively denoted by lowercase x and uppercase X characters. To differenciate between some physical constants and these notations, all the constants are denoted with an underline $\underline{x}$ or $\underline{X}$.

Mathematical symbols

x	A deterministic variable	
$\boldsymbol{x}$	A deterministic vector	$[x_1, \ldots, x_d]^\mathsf{T}$
$[x]$	A deterministic matrix	$\begin{bmatrix} x_{1,1} & \cdots & x_{1,n} \\ \vdots & \ddots & \vdots \\ x_{m,1} & \cdots & x_{m,n} \end{bmatrix}$
X	A random variable	
$\boldsymbol{X}$	A random vector	$[X_1, \ldots, X_d]^\mathsf{T}$
$[X]$	A random matrix	$\begin{bmatrix} X_{1,1} & \cdots & X_{1,n} \\ \vdots & \ddots & \vdots \\ X_{m,1} & \cdots & X_{m,n} \end{bmatrix}$

$\underline{x}, \underline{X}$ A constant

$\mathbb{E}$ The expectation $\mathbb{E}(X)$

$\mathbb{V}$ The variance $\mathbb{V}(X)$

$\mathbb{C}$ The covariance $\mathbb{C}(X_1, X_2)$

∇ The gradient of a scalar function $[\frac{\partial}{\partial x}, \frac{\partial}{\partial y}, \frac{\partial}{\partial z}]$

$\nabla\cdot$ The divergence of a vector function

$\nabla\times$ The curl of a vector function

Ω A domain in space $\Omega \subset \mathbb{R}^3$

Γ The boundary of a domain

$\boldsymbol{u}$ A unit length vector

$\langle x, y \rangle_\Omega$ The inner product over Ω $\int_\Omega xy \, d\Omega$

s_i The first order Sobol index of the i-th variable of a model

$s_i^{(t)}$ The total order Sobol index of the i-th variable of a model

δ The Dirac delta function

$\mathcal{N}(\mu, \sigma^2)$ A normal distribution centered on μ with a standard deviation σ

Physical symbols

$[l]$	The leadfield matrix	$\mathrm{V\,A^{-1}\,m^{-1}}$
$\boldsymbol{b}$	The magnetic flux density $\boldsymbol{b}(\boldsymbol{r})$	T
$\boldsymbol{d}$	The electric displacement $\boldsymbol{d}(\boldsymbol{r})$	$\mathrm{C\,m^{-2}}$
$\boldsymbol{e}$	The electric field $\boldsymbol{e}(\boldsymbol{r})$	$\mathrm{V\,m^{-1}}$
$\boldsymbol{h}$	The magnetic field $\boldsymbol{h}(\boldsymbol{r})$	$\mathrm{A\,m^{-1}}$
$\boldsymbol{j}$	The current density $\boldsymbol{j}(\boldsymbol{r})$	$\mathrm{A\,m^{-2}}$

$\boldsymbol{j}_\mathrm{f}$	The free/unbound current density $j_\mathrm{f}(\boldsymbol{r})$	$\mathrm{A\,m^{-2}}$
$\boldsymbol{j}_\mathrm{p}$	The primary current density	$\mathrm{A\,m^{-2}}$
$\boldsymbol{p}$	The dipole moment	$\mathrm{A\,m}$
$\boldsymbol{r}$	A position $[x, y, z]$ in space	m
κ	The electrical conductivity $\kappa(\boldsymbol{r})$	$\mathrm{S\,m^{-1}}$
μ	The magnetic permeability $\mu(\boldsymbol{r})$	$\mathrm{H\,m^{-1}}$
ρ	The electric resistivity $\rho(\boldsymbol{r})$	$\mathrm{\Omega\,m}$
ρ_f	The free/unbound charge density $\rho_\mathrm{f}(\boldsymbol{r})$	$\mathrm{C\,m^{-3}}$
$\underline{\mu}_0$	The vacuum permeability	$12.566 \times 10^{-7}\,\mathrm{H\,m^{-1}}$
$\underline{\varepsilon}_0$	The vacuum permittivity	$8.854 \times 10^{-12}\,\mathrm{F\,m^{-1}}$
$\underline{F}$	The Faraday constant	$96\,485.332\,\mathrm{C\,mol^{-1}}$
$\underline{R}$	The gas constant	$8.314\,\mathrm{J\,mol^{-1}\,K^{-1}}$
ε	The electric permittivity $\varepsilon(\boldsymbol{r})$	$\mathrm{F\,m^{-1}}$
i	The electrical current	A
m	The molar concentration m_i of element i	$\mathrm{mol\,m^{-3}}$
p	The membrane permeability p_i to element i	$\mathrm{mol\,m^{-1}\,s^{-1}\,Pa^{-1}}$
t	The time	s
u	The electric potential difference $v_1 - v_2$	V
v	The electrical potential	V

x

List of Abbreviations

CSF	Cerebrospinal fluid
CT	Computed tomography
BEM	Boundary element model
dlPFC	Dorsolateral prefrontal cortex
DTI	Diffusion tensor imaging
DWI	Diffusion weighted image
EEG	Electroencephalography
EPSP	Excitatory postsynaptic potential
FDM	Finite difference model
FEM	Finite element model
GM	Gray matter
GPR	Gaussian process regressor
HD-tDCS	High-definition transcranial direct current stimulation
IPS	Intraparietal sulcus
IPSP	Inhibitory postsynaptic potential
ITP	Induced transmembrane potential
MC	Motor cortex
MEP	Motor evoked potential

MREIT	Magnetic resonance electric impedance tomography
MRI	Magnetic resonance imaging
PSP	Postsynaptic potnetial
ROI	Region of interest
SA	Sensitivity analysis
SCP	Scalp
SKL	Skull
SKL CPT	Skull (Compact)
SKL ICPT	Skull (Inner table)
SKL OCPT	Skull (Outer table)
SKL SPG	Skull (Spongy)
SFT	Soft tissues
tDCS	Transcranial direct current stimulation
UA	Uncertainty analysis
UQ	Uncertainty quantification
vmPFC	Ventromedial prefrontal cortex
WM	White matter

1.

Introduction

The brain, being one of the most complex organs in the human body, has been studied for centuries to unravel its mysteries. Along the way, many powerful techniques have been developed to help better understand its inner mechanisms or even to influence its behaviour.

For instance, *electroencephalography (EEG)* is one of the oldest and easiest available methods to record the electric activity of the brain, with the first reported recording dating from 1924 [Tudor et al., 2005]. By placing electrodes on the scalp of a subject, researchers and practitioners acquire high frequency signals that can be analysed to reconstruct the actual brain activity that induced it. This process, referred to as source reconstruction, is far from trivial and relies on multiple simulations of the propagation of electric current in the head [Weinstein et al., 2000; Grech et al., 2008; Wendel et al., 2009; Darbas and Lohrengel, 2018; Zorzos et al., 2021].

On the other end of the spectrum, *transcranial direct current*

stimulation (tDCS) is a neuromodulation method, meaning it alters the behaviour of the brain. It consists in injecting a small electric current through the head of a subject. In this case, simulations are performed to gain insights on the effect of the stimulation and assess in which regions the current actually flows [Sadleir et al., 2010; Bikson et al., 2012; Thair et al., 2017; Lee et al., 2021].

In these two applications, modelling provides additional inner information about this otherwise closed black box that is the brain. Hence, techniques such as *boundary element methods (BEM)* and *finite element methods (FEM)* have been applied for decades to compute the electric field and current density throughout biological tissues [Mosher et al., 1999; Fuchs et al., 2002; Schimpf, 2007; Hallez et al., 2007]. These methods mainly depend on two important factors: the head geometry and the physical properties of the tissues.

First, the shape of the head and its different compartments serves as a support for the simulation. Each individual is different on a macroscopic scale, and so is its head. We do not have the same brain, nor the same skull or muscles. While BEM can capture these differences, it is limited by the assumptions that the tissues are continuous and isotropic, meaning that one tissue class is bounded by a single surface and that its properties are the same in the whole volume. This led to the use of FEM, which can represent the complex geometry of fragmented anisotropic tissues and allows the creation of highly realistic models.

Unfortunately, there is no easy and non-invasive way to accurately know the exact geometry of the different tissues composing the head. Nevertheless, with the advent of *computed tomography (CT)* and *magnetic resonance imaging (MRI),* it is now possible to approximate the shape of these tissues using segmentation techniques. However, most of the popular segmentation algorithms are limited to the five main tissue classes (*i.e.,* white matter, gray matter, cerebrospinal fluid, skull and soft tissues), even though recently published methods focus on increasing the number of tissue types that can automatically be differentiated [Puonti et al., 2020;

Taberna et al., 2021].

Since it is of main interest for the simulations, the effect of different geometries, and more precisely of the skull model, have been studied [Sadleir and Argibay, 2007; Dannhauer et al., 2011; Lanfer et al., 2012; Montes-Restrepo et al., 2014]. Indeed, the bone acts as an electrical insulator due to its low electrical conductivity compared to its adjacent tissues. While it is usually modelled as a single compartment, it is now more and more recognized that differentiating the soft and compact bone increases the accuracy.

Once the geometry of the tissues is determined, the physical properties of the tissues, and more precisely their electric conductivity, must still be specified to properly simulate the electric current. During the past century, the electric properties of the biological tissues have been measured in different environments (*i.e.*, in-vivo, ex-vivo and in-vitro) and conditions (temperature, age, health status, current frequency...) using several acquisition methods [Burger and Milaan, 1943; Geddes and Baker, 1967; Gabriel et al., 1996b,c,a; Gabriel, 1996; Latikka et al., 2001; Goncalves et al., 2003]. From these numerous measurements, the electric conductivity of the tissues has been shown to vary widely, both inter- and intra- subjects. Recently, the review from McCann et al. [2019] provided probability distributions of the conductivity of most of the tissues composing the human head. Still, the common practice when performing simulations is to arbitrarily set fixed values for these properties based on the literature.

Due to the variability in the published values, the influence of the chosen parameters and geometric models on the results of the simulations have been studied for the past decades and have been shown to induce erroneous electric field and potential estimations [Haueisen et al., 1995, 1997; Vallaghe and Clerc, 2009; Jochmann et al., 2011; Montes-Restrepo et al., 2014; Cho et al., 2015; Akalin Acar and Makeig, 2013; Wolters et al., 2006; Vorwerk et al., 2019a; Saturnino et al., 2019]. For instance, errors in the localisation of the reconstructed dipoles of up to $20\,$mm have been reported for basal

brain locations [Lanfer et al., 2012; Akalin Acar and Makeig, 2013]. Indeed, inaccuracies in the physical parameters directly result in errors in the forward models, and thus in the reconstructed sources localization or current flow. Similarly, the uncertainty in the conductivity parameters have been hypothesised as an explanation to the high variability in the responses to tDCS experiments [Saturnino et al., 2019].

These results are the spark that triggered the present thesis. But before stating the questions and problems we decided to tackle, there is an important topic to discuss in order to give some context about neuroscience and research in general. When Ioannidis published his groundbreaking paper entitled "Why most published research findings are false" [Ioannidis, 2005] and the term "reproducibility crisis" was coined, the whole research community started working toward better reproducibility. Many initiatives arose to increase replicability, improve data sharing and, in all senses, make better science.

This crisis highly affected, and is still affecting today, the neuroscience field. Considering this brief introduction to one of the biggest open issues in research, it was clear for us that the traditional simulation method relying on arbitrarily set physical properties was too error-prone and yielded too much uncertainty about the results and conclusions drawn from it. As stated above, many researchers studied the influence of these parameters and, while their results are of practical interest for future developments, there was no available tool to include these processes in traditional EEG or tDCS protocols. Indeed, most of these published papers were focusing on the results obtained for a single subject or a specific group, not on publishing a toolbox to achieve similar results. Consequently, their findings were usually confined to their specific models. Thus, we decided to develop a tool that would allow researchers and practitioners to include uncertainty analysis and sensitivity analysis in their experimental design. It could help the community to better understand the inter-individuals variability for tDCS

applications and yield useful insights about the confidence in EEG source reconstruction.

This was the starting point of the project and that is what I spent the last four years working on.

. Thesis plan

Considering the central role of the electric conductivity of the tissues in the electric current flow simulations, the lack of accurate non-invasive measurement technique of this property currently forces researchers and practitioners to make assumptions on their values. Unfortunately, the variability of these parameters have been shown to yield considerable variations in the reconstructed EEG sources and the computed current density for tDCS.

While numerous published studies performed *uncertainty quantification (UQ)* and *sensitivity analysis (SA)* on these exact simulations, they usually focused on a obtaining results, not on making the process of obtaining them easier for future analyses. Moreover, performing UQ and SA on such computationally expensive simulations is complex, both in terms of the time needed to obtain the values of interest (this time depends on several parameters such as the available hardware to run the process, the number of simulations required or the model complexity, just to name a few) and of the number of methods involved in the process. Still, these techniques yield valuable insights and should be part of any analysis with uncertain inputs.

To facilitate the adoption of these methods in the context of EEG and tDCS, we decided to develop a *Python* package called *Shamo*, which, in contrast to other EEG/tDCS simulation tools such as *SimNIBS* and *ROAST*, is built from the ground up to support UQ and SA and to provide a unified *application programming interface (API)* for analyses that require a single simulation or more, thus allowing people

to use the same tool and syntax for either a single electric current simulation in biological tissues, or a whole sensitivity analysis on such simulations.

In the present work, I demonstrate how to accurately model the head, account for the uncertainty in the parameters and derive sensitivity metrics with regard to these said parameters through the development of *Shamo*. The thesis is divided in three main parts.

First, the introduction gives a theoretical overview of the covered topics. Since *Shamo* is aimed toward neuroscientists but built by an engineer, it starts with a primer on neuroscience in Chapter 2 where the basics of neuroanatomy and neurophysiology are presented (See Section 2.1). Then, I introduce electroencephalography (Section 2.2) and transcranial direct current stimulation (Section 2.3), which are at the heart of this thesis. I finish with a short explanation of two ever evolving topics: head tissue segmentation and cortex parcellation in Sections 2.4 and 2.5 respectively. The process of segmenting the different tissues composing the head is of main interest for the simulation since it provides the geometric information required to build the head models. Due to the experience and time needed to manually delineate the tissues from structural images, automated tools have been developed and are readily available in toolboxes (*e.g.*, "unified segmentation" in *SPM*, *CAT12*, *freesurfer*, *FSL*...) [Ashburner and Friston, 2005; Perdue and Diamond, 2014; Huang and Parra, 2015; Mahmood et al., 2015; Huang et al., 2019; Puonti et al., 2020; Taberna et al., 2021]. Subsequently, most of the available simulation tools dedicated to EEG and tDCS have built their model generation method upon a specific automated segmentation algorithm. Indeed, developing a unique pipeline that performs both the segmentation and the model creation facilitates the process. Still, this comes at the cost of limiting the set of tissues that can be included in the geometry and, more importantly, it prevents the user from studying heads other than those of healthy adults, with which the automated segmentation algorithms only work. It also forces the user to work with potentially heavy

dependencies that might not be portable, or might not be free and open source. Another aspect of brain segmentation is gray matter parcellation, which provides practical methods to extract specific brain regions based on their function or structure. These regions are used as priors for analysis or as targets for stimulations. In this thesis, parcellation was mainly used in the context of tDCS, where certain brain areas are studied and stimulated.

After that, Chapter 3 focuses on the modelling aspects of the project. It opens with an introduction to the methods used to actually simulate the current flow in conductive materials in Section 3.1 where I describe how, under the quasi-static conditions, Maxwell's equations can lead to the definition of the generalised Poisson differential equation. Then, I explain how to solve this equation for a complex geometry using the finite element method, which is the most popular approach in simulation tools dedicated to EEG/tDCS. Afterward, I present the physical property we are most interested in: the electric conductivity (Section 3.2). In this section, I discuss the high variability of that property, as well as some methods used to model its anisotropy in certain tissues. Next, I introduce the main concepts of uncertainty quantification (UQ) and sensitivity analysis (SA) in Section 3.3. I also define the first and total order Sobol indices that are the sensitivity measurements used throughout the applications. Indeed, due to their ease of interpretation, these indices are widely used in the literature [Vallaghe and Clerc, 2009; Schmidt et al., 2015; Iooss and Lemaître, 2015; Ye and Hill, 2017; Saturnino et al., 2019; Razavi et al., 2021]. Still, because of their mathematical definitions, they require a tremendous amount of model evaluations in order to be accurately computed. To solve this problem, I discuss the commonly used surrogate modelling approach in Section 3.4. This method aims at building a simpler model that can be evaluated in place of the actual simulations. The technique I discuss relies on Gaussian process regressors.
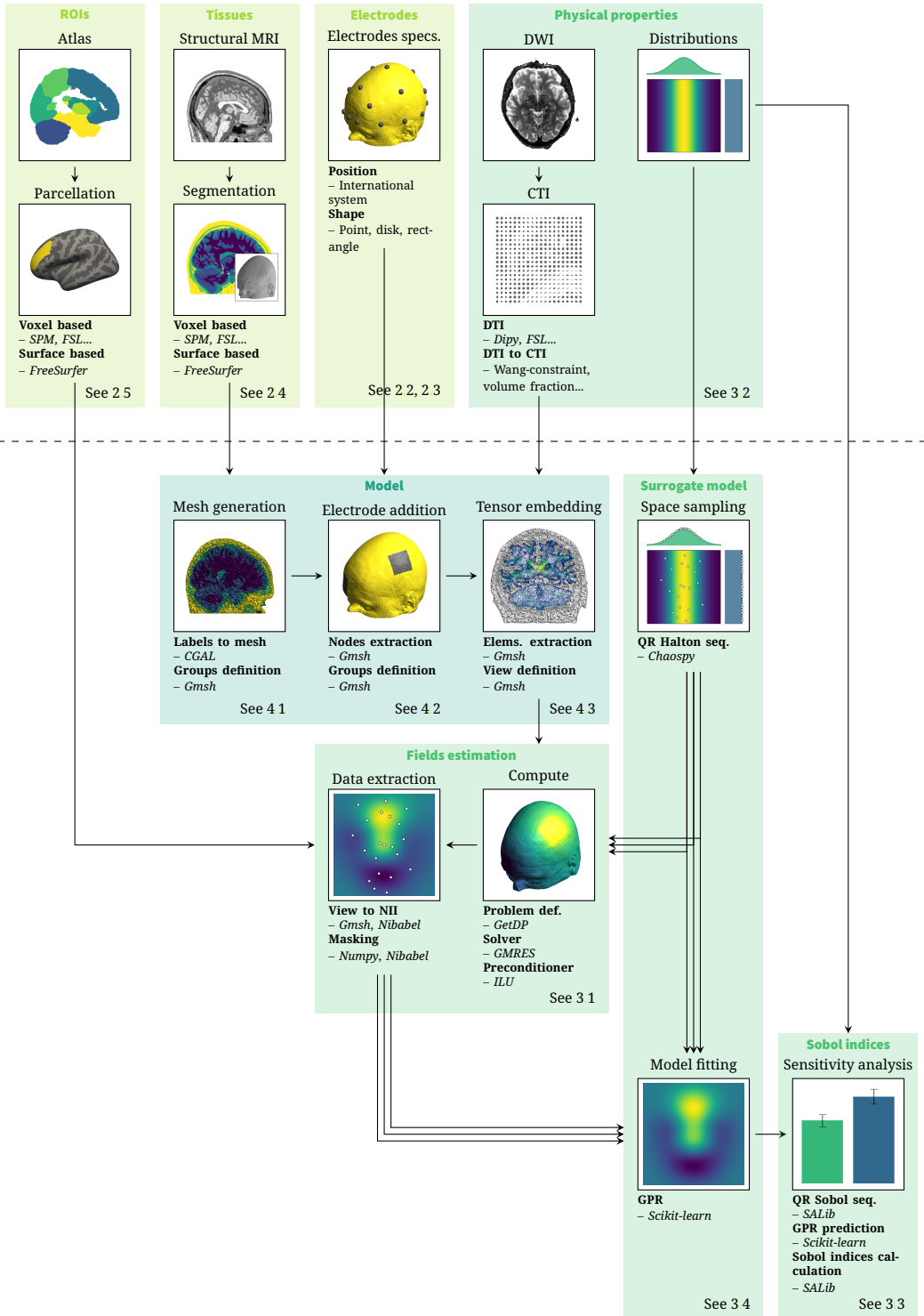
With all the required theory in hand, I then present *Shamo*, beginning by an overview of some of its main features without dis-

cussing their respective implementation in Chapter 4. Following the same steps as a user of the package, I show how the initial geometry of the models is built directly from an arbitrary segmentation (Section 4.1), thus making the tool agnostic of the segmentation method. In the process, I show how this approach also removes the need for a surface generation step and, thus, allows for more complex geometries. Thanks to these two specificities, I present how this approach easily generalises to other organic geometries and scales up to the whole body. Then, in Section 4.2, I quickly describe the different electrode models and compare them. Finally, in Section 4.3, I present how *Shamo* can account for the anisotropy of the tissues and discuss how this feature, if combined with accurate conductivity measurement techniques, could further simplify the model generation part by almost removing the need for segmenting the tissues initially or, at least, reducing the number of compartments included in the model.

Afterwards, I build upon these features to demonstrate the use of the tool in the two main applications it was built for: EEG in Chapter 5 and tDCS in Chapter 6. In the EEG application which is part of our first published article (See Appendix A), we study the influence of the conductivity parameters on the computed leadfield matrix while comparing different skull models. On the other hand, the application focusing on tDCS is the core of a manuscript currently in preparation (See Appendix B) and evaluates the electric field measured in different regions of interest and induced by six stimulation electrode montages in order to find an explanation to the high inter-subject variability reported in the literature.

Finally, in Chapter 7, I discuss the added value of *Shamo*, potential further investigations and features that could be added to extend the field of applications of the tool. Then, in Chapter 8, I complete the thesis with an overall conclusion.

The pipeline on the next page presents how the different processes interact with each other in the workflow implemented in *Shamo* (below the dashed line) with the corresponding sections where they are discussed.

ROIs

Atlas

Parcellation

Voxel based
– *SPM, FSL...*
Surface based
– *FreeSurfer*

See 2 5

Tissues

Structural MRI

Segmentation

Voxel based
– *SPM, FSL...*
Surface based
– *FreeSurfer*

See 2 4

Electrodes

Electrodes specs.

Position
– International
system
Shape
– Point, disk, rect-
angle

See 2 2, 2 3

Physical properties

DWI

Distributions

CTI

DTI
– *Dipy, FSL...*
DTI to CTI
– Wang-constraint,
volume fraction...

See 3 2

Model

Mesh generation

Electrode addition

Tensor embedding

Labels to mesh
– *CGAL*
Groups definition
– *Gmsh*

See 4 1

Nodes extraction
– *Gmsh*
Groups definition
– *Gmsh*

See 4 2

Elems. extraction
– *Gmsh*
View definition
– *Gmsh*

See 4 3

Surrogate model

Space sampling

QR Halton seq.
– *Chaospy*

Fields estimation

Data extraction

Compute

View to NII
– *Gmsh, Nibabel*
Masking
– *Numpy, Nibabel*

Problem def.
– *GetDP*
Solver
– *GMRES*
Preconditioner
– *ILU*

See 3 1

Model fitting

GPR
– *Scikit-learn*

See 3 4

Sobol indices

Sensitivity analysis

QR Sobol seq.
– *SALib*
GPR prediction
– *Scikit-learn*
**Sobol indices cal-
culation**
– *SALib*

See 3 3

Scientific contributions

The main original contributions of the thesis are:

— A general methodology to perform uncertainty and sensitivity analyses on computationally expensive simulation-based models. This workflow is general enough to be applied to different application fields and study model parameters ranging from physical properties to experimental design settings such as electrode placement. In this manuscript and the subsequent papers, it is successfully applied to both EEG and tDCS. This makes it more versatile than other similar tools that also propose toolboxes to perform UQ/SA. For instance, *SimNIBS* [Saturnino et al., 2019] is dedicated to stimulation simulations (tDCS/TMS).

— The use of Gaussian process regressors for the surrogate modelling step, which have the added advantages over the more traditional generalised polynomial chaos approach that they allow to easily compute confidence metrics about the estimated values [Owen et al., 2017] and are more flexible.

— The first tDCS simulation study investigating the three main sources of variability, namely head geometry, tissues properties and electrode placement on multiple experiments (different electrode montages targeting different regions of interest) using a single modelling approach.

— The development of a tool that is agnostic of the segmentation pipeline by design. This makes it more flexible than the competing software [Ziegler et al., 2014; Huang and Parra, 2015; Thielscher et al., 2015; Nielsen et al., 2018; Huang et al., 2019] that enforce a specific number and configuration of tissues. This feature allows *Shamo* to be used for a wider

range of models such as, but not limited to, non-standard heads (*i.e.*, other than healthy adults) and people with implants, prosthetics, or deformities.

— From a technological point of view, the reliance on a reduced set of dependencies, chosen based on the following criteria: they are all already published and validated, lightweight, work on most of the commonly used operating systems (both for personal computers and larger infrastructures such as HPC) and published under open source licenses. Thanks to these four conditions, *Shamo* has been successfully containerised, thus improving the portability and reproducibility of the results obtained with it. Hence, compared to *SimNIBS* and *ROAST* that both, at some point in their pipelines, rely either on *SPM* [Ashburner and Friston, 2005] or on heavy and non-portable dependencies such as *Freesurfer* [Destrieux et al., 2010; Li et al., 2013] or *FSL* [Jenkinson et al., 2012] (most of which are required only for the segmentation), *Shamo* can easily be ported onto HPC or cloud computing infrastructures. This is what allowed us to tackle a project as computationally expensive as the one described in Chapter 6.

These contributions have led to the following journal articles:

1. M. Grignard, C. Geuzaine, and C. Phillips. Shamo: A Tool for Electromagnetic Modeling, Simulation and Sensitivity Analysis of the Head, *Neuroinformatics*, Mar. 2022. ISSN 1559-0089. url: `https://doi.org/10.1007/s12021-022-09574-7`. (See Apendix A).

2. M. Grignard, C. Geuzaine, M. Hansenne, S. Majerus, and C. Phillips. Why tDCS models cannot be trusted yet? — A simulation study, preprint. url: `https://hdl.handle.net/2268/294662` (See Appendix B).

Part of this work has also been presented in the following international conferences:

1. M. Grignard, C. Geuzaine, and C. Phillips. Global sensitivity analysis of the EEG forward problem. Poster session presented at OHBM 2020, Online. url: `https://hdl.handle.net/2268/250120`.

2. M. Grignard, C. Geuzaine, and C. Phillips. Shamo v1.0 - Stochastic electromagnetic head modelling made easy. Poster session presented at OHBM 2021, Online. url: `https://hdl.handle.net/2268/263309`.

3. M. Grignard, C. Geuzaine, and C. Phillips. Shamo: A tool for electromagnetic modeling of the head. Oral presentation at ACOMEN 2022, Liège, Belgium. url: `https://hdl.handle.net/2268/294695`.

The source code of Shamo is available on Github [1] as well as the documentation [2] and tutorials [3].

---

1. `https://github.com/CyclotronResearchCentre/shamo`
2. `https://cyclotronresearchcentre.github.io/shamo/index.html`
3. `https://github.com/CyclotronResearchCentre/shamo-tutorials`

2.
Neuroscience

Electroencephalography and transcranial direct current stimulation are the two applications that *Shamo* is currently aimed at. Considering that they both rely on the biological and electrical mechanisms underlying brain activity, it is important to first introduce how the brain actually works. Then, based on this primer on neurophysiology, I give an overview of both EEG and tDCS.

In addition, I discuss the techniques used to segment structural images into multiple tissue classes and to extract specific cortex regions. Indeed, these methods are part of either the model definition process or the analysis of the results.

2.1. Brain activity

In this section, I first give an overview of the brain anatomy and functioning to provide sufficient information for the reader to understand the upcoming modelling chapter. Then, using a top-down approach, I focus on the microscopic scale to discuss the mechanisms of neurons and synapses.

2.1.1. Brain architecture

The brain is composed of three distinct parts: the *cerebrum*, *cerebellum* and *brainstem*, as shown in Figure 2.1a [Snell, 2010; Mtui et al., 2021].

The largest part, the *cerebrum*, is responsible for most higher functions, from sensory integration to emotion regulation and learning. It is further split into left and right hemispheres connected together by the *corpus callosum*, which transmits information bidirectionally. Even though the cerebrum looks symmetrical on a structural level, both hemispheres do not share all their functions.

The second part, located under the cerebrum, is called the *cerebellum* and is in charge of functions like balance and movement coordination. The cerebellum is connected to the cerebrum and to the *spinal cord* by the *brainstem*, which controls autonomic functions. Among other things, it takes part in the regulation of the sleep-wake cycle, and is in charge of respiration and cardiac acivity.

The whole brain as well as the spinal cord are surrounded by *cerebrospinal fluid (CSF)*. It is produced by the *choroid plexus*, located inside cavities of the brain called *ventricles* that are depicted

(a)

1 Cerebrum
2 Cerebellum
3 Brainstem

(b)

1 Lateral ventricles
2 Third ventricle
3 Fourth ventricle
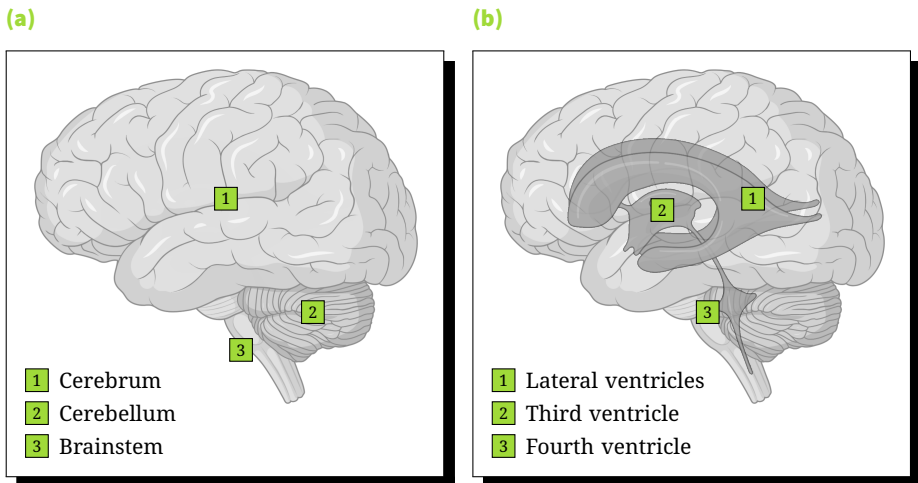
Figure 2.1 **(a)** **A sagittal view showing the different parts of the brain, and (b) the same view with visible ventricles.**

in Figure 2.1b. This fluid helps to absorb shocks and prevents injuries.

The surface of the cerebrum, *the cortex*, is folded in order to increase its surface area. The ridges are referred to as *gyri*, while the fissures are called *sulci*. Based on these sulci, the hemispheres have been divided into four distinct lobes: frontal, temporal, parietal, and occipital (See Figure 2.2).

Located above and behind the eyes, the *frontal lobe* is responsible for emotions, personality, judgement, concen-

Frontal lobe
Temporal lobe
Parietal lobe
Occipital lobe
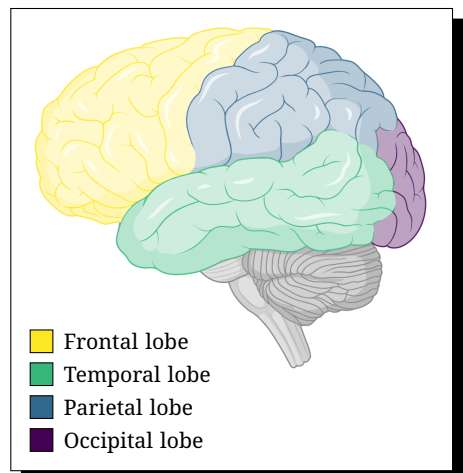
Figure 2.2 **The functional lobes presented on the left hemisphere.**

tration, etc. It also contains *Broca's area* which handles language production and the *motor strip* controlling movements. The *occipital lobe*, at the back of the brain, mainly handles vision. The *temporal lobe* manages memory and hearing. It also shares language interpretation with the *parietal lobe* through *Wernicke's area*. Finally, the parietal lobe processes signals from different senses and controls spatial perception. It also embeds the *sensory strip*, providing sense of touch and pain.

2.1.2. Neuron anatomy and functioning
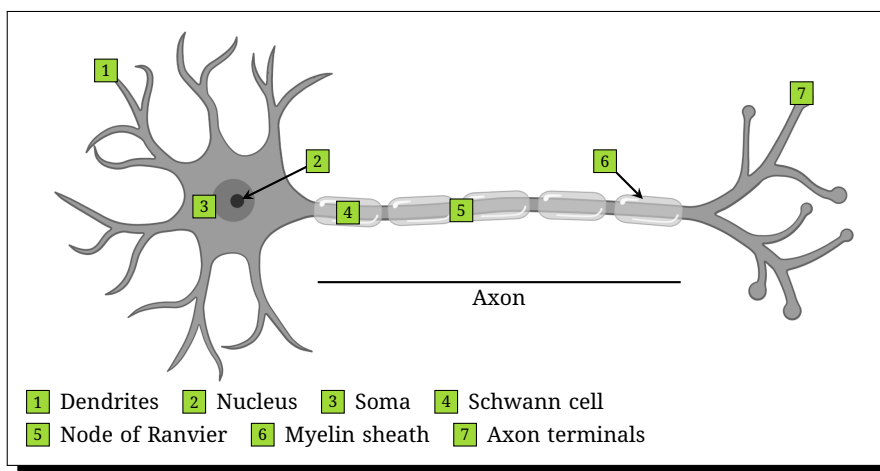
Figure 2.3   The anatomy of a neuron.

The cerebrum and cerebellum are respectively composed of around 16 billion and 70 billion *neurons* arranged in layers. Neurons are composed of two main parts: the cell body and the axon (See Figure 2.3).

The cell body, called *soma*, contains the nucleus, but also the mitochondria and all the other common components of any cell. Its

role is to keep the neuron functioning properly [Luengo-Sanchez et al., 2015]. This part is responsible for the colour of the *grey matter*. The *dendrites* are short processes of the soma that transmit impulses, also known as *afferent signals*, from other cells to the cell body [Malmivuo and Plonsey, 1995]. Impulses are transferred from the soma to other cells by a long nerve fibre, the *axon*. It may be covered with a discontinuous insulating layer called *myelin sheath*. The disjunctions of this coating are named *nodes of Ranvier* and mark the separation between two *Schwann cells*. The axons compose the *white matter*.

Synapse

(a)   **(b)**
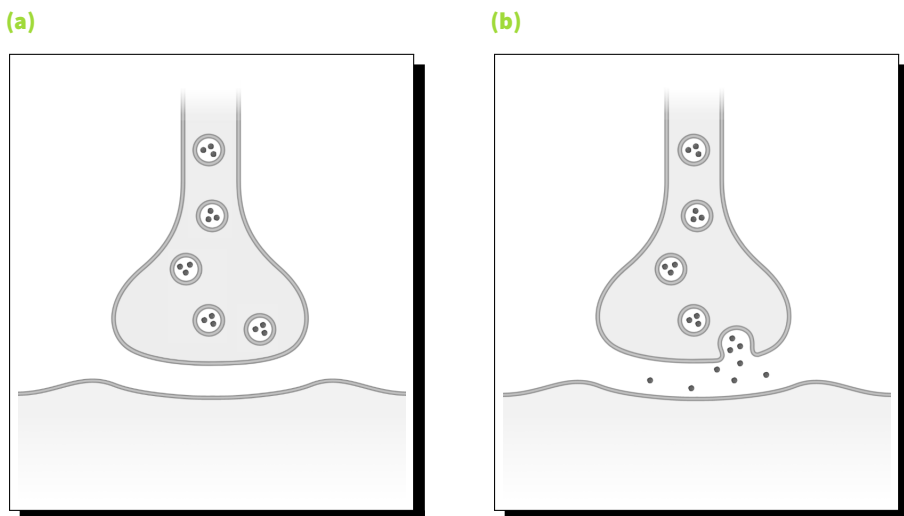
Figure 2.4 **The anatomy of a synapse (a) at rest and (b) activated.**

At its end, the axon splits into branches terminated by small rounded swellings containing the neurotransmitter substance, the *synaptic vesicles* or *terminal buttons*, that connect with other nerve cells to form *synapses*.

Impulses travel across synapses in only one direction, *i.e.* from the *presynaptic terminal* to the *postsynaptic terminal,* thanks to the anatomy of the synapse and to its biochemical mechanism. Indeed, between the two terminals lies a small gap of a few tens of nanometres, the *synaptic cleft*, that no current actually crosses (See Figure 2.4a. The presynaptic terminal has to release chemical transmitter to activate the postsynaptic terminal via its receptors, as presented in Figure 2.4b [Purves, 2004].

Cell membrane
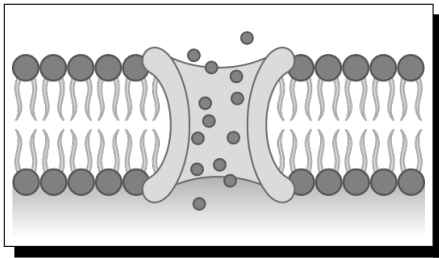
Figure 2.5   The cell membrane composed of two layers of phosphoglycerides and a macromolecular pore.

The nerve cells are enclosed by a thin membrane mainly constituted of fatty acids, the *phosphoglycerides*.

Those molecules are composed of a *phosphoric acid* attracted by water or *hydrophilic* and of *glycerides* repelled by water or *hydrophobic*. These opposed behaviours lead to the formation of a double layer of lipid with hydrophobic tails on the inside when placed in water, which forms the structure of the cell membrane (See Figure 2.5) [Thompson and Tillack, 1985].

Macromolecular pores in the membrane, the *ionic channels*, allow chloride (Cl^-), sodium (Na^+) and potassium (K^+) ions to flow through the membrane. These ions cause a difference of potential between the inside and the outside, the *trans-membrane potential* denoted by $u_m = v_{in} - v_{out}$ [Bullock, 1959]. Its value is typically between -60 and -70 mV and is regulated by Na^+ and K^+ ion pumps inside the membrane.

This resting potential is described by the *Goldman-Hodkin-Katz (GHK)* voltage equation [Reuss, 2008]. Under zero flux condition,

this equation provides the membrane voltage as a function of the concentration of the permeant ions (Na$^+$, K$^+$ and CL$^-$) and the permeabilities,

$$u_\mathrm{m} = -\frac{RT}{F} \ln \frac{p_\mathrm{Na} m_{\mathrm{Na}^+}^{(in)} + p_\mathrm{K} m_{\mathrm{K}^+}^{(in)} + p_\mathrm{Cl} m_{\mathrm{Cl}^-}^{(out)}}{p_\mathrm{Na} m_{\mathrm{Na}^+}^{(out)} + p_\mathrm{K} m_{\mathrm{K}^+}^{(out)} + p_\mathrm{Cl} m_{\mathrm{Cl}^-}^{(in)}} \qquad \textbf{Eq. 2.1}$$

where R is the gas constant ($8.314\,\mathrm{J\,mol^{-1}\,K^{-1}}$), T is the absolute temperature (K), F is the Faraday constant ($96\,485.332\,\mathrm{C\,mol^{-1}}$), p_i is the permeability of the membrane to element i ($\mathrm{mol\,m^{-1}\,s^{-1}\,Pa^{-1}}$) and $m_i^{(j)}$ is the concentration of ion i in solution j ($\mathrm{mol\,m^{-3}}$).

Excitability

Once neurotransmitters reach the postsynaptic receptors, the permeability of the membrane changes depending on the effect of the emitted neurotransmitters [Vanrumste, 2002; Schomer and Lopes da Silva, 2011]. The flow of ions and the membrane potential thus change. Neurotransmitters can produce stimulations of two types.

Excitatory stimulations are depolarising and result in a higher membrane potential due to an inflow of positively charged Na$^+$ ions. This depolarisation is referred to as the *excitatory postsynaptic potential (EPSP)*.

On the other hand, *inhibitory stimulations* are hyper-polarising and lead to an increase of the membrane potential correlated with an inflow of negatively charged ions (or an outflow of positively charged K$^+$ ions). It is called an *inhibitory postsynaptic potential (IPSP)*.

If the result of the numerous EPSPs and IPSPs occurring at a postsynaptic neuron, referred to as *net depolarisation*, is higher than a certain threshold, the membrane produces the *nerve impulse* that flows along the axon. Otherwise, it remains inactive as presented in Figure 2.6.

In this process, the global electrical potential can be split into two sources. *Postsynaptic potential (PSP)* is the potential of the membrane of the postsynaptic terminal resulting from all the EPSPs and IPSPs and *action potential* is the potential resulting from the excitation of the cell and corresponding to the propagation of the nerve impulse. The latter has a very short lifespan.
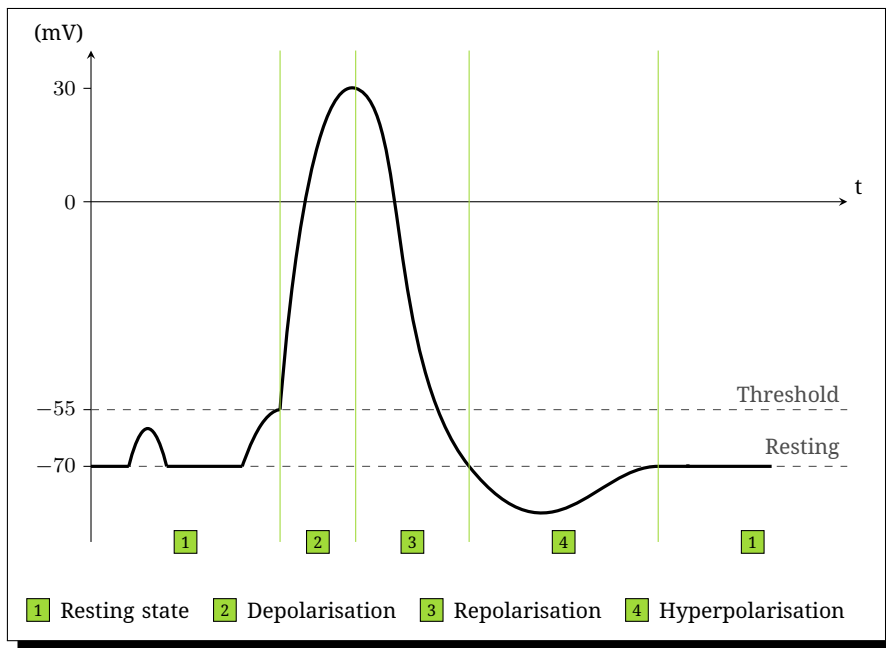

Figure 2.6 **A plot of the trans-membrane potential showing the action potential. If the stimulus potential does not reach the threshold, no pulse is emitted. Otherwise, a pulse where four phases are differentiated is emitted. The depolarisation where Na$^+$ ions enter the membrane, the re-polarisation where K$^+$ ions exit the membrane, leading to the hyper-polarisation. Finally, the resting state is reached once the equilibrium is recovered.**

2.2. Electroencephalography

Electroencephalography (EEG) is a non-invasive brain activity measurement technique [Schomer and Lopes da Silva, 2011]. It consists in measuring the electric potential on the scalp of a subject induced by the inner activity of the brain using electrodes, or *channels*, and a digital voltmeter (See Section 2.2.2). The resulting signal is called an *electroencephalogram* with normal amplitude up to $100\,\mu V$ with frequencies ranging from under $1\,\mathrm{Hz}$ up to $150\,\mathrm{Hz}$ (See Figure 2.7) [Synigal et al., 2020].
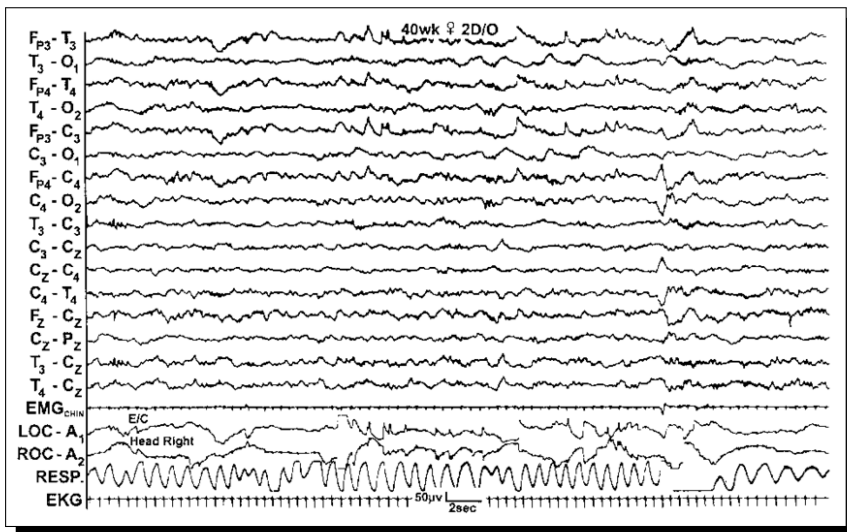
Figure 2.7   **An example of an electroencephalogram [Scher, 2011].**

As explained by Schaul [1998] and Schomer and Lopes da Silva [2011], the electrodes used for EEG can only detect the potential resulting from the sum of the PSPs occurring at numerous neurons (See Section 2.1). Indeed, due to their short duration, action poten-

tials are very unlikely to fire synchronously. On the other hand, even though their amplitude is lower, PSPs can last up to 30 times longer than action potentials. This means that the activity of neighbouring neurons can add up and gets recorded by the electrodes.

Once acquired, the recorded signal is preprocessed to remove artefacts resulting from non-physiological and physiological sources. Indeed, there are several factors that can deteriorate the quality of the signal, ranging from practical issues such as broken electrodes or a bad contact between the electrode and the skin to subject movements and cardiac pulses. These artefacts are usually removed from the data by visual inspection. However, the increasing volume of data to be processed has lead to the development of automated tools to achieve this task [Coppieters't Wallant et al., 2016a,b]. One of the papers I participated in aimed at validating such a tool [Chylinski et al., 2020].

After cleaning the EEG data, it can be used for different analysis (*e.g.*, time-frequency based analysis). The one we are interested in for this thesis is the *source reconstruction*, also referred to as *source imaging*. The goal of this process is to retrieve the electrical brain sources which induced the recorded signal and is further detailed in Section 3.1.

2.2.1. Applications

Since its invention, EEG has been applied to a variety of both medical and nonmedical applications.

One major medical application of EEG is the identification and prediction of seizures in epileptic patients [Noachtar and Rémi, 2009; Chen and Koubeissi, 2019], but it has also been investigated to detect other brain disorders such as Alzheimer's and Parkinson's diseases [Cassani et al., 2018; Geraedts et al., 2018; Ando et al., 2021; Miladinović et al., 2021], brain tumours and strokes [Hetkamp et al.,

2019; Shreve et al., 2019; Vatinno et al., 2022] or to assess traumatic brain injury [Rapp et al., 2015; Ianof and Anghinah, 2017].

EEG also helps better understanding fatigue [Tran et al., 2020b; Jing et al., 2020] and sleep cycles and disorders [Cox and Fell, 2020; Berthomier et al., 2020; Zhao et al., 2021]. It can even be used to study mental states and emotions [Liu et al., 2021; Rahman et al., 2021; Perrottelli et al., 2021] or to evaluate cognitive load [Antonenko et al., 2010; Friedman et al., 2019; Tamanna and Parvez, 2021].

The high frequency signature of the electric activity of the brain that EEG captures has also been evaluated as a brain-computer interface in the rehabilitation of subjects using brain controlled video games [Remsik et al., 2016; Baniqued et al., 2021] or to help people suffering from locked-in syndrome communicating or controlling a wheelchair [Al-qaysi et al., 2018; Wang et al., 2021a]. While first intended for medical aiding devices, these interfaces were also used for nonmedical applications such as controlling drones or video games [Kerous et al., 2018; Al-Nuaimi et al., 2020; Villegas et al., 2021].

2.2.2. Electrodes

Typical EEG electrodes have a diameter of approximately $10\,\text{mm}$ but some manufacturers provide electrodes with diameters as small as 7 or $4\,\text{mm}$ [Hajare and Kadam, 2021]. The way they are modelled is discussed in Section 4.2.

For standardisation purposes, various electrode placement setups have been proposed. Using such a guide to place the scalp electrodes for both EEG and tDCS (See Section 2.3) increases the quality of the recording by making it more reliable and reproducible.

Anatomical landmarks

To define a consistent and repeatable placement process, easily identifiable reference anatomical landmarks, also referred to as *fiducials*, have been selected.
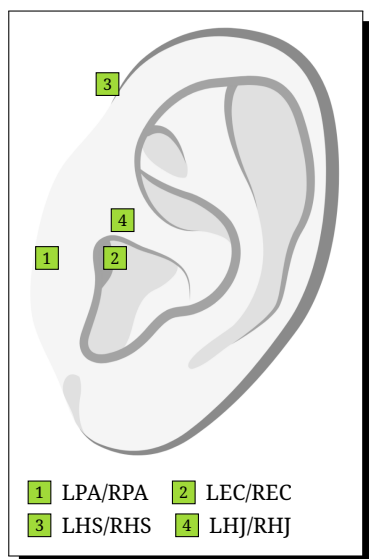
Figure 2.8 **The most commonly used ear anatomical landmarks.**

First, the *nasion (NZ)* locates the junction between the bridge of the nose and the forehead. At the opposite, the *inion (IZ)* is the highest point of the external occipital protuberance. Those two points define the anterior to posterior axis.

The choice for the left and right fiducials is not as straightforward. Indeed, there are several commonly used landmarks (See Figure 2.8). The default is to use left and right *pre-auricular points (LPA/RPA)* but, while they are palpable during an acquisition session, they are hard to identify in structural images.

This is the reason why laboratories tend to use other standards such as the *ear canal (LEC/REC)*, the *helix-scalp junction (LHS/RHS)* or the *helix-tragus junction (RHJ/LHJ)*. The latter is preferred since it is better defined in anatomical images.

> **Note** The notations for the different ear anatomical landmarks are sometimes mixed, which can lead to erroneous positioning of the electrodes in computer analysis. It is thus recommended, when sharing a dataset, to clarify which fiducials were actually used during the acquisition.

10-20 international system

The 10-20 international system is the most commonly used electrode placement scheme. The guide relies on splitting the distance between pairs of fiducials (*i.e.*, the two ears or the nasion and inion) using 10 % and 20 % ratios, as shown in Figure 2.9.

(a)

(b)
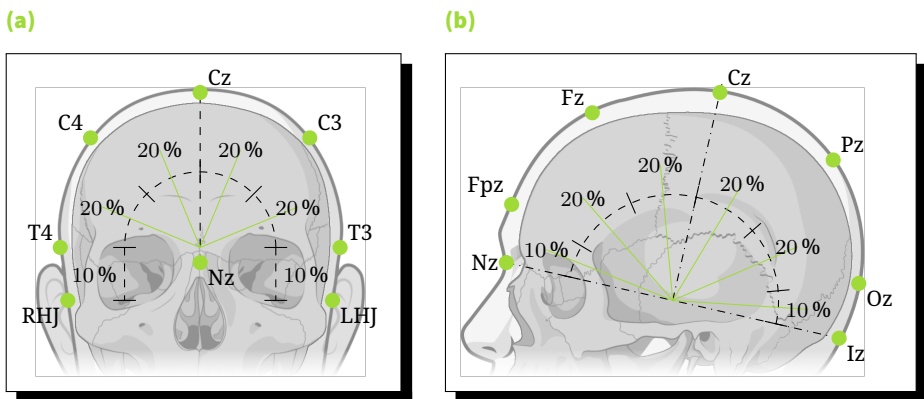
Figure 2.9   The EEG 10-20 international system ratios shown from (a) the front and (b) the side of the head.

In the proposed placement system, each sensor is labelled based on the brain hemisphere and lobe located directly underneath. Labels are composed of two parts, the lobe identifier and the position index. The 10-20 system defines notations for pre-frontal (Fp), frontal (F), parietal (P), central (C) and temporal (T) channels. For the numbering, left (respectively right) hemisphere electrodes use odd (respectively even) numbers, while those on the central line are indexed with "z" for zero.

To increase the spatial resolution of the recorded signal, other setups have been created by placing additional electrodes in-between those of the 10-20 system using ratios of 10 % and 5 % for the 10-10 and 10-5 systems respectively. Figure 2.10 provides a description of both the 10-20 and 10-10 systems.
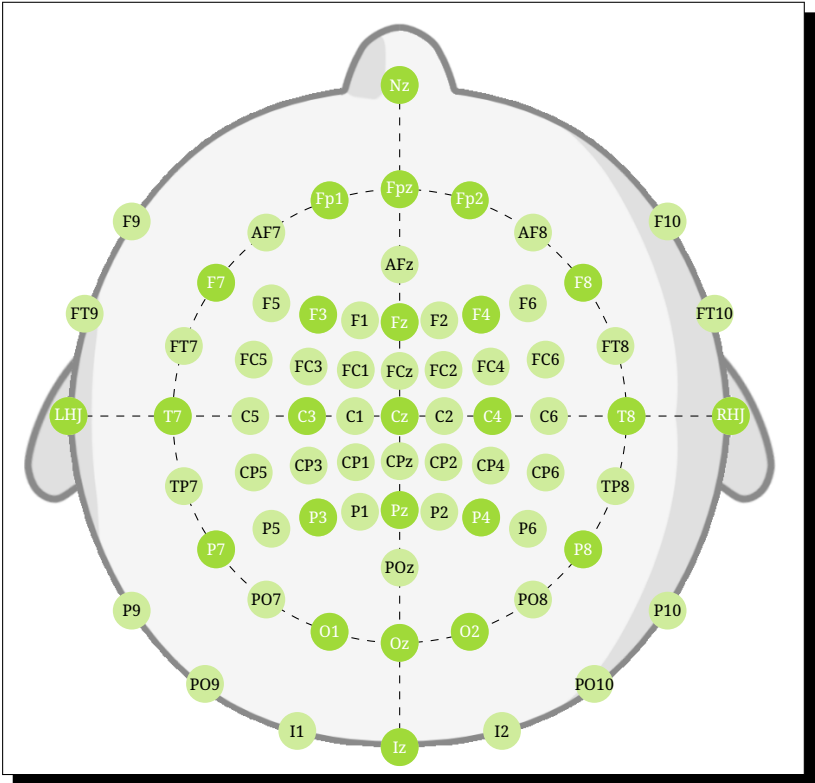
Figure 2.10   **The international EEG 10-10 electrode labels and positions with electrodes from the 10-20 system and fiducials highlighted.**

2.3. Transcranial direct current stimulation

Transcranial direct current stimulation (tDCS) is a non-invasive brain stimulation technique [Woods et al., 2016]. It consists in injecting a small amount of direct electric current, generally between 1 and $2\,\mathrm{mA}$ through the head of a subject, by the mean of large electrodes (around $5 \times 5\,\mathrm{cm}^2$) placed on the scalp using the EEG International system (See Section 2.2.2).

The stimulating electrode, the *anode*, is placed above the target brain region of interest. On the other hand, the reference electrode, the *cathode*, is located either above the same region from the opposite hemisphere in a *bipolar* electrode montage, on the contralateral orbit region in a *unipolar* montage or on a silent zone of the body such as the deltoid muscle, the chin, or the neck [Nitsche et al., 2008; Kropotov, 2016].
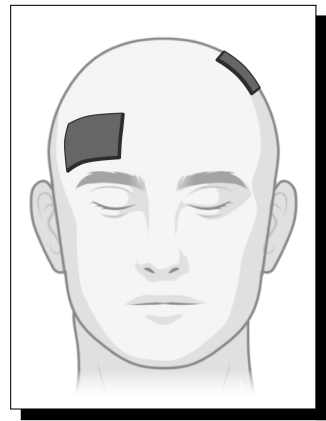
Figure 2.11 **An example of electrode montage for tDCS.**

> **Note** Transcranial direct current stimulation has been shown to be safe to use and well tolerated for both adults [Nitsche et al., 2003; Brunoni et al., 2011] and younger individuals [Buchanan et al., 2021].

The large electrodes used in traditional tDCS make simultaneous EEG recording very difficult since they interfere with the EEG

channels located around the stimulation electrodes [Spitoni et al., 2013]. In addition, they produce a diffused electric field, thus they are not suitable for precise target stimulation. To try solving these issues, *high definition transcranial direct current stimulation (HD-tDCS)* has been investigated [Datta et al., 2009; Borckardt et al., 2012; Edwards et al., 2013; Roy et al., 2014; Parlikar et al., 2021]. This method uses electrodes of size comparable to the ones used for EEG (*i.e.*, around 10 mm in diameter) arranged in a circle formation, with the stimulating electrode in the centre and multiple reference electrodes around. It has been shown to induce increased current density during the stimulation and to have a better spatial resolution [Dmochowski et al., 2011; Villamar et al., 2013].

Since the beginning of the century, both methods have received increased interest, mostly due to their affordability, their simplicity and their wide range of applications. For instance, searching for "tDCS" on PubMed yields 83 between 2001 and 2005 [1] and 4059 between 2016 and 2020 [2].

2.3.1. Applications

As described in the previous section, tDCS is an easy to perform, portable and affordable neuromodulation technique. Consequently, it has been investigated in a wide variety of applications.

For instance, it has been considered as a treatment for some neurological conditions such as Parkinson's disease, stroke [Hummel et al., 2005; Fregni et al., 2005; Boggio et al., 2007] and refractory epilepsy [San-Juan et al., 2015; Yang et al., 2019], but also for pain conditions like fibromyalgia [Fagerlund et al., 2015; Lloyd et al., 2020] and traumatic spinal cord injury [Ngernyam et al., 2015; Li

---

1. `https://pubmed.ncbi.nlm.nih.gov/?term=tDCS&filter=years.2001-2005`
2. `https://pubmed.ncbi.nlm.nih.gov/?term=tDCS&filter=years.2016-2020`

et al., 2021]. It has also been tested on psychiatric indications such as depression [Boggio et al., 2008; Jog et al., 2019; Razza et al., 2020], bipolar disorder [Dondé et al., 2018], addiction [Lapenta et al., 2018; Chen et al., 2020], schizophrenia [Agarwal et al., 2013] or anxiety disorders [Stein et al., 2020]. In addition to that, it has been evaluated as an enhancement device for healthy subjects [Ke et al., 2019; Weller et al., 2020].

The sheer volume of work relying on tDCS that is published every year and the wide variety of applications clearly indicates that there is a great interest in the method.

2.3.2. Physiological effects

Transcranial direct current stimulation cannot produce neuronal action potentials due to the low range of the generated static fields. Thus, it is often referred to as a neuromodulation technique rather than neurostimulation. Indeed, its main physiological mechanism is the modulation of the resting membrane potential of the pyramidal neurons composing the cortical surface, depending on their relative orientation [Nitsche and Paulus, 2000; Stagg et al., 2018]. If it yields a depolarisation of the membrane, it is supposed to increase the excitability of the neuron by lowering the afferent activity required to induce action potential. On the contrary, the neuronal activity is reduced if the electric fields results in a hyperpolarisation of the membrane [Cambiaghi et al., 2010; Zaghi et al., 2010; Stagg and Nitsche, 2011; Pelletier and Cicchetti, 2015].

The alteration of the membrane potential induced by tDCS is proposed to be approximately 0.2 to $0.5\,$mV [Radman et al., 2009; Opitz et al., 2016] which seems negligible in comparison to the resting state potential of the membrane of around $-70\,$mV and to the action potential threshold of -55 to $-50\,$mV (See Section 6.10 for a more in-depth analysis of the induced trans-membrane poten-

tial resulting from tDCS). Moreover, this induced potential does not outlast the stimulation.

Still, after-effects of tDCS have been observed in the following minutes up to the next 24 hours after the stimulation [Nitsche and Paulus, 2000, 2001; Jamil et al., 2017]. Some repeated protocols are even considered expanding the duration of these long-lasting effects to several weeks [Boggio et al., 2008; Reis et al., 2009]. Such long-term effects have been attributed to neuro-plasticity. For more information on the topic, I redirect the interested reader to the recent work of Stagg et al. [2018].

2.3.3. Variability

Whilst more and more research projects focused on tDCS in the last years, two major issues rose up: the inter-subject variability in the responses to the stimulation and the lack of reproducibility of some published results in follow-up studies.

> *" The main conclusion is that the after-effect of this type of tDCS on corticospinal excitability is highly variable.*
> — Wiethoff et al. [2014]

Indeed, the effects of tDCS are highly variable, with subject responses to the same protocol ranging from the expected one to its opposite to no response at all. The most concerning fact being the percentage of expected response, which is generally lower than 50% for protocols targeting the motor cortex and even smaller for cognitive tasks [Müller-Dahlhaus et al., 2008; Jacobson et al., 2012; Wiethoff et al., 2014]. In their systematic review, Horvath et al. [2015] showed that, over 30 neurophysiological measurements, tDCS only had a reliable effect on *motor evoked potential (MEP)* amplitude.

These variable results gave birth to numerous studies investigating different factors of variability such as anatomical features, age, sex or genetics [Laakso et al., 2015; Rudroff et al., 2020]. For a good overview of the variability induced by these factors and more, refer to the review of Li et al. [2015].

> *This work raises questions concerning the mechanistic foundations and general efficacy of this device – the implications of which extend to the steadily increasing tDCS psychological literature.*
>
> — Horvath et al. [2015]

The main solution being worked on currently to reduce the inter-subject variance is to tailor the protocol for each subject (*e.g.,* set the current intensity) based on individual measurements [Albizu et al., 2020]. Unfortunately, the recent work from Sallard et al. [2021] shows that this approach might not improve the efficacy of tDCS over the primary motor cortex.

2.4. Head tissue segmentation

The human head, like any other part of the body, is composed of several tissues. Unfortunately, extracting the spatial distribution of those tissues from anatomical images (*e.g.,* MRI and CT) is not an easy task. It is referred to as *segmentation* and has been studied for the past decades. New methods are still being developed nowadays. This problem is part of the family of the classification problems.

We denote the volume of the head by $\Omega_{\text{head}} \subset \mathbb{R}^3$ and its bounding surface by Γ_{head} [Darbas and Lohrengel, 2018]. The goal of the segmentation is to divide Ω_{head} into distinct subdomains Ω_i bounded
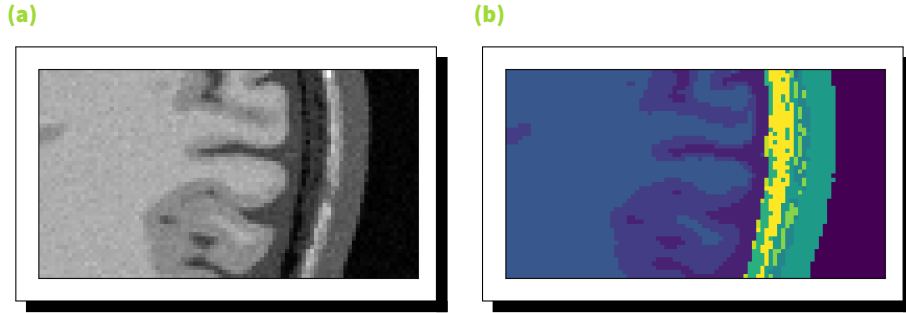
Figure 2.12 **(a)** A zoomed in view of a T1-weighed image and **(b)** the resulting segmented tissue classes. These images are based on data provided by the BrainWeb dataset [Aubert-Broche et al., 2006b].

by Γ_i where $i = 1, \ldots, n_{\text{tissues}}$, such that

$$\Omega_{\text{head}} = \cup_{i=1}^{n_{\text{tissues}}} \Omega_i,$$
$$\Omega_i \cap \Omega_j = \emptyset \ \forall \ i \neq j.$$

The anatomical images provide a discrete representation of the head, *i.e.* the data is acquired for small regular volumes called *voxels*. Based on the number of different modalities m, each voxel can be represented as a vector $\boldsymbol{x} = [x_1, \ldots, x_m]$. The segmentation process associates these vectors with a tissue class $y \in [0, n_{\text{tissues}}]$ by minimising the intra-class variance and maximising the inter-class variance, as shown in Figure 2.12.

One of the main parameters of this operation is the number of tissues to classify. Indeed, the human head is composed of a wide range of biological tissues that can be hard to differentiate using only non-invasive techniques (See Figure 2.13).

2.4.1. Manual segmentation

One of the existing methods to segment the head is to do it manually, meaning classifying each and every voxel of the volume by hand. This is generally used when subjects present deformities, or to segment non-healthy tissues such as tumors or lesions.

To help increase the efficiency of this slow task, tools have been developed such as *ITK-SNAP* [Yushkevich et al., 2006]. It makes it easier to produce binary masks for the tissues in 3D by providing useful features such as mask visualisation and flood filling wizard.

Nevertheless, manually segmenting the whole head of a subject remains inefficient and time-consuming. Moreover, by solely relying on the mastery of the tools and knowledge about the specific tissues classes of the operator, this method is highly error-prone and lacks of reproducibility, which are two major concerns in the field of neuroimaging.

1	WM	2	GM	3	CSF	4	Scalp
5	Blood vessels	6	Dura	7	Fat
8	Bone (Compact)	9	Bone (Spongy)

Figure 2.13 **A subset of the biological tissues composing the human head.**

Nowadays, manual segmentation is only required for tasks that automated segmentation tools are not able to perform, such as segmenting heads with abnormal or specific tissue classes.

2.4.2. Automated segmentation

To solve most of the issues raised by manual segmentation, fully automated whole head segmentation pipelines have been proposed [Ashburner and Friston, 2005; Perdue and Diamond, 2014; Huang and Parra, 2015; Mahmood et al., 2015] and new ones are still being published [Huang et al., 2019; Puonti et al., 2020; Taberna et al., 2021]. The benefits of using such techniques are an increased reproducibility and a lower processing time since multiple subjects can be worked on in parallel.

Unfortunately, it also comes at a cost: the number of tissues is fixed for each method and their usage is usually limited to healthy adults. Moreover, some of these tools are only able to segment the upper part of the head, while others can segment the whole head and neck. Depending on the end goal of the segmentation, these limitations might be important.

As an example, Figure 2.14 shows the result of the segmentation of a T1-weighted image from the IXI dataset using *MR-TIM* [Taberna et al., 2021].

For a good overview of the different techniques involved in automated segmentation, I recommend the review of Despotović et al. [2015].

2.4.3. Validity

One of the main issues with tissue segmentation, be it manual or automated, is the lack of ground truth. Indeed, without dissecting the head of the subject, it is impossible to verify the exactness of the generated masks.

As discussed later in Section 3.2, the physical properties of the different tissues vary widely. Thus, changing their geometry can affect the outcome of any process relying on both the shape and properties of the head compartments (See Section 3.1).
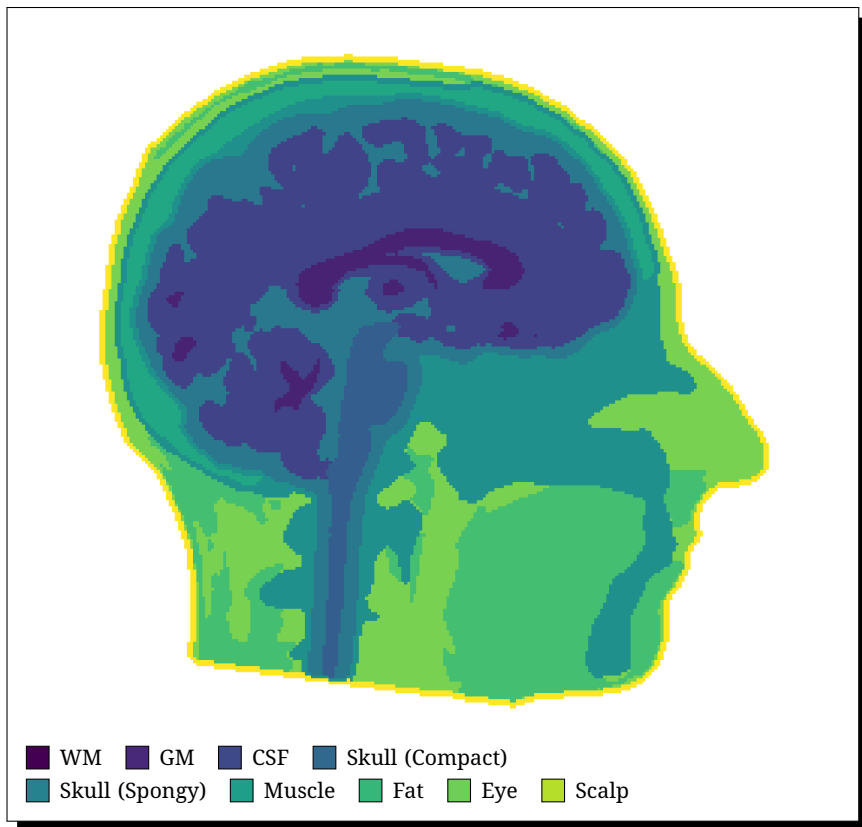
Figure 2.14   **A T1w image segmented with MR-TIM [Taberna et al., 2021].**

2.5. Cortex parcellation
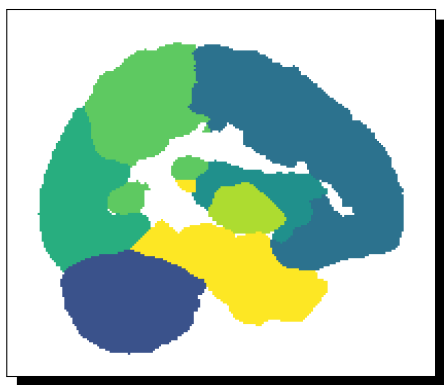
Figure 2.15   A cut of the MNI structural atlas provided with FSL.

While segmenting the different tissues can provide information about the overall structure of the head of a subject, a further step is required when studying a specific *region of interest (ROI)* of the cortex. Indeed, since different areas of the brain handle different functions (See Section 2.1), researchers often need to extract data related to a single functional or anatomical region, be it a lobe or a smaller part. As described in the tDCS application in Chapter 6 and in the corresponding paper (See Appendix B), this process is particularly useful to evaluate if the stimulation managed to induce an electric field with the expected magnitude in the ROI.

As the segmentation step focused on minimizing the intra-class variability, it is clear that one cannot rely on the same algorithms to differentiate those ROIs from structural data. Therefore, methods have been developed to achieve this exact task. They usually depend on a preliminary coregistration between the subject and a template.

> **Note** The process of coregistering one or multiple image on a reference one consists in aligning them. When the target image is a standardized space such as MNI [Grabner et al., 2006], the coregistration step is referred to as normalisation. The coregistration is said to be linear when either rigid (6 degrees of freedom) or affine (12 degrees of freedom) transformation are used. On the other hand, non-linear coregistration rely on a displacement field.

For cortex parcellation, two families of techniques coexist. The first uses volumetric atlases or ROI masks (See Figure 2.15), which are labelled structural images. An atlas, just like for the earth, is a map containing different regions. They are generally provided in the MNI template space [Grabner et al., 2006]. ROI masks can also be derived from functional tasks activation maps. This volumetric approach is the preferred one for people working with the *SPM* toolbox [Ashburner, 2000], *FSL* [Jenkinson et al., 2012] or *AFNI* [Cox, 1996].

The second family, made possible by the development of *FreeSurfer* [Dale et al., 1999], uses cortical surfaces atlases. This representation requires a computationally intensive surface reconstruction step, which results in the creation of a subject specific cortical surface and a template coregistered sibling. Atlases provided on such a template surface can then be mapped onto the subject surface. With the advent of computer speed, this approach has gained increased interest. This technique was used to determine the ROIs in Section 6.7.

3.
Modelling

After this introduction on the basics of brain anatomy and activity, I can now present the methods used to model the electric current flow through the head.

I first describe the mathematical tools involved in the simulations and the physical properties that the models account for. Then, I give an overview of sensitivity analysis and how surrogate modelling can help achieve it for computationally heavy models.

These techniques are further investigated in the applications presented in Chapters 5 and 6.

3.1. Electroquasistatic head model

In this section, I provide a quick introduction to the mathematical model used to simulate electric current flow in the head of a subject. This model relies on Maxwell's equations which, in the case I am focusing on here, reduce to a generalised Poisson equation.

After presenting these equations, I discuss the finite element method used to solve them. Finally, I explain how these simulations can be used in the context of neuroimaging to reconstruct brain activity from scalp recording of the electric potential or to assess the electrical effect of a stimulation.

3.1.1. Poisson's equation

Maxwell's equations govern the behaviour of any static or time-varying electromagnetic field. They require the definition of four vector fields: the *electric field e* (V m^{-1}), the *electric displacement d* (C m^{-2}), the *magnetic field h* (A m^{-1}) and the *magnetic flux density* or *magnetic induction b* (T).

These equations read as follows [Hämäläinen et al., 1993; Griffiths, 2017; Gratiy et al., 2017; Darbas and Lohrengel, 2018]:

$$\nabla \times e = -\frac{\partial b}{\partial t}, \qquad \text{Eq. 3.1a}$$

$$\nabla \times h = j_{\text{f}} + \frac{\partial d}{\partial t}, \qquad \text{Eq. 3.1b}$$

$$\nabla \cdot d = \rho_{\text{f}}, \qquad \text{Eq. 3.1c}$$

$$\nabla \cdot b = 0, \qquad \text{Eq. 3.1d}$$

where ρ_{f} is the *free charge density* ($\mathrm{C\,m^{-3}}$) and j_{f} the *free current density* ($\mathrm{A\,m^{-2}}$). Equations 3.1a, 3.1b and 3.1c are respectively referred to as *Faraday's law, Ampère-Maxwell's law* and *Gauss's law*.

Since all the materials can be considered as *linear* (See Definition 3.1) in the case of bio-electromagnetism, we have the following constitutive laws,

$$\boldsymbol{d} = \varepsilon\boldsymbol{e}, \qquad \text{Eq. 3.2a}$$

$$\boldsymbol{b} = \mu\boldsymbol{h}, \qquad \text{Eq. 3.2b}$$

in which ε is the *electric permittivity* of the material ($\mathrm{F\,m^{-1}}$) and μ its *magnetic permeability* ($\mathrm{H\,m^{-1}}$). The latter can be assumed as equal to that of the free space μ_0 ($12.556 \times 10^{-7}\,\mathrm{H\,m^{-1}}$) in biological tissues.

> **Definition 3.1** A material is considered as linear if its physical properties are constant and independent of the characteristics of the sources and fields applied to it.

By using the constitutive laws from Equations 3.2a and 3.2b in Maxwell's equations, we get

$$\nabla \times \boldsymbol{e} = -\mu_0 \frac{\partial \boldsymbol{h}}{\partial t},$$

$$\nabla \times \boldsymbol{b} = \mu_0 \left(\boldsymbol{j}_{\mathrm{f}} + \varepsilon \frac{\partial \boldsymbol{e}}{\partial t} \right),$$

$$\nabla \cdot \boldsymbol{e} = \frac{\rho_{\mathrm{f}}}{\varepsilon},$$

$$\nabla \cdot \boldsymbol{b} = 0.$$

In addition, *Ohm's law* provides a relation between the current density and the electric field,

$$\boldsymbol{j}_{\mathrm{f}} = \boldsymbol{j}_{\mathrm{p}} + [\kappa]\boldsymbol{e}, \qquad \text{Eq. 3.3}$$

with j_{p} the *primary current density* (*i.e.*, the neural induced current density) and $[\kappa] \in \mathbb{R}^{3\times3}$ the *electric conductivity* positive definite

tensor (S m^{-1}). For more information on the electrical conductivity of biological tissues, refer to Section 3.2. The $[\kappa]e$ term is sometimes called *return current*.

Quasi-static conditions

By combining Equations 3.1b and 3.3, we get

$$\boldsymbol{\nabla} \times \boldsymbol{b} = \underline{\mu_0} \left(\boldsymbol{j}_\mathrm{p} + [\kappa]\boldsymbol{e} + \varepsilon \frac{\partial \boldsymbol{e}}{\partial t} \right).$$

The frequencies of physiologically induced fields are low (*i.e.*, less than a few thousand hertz). Given the typical values of the electrical conductivity, displacement currents (the time-derivative term) can be neglected compared to the ohmic current, i.e.,

$$\left| \varepsilon \frac{\partial \boldsymbol{e}}{\partial t} \right| \ll |[\kappa]\boldsymbol{e}|,$$

and Ampère-Maxwell's law reduces to

$$\boldsymbol{\nabla} \times \boldsymbol{b} = \underline{\mu_0} \left(\boldsymbol{j}_\mathrm{p} + [\kappa]\boldsymbol{e} \right).$$ **Eq. 3.4**

Thus, the capacitive effect of the biological tissues can be neglected [Plonsey and Heppner, 1967], meaning that no charge can build up. Moreover, if the eddy currents created by the time variation of the magnetic field are also neglected, which is again a good approximation given the frequencies of interest, Faraday's law 3.1a becomes

$$\boldsymbol{\nabla} \times \boldsymbol{e} = 0.$$ **Eq. 3.5**

In other words, even though the sources change over time, the resulting fields behave as if they were stationary. This means that at a time t, the fields can be computed as if the sources were static. This is referred to as *quasi-static conditions*.

Generalized Poisson equation

Under the quasi-static conditions, Equation 3.5 implies that the electric field derives from a scalar potential v which is the *electric potential* (V),

$$\boldsymbol{e} = -\boldsymbol{\nabla} v. \qquad \text{Eq. 3.6}$$

On the other hand, no charge can be piled up and Equation 3.4 implies

$$\boldsymbol{\nabla} \cdot \boldsymbol{j}_{\mathrm{f}} = 0. \qquad \text{Eq. 3.7}$$

By combining Equations 3.3, 3.6 and 3.7 [Darbas and Lohrengel, 2018], we obtain

$$\boldsymbol{\nabla} \cdot ([\kappa] \boldsymbol{\nabla} v) = \boldsymbol{\nabla} \cdot \boldsymbol{j}_{\mathrm{p}},$$

where the right-hand side term $\boldsymbol{\nabla} \cdot \boldsymbol{j}_{\mathrm{p}}$ is known as the *current source density* ($\mathrm{A\,m^{-3}}$) [Hallez et al., 2007] and will be denoted by f in the rest of this chapter. The final form of *Poisson's differential equation* is

$$\boldsymbol{\nabla} \cdot ([\kappa] \boldsymbol{\nabla} v) = f. \qquad \text{Eq. 3.8}$$

Boundary conditions

As explained in Section 2.4, the domain determined by the head volume Ω_{head}, bounded by Γ_{head}, can be divided in several compartments Ω_i bounded by Γ_i and interconnected by interfaces $\Gamma_{i,j}$. Conditions set on Γ_{head} are called *boundary conditions*, while those set on interfaces $\Gamma_{i,j}$ are referred to as *transmission conditions*. At those interfaces and boundaries, two types of conditions are encountered.
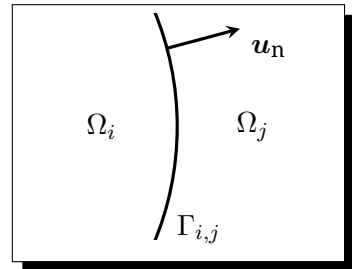
Figure 3.1 **Interface between compartments of the conductive volume.**

First, let us consider the interface between two subdomains. Since we use the quasi-static approximation, the current leaving the compartment Ω_i through the interface $\Gamma_{i,j}$ must enter the compartment Ω_j. We denote by $[\kappa]_i$ and $[\kappa]_j$ the electrical conductivity of the subdomains and by $\boldsymbol{u}_\mathrm{n}$ the normal unitary vector of the interface. This condition reads as

$$\boldsymbol{j}_i \cdot \boldsymbol{u}_\mathrm{n} = \boldsymbol{j}_j \cdot \boldsymbol{u}_\mathrm{n}$$
$$\Leftrightarrow ([\kappa]_i \boldsymbol{\nabla} v_i) \cdot \boldsymbol{u}_\mathrm{n} = ([\kappa]_j \boldsymbol{\nabla} v_j) \cdot \boldsymbol{u}_\mathrm{n}.$$

Eq. 3.9

When considering an interface between a domain Ω_i and the air $\Gamma_{i,\mathrm{air}}$, no current can cross the boundary. Thus, the right-hand side of Equation 3.9 is equal to 0. It gives the *homogeneous Neumann boundary condition*:

$$\boldsymbol{j}_i \cdot \boldsymbol{u}_\mathrm{n} = 0$$
$$\Leftrightarrow ([\kappa]_i \boldsymbol{\nabla} v_i) \cdot \boldsymbol{u}_\mathrm{n} = 0.$$

Eq. 3.10

For the boundaries $\Gamma_{i,j}$, the second boundary condition states that the electric potential is continuous across the interface,

$$v_i = v_j.$$

Eq. 3.11

In the special case of an interface between a domain and an electrode where an electric potential is imposed, it is referred to as a *Dirichlet boundary condition*.

3.1.2. Current dipole

As discussed in Section 2.2, the macroscopic brain activity measured while performing an electroencephalography results from the sum of the synchronised activation of several neurons. This electrical behaviour can be modelled as a point electric current dipole [Hallez et al., 2007; Darbas and Lohrengel, 2018].

Generally, a current dipole can be thought of as a conductive wire carrying electric current characterised by its position in space r_d, set to the centre of the two mono-poles, and its dipole moment vector $p \in \mathbb{R}^3$ (A m) such that

$$p = p\,u_d = i \cdot d\,u_d, \qquad \textbf{Eq. 3.12}$$

where i is the injected or removed amount of current (A), d is the distance between the two mono-poles (m) and $u_d = [u_x, u_y, u_z]$ is the direction vector going from the current sink to the current source. A point dipole is the special case where $d \to 0$ and $i \to \infty$ while p remains finite.

The primary current density introduced in Equation 3.3 due to a single point electric current dipole and calculated at a point r is

$$j_p(r) = p\delta(r - r_d),$$

with δ the three-dimensional *Dirac delta distribution* (m^{-3}), meaning that the primary current density is equal to 0 everywhere, except at the position of the dipole r_d.

Figure 3.2 **The electric potential induced by a current dipole oriented along the horizontal axis shown as equipotential lines. The dashed lines correspond to negative potential.**

Thanks to the *superposition principle* (See Definition 3.2), the primary current density resulting from n_d point electric current dipoles can be calculated with

$$j_p(r) = \sum_{m=1}^{n_d} p_m\delta(r - r_m), \qquad \textbf{Eq. 3.13}$$

where

$$r_m \neq r_l, \forall\, m \neq l$$
$$p_m \neq \mathbf{0}, \forall\, m \in \{1, \ldots, n_d\}.$$

> **Definition 3.2** The superposition principle states that, for a linear system, the output due to the sum of two different inputs is equal to the sum of the outputs due to each input taken separately.

This principle is generally used to decompose the current dipoles into three separate ones oriented along the Cartesian axes. Equation 3.12 becomes

$$p = p_x u_x + p_y u_y + p_z u_z,$$

with p_x, p_y and p_z the dipole components along each axis, equal to the orthogonal projections of p.

Using this source model, and introducing the notation $\delta(r - r_d) = \delta_{r_d}(r)$, the right-hand side of Equation 3.8 becomes

$$f = \boldsymbol{\nabla} \cdot \boldsymbol{j}_p = \sum_{m=1}^{n_d} \boldsymbol{\nabla} \cdot \boldsymbol{p}_m \delta_{r_m},$$

which is to be interpreted in the sense of distributions [Darbas and Lohrengel, 2018; Vorwerk et al., 2019b; Kovacevic et al., 2021].

3.1.3. Finite element method

While several methods exist to solve the forward problem [Hallez et al., 2007], only two can account for the anisotropic conductivity of the tissues (For more information on anisotropy, see Section 3.2): *finite element method (FEM)* and *finite difference method (FDM)*.

Both techniques rely on a discretisation of the volume conductor. Finite element models consist of an unstructured grid (here, composed of tetrahedron), also known as *mesh*, whereas finite difference models splits the volume on a regular grid. The projects I conducted during my thesis all use FEM. In the following sections, I

introduce the concept of mesh and the formulation of the forward problem developed for it.

3.1.4. Mesh

To solve the generalized Poisson equation using the finite element method, the volume conductor (*e.g.*, the head in the context of EEG or tDCS) must be discretised into small elements (*e.g.*, tetrahedron or hexahedron). While this step, referred to as *meshing*, can be performed in several ways, the goal is usually to produce a good quality conforming mesh (See Definition 3.3).

> **Note**   Meshes are composed of *vertices* linked together by *edges*. A closed edge loop defines a *face*, and a closed set of faces define an element (in the case of a 3D mesh).

> **Definition 3.3**   In a conforming mesh, two arbitrary elements e_i and e_j either do not intersect or share a vertex, an edge or a face.

The quality of a mesh can be evaluated with different metrics such as elements aspect ratio, skewness, orthogonality or smoothness. Those metrics determine how much an element differs from a reference one. In the case of tetrahedral meshes, the reference element is an equilateral tetrahedron.

While these metrics are helpful for quality assessment, they do not determine if the mesh is actually suitable to serve as a support for the simulation. Indeed, an important factor is the mesh size. While it is true that reducing the size of the elements leads to a more accurate and stable solution, it increases the size of the mesh and thus computational load of the simulation. Consequently, building a proper mesh requires maximising the quality of the elements

while limiting their count. For this purpose, the density of the mesh is usually increased in the regions where the gradient of the computed field is high (See Figure 3.3).

Since meshing the head of a subject is not a trivial task, tools dedicated to electromagnetic simulation of the head usually provide automated workflows to generate a mesh from structural images. In Section 4.1 I present the approach implemented during this thesis and compare it to other available methods.
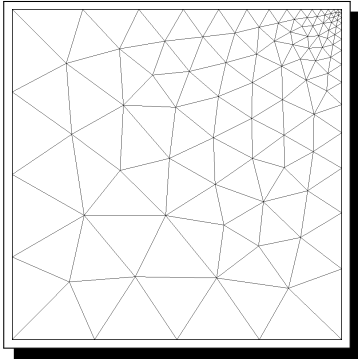
Figure 3.3 **A 2D triangular mesh with refined top right corner.**

Weak formulation

The generalized Poisson equation as expressed in Equation 3.8 is known as the *strong formulation*. A solution v to this formulation, also referred to as *classical solution*, only exists under assumptions (*e.g.*, continuous conductivity $[\kappa]$ and regular source term f) that are too restrictive for the considered problem.

Hence, a so-called *weak formulation* must be derived from Equation 3.8 [Bronzino, 1999; Hallez et al., 2007; Darbas and Lohrengel, 2018]. This new formulation can be obtained with the Galerkin method. Solving it amounts to finding v such that the expression

$$\langle \boldsymbol{\nabla} \cdot ([\kappa]\boldsymbol{\nabla} v),\ \hat{v} \rangle_{\Omega_{\text{head}}} = \langle f,\ \hat{v} \rangle_{\Omega_{\text{head}}} \qquad \textbf{Eq. 3.14}$$

is verified for all $\hat{v}$, which are called *test functions*. The notation $\langle x,\ y \rangle_{\Omega} \equiv \int_{\Omega} xy\ d\Omega$ is the inner product.

Assuming that the test functions $\hat{v}$ are differentiable, Green's theorem can be applied and leads to

$$- \langle [\kappa]\boldsymbol{\nabla} v,\ \boldsymbol{\nabla}\hat{v} \rangle_{\Omega_{\text{head}}} + \langle \boldsymbol{u}_{\text{n}} \cdot ([\kappa]\boldsymbol{\nabla} v),\ \hat{v} \rangle_{\Gamma_{\text{head}}} = \langle f,\ \hat{v} \rangle_{\Omega_{\text{head}}}. \qquad \textbf{Eq. 3.15}$$

When Dirichlet or homogeneous Neumann boundary conditions are applied on Γ_{head} (See Equation 3.11 and 3.10), the second term vanishes and the weak form becomes

$$- \langle [\kappa] \boldsymbol{\nabla} v, \ \boldsymbol{\nabla} \hat{v} \rangle_{\Omega_{\text{head}}} = \langle f, \ \hat{v} \rangle_{\Omega_{\text{head}}}, \qquad \textbf{Eq. 3.16}$$

which must hold for all the test functions $\hat{v}$.

As explained in the previous section, Ω_{head} is approximated by a set of small elements. The approximate solution $v_h \approx v$ is obtained by expressing v_h in terms of a finite number of *shape functions,* or *basis functions,* s_i, e.g. associated to the n_{vert} vertices of these elements (see Figure 3.4):
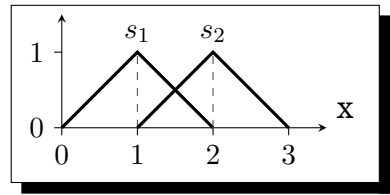
Figure 3.4   An example of a linear basis function for a 1D domain.

$$v_h(\boldsymbol{r}) = \sum_{i=1}^{n_{\text{vert}}} v_i \, s_i(\boldsymbol{r}). \qquad \textbf{Eq. 3.17}$$

The scalar coefficients v_i, $i = 1, \ldots, n_{\text{vert}}$, then become the unknowns of the problem.

Choosing the same functions s_i as test functions, and injecting Equation 3.17 into Equation 3.16, one obtains a linear system of equations of the form

$$[a] \cdot \boldsymbol{v} = \boldsymbol{f}, \qquad \textbf{Eq. 3.18}$$

with $[a] \in \mathbb{R}^{n_{\text{vert}} \times n_{\text{vert}}}$ a matrix with entries $a_{i,j} = -\langle [\kappa] s_i, \ s_j \rangle$ (which is called the *stiffness matrix*), $\boldsymbol{v} \in \mathbb{R}^{n_{\text{vert}}}$ the unknown vector, and $\boldsymbol{f} \in \mathbb{R}^{n_{\text{vert}}}$ the source right-hand side with entries $\boldsymbol{f}_i = \langle f, \ s_i \rangle$. With piecewise linear basis functions associated with the vertices of the mesh (so-called first order Lagrange functions), the basis functions are non-zero only in the elements sharing the corresponding vertices, leading to a sparse matrix $[a]$. The resulting linear system can then be solved efficiently using either sparse direct solvers or iterative linear solvers (conjugate gradients, multigrid...).

3.1.5. Forward and inverse problems

When simulating current flow in the head of a subject, researchers try to solve either the *forward problem* or the *inverse problem*. While the former is useful for both EEG and tDCS, the latter is of main interest for EEG.

Solving the forward problem consists in simulating the effect of known sources (*e.g.,* current dipoles or electrodes). It results in the definition of the different fields in the conductive volume. In bio-electromagnetism, the computed scalar field is generally the electric potential v, from which the electric field e and current density j can be derived.

On the other hand, the goal of the inverse problem is to infer the sources based on measured field values. This process is referred to as source reconstruction and is an important topic in functional imaging.

For tDCS, the forward problem amounts to solving Equation 3.8 for v. For EEG, on the other hand, the forward problem is used to define the so-called *leadfield matrix* $[l]$.

The computation of this matrix is achieved by calculating the electric potential at an acquisition site (generally an electrode placed on the scalp) located at r_{acq} resulting from a single electric dipole at r_{dip} characterised by a dipole moment p. This electric potential is denoted by

$$v(r_{acq}, r_{dip}, p) = l(r_{acq}, r_{dip}) \cdot p^\top, \qquad \text{Eq. 3.19}$$

where $l = [l_x, l_y, l_z]$ is called the leadfield ($V\,A^{-1}\,m^{-1}$). This equation is linear so it follows the superposition principle. It means that, for
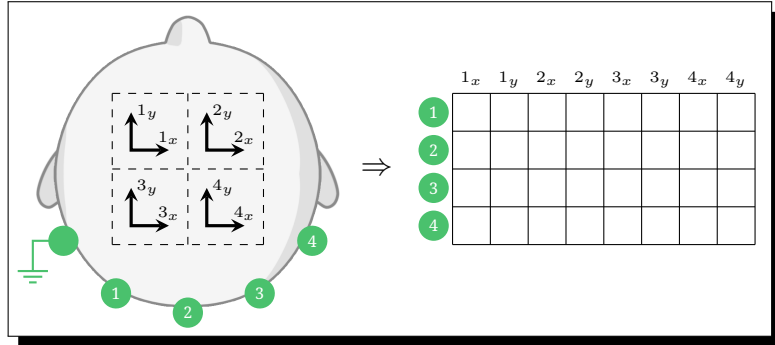
Figure 3.5 **The representation of the mapping from 4 source sites and 4 electrodes to the leadfield matrix for a simple 2D example. Sources define the columns, while electrodes correspond to the rows.**

n_{acq} acquisition sites and n_{dip} dipoles, the system becomes

$$\boldsymbol{v} = [l] \cdot \boldsymbol{p}^{\top}$$

$$
\begin{bmatrix} v_1 \\ \vdots \\ v_{n_{\mathrm{acq}}} \end{bmatrix} = \begin{bmatrix} \boldsymbol{l}_{1,1} & \cdots & \boldsymbol{l}_{1,n_{\mathrm{dip}}} \\ \vdots & \ddots & \vdots \\ \boldsymbol{l}_{n_{\mathrm{acq}},1} & \cdots & \boldsymbol{l}_{n_{\mathrm{acq}},n_{\mathrm{dip}}} \end{bmatrix} \cdot \begin{bmatrix} \boldsymbol{p}_1^{\top} \\ \vdots \\ \boldsymbol{p}_{n_{\mathrm{dip}}}^{\top} \end{bmatrix}.
$$

Eq. 3.20

A representation of the leadfield matrix is given in Figure 3.5 for a 2D example with four source sites and four electrodes.

Since the acquired data is usually noisy, an error term ϵ (V) is often added to the right-hand side of Equation 3.20, giving the final expression of the system

$$\boldsymbol{v}_{\mathrm{acq}} = [l] \cdot \boldsymbol{p} + \boldsymbol{\epsilon}.$$

Eq. 3.21

This definition of the forward and inverse problems identifies three key criteria which have an impact on the solution: the geometry of the volume conductor (See Sections 2.4 and 4.1), the electric conductivity of the tissues (See Section 3.2) and the position of the electrodes (See Section 4.2).

In this thesis, I focus on the forward problem. For the interested reader, the review of the methods available to solve it by Hallez et al. [2007] provides a good introduction and overview. For the inverse problem, the review from Grech et al. [2008] describes and compares several techniques for EEG source reconstruction.

Reciprocity principle

While building the leadfield matrix one column at a time by computing the electric potential measured on the electrodes due to a single source is possible for a simple geometry and a reduced number of sources, it quickly becomes time-consuming and computationally expensive for more realistic models.

For instance, in the case of high resolution finite element models, the number of source sites (columns) can be several orders of magnitude larger than the number of electrodes (rows). To solve this issue, Weinstein et al. [2000] proposed two methods relying on the *reciprocity principle* [Plonsey and Heppner, 1967]. The first evaluates sources at the centre of the mesh elements, it is referred to as the *element basis* method, while the second, the *node basis*, considers source sites at the coordinates of the nodes of the mesh. In this work, I only consider the element basis one.

This principle states that if one wants to measure the electric potential difference between two points located at r_a and r_b due to a single electric current dipole characterised by a dipole moment *p*, only the electric field at the dipole location r_{dip} resulting from a unit current injection between points a and b is required:

$$\frac{e \cdot p}{i} = v_a - v_b. \qquad \text{Eq. 3.22}$$

The a-th row of $[l]$ can thus be built by setting an electrode as the ground while injecting a current of $1\,\mathrm{A}$ through the a-th one and computing the electric field e in each element of the model. The three Cartesian components of the electric field recorded in the n-th element correspond to the components of $l_{m,n}$.

For a 3D finite element model, this method allows the computation of the leadfield matrix in $n_{\text{electrodes}} - 1$ iterations while, before, it required $3n_{\text{dip}}$ iterations.

3.2. Head tissues electric conductivity

In Section 3.1, I stated that $[\kappa] \in \mathbb{R}^{3 \times 3}$ is the electric conductivity positive definite tensor (See Definition 3.4) and is expressed in $\text{S}\,\text{m}^{-1}$. This property of the tissues and, more generally, of any material, defines its ability to carry electric current.

> **Definition 3.4**   A symmetric square matrix $[x] \in \mathbb{R}^{n \times n}$ is positive definite if the scalar resulting from $\boldsymbol{y}^{\top}[x]\boldsymbol{y}$ is strictly positive for any non-zero vector $\boldsymbol{y} \in \mathbb{R}^{n}$.

The tensor can be split into its eigenvectors

$$[u] = \begin{bmatrix} \boldsymbol{u}_1 \\ \boldsymbol{u}_2 \\ \boldsymbol{u}_3 \end{bmatrix}, \qquad \textbf{Eq. 3.23}$$

and eigenvalues which, for electric conductivity, correspond to the electric conductivity along each eigenvector $\boldsymbol{\kappa} = [\kappa_1, \ \kappa_2, \ \kappa_3]$, such that

$$[\kappa] = \begin{bmatrix} \kappa_1 & 0 & 0 \\ 0 & \kappa_2 & 0 \\ 0 & 0 & \kappa_3 \end{bmatrix} \cdot \begin{bmatrix} \boldsymbol{u}_1 \\ \boldsymbol{u}_2 \\ \boldsymbol{u}_3 \end{bmatrix} = \begin{bmatrix} \kappa_1 \boldsymbol{u}_1 \\ \kappa_2 \boldsymbol{u}_2 \\ \kappa_3 \boldsymbol{u}_3 \end{bmatrix} . \qquad \textbf{Eq. 3.24}$$

It is often modelled as an ellipsoid, as shown in Figure 3.6.
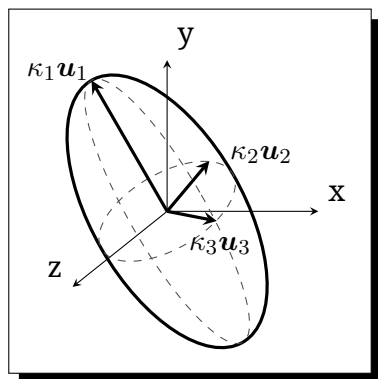
Figure 3.6 **An ellipsoid representing an electric conductivity tensor.**

An important concept to introduce about tensor fields is the difference between *isotropy* and *anisotropy*. The first refers to a material with constant conductivity in all directions, while the latter would conduct current differently based on the direction of the current flow.

In the case of an isotropic material, Equation 3.24 becomes

$$[\kappa] = \begin{bmatrix} \kappa & 0 & 0 \\ 0 & \kappa & 0 \\ 0 & 0 & \kappa \end{bmatrix} \cdot \begin{bmatrix} 1 & 0 & 0 \\ 0 & 1 & 0 \\ 0 & 0 & 1 \end{bmatrix} \equiv \kappa,$$

and $[\kappa]$ is reduced to a single scalar κ (*i.e.* the ellipsoid becomes a sphere). In simulations, most of the tissues are actually considered as isotropic.

Using a single value to characterise the electric conductivity across the whole volume of a tissue makes the choice of the value very important. This is why some tissues are recommended to be modelled as anisotropic. I discuss the different methods used to derive the conductivity tensors of the white matter and the skull in Section 3.2.2.

3.2.1. Reported values

Being of main interest for electromagnetic modelling of the head, the electric conductivity of the biological tissues has been studied since the last century [Burger and Milaan, 1943; Geddes and Baker, 1967; Gabriel, 1996; Gabriel et al., 1996a,b,c; Baumann et al., 1997; Oostendorp et al., 2000; Latikka et al., 2001; Akhtari et al., 2002; Goncalves et al., 2003] and new methods to acquire it are still being proposed [Akalin Acar et al., 2016].

Recently, McCann et al. [2019] published a review of the reported electrical conductivity of the human head tissues. The summary they extracted from 56 studies (filtered out of 211 articles) is shown in Figure 3.7 for the tissues we are interested in for this thesis. For each of these tissues, they provide the upper and lower bounds, the standard deviation and two mean values. They refer to these "means" as the "average mean", computed by giving an equal weight to all the reported measures, and as the "weighted average mean", where each record was weighted with regard to the quality of the study to which it belongs. They recommend using the weighted average mean for the tissues, so we only consider these throughout the whole thesis.

Note The weights used to compute the weighted average means resulted in some of the means being out of the intervals defined by the lower and upper bounds.

3.2.2. Anisotropy

As explained above, the physical properties of the tissues can be considered either isotropic or anisotropic. While it may seem reasonable to consider tissues such as the scalp as isotropic, it is less convincing to model the white matter, which can be seen as a set of insulated conductive wires, as a uniformly conductive volume. The same goes for the skull, which can be divided in sub-compartments (See Section 2.4).

Therefore, different models have been proposed to account for the variability of $[\kappa]$ in these tissues.
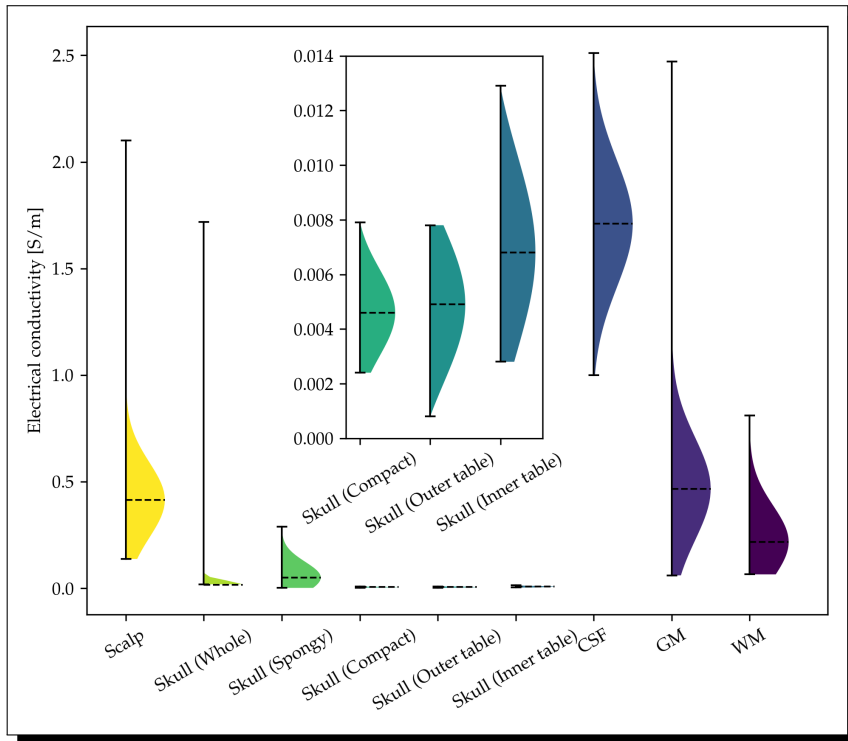
Figure 3.7 **The distributions of the electrical conductivity of the different tissues composing the head as reported by [McCann et al., 2019].**

White matter anisotropy

As described in Section 2.1, white matter is composed by the axons of the neurons. These axons are myelinated, meaning that they are electrically insulated to help increase the propagation of action potentials along their main axis. Hence, the electric current, be it induced by an external stimulation or by neuronal activity, flows more easily along these axons. Knowing this, researchers have developed different methods to obtain the conductivity tensor [Wu et al., 2018].

Electrical impedance tomography (EIT) [Koessler et al., 2017; Sajib et al., 2015] and *magnetic resonance EIT (MREIT)* [Liu et al., 2009; Chauhan et al., 2018] both consist in injecting a small low frequency current through the head of the subject and measuring the resulting scalp potential. This information is then used to solve an inverse problem in order to reconstruct the conductivity tensor. In MREIT, additional information about the induced magnetic field is recorded.

Both methods suffer from the presence of the skull, which plays the role of an insulator, and thus struggle to image the conductivity of the tissues located inside. Moreover, the resulting inverse problem is ill-posed, making it hard to solve for the anisotropic conductivity of the white matter.

The most promising approaches rely on the acquisition of *diffusion weighted images (DWI)* which are processed to perform *diffusion tensor imaging (DTI)* [Huisman, 2010]. This operation results in the generation of a tensor providing information about the microstructure of the tissues. Just like the conductivity tensor presented earlier, it can be represented by ellipsoids.

Tuch et al. [2001] were the first to propose a direct link between the diffusion tensor and the electrical conductivity tensor in the white matter. They proposed a linear relationship between the two, meaning that both tensors share the same eigenvectors. The derived linear relation is given by

$$\kappa_i = \frac{\kappa_{\text{out}}}{d_{\text{out}}} d_i,$$

<div align="right">**Eq. 3.25**</div>

where κ_i and d_i are respectively the electric conductivity and the intracellular diffusion coefficient ($\text{m}^2\,\text{s}^{-1}$) along the i-th eigenvector and κ_{out} and d_{out} are the extracellular conductivity and diffusion coefficient. In their paper, Tuch et al. [2001] found a conversion coefficient of $0.844 \pm 0.0545\,\text{S}\,\text{s}\,\text{mm}^{-3}$.

Unfortunately, the extracellular properties are difficult to obtain. Hence, the linear model is difficult to use in practice. To solve

this problem, other solutions, more aimed toward simulation, have been published.

The easiest methods to use are *Wang-constraint* [Wang et al., 2001] and *volume constraint* [Wolters et al., 2006] models. Both, just like the linear model proposed by Tuch et al. [2001], keep the eigenvectors of the diffusion tensor and use the empirical value of the conductivity of the white matter κ_{WM} and the anisotropy ratio $\kappa_{\text{WM}}^{(rad)}/\kappa_{\text{WM}}^{(tan)}$, where $\kappa_{\text{WM}}^{(rad)}$ and $\kappa_{\text{WM}}^{(tan)}$ are respectively the conductivity perpendicular and in the direction of the axon, to derive the eigenvalues of the tensor.

The Wang-constraint model (See Figure 3.8) reads as

$$\kappa_{\text{WM}}^{(rad)}\kappa_{\text{WM}}^{(tan)} = \kappa_{\text{WM}}^{2},$$

<div align="right">**Eq. 3.26**</div>

while the volume constraint model is defined by

$$\frac{4}{3}\pi\kappa_{\text{WM}}^{(rad)}(\kappa_{\text{WM}}^{(tan)})^2 = \frac{4}{3}\pi\kappa_{\text{WM}}^{3}.$$

<div align="right">**Eq. 3.27**</div>

Skull anisotropy

Modelling the electric conductivity of the skull is another issue. Indeed, as shown in Section 2.4, it is composed of tissues of different densities (and physical properties). Since the skull acts as an insulator, due to its low conductivity, and surrounds the whole brain, it is very important to accurately model it. Two approaches have been studied in the past decade to account for the anisotropy of the skull.

The first and most straightforward one relies on an accurate segmentation of the compact and spongy compartments. Once those compartments are defined, one can give them different sets of properties (See Figure 3.9a). Unfortunately, until recently, it was hard to automatically delineate the different compartment of the skull from structural magnetic resonance images due to the low signal
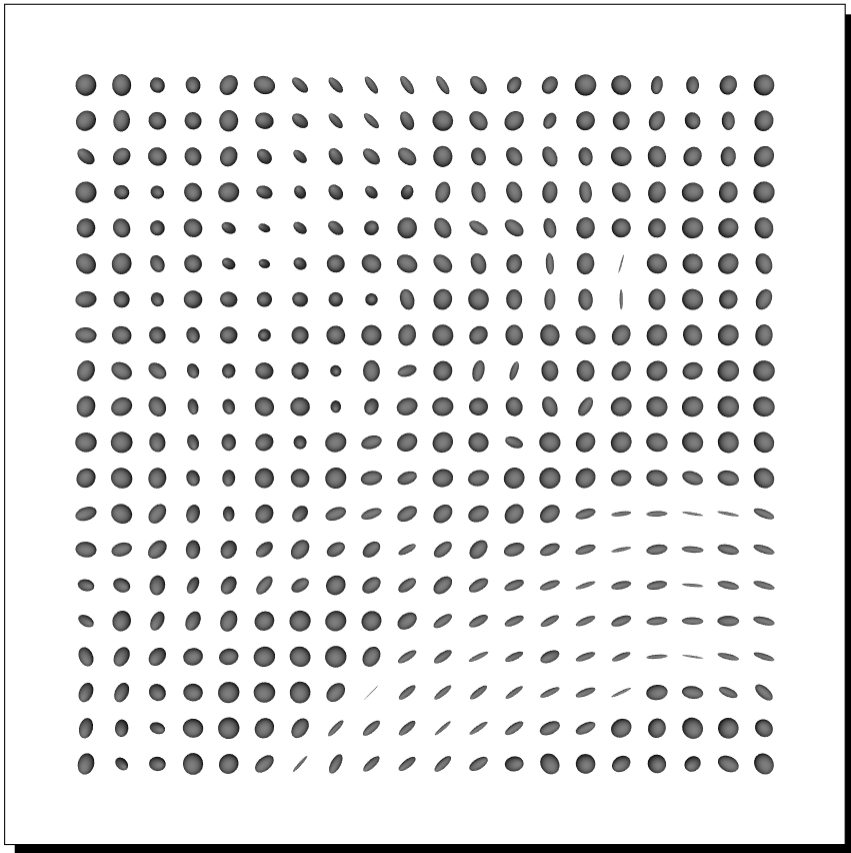
Figure 3.8 A slice of a conductivity tensor processed with the Wang-constraint model for a white matter conductivity of 0.14 S/m.

acquired in this region. People focusing on this approach often re-lied on CT scans to get better information about the different layers. The work of Montes-Restrepo et al. [2014] provides a good overview of the different models that can be generated using different seg-mentation techniques.

The other method is comparable to the one used to model the anisotropy of the white matter. Based on empirical measurements, it was determined that the conductivity of the skull differed when acquired tangentially or orthogonally of its surface. Thus, the aniso-tropy of the skull can be modelled by a conductivity tensor using the same constraints as for white matter (See Equations 3.26 and 3.27) as presented in Figure 3.9b.

In their paper, Sadleir and Argibay [2007] conclude that the dif-ference between the two approaches is not negligible due to the fact that modelling the different layers with a conductivity ratio of $1 : 10$ is drastically different from modelling a single compartment with anisotropy ratio of $1 : 10$. This is why we considered the mul-tilayer model in our first paper (See Chapter 5 and Appendix A).

3.3. Sensitivity and uncertainty analysis

In his book, Saltelli [2008] defines *sensitivity analysis (SA)* as:

> ” The study of how uncertainty in the output of a model (nu-merical or otherwise) can be apportioned to different sources of uncertainty in the mode input.
>
> — Saltelli [2008]

while he states that *uncertainty analysis (UA)* or *uncertainty quan-tification (UQ)* are performed to quantify the uncertainty on the
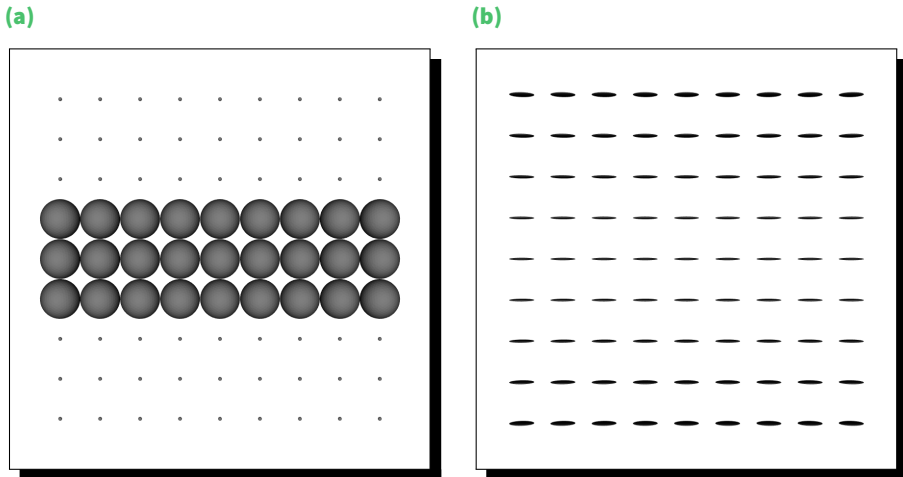
Figure 3.9 **Skull conductivity: the conductivity tensor resulting from (a) the 3 layers approach using the conductivity values recommended by McCann et al. [2019] and (b) the tensor approach using the Wang-constraint model and an anisotropy ratio of 1:10.**

output of a model. These processes are of main interest when conclusions or diagnostics are drawn from the results of a model, like it is the case for EEG source reconstruction. They are also useful to explain the variation in some published results (*e.g.*, for tDCS).

Before going further, I have to define the difference between *local* and *global* sensitivity analysis. Local sensitivity analysis studies the variation of the output of the model at a specific point in the input parameters space due to a small variation in the input. Even though such information can be interesting, in the context of electromagnetic modelling, we are more concerned about the big picture, *i.e.*, the influence of an input parameter on the output across the whole input space. This is referred to as global sensitivity. Generally, local sensitivity and global sensitivity are respectively used to study the result of a model and the model itself.

In this section, I focus on global sensitivity, and more precisely on one method: the computation of Sobol indices [Sobol, 2001; Saltelli et al., 2010].

3.3.1. Sobol indices

Sobol indices are used to determine the sensitivity of a model to its input parameters. To explain how they are calculated, let

$$Y = f(\boldsymbol{X}),$$

be a model, with Y a random scalar output and $\boldsymbol{X} = [X_1, X_2, \ldots, X_n]$ the vector of n independent random scalar input factors, where $X_i \in [0, 1]$.

Sobol [2001] proposed a decomposition of this model into

$$f = f_0 + \sum_{i=1}^{n} f_i + \sum_{i=1}^{n} \sum_{j>i} f_{i,j} + \cdots + f_{1,2,\ldots,n}, \qquad \text{Eq. 3.28}$$

where each term only depends on the parameters present in its index (*i.e.*, $f_i = f_i(X_i)$, $f_{i,j} = f_{i,j}(X_i, X_j)$). While this decomposition always yields 2^n terms, the choices of possible values for each of these terms is infinite. Still, Sobol proved that, if the mean of each term is equal to zero, they are all orthogonal. This means that they can be determined by

$$f_0 = \mathbb{E}_{\boldsymbol{X}}(Y), \qquad\qquad\qquad \text{Eq. 3.29}$$
$$f_i = \mathbb{E}_{\boldsymbol{X}_{\setminus i}}(Y \mid X_i) - f_0, \qquad\qquad \text{Eq. 3.30}$$
$$f_{i,j} = \mathbb{E}_{\boldsymbol{X}_{\setminus i,j}}(Y \mid X_i, X_j) - f_i - f_j - f_0, \qquad \text{Eq. 3.31}$$

where $\boldsymbol{X}_{\setminus i}$ denotes the parameters space minus the i-th dimension and $\mathbb{E}_{\boldsymbol{X}_{\setminus i}}(Y \mid X_i)$ is the expected value of Y conditioned on the value of X_i.

Consequently, the variance of the terms of the decomposition are measures of importance. This leads to the definition of the so-called *first-order Sobol indices*

$$s_i = \frac{\mathbb{V}_{X_i}(\mathbb{E}_{\boldsymbol{X}_{\setminus i}}(Y \mid X_i))}{\mathbb{V}_{\boldsymbol{X}}(Y)}. \qquad\qquad \text{Eq. 3.32}$$

These indices describe the main effect of each input parameter to the overall variance of the model. Following the decomposition of the model from Equation 3.28, it comes that

$$\sum_{i=1}^{n} s_i \leq 1.$$

Indeed, the first order indices alone do not account for any interaction between the input factors.

> **Note** Interacting factors are factors whose effect on Y cannot be expressed as the sum of their respective main effects.

If the sum of the first order indices is much smaller than 1, then, the interactions are non-negligible. While any order index could be computed based on the previous decomposition, the number of terms grows exponentially. Thus, Sobol proposed the *total order Sobol indices*

$$s_i^{(t)} = \frac{\mathbb{E}_{\boldsymbol{X}_{\backslash i}}(\mathbb{V}_{X_i}(Y|\boldsymbol{X}_{\backslash i}))}{\mathbb{V}_{\boldsymbol{X}}(Y)} = 1 - \frac{\mathbb{V}_{\boldsymbol{X}_{\backslash i}}(\mathbb{E}_{X_i}(Y|\boldsymbol{X}_{\backslash i}))}{\mathbb{V}_{\boldsymbol{X}}(Y)}, \qquad \textbf{\textcolor{green}{Eq. 3.33}}$$

which measure the total effect of a factor, meaning the sum of all its indices of order 1 to n. As opposed to s_i, the sum of $s_i^{(t)}$ can be greater than 1.

The total Sobol indices are of main interest since they point out the parameters that could be fixed to any value in their range without affecting the outcome of the model. Indeed, if $s_i^{(t)} \approx 0$, the i-th factor can be considered as having no effect on the output. Thus, any reasonable value of this parameter could be used.

Considering the numerators of these indices, Jansen [1999] refers to $\mathbb{V}_{X_i}(\mathbb{E}_{\boldsymbol{X}_{\backslash i}}(Y \mid X_i))$ as the *top marginal variance* which is the expected reduction in variance induced by fixing X_i and to $\mathbb{E}_{\boldsymbol{X}_{\backslash i}}(\mathbb{V}_{X_i}(Y|\boldsymbol{X}_{\backslash i}))$ as the *bottom marginal variance*, *i.e.*, the expected variance that would remain after fixing all the parameters but X_i.

(a)
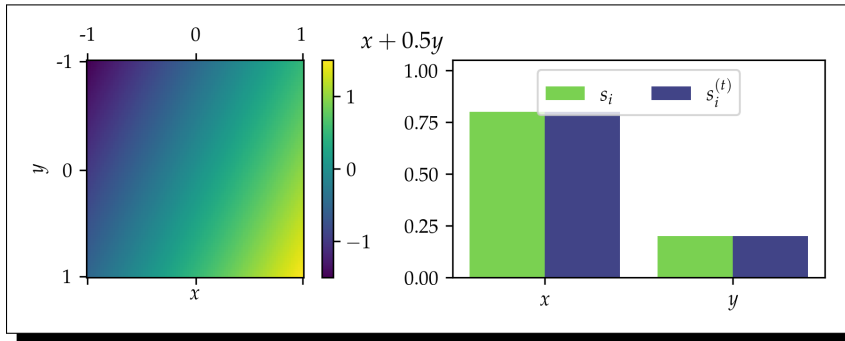
(b)
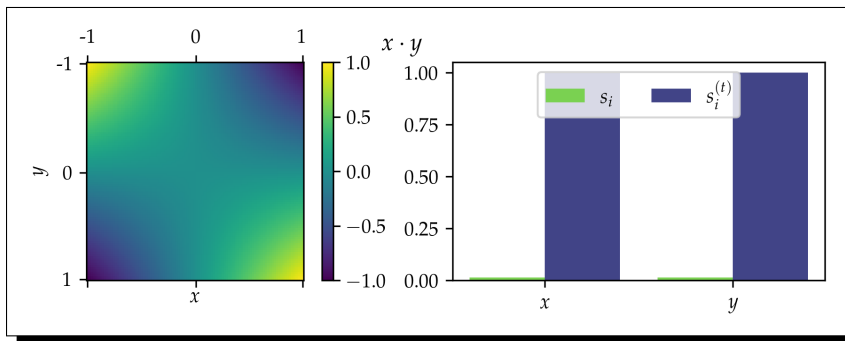
(c)
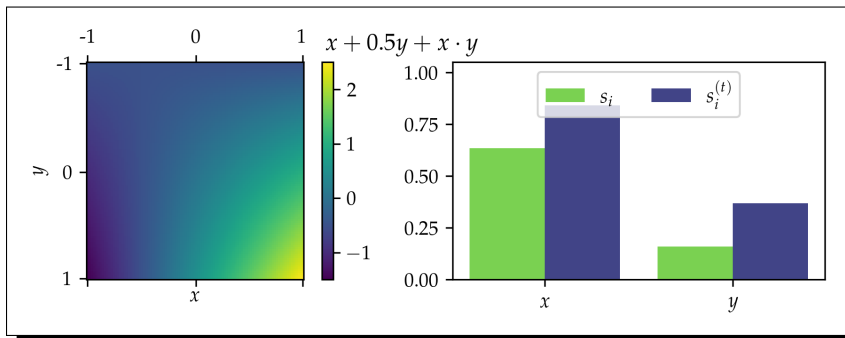
Figure 3.10 **The function values and computed first and total order Sobol indices for (a) a function with no factors interaction, (b) a function with only factor interactions and (c) a function with both main effects and interactions.**

To better explain the two types of indices, Figure 3.10 gives three examples. First, the function $f(x, y) = x + 0.5y$. There is no interaction between the parameters, thus, the first and total orders are the same. Since y has a lower coefficient, its indices are lower than those of x. Next, the function $f(x, y) = x \cdot y$ only has interaction terms. Hence, the first order indices are negligible. Finally, the function $f(x, y) = x + 0.5y + x \cdot y$ has both main effects and interactions, the values of $s_i^{(t)}$ are thus greater than those of s_i.

3.3.2. Computation

The computation of s_i and $s_i^{(t)}$ both require to evaluate the model on a set of points of the parameters space. To limit the number of evaluations, Saltelli et al. [2010] proposed a method to compute both the first and the total order indices simultaneously.

This technique considers two sampling matrices $[a]$ and $[b] \in \mathbb{R}^{m \times n}$ where each of the m row contains the coordinates of a point in the parameters space. These matrices are used to build $[a_b^{(i)}]$ which is a copy of $[a]$ where the i-th column is from $[b]$ and, conversely, the matrix $[b_a^{(i)}]$ where the i-th columns comes from $[a]$.

Using either $[a]$ and $[b_a^{(i)}]$ or $[b]$ and $[a_b^{(i)}]$, one can compute s_i and $s_i^{(t)}$. Indeed, considering that

$$\mathbb{V}(Y) = \mathbb{E}(Y^2) - \mathbb{E}(Y)^2, \qquad \text{Eq. 3.34}$$

one can demonstrate that

$$\mathbb{V}_{X_i}(\mathbb{E}_{\boldsymbol{X}_{\setminus i}}(Y \mid X_i)) = \frac{1}{m} \sum_{j=1}^{m} f([b]_j) f([a_b^{(i)}]_j) - f_0^2, \qquad \text{Eq. 3.35}$$

$$\mathbb{V}_{\boldsymbol{X}_{\setminus i}}(\mathbb{E}_{X_i}(Y \mid \boldsymbol{X}_{\setminus i})) = \frac{1}{m} \sum_{j=1}^{m} f([a]_j) f([a_b^{(i)}]_j) - f_0^2. \qquad \text{Eq. 3.36}$$

Here, I develop the demonstration for s_i. Applying Equation 3.34 to $\mathbb{V}_{X_i}(\mathbb{E}_{\boldsymbol{X}_{\backslash i}}(Y \mid X_i))$, it gives

$$\mathbb{V}_{X_i}(\mathbb{E}_{\boldsymbol{X}_{\backslash i}}(Y \mid X_i)) = \int \mathbb{E}^2_{\boldsymbol{X}_{\backslash i}}(Y \mid X_i) dX_i - \left(\int \mathbb{E}_{\boldsymbol{X}_{\backslash i}}(Y \mid X_i) dX_i \right)^2,$$

<div align="right">**Eq. 3.37**</div>

where the second integral reduces to $\mathbb{E}(Y)^2 \equiv f_0^2$. Regarding the first integral, we can write

$$\mathbb{E}^2_{\boldsymbol{X}_{\backslash i}}(Y \mid X_i) = \mathbb{E}_{\boldsymbol{X}_{\backslash i}}(Y \mid X_i) \, \mathbb{E}_{\boldsymbol{X}'_{\backslash i}}(Y \mid X_i)$$

$$= \int f(X_1, X_2, \ldots, X_i, \ldots, X_n) d\boldsymbol{X}_{\backslash i}$$

$$\times \int f(X'_1, X'_2, \ldots, X_i, \ldots, X'_n) d\boldsymbol{X}'_{\backslash i}$$

$$= \iint f(X_1, X_2, \ldots, X_i, \ldots, X_n)$$

$$\times f(X'_1, X'_2, \ldots, X_i, \ldots, X'_n) d\boldsymbol{X}_{\backslash i} d\boldsymbol{X}'_{\backslash i}.$$

Hence, the integral becomes

$$\int \mathbb{E}^2_{\boldsymbol{X}_{\backslash i}}(Y \mid X_i) dX_i = \iint f(X_1, X_2, \ldots, X_i, \ldots, X_n)$$

$$\times f(X'_1, X'_2, \ldots, X_i, \ldots, X'_n) d\boldsymbol{X} d\boldsymbol{X}'_{\backslash i}.$$

The matrices $[b]$ and $[a_b^{(i)}]$ defined above share the same values of X_i and, thus, allow the computation of the integral in a discrete manner

$$\int \mathbb{E}^2_{\boldsymbol{X}_{\backslash i}}(Y \mid X_i) dX_i \approx \frac{1}{m} \sum_{j=1}^{m} f([b]_j) f([a_b^{(i)}]_j). \qquad \text{**Eq. 3.38**}$$

This solution coupled with the one for $s_i^{(t)}$ require $2m$ evaluations of the model to determine $[a]$ and $[b]$ and mn evaluations to determine $[a_b]$. In total, $(2+n)m$ evaluations of the model have to

be computed, where m must be large enough. Saltelli et al. [2010] recommends values of m higher than 500.

During this thesis, the implementation provided in *SALib* [Herman and Usher, 2017] and relying on the presented method was used.

3.3.3. Parameters space sampling

As explained above, the computation of Sobol indices require several evaluations of the model for different sets of values of the input parameters. While one could use random samples, this is not suitable for high dimensional parameters space, and it does not ensure a proper coverage of the space.

To solve this issue, several *quasi-random sequences*, or *low-discrepancy sequences*, have been proposed [Halton, 1960; Sobol, 1967]. As opposed to the random sampler, quasi-random sequences draw new points of the space based on those that have already been evaluated in order to maximize the coverage. Figure 3.11 shows a comparison of different sampling sequences on a 2D parameters space for three sample sizes.

During this thesis, both Halton [Halton, 1960] and Sobol [Sobol, 1967] sequences are used for various means.

3.4. Surrogate modelling

As described in the previous section, the computation of Sobol indices requires numerous evaluations of the model of interest. Unfortunately, when each evaluation is expensive to acquire, be it in terms of computational time or, for wet science, in terms of
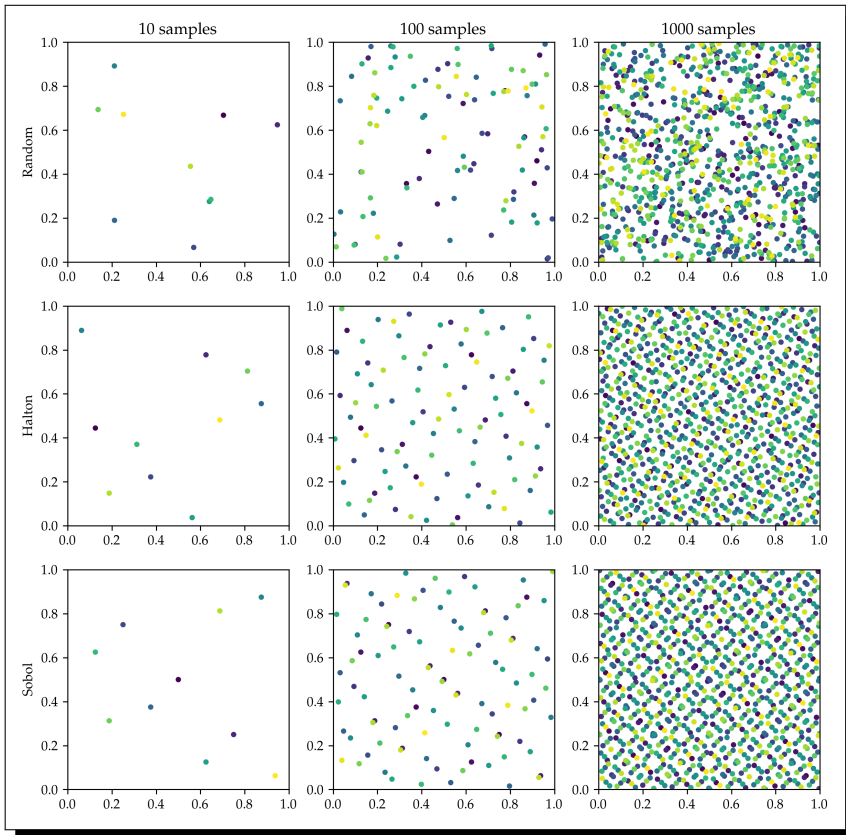
Figure 3.11   A comparison of the samples drawn from a 2D parameters space with different sampling sequences (rows) and different sample sizes (columns). The colour of the points determine in which order they are drawn. Yellow points are the latest.

material or acquisition time, it is not feasible to obtain the recommended $(2 + n)m$ samples where $m \geq 500$ and n is the number of factors of the model.

A solution is to use a low number of evaluations to build a so-called *surrogate model* $\hat{f}$, which, as opposed to the *real model* f, is cheap to evaluate. This model is built such that

$$\hat{f}(\boldsymbol{x}) \approx f(\boldsymbol{x}),$$

for any given parameters set $\boldsymbol{x}$, and can then be used to compute the Sobol indices in place of the real model.

In the context of a scalar output model, a surrogate model is nothing more than a regressor. Depending on the research fields, several techniques have been proposed and successfully used to construct such an emulator. *Generalised polynomial chaos (gPC)* and *Gaussian process regressors (GPR)* [Rasmussen and Williams, 2006] are the two most represented.

While both methods can yield fast, good quality and deterministic surrogate models [Owen et al., 2017], the GPR approach, thanks to its stochastic nature, has some additional advantages, such as its abilities to be updated by increasing the sample size without needing to rebuild the whole model, and to provide a measure of the confidence on the predicted results. This is very interesting because, when using a GPR, all the results are actually random variables that account for the uncertainty lying in the model itself. That can help to draw more educated conclusions on the computed indices. Moreover, this uncertainty can be used as the convergence criterion mentioned above. Finally, Gaussian processes are very versatile and can model a wider range of behaviours. Indeed, generalised polynomial chaos has been shown to be a special case of GPR [Schobi et al., 2015]. For this reason, I use GPR throughout my thesis.

In the next paragraphs, I give an overview of how Gaussian processes work and can be used to build a surrogate model.
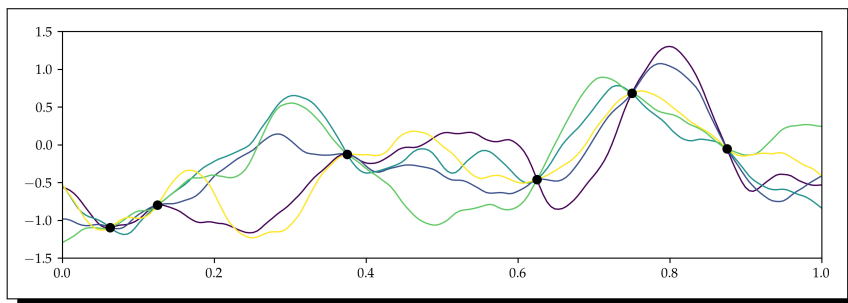
Figure 3.12   **An example of five possible functions fitting the given six data points.**

3.4.1. Gaussian process regressor

When dealing with a regression problem where one wants to fit a model to some previously acquired data, there are potentially an infinite number of possible functions that could represent the data as presented in Figure 3.12.

The traditional parametric approach (*e.g.*, linear or polynomial regression) would only yield one possible function out of this infinite number of possibilities that it considers "the best fit". Since all those functions are fitting the given data, what would make one of them be better than the others. In other words, what makes the unique solution of a polynomial regression the only valid option? Nothing.

Gaussian processes solve this problem. Indeed, they are often referred to as probability distributions over all the possible functions [Rasmussen, 2004; Görtler et al., 2019], but before I can explain why they are presented like so, I first need to introduce the basics.
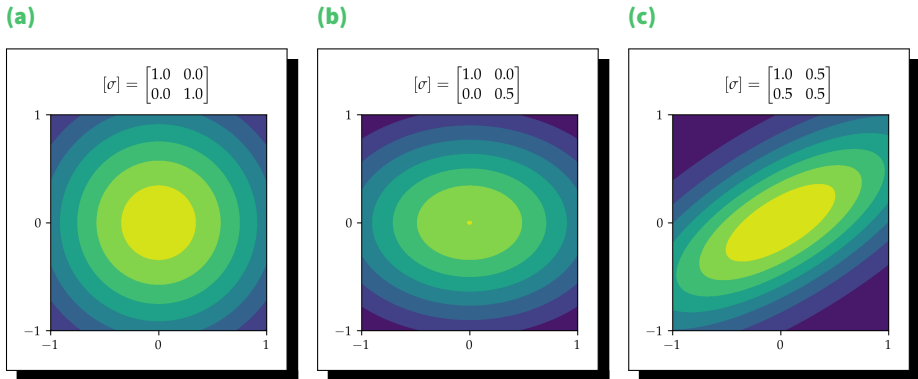
Figure 3.13   Examples of 2D multivariate Gaussian distributions for different covariance matrices.

Multivariate Gaussian distribution

The main building block of the Gaussian processes is the multivariate Gaussian distribution. Such a distribution is defined by two parameters: its mean vector $\boldsymbol{\mu} = [\mu_1, \ldots, \mu_n]^\top$ and its covariance matrix $[\sigma]$.

Each component of $\boldsymbol{\mu}$ determines the expected value of the corresponding dimension. On the other hand, the elements of the diagonal of $[\sigma]$ correspond to the variance σ_i^2 of the i-th dimension and the off-diagonal elements $\sigma_{i,j}$ give the correlation factor between the i-th and j-th dimensions. This matrix shapes the distribution as shown in Figure 3.13.

If a random variable $\boldsymbol{X} = [X_1, \ldots, X_n]^\top$ follows a multivariate Gaussian distribution, it is denoted by

$$\boldsymbol{X} \sim \mathcal{N}(\boldsymbol{\mu}, [\sigma]),$$

and the covariance matrix is given by

$$[\sigma] = \mathbb{C}(\boldsymbol{X}, \boldsymbol{X}) = \mathbb{E}\left((\boldsymbol{X} - \boldsymbol{\mu})(\boldsymbol{X} - \boldsymbol{\mu})^\top\right).$$

One important characteristic of the multivariate Gaussian distribution is that it is closed under marginalisation and condition-

ing, meaning that these operations also yield Gaussian distributions. To better explain what they both are, let a probability distribution be defined as

$$P_{X,Y} = \begin{bmatrix} X \\ Y \end{bmatrix} \sim \mathcal{N}\left(\begin{bmatrix} \mu_X \\ \mu_Y \end{bmatrix}, \begin{bmatrix} [\sigma_X, X] & [\sigma_X, Y] \\ [\sigma_Y, X] & [\sigma_Y, Y] \end{bmatrix} \right).$$ **Eq. 3.39**

First, marginalisation allows the extraction of partial probability distributions of X and Y such that

$$X \sim \mathcal{N}(\mu_X, [\sigma_X, X]),$$
$$Y \sim \mathcal{N}(\mu_Y, [\sigma_Y, Y]),$$

implying that the marginal distribution of X (or Y) is the probability distribution of X (or Y) when the values of Y (or X) are not considered. The probability of this marginal distribution of X being equal to x is obtained by computing the average conditional probability over all the possible values of Y

$$p_X(x) = \int_y p_{X \mid Y}(x \mid y) p_Y(y) dy = \mathbb{E}_Y(p_{X \mid Y}(x \mid y)).$$

Next, conditioning is used to compute the probability of a random variable depending on another

$$P_{X \mid Y} \sim \mathcal{N}(\mu_{X \mid Y}, [\sigma_{X \mid Y}]),$$ **Eq. 3.40**

with

$$\mu_{X \mid Y} = \mu_X + [\sigma_X, Y][\sigma_Y, Y]^{-1}(Y - \mu_Y),$$
$$[\sigma_{X \mid Y}] = [\sigma_X, X] - [\sigma_X, Y][\sigma_Y, Y]^{-1}[\sigma_Y, X],$$

where $\mu_{X \mid Y}$ only depends on the conditioned variable, while $[\sigma_{X \mid Y}]$ is independent of it.

These two operations are at the core of GPR.

Gaussian processes

Now, we have all the tools we need to explain how Gaussian processes work. In fact, GPR are nothing more than multivariate Gaussian distributions. Their goal is to determine the underlying distribution based on training data Y in order to predict function values on test data X.

Similarly to what is described in Equation 3.39, the joint distribution $P_{X,Y}$ is a multivariate Gaussian distribution spanning all the possible values of the function to model. Using Bayesian inference, we want to update the model with the training data and find $P_{X\,|\,Y}$ (See Equation 3.40).

If we want to predict the value of n test points, each of them is considered as a random variable. Thus, the resulting distribution $P_{X\,|\,Y}$ has n dimensions. Sampling this distribution yields a n dimensional vector in which each element correspond to a function value. Hence, the distribution itself spans over a functional space and encapsulates all the possible function outputs for the n test points.

The last two things to explain are the methods used to determine both μ and $[\sigma]$. The first, referred to as the *regression term*, is often set to 0 [Chen et al., 2016]. Indeed, it is easy to centre the data (*i.e.,* removing the mean) before fitting the model and add it back after predicting. The latter, on the other hand, is defined using a *covariance function,* or *kernel* $k(x_i,\,x_j)$.

This function ultimately defines the characteristics of the functions that are considered by the model. The explanation of the role of the kernel, as well as the different types and combinations of kernels that are available, is beyond the scope of this thesis and I recommend reading the work of Rasmussen and Williams [2006]. For the purpose of this work, it is only important to understand that the kernel gives an idea of the similarity between two points. Thus, it yields a high value for points that are close from each other and low values for points that are far from each other.

In the present work, I followed the recommendations of [Chen

et al., 2016] and used a composite kernel built by adding a constant kernel and a Matérn kernel which is one of the most used kernels with the *radial basis function (RBF)* and is defined by

$$k(\boldsymbol{x}_i,\ \boldsymbol{x}_j) = \frac{1}{\gamma(\nu)2^{\nu-1}} \left(\frac{\sqrt{2\nu}}{l} d(\boldsymbol{x}_i,\ \boldsymbol{x}_j) \right)^{\nu} b_{\nu} \left(\frac{\sqrt{2\nu}}{l} d(\boldsymbol{x}_i,\ \boldsymbol{x}_j) \right),$$

<div align="right">Eq. 3.41</div>

where $d(\boldsymbol{x}_i,\ \boldsymbol{x}_j)$ is the Euclidean distance between the two points and b_{ν} and γ are respectively a modified Bessel function of the second kind and the gamma function.

The main difference between these two kernels is that, while the RBF constraints the possible functions to be infinitely differentiable, the Matérn kernel uses the value of its parameter ν to control the smoothness of the resulting functions. In our case, it is set to 2.5, yielding twice differentiable functions. This choice is justified by the fact that the difference between the solutions of two current simulations configured with parameters sets that are close to each other is expected to be small. Consequently, the smoothness of the modelling function is supposed to be high. Still, constraining the functions to be infinitely differentiable seemed to be a big prior. Thus, we settled on the Matérn kernel.

The output of a Gaussian process regressor using the parameters described above and applied to the example from Figure 3.12 is presented in Figure 3.14. As expected from a Bayesian technique, the credibility interval is narrow close to the training points, while it gets wider the further from it.

Gaussian processes for uncertainty and sensitivity analysis

To wrap up this section, it is interesting to get back to its starting point: the computation of Sobol indices. Indeed, a surrogate model, in the context of sensitivity analysis, is useful only if the number of samples required to build it is small compared to the number of samples required to compute the sensitivity indices. Moreover, I
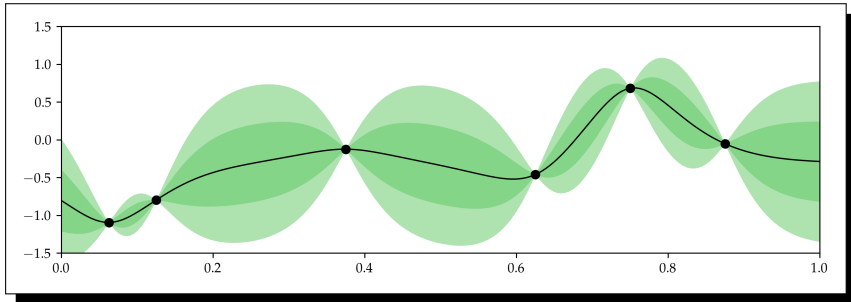
Figure 3.14   A Gaussian process regressor built on 6 training points. The light area corresponds to the 95% credibility interval, while the darker area shows the 68% credibility interval.

stated that Gaussian processes could be used to propagate the uncertainty lying in the model up to the computed Sobol indices.

While mathematical methods specific to Gaussian processes have been proposed to achieve this [Oakley and O'Hagan, 2004; Marrel et al., 2009], I find it easier to explain the most straightforward technique.

Considering a GPR built on a few model evaluations, the mean posterior distribution is generally used as a regressor. This goes against the Bayesian approach, since there is no reason to think that the mean of the posterior is better than any other possible function lying in the posterior.

Thus, to leverage the uncertainty encapsulated in the GPR in order to picture the uncertainty in the resulting Sobol indices, one simply has to compute these indices for several (potentially a large number) samples drawn from the posterior distribution. Doing so, the indices can be considered as random variables S_i and $S_i^{(t)}$. Hence, we have

$$s_i = \mathbb{E}(S_i), \qquad \text{Eq. 3.42}$$

$$s_i^{(t)} = \mathbb{E}(S_i^{(t)}), \qquad \text{Eq. 3.43}$$

and the variance of the random variables indicates the accuracy of the indices.

In Figure 3.15, I applied this method to the examples presented in the previous section. A GPR is built using only 10 samples drawn using a Halton sequence. This model is then used in place of the actual model to compute the Sobol indices using 128 samples from the posterior distribution (including the mean). The error bars span over $95\,\%$ of the estimated values. With as few as 10 samples, this technique is able to compute Sobol indices comparable to the real ones with a reasonable accuracy for the different functions.

One downside of the GPR is that, since the model is non-parametric, each evaluation of the model relies on all the training data. Consequently, the more training data is used, the heavier the model is. This has to be considered for problems with high dimensionality, since the number of evaluations of the actual model required to build the surrogate model grows with the number of input parameters.

(a)

(b)

(c)
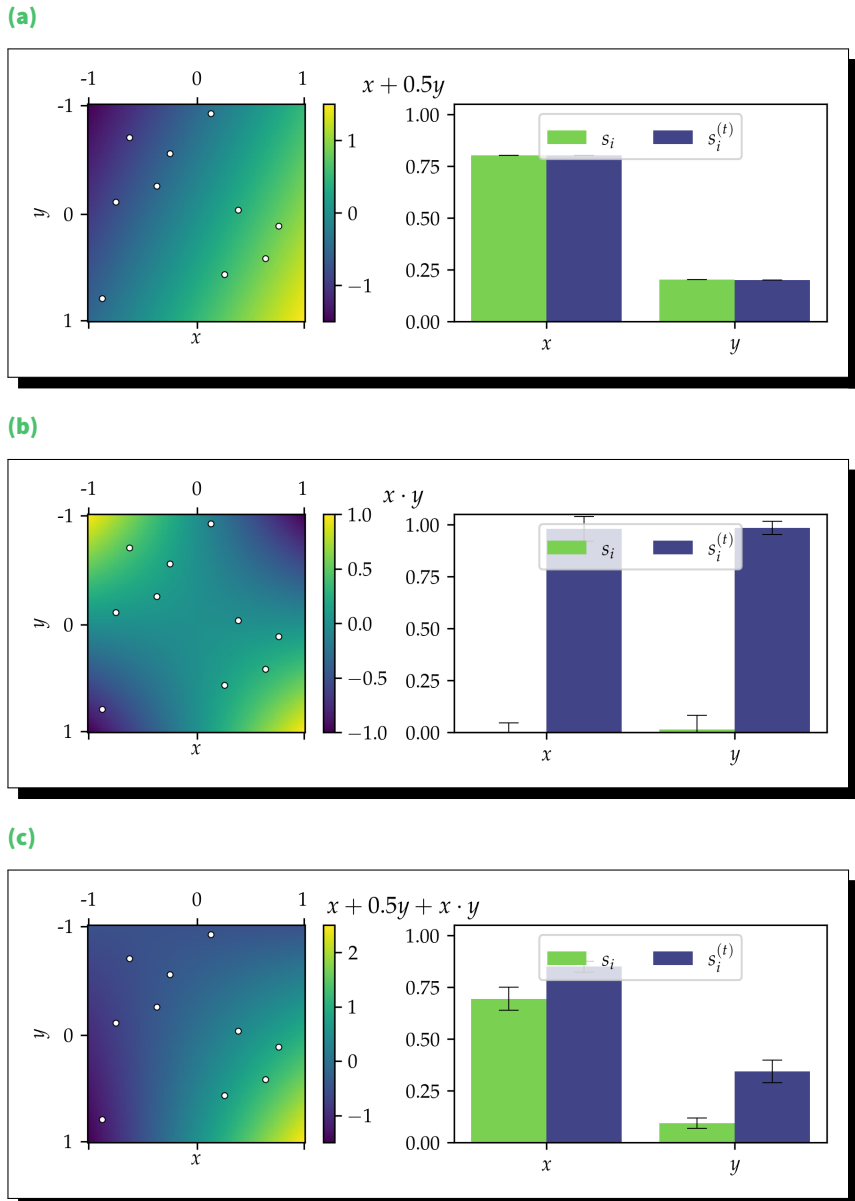
Figure 3.15 **The function values and computed first and total order Sobol indices based on Gaussian processes built on 10 samples for (a) a function with no factors interaction, (b) a function with only factor interactions and (c) a function with both main effects and interactions.**

4.

Shamo

The main goal of *Shamo* is to provide an easy way to run uncertainty quantification and sensitivity analysis on computationally expensive problems like EEG leadfield computation and tDCS simulation. In order to provide an end-to-end solution to the users, going from mesh generation to sensitivity analysis, some useful functionalities were developed.

In the following sections, even though building the code base took most of my time, I do not get into the details of the implementation (I redirect the interested reader to the Github repository[1] of the project and its documentation[2]). In order to improve the maintainability and overall quality of the tool, I decided to build upon already published and validated tools and focused on providing a unified interface.

With this in mind, the surrogate modelling with Gaussian processes is achieved with *Scikit-learn* [Pedregosa et al., 2011b] and

---

1. `https://github.com/CyclotronResearchCentre/shamo`
2. `https://cyclotronresearchcentre.github.io/shamo/index.html`

Shamo provides tools to easily extract the training data from a series of simulations. The same way, the sensitivity indices are computed with *SALib* [Herman and Usher, 2017]. Thus, I do not describe how these functionalities are implemented in the package.

Instead, I focus on some interesting functionalities that are part of *Shamo* and the decisions that lead to their creation. These characteristics of *Shamo* are mainly concentrated on the generation of the finite element models, since it is the most sensitive part of the simulation. Indeed, since this is the starting point of all the further analyses, building a bad model can only yield bad results.

4.1. Mesh generation

As explained in Section 3.1, the finite element method used to solve Poisson's equation relies on a discretisation of the conductor volume into small elements. This process, referred to as *meshing*, is a key step in the modelling of current in the head of a subject (or in any conductive medium).

The traditional approach to mesh a whole head is inherited from the boundary element method. Indeed, it consists in generating the interfaces of the different tissues and then filling the space inbetween with volume elements. Unfortunately, it is not trivial to generate proper non-intersecting manifold surfaces (See Definition 4.1) for each tissue class. To ensure that all the surfaces are manifolds, they often require post-processing using tools such as *MeshFix* [Attene, 2010] to remove self-intersecting polygons and fill holes.

> **Definition 4.1**   A manifold surface is a surface that completely encloses a volume and, thus, presents no hole.

Due to the complexity of generating a mesh, most of the tools available to simulate current in the head rely on a specific segmentation and meshing pipeline, where both steps are intertwined and cannot be performed separately. Following what is mentioned in Section 2.4, the fact that automated segmentation pipelines often fail at segmenting non-standard heads (*e.g.*, non-healthy tissues, deformities…) is a major limitation of this all-in-one approach.

To solve this issue, *Shamo* provides a meshing tool that takes as input a segmented volume (or a series of binary masks), irrespective of how it was generated or its shape. Generating the mesh directly from a labelled image is performed with *CGAL* [Project, 2020] and *Gmsh* [Geuzaine and Remacle, 2009] tools. These are industrial grade software that are already used in other similar applications such as *SimNIBS* [Thielscher et al., 2015] or *ROAST* [Huang et al., 2019].

With this technique, the user can perform the segmentation with any tool of his choice, even manually if needed. It means that the number of tissues included in the model is only limited by what tissue masks the user is actually able to produce. In Figures 4.1 and 4.2, I show two different meshes built from two labelled images containing different numbers of tissue classes, 5 and 10 respectively. Both labelled volumes are derived from the MIDA model [Iacono et al., 2015].

While a model as complex as the one presented in Figure 4.2 is still not the norm in research and clinical applications, having a tool that can build such a fine-grained model could be of great interest for more specific studies. For instance, this model includes blood vessels, meaning that, potentially, their conductivity could be accounted for in the simulations.
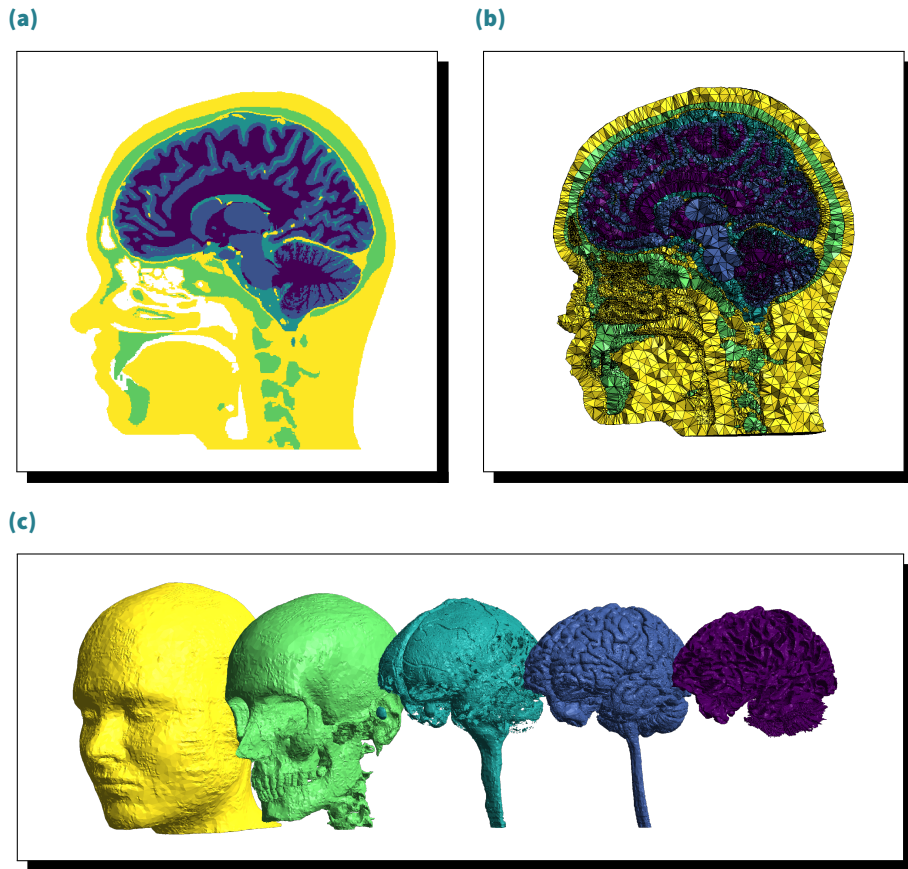
Figure 4.1 (a) A 5 tissues labelled image, (b) the mesh built from this labelled image and (c) the surfaces of the different tissues composing the mesh built with Shamo.

(a)

(b)

(c)
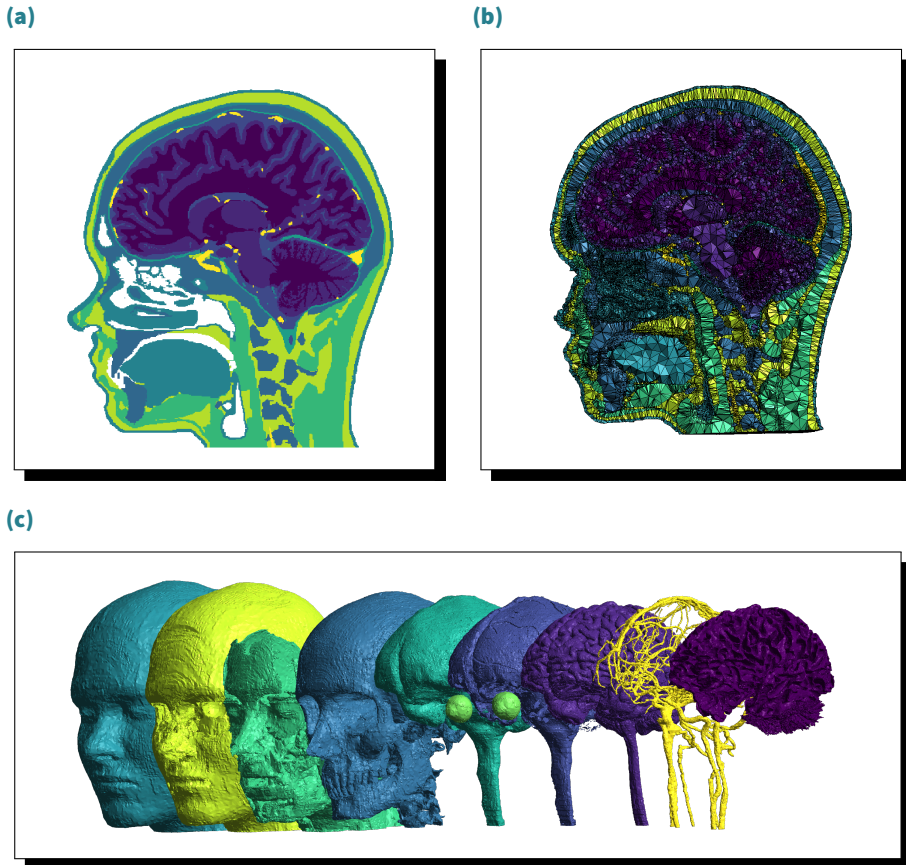
Figure 4.2 **(a)** A 10 tissues labelled image, **(b)** the mesh built from this labelled image and **(c)** the surfaces of the different tissues composing the mesh built with Shamo.
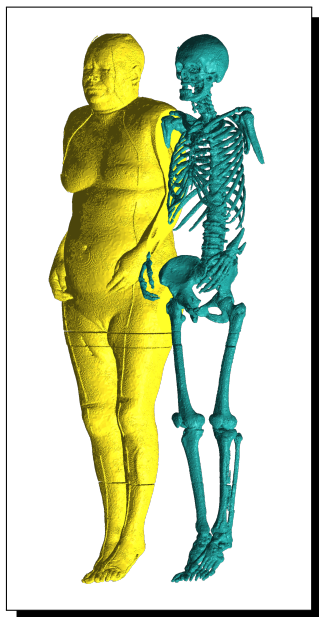
Figure 4.3 **The surfaces of the soft tissues and skull built from the Visible Human project using Shamo.**

Moreover, this also allows one to use *Shamo* to simulate current in any conductor with an organic shape, not limited to the head. The tool could eventually be used for a whole body simulation, or to study specific organs or regions. In addition, it gives the ability to include prosthetics or foreign bodies in the models.

To better emphasise the flexibility that this pipeline brings, I used *Shamo* to mesh a segmented version of the Visual Human Project where bones and soft tissues are differentiated (See Figure 4.3). It shows that the method can be applied to larger, not just head related, models.

The last thing to mention while discussing the mesh generation in *Shamo* is that the size of the element can also be explicitly specified for each tissue. This allows to better refine regions of interest if needed or, conversely, to coarsely mesh regions that are far from the effect to be modelled (*e.g.*, the shoulders in a tDCS simulation where the model includes the whole upper body).

4.2. Electrodes

Shamo was mainly developed for EEG and tDCS applications, both of which rely on a set of electrodes placed on the scalp of the subjects. In the real world, as described in Sections 2.2 and 2.3, the

electrodes usually have two main types of geometries: small circular electrodes for EEG and HD-tDCS or large rectangular patches for tDCS.

There are three common ways to model these real world objects in simulations. The first and most detailed one meshes the electrodes as 3D objects, including the added gel and casing. This method is not implemented in *Shamo*.

Starting from the realistic model, the first possible simplification is to consider only the contacting surface of the electrodes. Two methods exist to model this surface. One is to use conform surfaces, *i.e.* the contact surface is computed exactly with respect to the support, and the other relies on the already performed discretisation. The conform approach, even though more realistic, requires editing the mesh of the support surface and its underlying volume. The second one, implemented into *Shamo* and inspired by the work of Ziegler et al. [2014], uses the already generated surface mesh and extracts the elements that are inside the expected interface (*i.e.*, their barycentre lies inside the contact surface).

Finally, and this can only be considered for small circular electrodes, the surface of contact can be reduced to a single point in its centre. For the rest of this work, I refer to the electrodes produced by the non-conform approach as *surface electrodes* and those resulting from the pointwise method as *point electrodes*. An illustration of the difference between these three methods is shown in Figure 4.4.

Model	Included
Point	■
Surf. (Not conform)	■
Surf. (Conform)	☐
Volume	☐

Table 4.1 **The electrode models included in Shamo.**

Table 4.1 shows which of these models are included in *Shamo*.
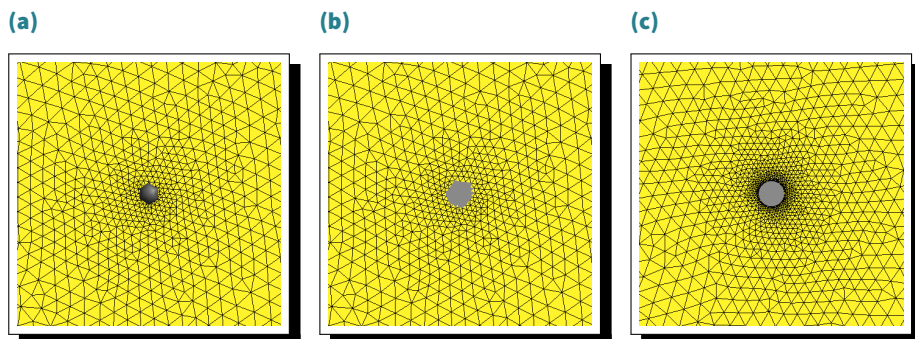
Figure 4.4   An illustration of (a) a point electrode, (b) a surface electrode built using the non-conform method and (c) the same electrode using the conform approach.

4.2.1. Comparison

To assess these different electrode models (*i.e.*, point electrode, surface electrode and conform electrode), I computed the magnitude of the current density induced by the injection of $1\,\text{A}$ into an isotropic cube with edge length of $20\,\text{cm}$. The anode and the cathode were placed in the middle of opposite faces. This simple simulation was repeated for two electrode sizes (*i.e.*, radius) and the relative difference

$$d = \frac{|\boldsymbol{j}_1| - |\boldsymbol{j}_2|}{|\boldsymbol{j}_1|}$$

between each pairs of the three electrode models was computed. The obtained results are presented in Figures 4.5 and 4.6 for circular electrodes with diameters of 1 and 5 cm respectively.

Apart from some numerical artefacts in the corners of the cube (See the note below), the regions where the differences between the models is not negligible are really close to the electrodes themselves. The point electrode is the one yielding the highest differences with the conform model.

> **Note**   The magnitude of the current density close to the corners of the cube on is very low, since almost no current passes through these regions. Thus, even though the relative error is higher there, the absolute error remains negligible.

As expected, when compared to a small conform electrode, the regions where the difference is high remain close to the electrodes. This is not the case when the electrodes to model become larger. Consequently, point electrodes can be used to model EEG electrodes but should not be considered for larger patches such as those employed in tDCS.

On the other hand, the non-conform electrodes are comparable to the conform ones for small and large electrodes. Indeed, when simulating current flow through the head of a subject, the regions of interest are located in the brain (possibly deep) which is surrounded by the skull playing the role of an insulator. Thus, the fact that both the point and non-conform surface electrodes induce almost the same current density as the conform surface in such regions allowed us to use these simpler models (Point electrodes for EEG or HD-tDCS and surface electrodes for tDCS). In *Shamo*, point and surface electrodes are interchangeable and can even be mixed in a single model if needed.
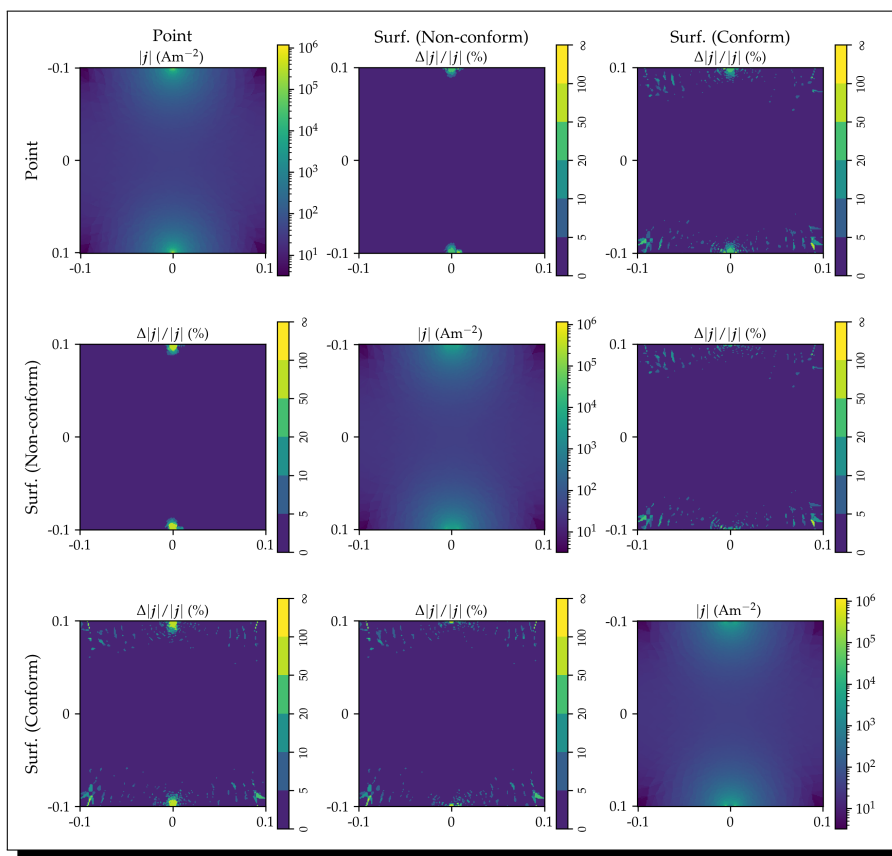
Figure 4.5   A comparison of the current density induced in a cube resulting from the injection of a 1 A current through electrodes with 1 cm diameter. The diagonal figures show the measured current density while the off-diagonal ones show the relative difference between the corresponding pairs.
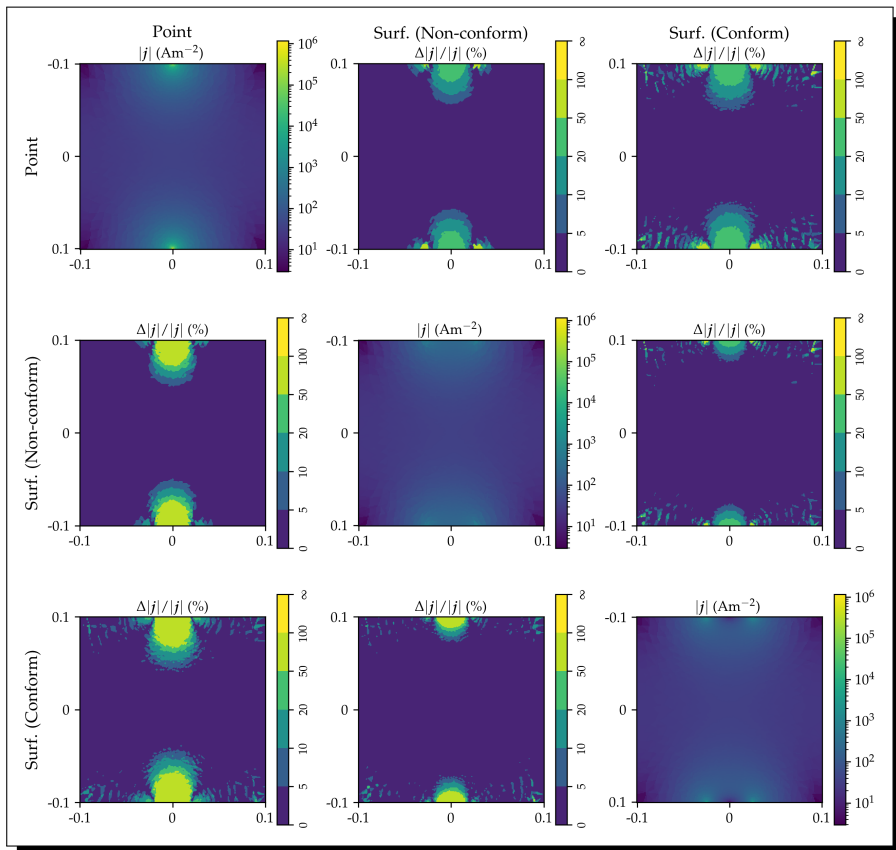
Figure 4.6 **A comparison of the current density induced in a cube resulting from the injection of a 1 A current through electrodes with 5 cm diameter. The diagonal figures show the measured current density while the off-diagonal ones show the relative difference between the corresponding pairs.**

4.3. Tissues properties

As discussed in Section 3.2, the electric conductivity of the biological tissues can be considered as either isotropic or anisotropic. While, most of the time, researchers and practitioners use isotropic properties to solve the EEG forward problem and simulate tDCS, it has been shown that anisotropy of both the white matter and the skull influence these processes [Marin et al., 1998; Haueisen et al., 2002; Wolters et al., 2006; Bangera et al., 2010; Güllmar et al., 2010; Vorwerk et al., 2014].
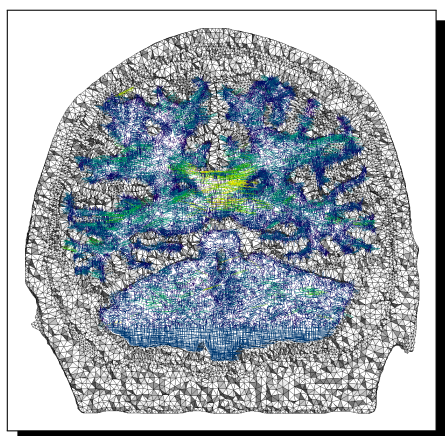
Figure 4.7 **A slice of a model including a tensor for white matter anisotropy. The conductivity across the corpus callosum appears greater than in the rest of the tissue.**

Consequently, *Shamo* provides different ways to embed anisotropic fields into finite element models that can then be used to define the properties of the tissues during the simulations. This opens some possibilities, since isotropic properties can also be modelled using a conductivity tensor with orthogonal eigenvectors and equal eigenvalues.

To better explain all the implications of this functionality, I built two spherical models that only share the mesh of their outer surface (*i.e.*, the surface of the scalp). The first model contains the five main tissue classes composing the head, namely white matter, gray matter, cerebrospinal fluid, skull and scalp, modelled as concentric spheres. This model can be though of as a boundary element model

in which the volumes between the tissue interfaces have been filled with tetrahedron. On the other hand, the second model was obtained by keeping only the outer surface of the first one and filling it with tetrahedron. We refer to those models as the *model 5t* and *model 1t* respectively.

Both models were edited to add two point electrodes on opposite sides of the spheres. This is why they share their external surface mesh, since it ensures that the nodes on which the electrodes are placed are located at the exact same coordinates. Figure 4.8 presents the two meshes and the boundaries of the different compartments, as well as a cut of the resulting meshes.

First, let us consider the case where all the tissues are isotropic. In this case, the traditional approach would be to build a model similar to 5t and to set the electric conductivity of each compartment during the simulation. Another option would be to define a tensor that encapsulates the isotropic properties of the different tissues and spanning over the whole volume and to embed it in a model composed of only one compartment, such as 1t. We compared the values of the magnitude of the current density resulting from the injection of an electric current of $2\,\mathrm{mA}$ between the two electrodes for both methods. The results are presented in Figure 4.9a and the conductivity values used in these simulations are given in Table 4.2.

Tissues	κ (Sm^{-1})
Scalp	0.4137
Skull	0.0160
CSF	1.7100
GM	0.4660
WM	0.2167

Table 4.2 **The values of electrical conductivity used in the simulations.**

The relative difference between the magnitude of the current density computed with the different models is negligible almost everywhere in the sphere, apart from around the interfaces. Indeed, in model 5t, the interfaces are modelled by smooth spheres. In opposition, model 1t does not contain any smooth interface and, consequently, in those regions, the difference between the models is greater. Nevertheless, it seems that the error around the central sphere representing the white matter is negligible.

(a)

(b)

(c)

(d)
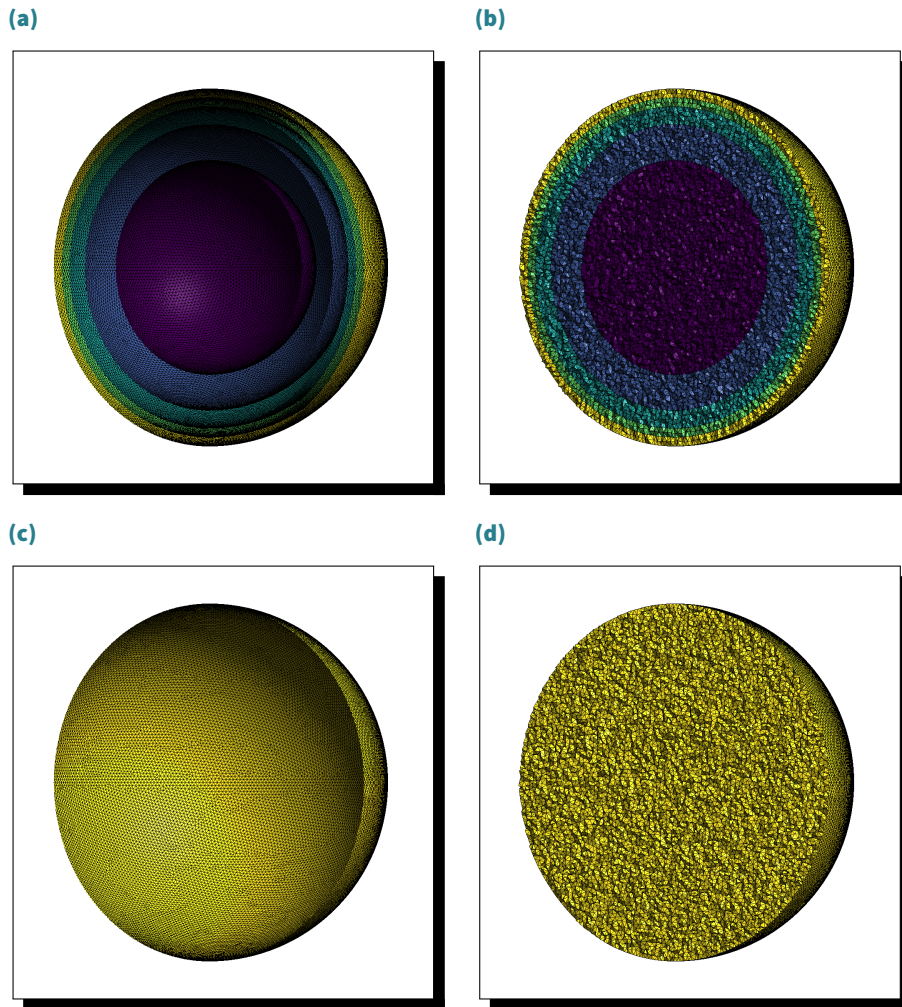
Figure 4.8   The boundaries of the compartments from (a) model 5t and (c) the model 1t and their respective finite element models (b) and (d).

Now, it is also possible to consider anisotropic tissues. For this example, I set the conductivity of the white matter to be 10 times higher along the y-axis than along the other axes. Using the same method as in the previous simulations, the conductivity of the isotropic compartments is set during the simulation for model 5t while it is encapsulated in the tensor for model 1t. The results of these simulations are shown in Figure 4.9b.

Similarly to the previous simulations, the relative difference is greater around the interfaces. The difference is that, this time, the interface between the isotropic gray matter and the anisotropic white matter is higher. The reason for that is the same (*i.e.*, the difference of smoothness of the interfaces), but it is amplified by the difference between the conductivity of the two media.

Being able to model the conductivity of different tissues using a mesh that only contains a single compartment can be useful for multiple reasons. First, meshing the whole head without needing the boundaries of the different compartments could reduce the complexity of the mesh generation process. While the previously presented meshing method already tackles this problem, using a single compartment could also be useful in cases where no previous segmentation is needed. For instance, using MR-EIT, one could provide a continuous field of conductivity across the whole head without specifying the number of tissues and their respective distribution.

Still, building such a mesh yields more noisy interfaces between the compartments, meaning that, for convoluted tissues of interest such as gray matter, this method could produce non-negligible errors. In the previous examples, I only considered either as many compartments as tissues or a single one. However, a hybrid approach could be implemented. In such approach, the traditional model composed of only five tissue classes could be enhanced by virtually increasing the number of tissues embedded using different tensors for each compartment. For instance, the soft tissue compartment usually contains the skin, fat, muscles, and blood ves-
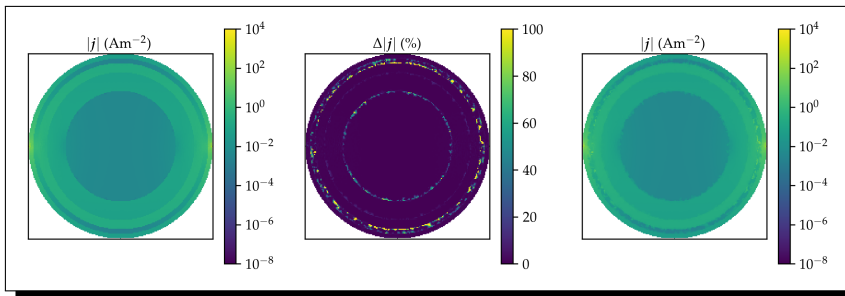
(a)
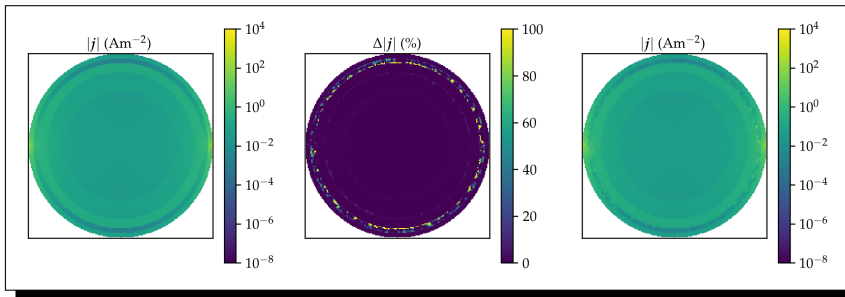
(b)

Figure 4.9 **A comparison of the current density resulting from the injection of a 2 mA induced in a multi-shell sphere, with conductivity set as a single value for each compartment, and a single-shell sphere, with conductivity determined as a tensor. The conductivity of the central sphere is defined as (a) isotropic and (b) anisotropic in both models. The middle figure represents the relative difference between (left) model 5t and (right) model 1t. The cut is along the xz-plane.**

sels. While modelling the blood vessels using a tensor would require to set a very small mesh size, it would be easy to differentiate fat, muscles and skin.

This technique, as explained in Section 3.2, was mainly considered for the skull in order to separate the compact and soft bone, but with *Shamo*, nothing prevents the user to apply it to other tissue classes.

5.

EEG applications

While the development of *Shamo* is at the heart of my thesis, it is not the actual goal. Indeed, the question that first lead to the development of *Shamo* concerned the reported inaccuracies in the determination of the sources (localisation and magnitude) of the EEG signal recorded due to the uncertainty in the electric conductivity of the biological tissues. Researchers studied the influence of these parameters and of other model choices, such as skull modelling and tissues anisotropy, and showed that it induces erroneous electric field and potential estimations [Haueisen et al., 1995, 1997, 2002; Vallaghe and Clerc, 2009; Jochmann et al., 2011; Dannhauer et al., 2011; Lanfer et al., 2012; Akalin Acar and Makeig, 2013; Montes-Restrepo et al., 2014; Cho et al., 2015; Akalin Acar and Makeig, 2013; Wolters et al., 2006; Vorwerk et al., 2019a; Saturnino et al., 2019].

As described in Section 2.2, the source reconstruction is performed in two steps: solving the forward then the inverse problems. Since *Shamo* is dedicated to the forward simulations, we de-

cided to study the influence of the conductivity parameters on the computed leadfield matrix for a single subject.

In addition to these physical parameters, we compared three skull models. Indeed, skull acts as an electrical insulator. Thus, different representation of this tissue have been proposed [Sadleir and Argibay, 2007; Dannhauer et al., 2011; Lanfer et al., 2012; Montes-Restrepo et al., 2014]. Usually, a single compartment is used to model the skull. This is partly due to the fact that further segmenting it into spongy and compact bone is not trivial and not included in most of automated segmentation pipelines. Still, recently, methods have been published to differentiate the two tissue classes [Puonti et al., 2020; Taberna et al., 2021]. An anisotropic model, where the radial and tangential conductivity differ, have also been studied by Fuchs et al. [2007]. In the present application, we compared only models differing in geometry, with isotropic conductivity in each tissue compartment, and did not consider the tensor approach.

The results of this application are partly available in our published work (See Appendix A).

5.1. Dataset

For this study, we considered a single subject based on the multimodal imaging-based detailed anatomical model of the human head and neck (MIDA) [Iacono et al., 2015]. This model consists of a $350 \times 480 \times 480$ magnetic resonance image with voxels of $0.5 \times 0.5 \times 0.5$ mm^3 segmented into 116 different tissue classes.

No other image is provided with it (*e.g.*, the original T1-weighted or diffusion weighted images). Thus, the models we derived did not include an anisotropy tensor for the white matter.

5.2. Finite element models

In order to evaluate the effect of different skull models on the EEG forward problem, we derived 3 different finite element models with distinct skull structure. The first step to build these geometries was to merge the structures of the MIDA model into the main tissue classes we were interested in, namely, white matter (WM), gray matter (GM), cerebrospinal fluid (CSF), the different compartment of the skull and the remaining tissues that we classified as soft (SFT). Then, the most complex FEM was built using *Shamo*. It defines a four compartments skull. The lower part, common to all three models (SKL), the inner and outer tables (respectively SKL ICPT and SKL OCPT) and the spongy (SKL SPG). This model, which considers 3 different skull volumes for the upper part, is referred to as *model 3*.

The resulting mesh was composed of 1.355×10^6 tetrahedra. To make sure that the results produced with the different models were comparable, we then used this initial geometry to define *model 1* and *model 2* which respectively used a single compartment for the whole skull (SKL) and a three compartments skull comprising the lower part (SKL), the spongy (SKL SPG) and the compact (SKL CPT) bone (*i.e.*, 2 skull volumes for the upper part). This was achieved using *Gmsh* [Geuzaine and Remacle, 2009].

The three different skull representations and the mesh of model 3 are shown in Figure 5.1.
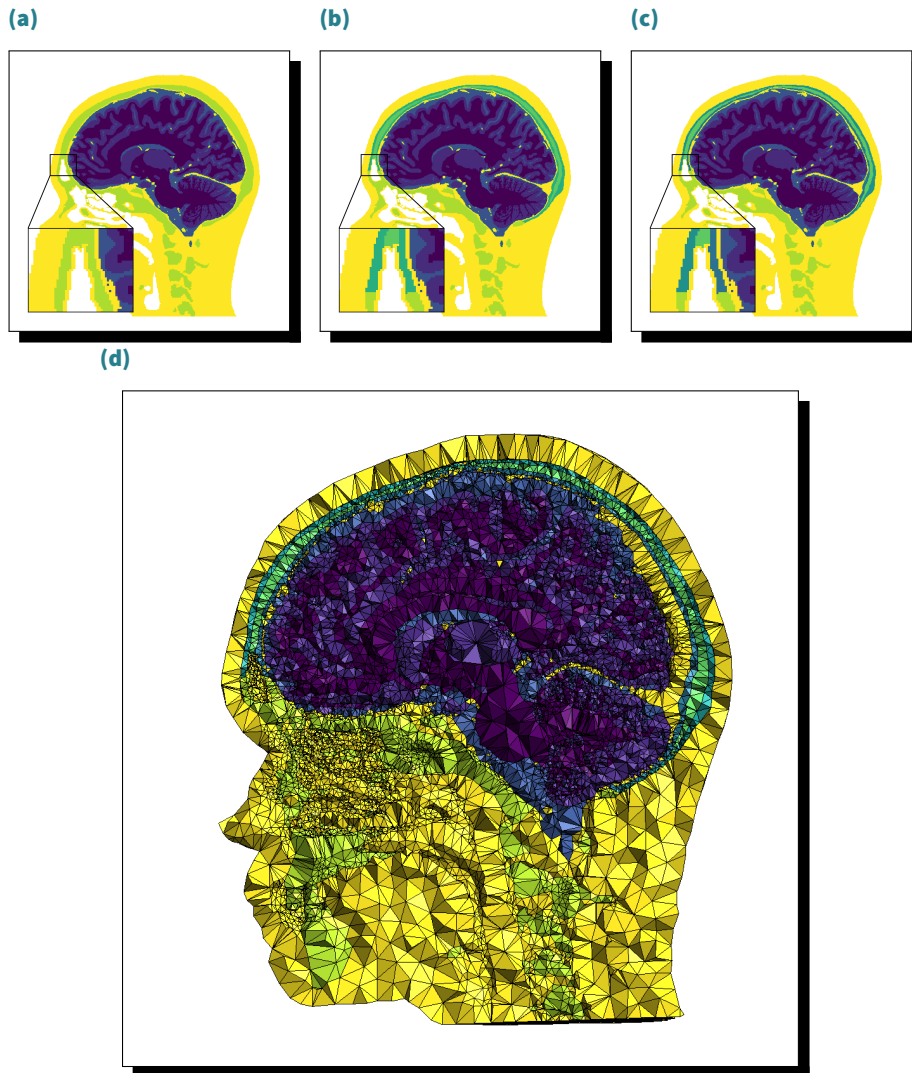
Figure 5.1   A sagittal cut of (a) the segmented images for model 1 where the skull is a single isotropic compartment, (b) for model 2 with spongy and compact bone differentiated (upper part only), (c) for model 3 where the outer and inner tables of the skull are differentiated (upper part only) and (d) the mesh corresponding to model 3. In (a), (b) and (c), the lower part of the skull is the same.

5.3. Electrode placement

After building these finite element models, 63 point electrodes were added (See Section 4.2) based on the international 10-10 EEG system, including the fiducials for the nose, left and right ears, and inion (See Section 2.2.2). For the simulations presented below, the latter serves as the reference, while the other fiducials are not considered in the building process of the leadfield matrix. Thus, 59 electrodes were included, as shown in Figure 5.2.
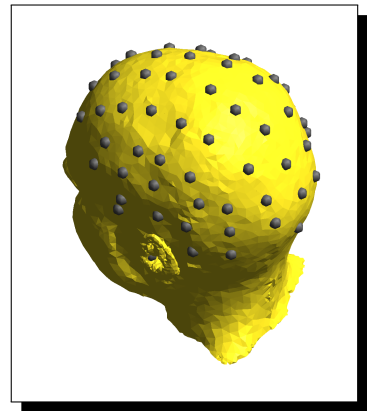
Figure 5.2 **The electrodes from the international 10-10 EEG system used to build the leadfield matrix.**

5.4. Electric conductivity of the tissues

As discussed in Section 3.2, the review of the electric conductivity measurements of the different tissues composing the head from McCann et al. [2019] leads to truncated normal distributions of this property for most of the tissue classes, as summarised in Table 5.1. These informed probability distributions were used for a first set of models, based on the 3 meshes described in Section 5.2, that we refer to as *model 1A*, *model 2A* and *model 3A*.

In addition to these empirical distributions, we defined a uniform distribution spanning the whole range of the reported con-

Tissues			Parameters (Sm^{-1})				Model		
Name	Abbr.	Col.	Min.	Max.	Mean	Std.	1	2	3
Scalp	SCP	▮	0.1370	2.1000	0.4137	0.1760	■	■	■
Skull (Whole)	SKL	▮	0.0182	1.7180	0.0160	0.0190	■	■	■
Skull (Spongy)	SKL SPG	▮	0.0012	0.2890	0.0497	0.0735	□	■	■
Skull (Compact)	SKL CPT	▮	0.0024	0.0079	0.0046	0.0016	□	■	□
Skull (Outer table)	SKL OCPT	▮	0.0008	0.0078	0.0049	0.0029	□	□	■
Skull (Inner table)	SKL ICPT	▮	0.0028	0.0129	0.0068	0.0036	□	□	■
Cerebrospinal fluid	CSF	▮	1.0000	2.5100	1.7100	0.2981	■	■	■
Gray matter	GM	▮	0.0600	2.4700	0.4660	0.2392	■	■	■
White matter	WM	▮	0.0646	0.8100	0.2167	0.1703	■	■	■
Extended	EXT	-	0.0008	2.5100	-	-	-	-	-

Table 5.1 **The tissues and their respective electric conductivity parameters used for the different models.**

ductivity values for all the tissue classes considered. We called it the *extended distribution (EXT)*. It represents a worst case scenario where no prior information on the electric conductivity of the tissues would be available. We applied this distribution to all the tissues of a second set of models further referred as *model 1B, model 2B* and *model 3B*.

5.5. Leadfield matrices

Following the reciprocity principle applied on element basis, described in Section 3.1.5 and implemented in *Shamo,* the computed leadfield matrix resulting from a single simulation, referred to as $[l]_{\text{full}}$ was too large for practical use (*e.g.*, source reconstruction or, in this case, sensitivity analysis). Indeed, given that the current sources should only appear in the gray matter, that the mesh for this particular tissue is made of about 368000 tetrahedra, and that we have considered 59 active electrodes, the size of $[l]_{\text{full}}$ was $59 \times 3 \times 368000$.
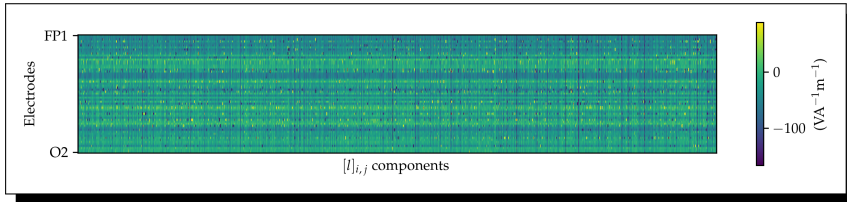
Figure 5.4   The leadfield matrix computed for model 3 using the mean conductivity values for all the tissues.

A solution is to reduce the spatial resolution. In their paper, Michel and Brunet [2019] state that the definition of the spatial resolution is a sensitive problem but that increasing it, *i.e.,* lowering the minimum distance between two potential source sites, does not lead to a linear increase in the accuracy of the reconstructed sources. Actually, this accuracy has a limit due to the fact that the amount of information provided to the inverse problem remains constant since the number of electrodes is fixed.
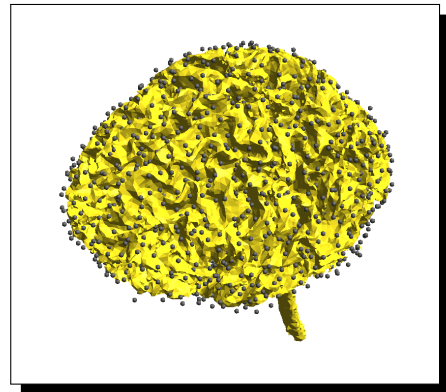
Figure 5.3   The remaining 2127 potential source sites embedded in the generated leadfield matrices.

Therefore, we fixed the minimum source-to-source distance to $7.5\,\mathrm{mm}$. This yielded a total of 2127 sources (See Figure 5.3) and, thus, a leadfield matrix $[l] \in \mathbb{R}^{59 \times 6381}$ which was way more manageable than $[l]_{\mathrm{full}}$. The reduced leadfield matrix computed for model 3 with the mean conductivity values is shown in Figure 5.4.

5.6. Uncertainty quantification and sensitivity analysis

The goal of this study was to assess the influence of the different skull models and of the uncertainty on the electric conductivity of the tissues on the computation of the forward model. As explained in Section 3.3, the expressions for the Sobol indices require a single scalar output. Therefore, we chose to investigate the uncertainty and the sensitivity of the whole matrix to the values of the conductivities $\kappa = [\kappa_{WM}, \ldots, \kappa_{SCP}]$ by considering a distance metric $m(\kappa)$ relative to the leadfield matrix computed for the mean conductivity values $[l]_{ref} = [l(\bar{\kappa})]$

$$m(\kappa) = ||[l(\kappa)] - [l]_{ref}||_F, \qquad \textbf{Eq. 5.1}$$

where $[l(\kappa)]$ is the leadfield matrix computed with the electric conductivity of the tissues set to κ and $||\ldots||_F$ is the Frobenius norm.

For both the uncertainty quantification and sensitivity analysis, 101 simulations were performed for each of the 6 models. The first simulation was built with $\bar{\kappa}$ (and are the same for models A and B) while the 100 others used electric conductivity values determined by sampling the parameters space with a Halton sequence. Thus, we used a total of 603 simulations.

5.6.1. Uncertainty quantification

The results from these simulations allowed us to compute the above-mentioned metric for the different models. The distributions we obtained are shown in Figure 5.5. The unit of the metric
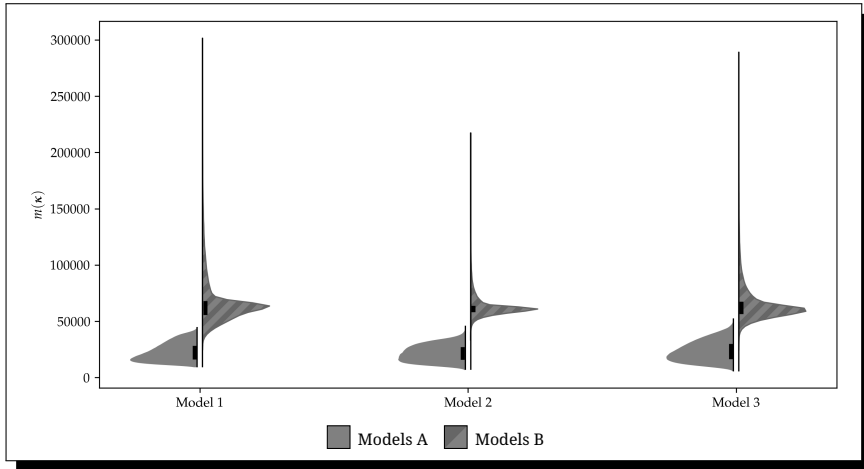
Figure 5.5   **The distributions of the metric computed for the different models.**

is not interpretable, since it depends on the number of elements in the matrix, but it still allows us to directly compare the different models.

5.6.2. Models comparison

To compare the outputs of the models pairwise, we used multiple Bayesian linear models with Bambi [Capretto et al., 2020] which is based on PyMC3 [Salvatier et al., 2016]

$$Y \sim \mathcal{N}(\mu, \sigma^2),$$ **Eq. 5.2**

where Y is dependent variable (*i.e.*, the metric) and

$$\mu = \alpha + \beta \cdot X + \epsilon,$$ **Eq. 5.3**

with α the intercept, β the slope, X the independent variable (*i.e.*, the model) and ϵ the error term. For all the models below, weakly

informative priors were set [Westfall, 2017] and they were fitted using the no-u-turn sampler (NUTS) [Hoffman and Gelman, 2011].

To assess the significance of the effect of the independent parameter on the metric, we used the $95\,\%$ *highest density interval (HDI)* and the *region of practical evidence (ROPE)* [Kruschke and Liddell, 2018]. In this method, the ROPE represents a range of values that are considered equivalent to the null value. If the $95\,\%$ HDI lies completely inside of the ROPE (or if they intersect for more than $97.5\,\%$), one can conclude that the parameter is null. Conversely, if the $95\,\%$ HDI does not intersect with the ROPE (or if they intersect for less than $2.5\,\%$), the parameter can be considered non-null. The boundaries of the ROPE were set to $\pm 0.1 \cdot \mathrm{std}(Y)$.

Ref.	Comp.	β (95 % HDI)	ROPE
1B	1A	$[-45\,119.7,\ -44\,163.3]$	± 2800.2
2B	2A	$[-41\,468.7,\ -40\,971.3]$	± 2235.2
3B	3A	$[-41\,881.5,\ -41\,159.2]$	± 2459.7

Table 5.2 **The 95 % HDI and ROPE of the slopes computed when comparing the results of different conductivity priors.**

First, we compared the results from the models A and B. To do so, the values of X were set to 0 for metrics computed with models B and to 1 for those resulting from models A. This way, the slope represents the expected reduction of the metric when moving from setting very weak priors on the conductivity of the tissues to setting more constrained priors. The $95\,\%$ HDI computed for the different β are presented in Table 5.2. For all three models, using the more informed probability distributions for the conductivity of the tissues yields a large reduction of the metric.

Ref.	Comp.	β (95 % HDI)	ROPE
1A	2A	$[-1151.1,\ -745.1]$	± 749.5
1A	3A	$[\ 585.1,\ 1054.3]$	± 831.2
2A	3A	$[\ 1546.2,\ 2003.8]$	± 804.0
1B	2B	$[-4860.1,\ -3871.6]$	± 1759.1
1B	3B	$[-2835.5,\ -1738.9]$	± 1980.4
2B	3B	$[\ 1686.0,\ 2456.6]$	± 1363.3

Table 5.3 **The 95 % HDI and ROPE of the slopes computed when comparing the results of different skull models.**

Then, we compared the skull models two-by-two (*i.e.*, 1-2, 1-3 and 2-3). The results are displayed in Table 5.3. The greyed out rows show the cases where the $95\,\%$ HDI of the slope intersects with

the ROPE for more than 2.5 % and less than 97.5 %. For those, we cannot conclude whether there is, or not, a difference. Still, for both 2A-3A and 2B-3B, the slope is positive.

5.6.3. Sensitivity analysis

After building Gaussian process regressors for each of the six models, we computed the first and total order Sobol indices as described in Section 3.3. They are presented in Figure 5.6.

5.7. Discussion

As we would have anticipated, Figure 5.5 and the results from Table 5.2 show that the variability and average of the samples of models A are lower than the ones of their corresponding models B. Indeed, as explained earlier, using the extended uniform distribution is equivalent to having a very weak prior on the electric properties of the tissues. This yields wider distributions of the computed metric with larger discrepancies on average than the outputs of the models with more constraining priors. Thus, using more informed probability distributions for the electric conductivity reduces the intrinsic variability of the output of the models.

Still, we would have expected a reduction of the variability between models 1A and 2A/3A and an increase between models 1B and 2B/3B. Indeed, the skull models include an increasing number of compartments from models 1 to 3. For those considering the constrained probability distributions of κ from McCann et al. [2019], since the ranges of these distributions is orders of magnitude smaller for compact skull, outer and inner tables than for

(a)
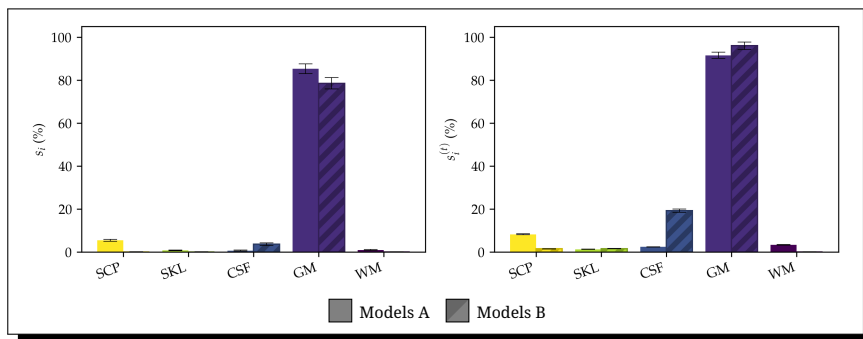
(b)
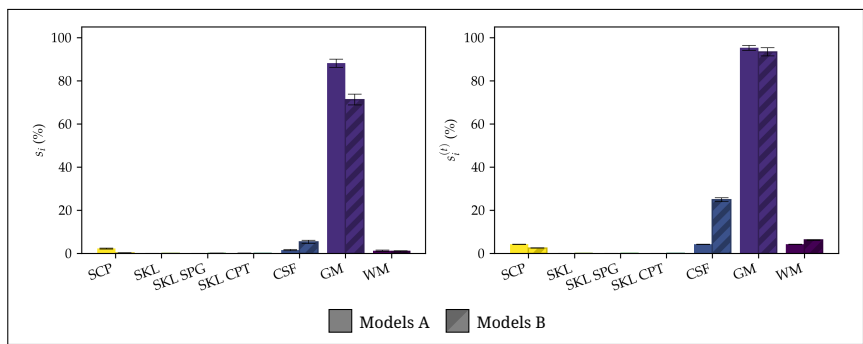
(c)
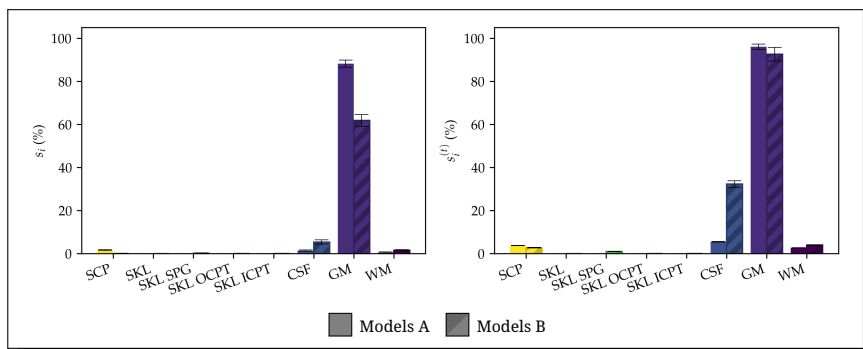
Figure 5.6 **The computed first (left) and total (right) order Sobol indices for (a) models 1A and 1B, (b) models 2A and 2B and (c) models 3A and 3B.**

the whole skull, the uncertainty lying in the model inputs is lower in models 2A/3A than in model 1A. Consequently, one could expect a reduction of the uncertainty in the output metric. Similarly, models B employ the extended distribution for all of their tissues. Hence, increasing the number of tissues in the model increases the uncertainty in the inputs of the simulations and should yield a higher uncertainty on the output.

The computed Sobol indices provide an explanation to this counter-intuitive behaviour. In Figure 5.6, the computed s_i and $s_i^{(t)}$ corresponding to any skull related tissue (SKL, SKL SPG, SKL CPT, SKL OCPT and SKL ICPT) are so close to 0 that they are all negligible. It means that the variance of the computed metric is not explained by the uncertainty stemming from their electric conductivity. Moreover, the comparison of the skull models shows that differentiating the compact and spongy bone compartments could yield a lower average metric and thus a smaller difference with the reference matrix. Yet, further dividing the compact skull into its inner and outer tables increases the uncertainty in the model output.

On the other hand, the conductivity of gray matter alone explains about $90\,\%$ of the overall variance of the metric for all the models. Since the extent of the range of the conductivity probability distribution for this tissue is one of the largest reported, and considering the related Sobol indices, our results indicate that, in order to obtain a better accuracy in the EEG forward solution, researchers should focus on acquiring more accurate values of κ_{GM}.

5.8. Conclusion

In this first application, we assessed the influence of the uncertainty of the tissues electric conductivity and of different skull mod-

els on the computed EEG forward solution for a single subject. The goal was to demonstrate the functionalities of *Shamo* while, first, performing an experiment similar to what we would like to become the norm in EEG source reconstruction and, second, hinting at which tissue models and conductivity one should focus on.

The interest of *Shamo* for such study is discussed in Chapters 7 and 8. Here, I focus on the application itself.

The results presented above confirm that the uncertainty on the tissues electric conductivity induces variability in the computed EEG forward solution, and that improving the accuracy of these parameters reduces the variation in the output. For our specific case, the process revealed that adding the spongy bone compartment to the model could reduce the variability of the output, but that this is not one of the key parameters for improving the accuracy. While such claim goes against the results of Vorwerk et al. [2019a], this can be explained by the difference in the input distributions used. Indeed, those considered here are much wider for gray matter, while much tighter for the different skull compartments. Our results also corroborate those from Van Uitert et al. [2004] and Saturnino et al. [2019] which conclude that the tissues closer to the dipoles have more influence than those far away.

To conclude, this EEG application shows that it is important to determine accurately the electric conductivity of the tissues composing the head of a subject in order to compute an accurate EEG forward solution.

6.

TDCS applications

Another important question that *Shamo* tries to address is to determine the source of variability in reported results from transcranial direct current stimulation. Indeed, the ever-increasing number of tDCS papers tend to show that tDCS suffers from two major issues: the high inter-subject variability in the response to the stimulation and the lack of reproducibility of some published results in follow-up studies.

With a percentage of expected response generally lower than 50% [Müller-Dahlhaus et al., 2008; Jacobson et al., 2012], the method reliability is questionable. Wiethoff et al. [2014] concludes that the after-effect of tDCS on corticospinal excitability is highly variable, and the systematic review of Horvath et al. [2015] rose questions about the efficacy of such device and the underlying mechanisms.

In our paper (See Appendix A), *Shamo* was also applied to tDCS: as for the EEG forward problem, the key question was the sensitivity to tissue conductivity in a single head model. These results

are briefly summarized in Section 6.1. The following sections then tackle tDCS and its sensitivity in a broader sense (The related paper in available in Appendix B).

6.1. Preliminary results
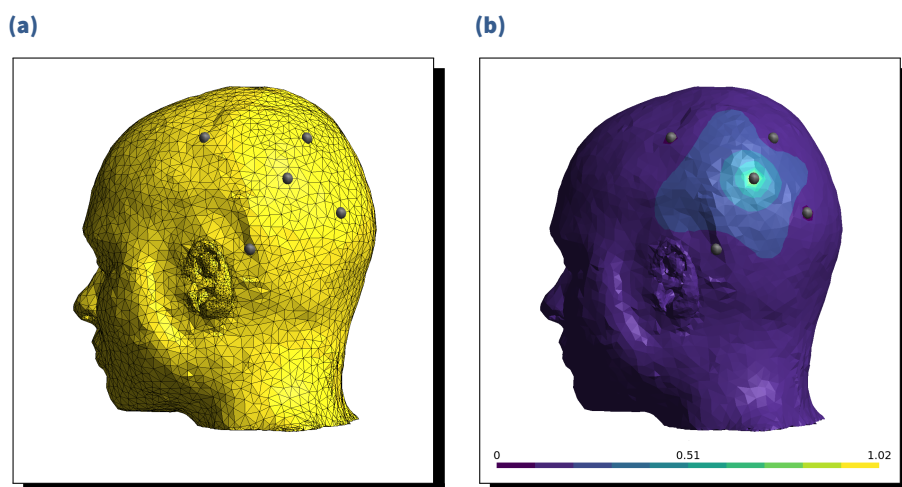
Figure 6.1 **(a) The electrode montage used for the simulations and (b) the electric potential measured on the scalp resulting from the reference simulation, where the electric conductivity was set to the reference value for each tissue.**

In this experiment, we simulated a HD-tDCS experiment where electrode P3 was set as a $4\,\mathrm{mA}$ injector and electrodes TP9, C3, P1 and O1 were set to ground. We used the mesh and conductivity distributions from model 3A as presented in Sections 5.2 and 5.4. Figure 6.1a presents the electrode montage used for this analysis, while Figure 6.1b shows the electric potential measured on the scalp

for a simulation using this montage and where the electric conductivity of the tissues was set to their respective reference value.

To study the sensitivity of the model to the conductivity parameters, we defined the metric of interest as the average of the norm of the current density $|\vec{j}|$ ($\mathrm{A\,m^{-2}}$) in an arbitrary small region of $368\,\mathrm{mm^3}$ located $22.6\,\mathrm{mm}$ under CP3.

Similarly to the EEG application, we sampled the input parameters space using 100 samples drawn from a Halton quasi-random sequence [Halton, 1960], performed a simulation for each of these and extracted the metric of interest (See Figure 6.2 for an overview of the distribution of the output metric).

Figure 6.2   The distribution of the output metric.

Then, we computed both the first and total order Sobol indices for this metric. The results are displayed in Figure 6.3. From these sensitivity indices, we can see that the metric is most sensitive to the electric conductivity of both the scalp and the soft compartment of the skull (by order of importance). This comes as no surprise, since all the electrodes are placed relatively close to each other on the surface of the scalp. Consequently, most of the current remains concentrated in this compartment since it follows the path of least resistance. More-

Figure 6.3   The computed first and total order Sobol indices.

over, s_i and $s_i^{(t)}$ are almost equal for each tissue class. Thus, we can conclude that, in this particular configuration, there is almost no interaction between the different parameters and that regions not located directly under the stimulating electrode are weakly affected by the stimulation.

6.2. tDCS experimental setups

After these preliminary results, we decided to focus on tDCS rather than HD-tDCS since the current is supposed to cross the whole head, and should thus be more sensitive to the different tissues electric conductivity. As for the EEG application, we did not want to focus solely on the conductivity of the tissues.

Hence, we first identified three sources of variability in tDCS experiments designs: the subject head geometry, the physical properties of the tissues, and the electrode placement. To evaluate the effect of these parameters, we performed a simulation study by computing the electric field induced in four different regions of interest (ROI) of the left hemisphere by the injection of 2 mA with six electrode montages (See Table 6.1) and calculated the *induced transmembrane potential (ITP)* on different head geometries (*i.e.*, 20 synthetic subjects). Previous studies reported ITP values between 0.2 and 0.5 mV [Radman et al., 2009; Opitz et al., 2016].

In the process, we account for an error of 1 cm on the anode placement in four directions relative to the reference EEG 10-20 position and for the uncertainty on the electric conductivity of the biological tissues.

Anode	Cathode	ROI	Bipolar	Unipolar
C3	C4	■ MC	■	☐
C3	Fp2		☐	■
F3	F4	■ dlPFC	■	☐
F3	Fp2		☐	■
F7	F8	■ vmPFC	■	☐
P3	P4	■ IPS	■	☐

Table 6.1 **The electrode montages considered and the regions of interest they target.**

6.3. Dataset

As opposed to the previous applications, we wanted to include multiple subjects in the analysis. For this purpose, we used the dataset of 20 simulated normal healthy adults (10 males and 10 females) made available by BrainWeb [1].

For each subject, this dataset provides a structural T1-weighted generated based on a SFLASH sequence (TR $=22$ ms, TE $=9.2$ ms, flip angle $=30°$ and 1 mm isotropic voxel size), 12 fuzzy tissue probability maps and a discrete segmented volume with $0.5 \times 0.5 \times 0.5$ mm^3 voxels [Aubert-Broche et al., 2006a,b].

From these images, we only used the T1-weighted and discrete models converted into NIfTI files using *Nibabel* [Brett et al., 2020] and sorted following BIDS specifications [Gorgolewski et al., 2016].

---

1. https://brainweb.bic.mni.mcgill.ca/

6.4. Finite element models

To generate the finite element models, we had to clean the labelled volumes in order to remove external objects and noise in four consecutive steps (See Figure 6.4a).

First, subjects 18 and 42 included big objects adjacent to the scalp label. Hence, we manually created binary masks using *itk-SNAP* [Yushkevich et al., 2006] to remove these without deteriorating the surface of the scalp. Other subjects presented external objects, but they were separated from the head by at least one layer of voxels, so we did not have to execute this manual step for them.

Next, we computed whole head binary masks. These masks embedded some noise in the form of small clusters, mainly around the eyes and the neck. To remove those, we performed an iterative binary opening using SciPy [Virtanen et al., 2020] until no difference between two iterations was measured.

This step resulted in the definition of some clusters (*e.g.*, the head and external objects). To remove every remaining non-head object, we kept only the largest cluster.

Finally, we performed morphological operations to enforce at least one layer of CSF around the gray matter and one

SEG-11				SEG-05	
Tissue	Label			Tissue	Label
WM	3	→		WM	1
GM	2	→		GM	2
CSF	1	→		CSF	3
SKL	7	→		SKL	4
MRW	11				
FAT	4	→		SFT	5
MSL	5				
SKN	6				
BLD	8				
FAT2	9				
DURA	10				

Table 6.2 Tissue merging rules used to convert the original SEG-11 model into the SEG-05 used in this work. The tissues and abbreviations are white matter (WM), gray matter (GM), cerebrospinal fluid (CSF), skull (SKL), bone marrow (MRW), fat (FAT/FAT2), muscle (MSL), skin (SKN), blood vessels (BLD), dura matter (DURA) and soft tissues (SFT).

layer of soft tissues around the skull. This yielded the labelled images containing 11 tissues that we refer to as *SEG-11*.

While we could have directly used these 11 tissues to build the finite element models (as explained in Section 4.1), we wanted to use the most common model in research and clinical applications and thus reduced its complexity. This simpler model only includes the 5 usual tissue classes, namely, white matter (WM), gray matter (GM), cerebrospinal fluid (CSF), skull (SKL) and soft tissues (SFT). Therefore, we merged tissues from the SEG-11 models into these and obtained the *SEG-05* models. The merging rules are shown in Table 6.2 and the resulting labels are presented in Figure 6.4b for subject 41.

Finally, the SEG-05 images were processed with *Shamo* to generate the 20 subject specific finite element models. These models contain more than 2×10^6 tetrahedra, and a sagittal cut of the one produced for subject 41 is shown in Figure 6.4c.

6.5. Electrode placement

Since one of the goals of this study was to evaluate the effect of an error on the placement of the electrodes, we considered 5 different positions of the anode for each experiment. These placements are the reference one, where the anode is centred on the international EEG 10-20 system position, and the other four result from a displacement of $1\,$cm in central (C)/lateral (L) and anterior (A)/posterior (P) directions. The central-lateral axis goes from the ears toward the symmetry axis of the head, while the anterior-posterior axis goes from the front to the back of the head.

To easily refer to the different stimulating electrodes, we named them after their reference 10-20 position and their displacement. For instance, the P3 anode displaced of $1\,$cm in the central direction if referred to as "P3C".
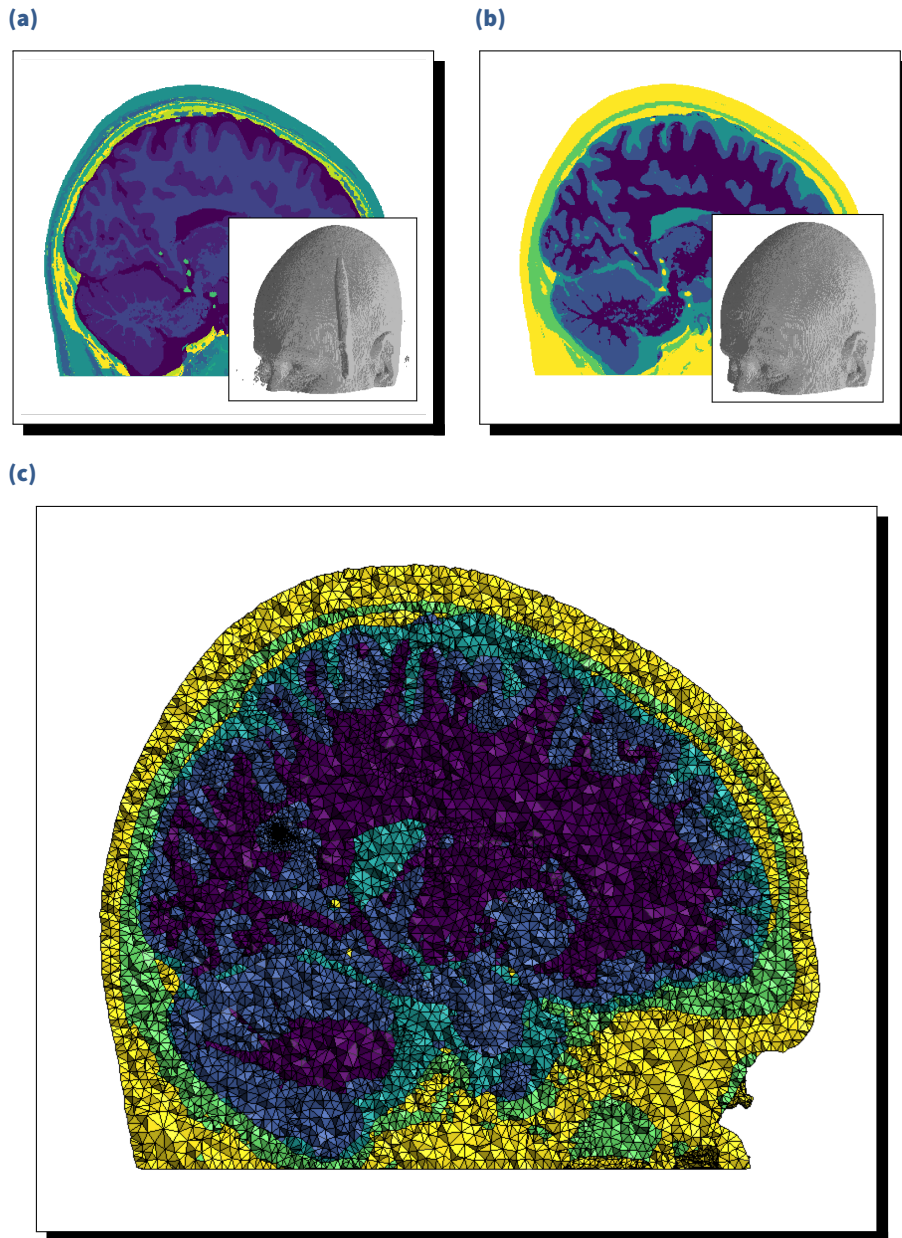
Figure 6.4 **(a)** The original segmented volume, **(b)** the SEG-05 labels obtained after cleaning and merging and **(c)** the resulting mesh built with Shamo for subject 41.

The BrainWeb dataset does not include any electrode information. Consequently, we first located manually the landmarks described in Section 2.2.2, namely, the nasion (NZ), the inion (IZ), and the left and right helix-tragus junctions (LHJ/RHJ) in subject space coordinates using *MRIcron* [Rorden et al., 2007].

Based on these landmarks, we followed the method proposed by Jurcak et al. [2005] to virtually place all the electrodes of the EEG 10-20 system. This technique starts by the generation of a high definition surface mesh of the whole head, which we produced using *Shamo*. The rest of the procedure relies on the extraction of curves on which the geodesic distance between two points is evaluated, in order to follow the distance ratios prescribed by the standard and their displaced counterparts. The resulting positions for subject 41 are presented in Figure 6.5.
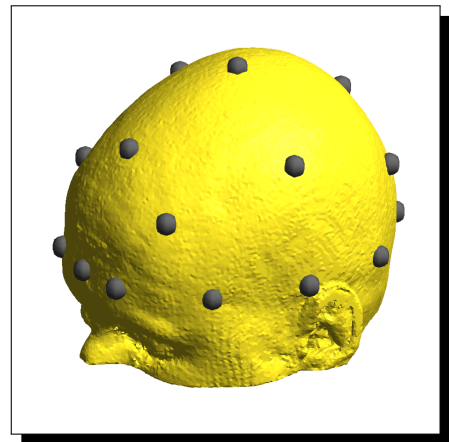
Figure 6.5   **The computed positions of the EEG 10-20 international system electrodes for subject 41.**

Finally, using the meshes described above and the computed electrode positions, we produced a finite element model for each electrode montage. The electrodes were modelled as 5×5 cm^2 patches, which yielded 30 models per subject (*i.e.*, a total of 600 models altogether). Examples of the built models are shown in Figure 6.6 for subject 41.

(a)

(b)

(c)

(d)

(e)

(f)
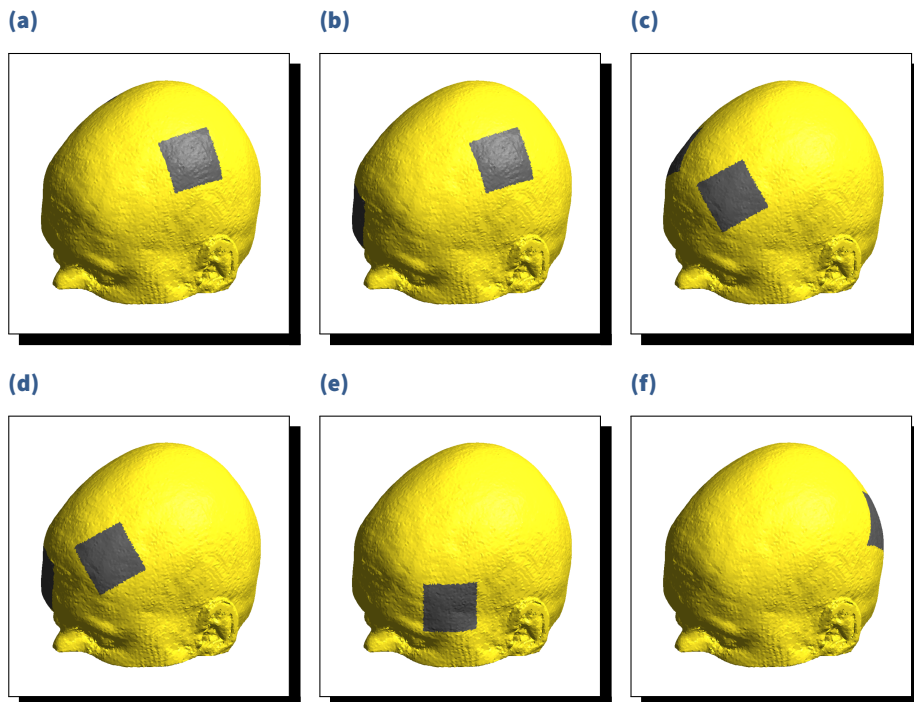
Figure 6.6 **The finite element models of the reference electrode montages for (a) C3-C4, (b) C3-Fp2, (c) F3-F4, (d) F3-Fp2, (e) F7-F8 and (f) P3-P4 electrodes for subject 41.**

6.6. Electric conductivity of the tissues

Just like for the EEG application and preliminary results, we considered the electrical conductivity values published by McCann et al. [2019]. The electric conductivity for the soft tissues (SFT) was set as the one reported for the scalp since its range encompasses the ranges of fat, muscles and blood which are the three main classes we merged into it.

Using a Halton quasi-random sequence [Halton, 1960], we drew 20 different *conductivity profiles* $\kappa = [\kappa_{\text{WM}}, \kappa_{\text{GM}}, \kappa_{\text{CSF}}, \kappa_{\text{SKL}}, \kappa_{\text{SFT}}]$ by sampling the 5D conductivity space defined by the probability densities defined in Table 6.3.

In addition to these profiles, we also considered the reference one, defined as the $\bar{\kappa} = [\bar{\kappa_{\text{WM}}}, \bar{\kappa_{\text{GM}}}, \bar{\kappa_{\text{CSF}}}, \bar{\kappa_{\text{SKL}}}, \bar{\kappa_{\text{SFT}}}]$. Thus, a total of 21 conductivity profiles were used in the simulations.

Tissues			Electrical conductivity (Sm^{-1})			
Name	Abbr.	Col.	Min.	Max.	Mean	Std.
White mater	WM		0.0646	0.8100	0.2167	0.1703
Gray matter	GM		0.0600	2.4700	0.4660	0.2392
Cerebrospinal fluid	CSF		1.0000	2.5100	1.7100	0.2981
Skull	SKL		0.0182	1.7180	0.0160	0.0190
Soft tissues	SFT		0.1370	2.1000	0.4137	0.1760

Table 6.3 **The tissues and their respective electric conductivity parameters as reported by McCann et al. [2019].**

6.7. Regions of interest

As explained in Table 6.1, each electrode montage targets a specific region of interest in the left hemisphere. To extract individual binary masks of these brain areas for each subject, we relied on three different cortical surface atlases (See Section 2.5: Brodmann [Fischl et al., 2008], CP-MMP 1.0 [Glasser et al., 2016] and MarsAtlas [Auzias et al., 2016].

Unfortunately, the latter is not available in fsaverage space (*i.e.*, the standard space for *FreeSurfer* defined as a reference cortical surface) [Mills, 2016]. However, it has been published in Colin27 space [Holmes et al., 1998]. To produce the proper labels in fsaverage space from MarsAtlas, we first converted the segmented volume into labels in the native space of the subject. Next, we registered these labels onto fsaverage cortical surface with the surface registration tools from *FreeSurfer* [Dale et al., 1999]. The resulting labels for the four regions of interest are displayed on fsaverage in Figure 6.7.

Once all the labels were extracted and projected on fsaverage, we registered them on the cortical surfaces of each subject and converted them into binary masks coregistered on the SEG-05 images.

| ■ MC | ■ dlPFC | ■ vmPFC | ■ IPS |
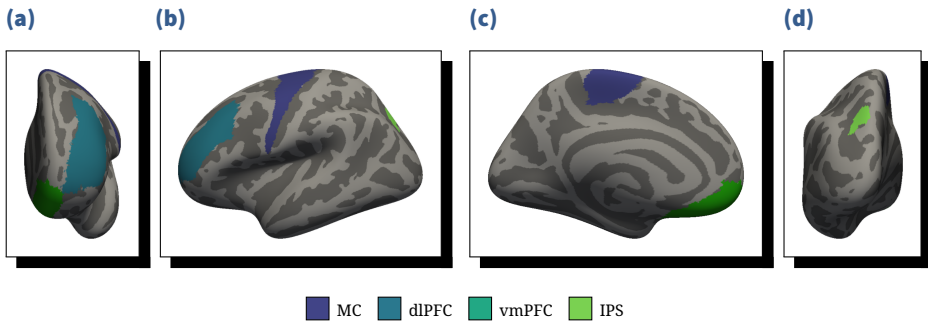
Figure 6.7   **The left hemisphere regions of interest considered in this study and extracted from Brodmann [Fischl et al., 2008], HCP-MMP 1.0 [Glasser et al., 2016] and MarsAtlas [Auzias et al., 2016] atlases displayed on the inflated surface of fsaverage.**

6.8. Simulation results

Considering the 20 subjects, their respective 30 finite element models and the 21 conductivity profiles, we ran a total of 12600 simulations where we computed the electric potential v (V), the electric field e (V m^{-1}), and the current density j (A m^{-2}) resulting from the injection of a 2 mA current by the anode.

To ease further processing, these fields were converted into NIfTI images by sampling them on a regular $1 \times 1 \times 1$ mm^3 grid with the same orientation as the SEG-05 image. Then, by applying the ROI binary masks to these images, we extracted the values of these fields for all the voxels of the regions of interest in each simulation and stored it in a *DuckDB* database [Raasveldt and Mühleisen, 2019]. In addition, we computed both the components normal and tangential to the cortical surface of e and j. Finally, we calculated the average absolute values for all the previously described metrics for each ROI and simulation.

(a) **(b)**

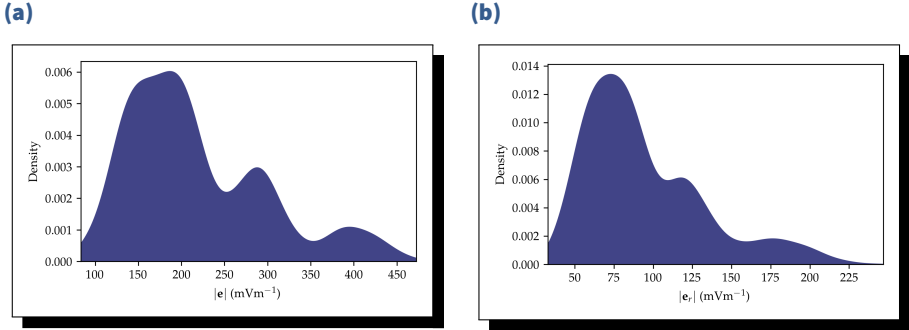| MC (C3-C4) | MC (C3-Fp2) | dlPFC (F3-F4) | dlPFC (F3-Fp2) | vmPFC (F7-F8) | IPS (P3-P4) |
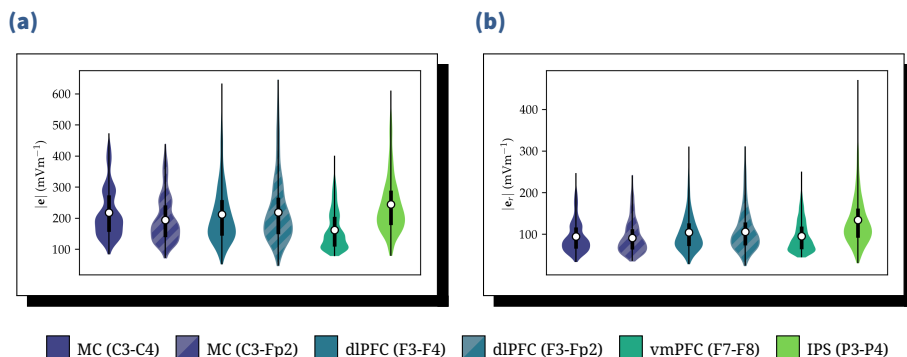
Figure 6.8 **The average absolute value of (a) the magnitude of the electric field and (b) its radial component for the ROIs targeted by the 6 different experiments.**

For the rest of this work, we mainly focused on the magnitude of the electric field $|e|$ and on the magnitude of its radial component (*i.e.*, the component normal to the cortical surface) $|e_r|$. An overview of these two metrics, for the 6 different montages, is presented in Figure 6.8 and a more in-depth view of the results for the different experiments is available in Section C.1.

Overall, the mean absolute magnitude of the electric field $|\bar{e}|$ ranges from 47.2 to $644.2\,\mathrm{mV\,m^{-1}}$ and its component normal to the cortical surface $|\bar{e_r}|$ from 24.2 to $470.7\,\mathrm{mV\,m^{-1}}$.

In order to better picture the results, I show the data obtained for the C3-C4 electrode montage targeting the motor cortex all along the following sections. Figure 6.9 shows the results for this specific montage, and the outcome of the other experiments are provided in Annex C.
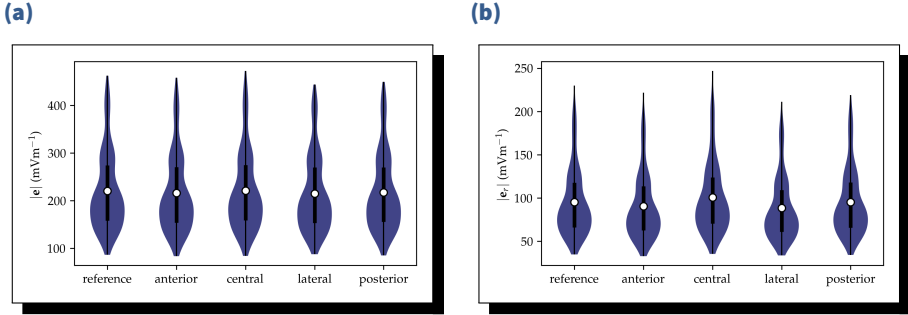
Figure 6.9 **The average absolute value of (a) the magnitude of the electric field and (b) its radial component for the C3-C4 electrode montage targeting the motor cortex.**

6.9. Models comparison

Just like we did for the EEG application in Section 5.6.2, we compared the results from different models using Bayesian linear models defined with Bambi [Capretto et al., 2020]. The basic expression for these is still

$$Y \sim \mathcal{N}(\mu, \sigma^2),$$ **Eq. 6.1**

but the expression of μ was extended to include multiple slopes as

$$\mu = \alpha + \boldsymbol{\beta} \cdot \boldsymbol{X} + \epsilon,$$ **Eq. 6.2**

where $\boldsymbol{\beta} = [\beta_1, \ldots, \beta_n$ is the vector containing the different slopes and $\boldsymbol{X} = [X_1, \ldots, X_n]^\top$ are the independent variables. We refer to the models followings these expressions as *pooled*.

Indeed, as opposed to the EEG application, here, we considered multiple subjects. Thus, we also evaluated mixed effect models to account for the variability induced by the subjects themselves. The

mixed effect models, referred to as *hierarchic*, have different expressions for μ, α and β for each subject

$$\mu_i = \alpha_i + \boldsymbol{\beta}_i \cdot \boldsymbol{X} + \epsilon, \qquad \textbf{Eq. 6.3}$$

$$\alpha_i = \alpha^{(\text{com})} + \alpha_i^{(\text{sub})}, \qquad \textbf{Eq. 6.4}$$

$$(\beta_j)_i = \beta_j^{(\text{com})} + \left(\beta_j^{(\text{sub})}\right)_i, \qquad \textbf{Eq. 6.5}$$

where $\alpha^{(\text{com})}$ and $\beta_j^{(\text{com})}$ are respectively the common intercept and slopes and $\alpha_i^{(\text{sub})}$ and $\left(\beta_j^{(\text{sub})}\right)_i$ are the subject specific contributions to the intercept and slopes.

These models were also fitted using weak priors set automatically [Westfall, 2017] and the NUTS sampler [Hoffman and Gelman, 2011]. The significance of a parameter was assessed using the 95 % HDI and ROPE method [Kruschke and Liddell, 2018] (See Section 5.6.2 for an explanation of the method).

In the next paragraphs, I describe the different linear models that we built in order to compare the results and their respective outputs.

6.9.1. Anode placement

Figure 6.10 presents the results of the simulations obtained by displacing the anode of the C3-C4 electrode montage and targeting the motor cortex of $1\,\text{cm}$ with regard to the reference EEG 10-20 position.

We defined the models to assess the difference between the measurements computed for each of the 5 anode placements from Sec-
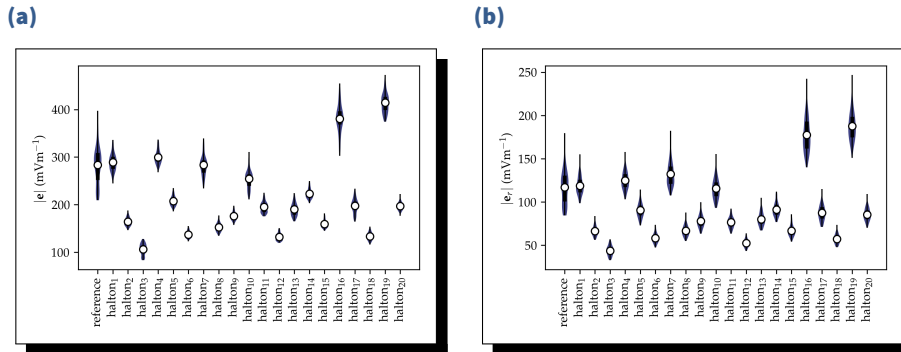
(a)

(b)

Figure 6.10   The average absolute value of (a) the magnitude of the electric field and (b) its radial component for the C3-C4 electrode montage targeting the motor cortex, grouped by anode placement.

tion 6.5 as

$$\mu = \alpha + \sum_{p=1}^{4} \beta_p \cdot X_p + \epsilon,$$

$$\mu_i = \alpha_i + \sum_{p=1}^{4} (\beta_p)_i \cdot X_p + \epsilon,$$

where p corresponds to a specific displacement of the anode (anterior, central, lateral or posterior) and X_p is either 0 or 1 based on the anode used to obtain the record.

Table C.2 presents the 95% HDI of the different slopes computed for the hierarchic model. The gray cells show the intervals that intercept at least 2.5% with the ROPE. Most of the calculated intervals intercept with the ROPE, but none of them is fully included in it. Consequently, we cannot state that a $1\,\mathrm{cm}$ displacement of the anode has a significant effect on the electric field induced in the ROI or not.

Still, by computing the ratio between the boundaries of the β_p and the intercept, we obtain that such a displacement can yield a relative difference to the reference of up to 27.6% for $|\bar{e}|$ and 27.1% for $|\bar{e_r}|$.

(a)

(b)

Figure 6.11 The average absolute value of **(a)** the magnitude of the electric field and **(b)** its radial component for the C3-C4 electrode montage targeting the motor cortex grouped by conductivity profile.

6.9.2. Conductivity profile

Similarly to the anode placement, Figure 6.11 shows the results computed for the C3-C4 electrode montage.

Using the same method as previously, we compared the values of both $|\bar{e}|$ and $|\bar{e}_r|$ calculated for the 20 conductivity profiles drawn using the Halton sequence with the values obtained for the reference one. Thus, we transformed the linear models into

$$\mu = \alpha + \sum_{k=1}^{20} \beta_k \cdot X_k + \epsilon,$$

$$\mu_i = \alpha_i + \sum_{k=1}^{20} (\beta_k)_i \cdot X_k + \epsilon.$$

In these expressions, k refers to one of the 20 conductivity profiles established using the quasi-random Halton sequence and X_k is 1 or 0.

The computed $95\,\%$ HDI for the different slopes of the hierarchic models are shown in Tables C.3 and C.4. As opposed to the anode placement, the majority of the $95\,\%$ HDI fall completely outside the ROPE, indicating that the uncertainty on the conductivity of the tissues has a significant influence on the electric field computed in the ROI.

Moreover, by calculating the same absolute ratio between the different β and α, we found that some conductivity profiles could induce a difference relative to the reference of up to $112.5\,\%$ and $146.6\,\%$ for $|\bar{e}|$ and $|\bar{e}_r|$ respectively.

6.9.3. Bipolar and unipolar electrode montage

As shown in Table 6.1, we simulated a bipolar and a unipolar electrode montage to stimulate both the MC and the dlPFC. In order to compare the values of $|\bar{e}|$ and $|\bar{e}_r|$ computed for each pair, we fitted the models with the following expected values,

$$\mu = \alpha + \beta_{\text{uni}} \cdot X_{\text{uni}} + \epsilon,$$
$$\mu_i = \alpha_i + (\beta_{\text{uni}})_i \cdot X_{\text{uni}} + \epsilon,$$

with X_{uni} equal either to 1 if the montage is unipolar or to 0 otherwise. For the electrode montages targeting the motor cortex, Figure 6.12 presents the results of both the unipolar and bipolar montages.

The values of β_{uni} are presented in Table C.1 for the hierarchic model. Using the unipolar montage when stimulating the MC yields an electric field of up to $13.7\,\%$ lower than with the bipolar montage (However, the significance of the effect on the normal component of the electric field is undetermined). On the other hand, both montages yield equivalent radial component of the electric field when targeting the dlPFC.
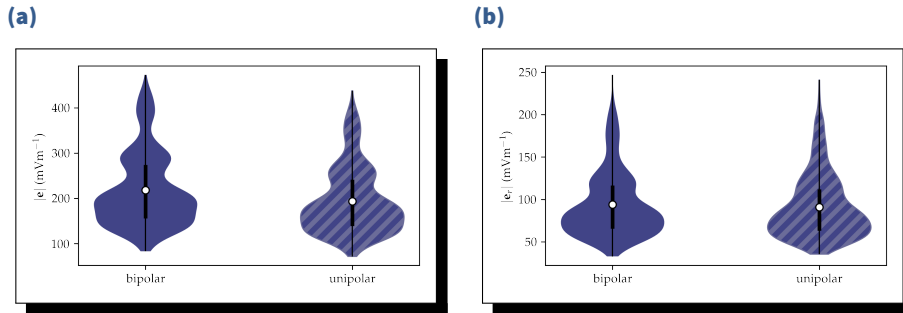
(a)

(b)

Figure 6.12 **The average absolute value of (a) the magnitude of the electric field and (b) its radial component for the electrode montages targeting the motor.**

6.10. Induced transmembrane potential

The steady-state induced trans-membrane potential, denoted by Δu_i (mV), is the potential difference measured between the inside u_{in} and the outside u_{out} of the cell membrane added to the resting state potential Δu_r and due to an external stimulation,

$$u_{in} - u_{out} = \Delta u_r + \Delta u_i.$$

While tDCS is not able to trigger action potentials, it is generally accepted that it generates an induced trans-membrane potential which hyperpolarizes the neuron membranes under the anode and depolarizes it under the cathode [Pelletier and Cicchetti, 2015; Tanaka et al., 2020]. In the present work, we compute the ITP resulting from the different simulations using analytical expressions for both spherical and spheroidal cells.

6.10.1. Spherical cell

The theoretical steady-state ITP resulting from an external electric field e (V m^{-1}) in a spherical cell of radius r_1 (m) with a non-conductive plasma membrane is described by Schwann's equation [Schwan, 1994]

$$\Delta u_\mathrm{i} = \frac{3}{2}|e|r_1\cos(\theta),$$ **Eq. 6.6**

with θ the angle between the electric field and the vector going from the centre of the cell to the point of the membrane where the ITP is calculated.

Consequently, the maximum value of Δu_i is obtained for $\theta = \pi$. To avoid using an arbitrary value for r_1, we finally compute

$$\frac{\max(\Delta u_\mathrm{i})}{r_1} = \frac{3}{2}|e|.$$ **Eq. 6.7**

6.10.2. Spheroidal cell

Pyramidal cortical cells are not spherical, thus we also consider spheroidal cells $r_1 > r_2 = r_3$ with a shape ratio $\gamma = r_1/r_2$ and elongated along the normal to the cortical surface. For such cells, Valic et al. [2003] gives the following expression of the ITP,

$$\Delta u_\mathrm{i} = |e|\sin(\varphi)\frac{r_2\sin(\theta)}{1 - l_x} + |e|\cos(\varphi)\frac{r_1\cos(\theta)}{1 - l_z},$$ **Eq. 6.8**

where φ is the angle between the electric field and the main axis of the cell and l_x and l_z are the depolarization factors

$$l_z = \frac{1 - \lambda^2}{2\lambda^3}\left(\log\left(\frac{1+\lambda}{1-\lambda}\right) - 2\lambda\right),$$ **Eq. 6.9**

$$l_x = \frac{1}{2}(1 - l_z),$$ **Eq. 6.10**

with $\lambda = \sqrt{1 - (1/\gamma)^2}$.

Since we already computed the tangential and radial components of the electric field denoted by $|e_t|$ and $|e_r|$, we have

$$\Delta u_{\mathrm{i}} = |e_t| \frac{r_2 \sin(\theta)}{1 - l_x} + |e_r| \frac{r_1 \cos(\theta)}{1 - l_z},$$ **Eq. 6.11**

which is maximized when

$$\theta = \theta_{\max} = \mathrm{atan}\left(\frac{|e_t|(1 - l_z)}{|e_r|\gamma(1 - l_z)} \right).$$ **Eq. 6.12**

Following what we did for the spherical cell, we derive the size independent expression

$$\frac{\max(\Delta u_{\mathrm{i}})}{r_1} = |e_t| \frac{\sin(\theta_{\max})}{\gamma(1 - l_x)} + |e_r| \frac{\cos(\theta_{\max})}{1 - l_z}.$$ **Eq. 6.13**

6.10.3. Computed values

Using these two cell models, we calculated the maximum ITP ratios for all the simulations (See Table C.5). As for the model comparison, I present the results calculated for the C3-C4 electrode montage in Figure 6.13.

Across all the experiments, the spherical and spheroidal cell models respectively yield values ranging from 70.9 to $966.3\,\mathrm{mV\,m^{-1}}$ and from 21.5 to $441.5\,\mathrm{mV\,m^{-1}}$.

6.11. Discussion

First, the results pertaining to the anode placement error are in line with the ones published by Ramaraju et al. [2018]. Indeed,
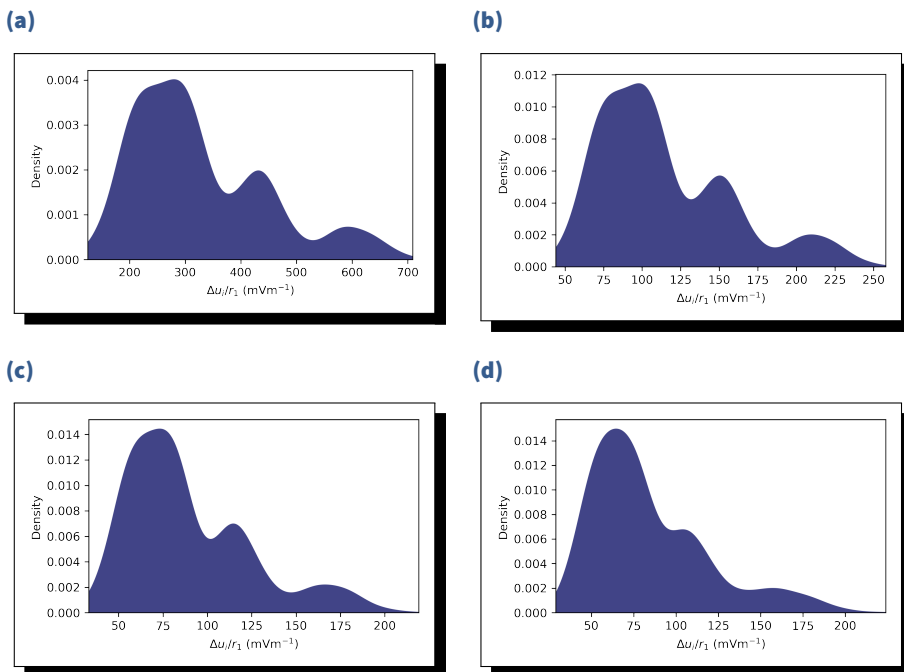
Figure 6.13 **The computed induced transmembrane potential for (a) the spherical model, and (b), (c) and (d) the spheroidal models with shape ratios of 10/8, 10/5 and 10/2 respectively.**

we find that the F3-Fp2 electrode montage is more sensitive to the anode placement than the others. However, the $27.6\,\%$ change in the mean absolute electric field in the left dlPFC is on par with the $38\,\%$ they measured in the left frontal lobe.

While such a difference is non-negligible, it results from a displacement of $1\,$cm of the anode. Considering the work of Rich and Gillick [2019] which showed that the inter- and intra-rater error on the electrode placement is lower than $1\,$cm, the shift in the anode position we studied can be regarded as an upper bound to the plausible experimental deviation. As a result, the actual variation of the electric field induced in the ROI due to a misplaced electrode is expected to be smaller than what we calculated here.

On the other hand, the results of the models assessing the effect of different conductivity profiles are concerning. As for the anode placement, the F3-Fp2 electrode montage is the most influenced, with a difference of up to $112.5\,\%$ on $|\bar{e}|$. Still, it is interesting to note that the direction of the electric field varies the most in the IPS when using the P3-P4 electrode montage. Indeed, the maximum relative difference can be up to $146.6\,\%$ on $|\bar{e_r}|$.

These considerable variations lead us to question the information we can extract by modelling tDCS. Until we can feed the models with more educated priors about the electrical conductivity of the biological tissues, the randomness of the outputs makes it almost impossible to gain insights and draw conclusions about the electric effect of the stimulation. Moreover, the conventional way of modelling tDCS, which involves setting almost arbitrary values to the electrical conductivity of the tissues based on the literature, identical for each subject, appears as too big an assumption. Techniques such as *magnetic resonance electric impedance tomography (MREIT)* [Woo and Seo, 2008] and *conductivity tensor imaging (CTI)* [Marino et al., 2021] could provide a better description of the electric properties of the tissues of each subject.

Finally, tDCS is expected to generate an induced transmembrane potential of around $0.5\,$mV if the neurons of the target region of in-

terest [Radman et al., 2009; Opitz et al., 2016]. The values we obtain analytically, considering $r_1 = 1$ mm, are at most of the same order of magnitude but can be smaller by up to a factor of 20. Once again, this value relies heavily on the conductivity profile of the models. Still, computing ITP values of 0.02 mV, as compared to a resting potential of -70 mV and a reference action potential threshold of -55 mV, highlights the questionable validity of tDCS as a neuromodulation technique. This concern has already been raised by other papers before (See Section 2.3).

Still, it is important to mention that, since the present study only focused on simulations, we cannot draw conclusions on the functional long-lasting effect of the different experiments.

6.12. Conclusion

In the present work, we studied the influence of an error of placement of the anode and of the unknown conductivity profile on the computed electric field resulting from 6 different tDCS experiment targeting 4 regions of interest on 20 subjects using a simulation tool. A total of 12600 simulations were performed.

The models used in this paper show that a reasonable anode placement yields a negligible to moderate effect on the electric field induced in the ROI. They also highlight that the uncertainty on the electrical conductivity of the tissues makes it practically impossible to assess the electrical effect of the stimulation in the ROI and that using fixed standard values could potentially yield highly biased results.

We also computed the induced trans-membrane potential induced by the stimulation for different simple cell models. The overall size of the computed ITP is concerning. All those results corroborate what was introduced in Section 2.3.

While we did not perform functional experiments in parallel to the modelling work, the overall results presented through this application force us to call for caution when designing, modelling and analysing a tDCS experiment.

7.

Discussion

In the introduction, I explained that the reproducibility crisis and raising concerns about the high variability in reported results initiated the development of *Shamo*. Thus my goal was to build a tool that could be used on a subject basis to perform uncertainty quantification and sensitivity analysis in order to better understand the inter-subject variability and to allow researchers and practitioners to draw more cautious and informed conclusions.

One of the main issues for simulation based studies like those we performed was the amount of computing power required to actually achieve UQ/SA. The combined usage of Gaussian processes regressors to serve as surrogate models and of high performance computing infrastructures made it possible in a timely manner. Indeed, using GRP as a metamodel highly reduces the number of evaluations of the actual model required, which reduces the cost of the final analysis while encapsulating the uncertainty in the surrogate model itself due to its Bayesian approach. Consequently, the num-

ber of evaluations performed becomes a user adjustable variable and directly correlates with the width of the credibility interval of the computed metrics (*e.g.,* the Sobol indices for SA). In Section 6, we used Bayesian linear models instead of Gaussian process regressors to account for the hierarchical nature of the data. These linear models, as their name suggests and just like GPR, provide information about the uncertainty in the results. At the same time, this application demonstrated the usability of *Shamo* for a study with multiple subjects.

When performing EEG source reconstruction or simulating tDCS, constructing a mesh with appropriate properties is not a trivial task and, as discussed in Section 4.1, researchers often rely on pipelines where the segmentation step is intertwined with the meshing step. *BrainStorm* [Tadel et al., 2011] provides an interface to those all-in-one pipeline as implemented in *Brain2Mesh* [Tran et al., 2020a], *SimNIBS* [Thielscher et al., 2015], *ROAST* [Huang et al., 2019] and *FieldTrip* [Oostenveld et al., 2011]. By decoupling these two operations, *Shamo* opens up a whole new horizon of possibilities. Indeed, building a mesh directly from a segmented image solves many issues. First, it removes the limitation on the number of tissues embedded in the model and allows the user to generate the tissue masks using the method of his choice. As demonstrated in our EEG application (See Section 5), this feature is useful to compare different geometries. Moreover, the separation of the segmentation and mesh generation processes gives the ability to model non-standard heads or even other parts of the body. This could be used, for instance, to model people with prosthetics or deformities or even just to study a very complex model such as the MIDA model composed of 116 tissues [Iacono et al., 2015]. Finally, the fact that *Shamo* does not implement a segmentation pipeline limits the number of dependencies and favours the portability of the tool. When compared to competing software such as *SimNIBS* or *ROAST* that have some common dependencies with the presented tool (*i.e., Gmsh* and *GetDP*), *Shamo* does not require heavy, non-portable third-party

tools nor tools with restrictive licenses.

Another important difference between *Shamo* and the other cited toolboxes is how meshes are built: while most tools build the 3D mesh first by 2D meshing the compartment interfaces, *i.e.* building a boundary element model, and then by filling the volumes with tetrahedral elements, the presented technique does not require building and cleaning the tissue surfaces. This cleaning step can be complex and time-consuming, since it needs to make sure that none of the independent surfaces intersect.

After building the geometry, adding the electrodes is the next step. As discussed in Section 4.2, *Shamo* does not provide a method to add conform electrodes (*i.e.*, electrodes with exact shapes) and uses the already generated triangular elements to define the contacting surfaces. This yields some approximations in the computed fields around the electrodes themselves, but hardly any difference further away. This method, however, is inspired by the one implemented in the work of Ziegler et al. [2014]. In addition to these surface electrodes, *Shamo* also provides point electrodes that ship with the advantage that running multiple simulations for different stimulating electrode while keeping the same reference only requires to define the problem once. Adding the conform electrodes to the package would make it complete and leave the choice of electrode model to the user.

Finally, as shown in Section 4.3, another functionality of *Shamo* is its ability to account for anisotropy. This also provides a method to build a model with a single tissue class and to specify the properties of each element with a tensor or, with a hybrid technique, it can virtually increase the number of tissues included in the finite element models. This approach, coupled with techniques such as *magnetic resonance electric impedance tomography (MREIT)* [Jahng et al., 2021; Soullié et al., 2021], could potentially remove the need to accurately segment more tissues than the current five most common ones while providing more individualised results based on actual measurements. Indeed, while using a single compartment for

the whole head might not be compatible with the usual methods, one could imagine using a 5 tissues model where the properties of each tissue are governed by tensors and thus encapsulate the different subclasses just like Tuch et al. [2001] did for the soft and compact bone, but applied to soft tissues composed of fat, muscles, blood vessels and skin. Without planning for the future, accounting for the anisotropy of the white matter is becoming more and more usual.

While the model definition steps differ from other similar tools, it is worth noting that the processing pipeline used in *Shamo*, based on *Gmsh* [Geuzaine and Remacle, 2009] and *GetDP* [Geuzaine, 2007], is already the one powering *SimNIBS* [Thielscher et al., 2015] and *ROAST* [Huang et al., 2019], two well established pieces of software. Furthermore, the implemented problem definitions have been validated previously by Ziegler et al. [2014]. Making use of these industrial grade tools ensures the quality and reliability of the solutions. It also provides an easy way to extend *Shamo* with new applications such as TMS or MEG. Indeed, since the simulation part is performed with GetDP, adding new simulation types only requires the definition of the corresponding problem file and of the wrapping *Python* classes that would store the input parameters. The problem file contains the corresponding weak formulation that, in the case of TMS and MEG, have already been studied [Thielscher et al., 2015; Piastra et al., 2018]. In addition, just like for EEG and tDCS where the electrodes can be modelled in different ways, multiple coil models could also be added by leveraging the available mesh edition methods.

Recently, *SimNIBS* added a module for uncertainty quantification and sensitivity analysis [Saturnino et al., 2019] based on *generalised polynomial chaos (gPC)*. This shows the importance of such analysis in the context of the simulation of head current. As opposed to *SimNIBS*, *Shamo* was built directly for these types of analyses. Consequently, running a single simulation using deterministic conductivity values or performing an uncertainty analysis by spec-

ifying the properties as random variables rely on the same interface. Moreover, *Shamo* was created to be extended, meaning that the users are not limited to evaluating the effect of the uncertainty in the conductivity parameters but can actually define new parameters. A simple example where the injected current is specified as a random variable is implemented. While both gPC and GPR can be used to build fast, accurate and deterministic surrogate models, choosing GPR provides more information on the outcome than the gPC approach. Indeed, the output of this metamodel is a random variable that encapsulates the uncertainty on the computed metric. Thus, the user not only obtains the metric he is interested in, but is also informed of its confidence interval. Furthermore, the fact that GPR uses a kernel to constrain the range of possible functions makes it more flexible than gPC [Owen et al., 2017]. Still, it is well known that GPR scales as $O(n^3)$, where n is the size of the training dataset. This means that for a large number of random input parameters, when the number of evaluations of the actual model increases, gPC can still be relevant. Possible alternatives would be to use sparse Gaussian processes that scale as $O(nm^2)$, where $m < n$ [Schirru et al., 2011; Bauer et al., 2016].

An interesting side effect of building a surrogate model to perform uncertainty quantification and sensitivity analysis is that it can be used for a completely different purpose: optimising the input parameters. Indeed, while the main application of Shamo is to model and propagate the uncertainty lying in the physical properties of the tissues that cannot be optimised due to their random nature, the same workflow could be used to study the effect of the electrode placement, just like in Chapter 6. The obtained regressor could then be used in order to find the electrode position that yields the optimal effect (*e.g.*, the highest mean electric field in a region of interest). The literature on this topic is quite scarce and usually limited to simulation applications, but the reported increase in the measured electric field in the ROI are high [Dmochowski et al., 2011; Khorrampanah et al., 2020]. Still, this could help to improve

the efficacy of tDCS on non-homogenous populations.

Now that the added value of *Shamo* has been discussed, what are the perspectives of this package? As stated previously, performing uncertainty quantification could highly improve the quality and understanding of simulation results. By providing a single user-friendly interface to either run a single simulation or several dozens, *Shamo* facilitates the adoption of those otherwise complex analyses. Still, while the tDCS application in Section 6 shows that the tool can be used for a study with multiple subjects, we limited ourselves to simulations and thus could not correlate the outcomes of our experiments with actual behavioural or physiological data. Thus, the very next step of this project should be to focus on evaluating the actual benefit of such added information on a real-case study.

From a more technical point of view, adding the conform electrodes as discussed above would allow *Shamo* to be on par with the standards of the field. To further ease its adoption, it would be interesting to provide methods to convert the generated models to/from other competing software formats. This would allow the users to build the finite element models with tools they already know and master such as *SimNIBS* and to use *Shamo* to perform the simulations and analyses or, the other way round, to use the mesh generation method of *Shamo* and run the simulations with other packages. One could also compare the results and performances of the tools one-to-one with the exact same model. Adding solution to other problem types, such as TMS and MEG, would naturally broaden the potential user base.

Still, no matter the level of details of the model, the absence of an actual method to determine the electrical conductivity of the tissues prevents researchers from producing truly realistic and accurate models. Indeed, the benefit of adding more tissues in the geometry is limited by the uncertainty lying in the properties of those additional compartments. In order to improve the accuracy of the simulations, one should focus on reducing this uncertainty

rather than on improving tissue segmentation. In this context, uncertainty and sensitivity analyses can help make better informed choices of parameters values and provide information on which parameter really matter. Since the sensitivity of the simulations to the conductivity of the tissues depends both on the geometric model (*i.e.*, number of compartments and electrode placement) and on the problem to be simulated, we recommend using UQ and SA to increase the understanding of the results sensitivity profile and find out which parameters have little influence on the outcome.

8.

Conclusion and perspectives

The intent of this work was to investigate the uncertainty and sensitivity of simulation-based analyses such as EEG and tDCS. It led to the development of a tool to perform uncertainty quantification and sensitivity analysis on such computationally expensive modelling applications. Consequently, we published *Shamo*, a lightweight and portable Python package which defines a user-friendly programming interface to several well established pieces of software, giving the user a single tool to go from finite element model generation to sensitivity analysis.

We showed the usability of this tool on two applications, one of which has already been published (See Appendix A) while the manuscript for the other is available as a preprint (See Appendix B). On the one hand, the EEG application highlighted the flexibility of

the proposed pipeline in terms of model generation by studying three different skull geometries on a single subject. On the other hand, the tDCS application highlighted the scalability of the technique with regard to the number of subjects as well as to the number of factors of variability. Indeed, not only did it allow evaluating the effect of the uncertainty of the electric conductivity of the tissues on several tDCS experiments, but also the effect of head geometry and electrode placement.

By releasing this extendable toolbox, we provide researchers and practitioners with a practical method to include UQ and SA in their experimental protocols. As a first "real world" test, the workflow is slated to be soon used in a real cognitive experiment, which is the very next step after the two simulation studies we performed. It should be noted that, compared to other toolkits like *SimNIBS* or *ROAST*, *Shamo* can easily handle non-standard head models, which is of main interest for clinical applications, where patients are not always healthy adults. From a computational point of view, *Shamo* can be used on any platform ranging from a laptop to high-performance clusters, the latter obviously allows faster UQ and SA calculation. Moreover, without needing to modify the code base, the described approach can readily be used to optimise the electrode placement for a tDCS experiment. For instance, based on the results obtained in Chapter 6, we are already able to estimate an optimal position for the anode in order to maximise the induced electric field in the ROI based on a reduced set of simulations. Thanks to its versatile model generation technique and problem solver relying on *GetDP*, it could also be used for *electrocardiography (ECG)* using the exact same methods.

In the near future, *Shamo* could easily be extended to adapt to a wider range of applications by adding support for TMS and MEG, those problems being the magnetic equivalent of tDCS and EEG, or even *electroconvulsive therapy (ECT)* [Rojas et al., 2022] and *focused ultrasound (FUS)* neuromodulation [Kamimura et al., 2020]. Considering its extendability and flexibility, future additions could

target problems that are relatively far from its initial head modelling purpose. The scope of such applications could include the investigation of the effect of extremely low frequency stimulation on cellular processes [Collard and Hinsenkamp, 2015] or dosimetry of radio frequency magnetic waves in biological tissues [Wang et al., 2021b].

When considering living tissues, most of the fields relying on simulations face the same issues as tDCS or EEG. Thus, *Shamo* could serve as a framework providing the foundation required to build sensitivity analysis pipelines. This could help better understand the sources of variability, but could also provide a way to draw more educated conclusions. Uncertainty quantification and sensitivity analysis are powerful tools that could provide partial answers to the reproducibility crisis. The developments that took place during this thesis make them accessible for complex simulation based models.

To conclude this thesis, I would like to cite these two quotes:

> *" All models are wrong, but some are useful.*
> — George E. P. Box [1978]

and

> *" The only good statistics is Bayesian statistics.*
> — Lindley [1975]

Bayesian statistics allow researchers to account for what they do not know about their models, that are consequently "wrong" and inexact, and to draw "useful" and educated conclusions. *Shamo* adheres to this philosophy, and so do I. I am convinced that uncertainty and sensitivity analyses are part of the solution to the reproducibility crisis along with FAIR data sharing, tool containerisation and reproducible pipeline orchestration and that it is our role, as engineers, to build tools that help to improve the way science works.

Appendix

A.

Paper 1

This appendix contains the original text of the first paper written in the context of this thesis, entitled *"shamo: A tool for electromagnetic modeling, simulation and sensitivity analysis of the head"* and published in Neuroinformatics in March 2022[1].

Shamo: A tool for electromagnetic modeling, simulation and sensitivity analysis of the head

Martin Grignard [2], Christophe Geuzaine [3] and Christophe Phillips[2]

Accurate electromagnetic modeling of the head of a subject is of main interest in the fields of source reconstruction and brain stimulation. Those processes rely heavily on the quality of the model and, even though the geometry of the tissues can be extracted from magnetic resonance images (MRI) or computed tomography (CT), their physical properties such as the electrical conductivity are difficult to measure with non intrusive techniques. In this paper, we propose a tool to assess the uncertainty in the model parameters, the tissue conductivity, as well as compute a parametric forward models for electroencephalography (EEG) and transcranial direct current stimulation (tDCS) current distribution.

A.1. Introduction

Accurate electromagnetic modeling of the head is of main interest for electrophysiological source reconstruction techniques (EEG/MEG) and brain stimulation (tDCS/tMS). Such modeling must capture both the spatial distribution of the tissues and their physical properties like their electrical

---

2. GIGA CRC In-Vivo Imaging, University of Liège, Belgium
3. Department of Electrical Engineering and Computer Science, University of Liège, Belgium

conductivity. The former can be extracted from different anatomical imaging techniques as magnetic resonance imaging (MRI) and computed tomography (CT) but the latter is very difficult to measure *in vivo* on a subject basis, even if some properties can be derived from specific MRI sequences [Tuch et al., 2001; Wu et al., 2018].

Anatomically realistic models must therefore rely on values of physical parameters reported in the literature. The electrical conductivity of biological tissues have been studied since the last century [Burger and Milaan, 1943; Geddes and Baker, 1967; Gabriel et al., 1996b,c,a; Latikka et al., 2001; Goncalves et al., 2003] and new methods are still published to measure them accurately for each subject [Akalin Acar et al., 2016]. The reported values have been shown to vary both inter- and intra-subject due to temperature, health status, age, or depending on the acquisition method and environment, e.g. *in vivo* vs. *ex vivo* [McCann et al., 2019].

Due to the variability in the published values, the influence of the chosen parameters and geometric models on the results of the simulations have been studied for the past decades and shown to induce erroneous electric field and potential estimations [Haueisen et al., 1995, 1997; Vallaghe and Clerc, 2009; Jochmann et al., 2011; Montes-Restrepo et al., 2014; Cho et al., 2015; Akalin Acar and Makeig, 2013; Wolters et al., 2006; Vorwerk et al., 2019a; Saturnino et al., 2019]. Errors in the localisation of the reconstructed dipoles of up to 20 mm have been reported for basal brain locations [Lanfer et al., 2012; Akalin Acar and Makeig, 2013]. Indeed, inaccuracies on the physical parameters directly result in errors in the forward models, and thus in the reconstructed sources localization or current flow.

In order to mitigate the variability in the results, different models for the skull have been proposed [Sadleir and Argibay, 2007; Dannhauer et al., 2011; Lanfer et al., 2012; Montes-Restrepo et al., 2014] since it acts as an electrical insulator, in EEG and tDCS, due to its low conductivity compared to the other tissues. While it is generally modeled as a single compartment, partly due to the fact

that further segmenting it into spongy and compact bone is still not included in most of automated segmentation pipelines, models differentiating these two compartments have recently been proposed [Puonti et al., 2020; Taberna et al., 2021]. Conductivity tensors have also been considered where the radial and tangential conductivity differ [Fuchs et al., 2007].

The same approach applied to white matter lead to different models of its anisotropy which have been first correlated with the water self diffusion tensor derived from diffusion weighted MR images (DWI) [Tuch et al., 2001]. Later, the equilibrium, volume fraction and electrochemical models have been proposed [Wu et al., 2018]. The influence of such anisotropy on EEG forward and inverse problems have also been studied [Güllmar et al., 2010; Bashar et al., 2010]. Conductivity tensor imaging is still an open topic with promising advances [Ziegler et al., 2014; Sajib et al., 2016; Katoch et al., 2019].

In the past, sensitivity analysis have been mainly conducted as the final goal of the studies. However, quantifying uncertainty in individual models could help better understand the observed inter-subject variability in brain stimulation and source reconstruction in broader studies. This is why we introduce *shamo*, a *Python* open source package [4] dedicated to stochastic electromagnetic modeling of the head and sensitivity analysis of the results.

This toolbox aims at providing a unique solution for electro-magnetic head modeling in both source reconstruction and brain stimulation problems. While tools already exist for each of these fields separately, for example *Brainstorm* [Tadel et al., 2011] or *MNE* [Gramfort et al., 2013] for EEG and *SimNIBS* [Thielscher et al., 2015] or *ROAST* [Huang et al., 2019] for tDCS to only name a few, *shamo* offers an integrated solution. Moreover *shamo* provides a single, easily extendable, API to perform mesh generation, simulation and sensitivity analysis.

To highlight the mechanisms involved in our package and demon-

---

4. `https://github.com/CyclotronResearchCentre/shamo`

strate its usability and flexibility on actual cases, we apply it to the EEG forward problem and to trans-cranial direct current stimulation (tDCS) simulation. Both analyses are performed on a realistic finite element model (FEM) derived from the MIDA model [Iacono et al., 2015]. To evaluate the impact of different geometries for the skull, we build three different models, considering either one, two or thee layers for the skull, with different electrical conductivity values for the inner and outer tables for the latter.

The sensitivity is then assessed through the computation of Sobol indices [Sobol, 2001]. The random input parameters considered are the values for the electrical conductivity of the tissues. To model their probability density functions, we use the truncated normal distribution published in the recent review from McCann et al. [2019] as well as a unique uniform distribution, in a worst case scenario. In the process, we compute surrogate models that, for the EEG forward problem, results in a parametric leadfield matrix that can be used to generate new forward models for any set of electrical conductivity and, for the tDCS simulation, generates a model that can compute the current density in a region of interest for the same ranges of electrical conductivity.

A.2. Materials and methods

In order to simulate the current flow inside the brain, a mathematical model is required. It must account for both the geometry of the tissues and their properties. This section covers the model generation, its parametrization, and sensitivity analysis.

A.2.1. Finite element model generation

To begin with, we focus on the geometrical aspect of the models, for which several construction methods have been proposed [Hallez et al., 2007]: going from a simple multi-shell sphere to a fully fledged finite element model (FEM). Two key features of FEM are its ability to capture complex shapes and to allow for anisotropic conductivity (in the form of a finite element field). Pipelines have been developed to help researchers produce these models [Windhoff et al., 2013; Nielsen et al., 2018; Huang et al., 2019; Vorwerk et al., 2018]. As described by Huang et al. [2019], most of the available solutions for automated segmentation rely either on *Matlab*, through *SPM*'s "Unified Segmentation" tool [Ashburner and Friston, 2005] and its toolboxes or on *FSL* and *FreeSurfer* [Smith et al., 2004; Fischl et al., 2004]. The ensuing model generation step is generally tied to this specific segmentation method. Unfortunately this prevents geometries for atypical non-healthy subjects or simply to include other tissue types.

In *shamo*, we consider a FEM approach and mesh generation but eschew the segmentation step. In effect the mesh is produced directly from a segmented volume, i.e. where voxels are labeled as being of one of any number of tissue classes. This allows us to work with more intricate structures and even to model atypical cases, e.g. with prosthesis or abnormal tissue distributions (lesions, tumor, resection,...), by using manually segmented volumes or custom automated segmentation pipelines.

For this work, we start from the multimodal imaging-based detailed anatomical model of the human head and neck (MIDA) [Iacono et al., 2015]: a $350 \times 480 \times 480$ matrix of $0.5 \times 0.5 \times 0.5$ mm^3 voxels including 116 different structures. Based on this model, we define three geometries with 5 to 7 different tissues (see Table A.1), differing in how the skull is modeled.

First we merge the structures of the MIDA model to keep only

Tissue			Parameters (Sm^{-1})				Model		
Name	Abbr.	Color	Min.	Max.	Mean	Std.	1	2	3
Scalp	SCP		0.1370	2.1000	0.4137	0.1760	■	■	■
Skull (Whole)	SKL		0.0182	1.7180	0.0160	0.0190	■	■	■
Skull (Spongy)	SKL SPG		0.0012	0.2890	0.0497	0.0735	□	■	■
Skull (Compact)	SKL CPT		0.0024	0.0079	0.0046	0.0016	□	■	□
Skull (Outer table)	SKL OCPT		0.0008	0.0078	0.0049	0.0029	□	□	■
Skull (Inner table)	SKL ICPT		0.0028	0.0129	0.0068	0.0036	□	□	■
Cerebrospinal fluid	CSF		1.0000	2.5100	1.7100	0.2981	■	■	■
Gray matter	GM		0.0600	2.4700	0.4660	0.2392	■	■	■
White matter	WM		0.0646	0.8100	0.2167	0.1703	■	■	■
Extended	EXT	-	0.0008	2.5100	-	-	-	-	-

Table A.1 **The tissues used in this work with the parameters of the corresponding electrical conductivity distributions from McCann et al. [2019]. The last three columns show which tissues are included in each model.**

the main head tissues: white matter, gray matter, cerebrospinal fluid, scalp and the different parts of the skull. Then in model 1, the upper part of the skull is represented as a single isotropic volume; for model 2, the upper part of the skull is separated into spongia and compacta; for the model 3, the latter is further divided into outer and inner tables. Note though that the lower part of the skull is the same for all our models and is modelled as a homogeneous tissue class. The resulting models are illustrated in Figure A.1.

To generate the FEM tetrahedral mesh, we use *CGAL* [Project, 2020] with the labeled image of model 3. The resulting mesh, with 1.355×10^6 tetrahedra, then serves as a base for the other 2 models that only require the merging of some skull sub-compartments. This merging is performed with *Gmsh* [Geuzaine and Remacle, 2009], which is also used to annotate the mesh by specifying the names of the tissues and adding the electrodes on the scalp. For the EEG forward problem we consider the 63 electrodes of the international 10-10 system [Nuwer, 2018] including the fiducial markers for the nose, the left and right ears and the inion. The latter is considered as the reference for the rest of this work. For tDCS, we use a subset of these electrodes: P3, TP9, C3, P1 and O1) where P3 is the current injector.
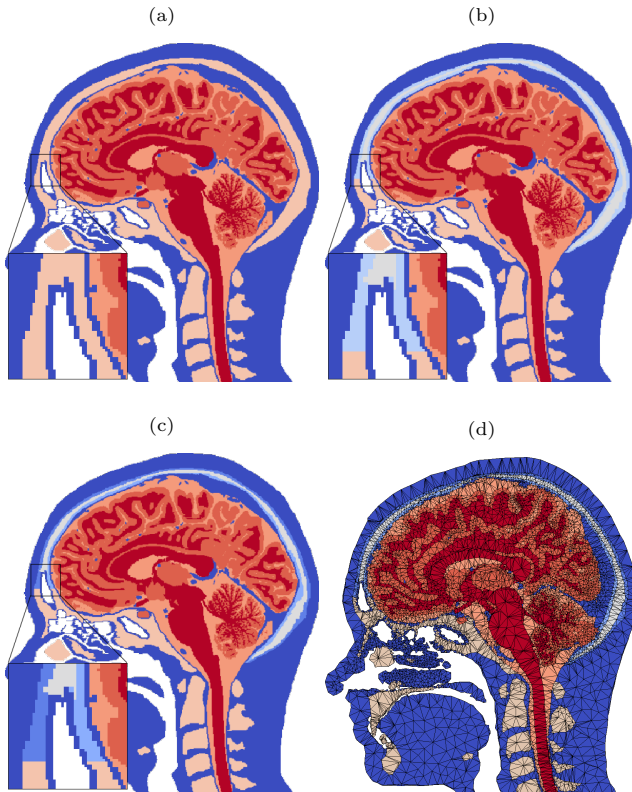
Figure A.1   Sagittal cuts of (a) the segmented images for model 1 where skull is a single isotropic compartment, (b) for model 2 with spongy and compact bone differentiated, (c) for model 3 where the outer and inner tables of the skull are differentiated and (d) the mesh corresponding to model 3. In (a), (b) and (c), the lower part of the skull is the same.

A.2.2. Electromagnetic modeling

Since capacitive effects can be neglected in the brain tissues for the frequency range involved in brain activity [Plonsey and Heppner, 1967], the so called quasi-static approximation applies: the electromagnetic fields at time t only depend on the active sources at this time. In such conditions, Maxwell's equations reduce to a generalized Poisson equation [Malmivuo and Plonsey, 1995; Hallez et al., 2007] that provides a relationship between the electric potential in any point of a volume conductor and the current sources. We first define the current density j (Am^{-2}) and the source volume current density ρ_s (Am^{-3}) [Schimpf, 2007]. They are linked together by the expression

$$\nabla \cdot j = \rho_\text{s}. \qquad \text{Eq. A.1}$$

The current density j is linearly related to the electric field e (Vm^{-1}) through Ohm's law

$$j = \sigma e \qquad \text{Eq. A.2}$$

where σ, the conductivity, can be a tensor field. Anisotropy of the white matter has been shown to influence source reconstruction [Haueisen et al., 2002; Güllmar et al., 2010] and the pipeline allows for anisotropic tissues yet, in this work, σ is considered isotropic because no diffusion weighted images (DWI) is available in the MIDA data. The quasi-static conditions described above allow us to write the relationship between the electric field and the electric potential field v (V) as

$$e = -\nabla v. \qquad \text{Eq. A.3}$$

Then combining Equations **Eq. A.1**, **Eq. A.2** and **Eq. A.3** leads to the generalized Poisson equation:

$$\nabla \cdot (\sigma \nabla (v)) = -\rho_\text{s}. \qquad \text{Eq. A.4}$$

Finally a homogeneous Neumann boundary condition is set on the interface between the conductor volume and the air, and a Dirichlet condition is added to set the reference electrode. We use *GetDP* [Geuzaine, 2007] as a solver for the finite element model described in section A.2.1. *GetDP* is an industrial grade solver and is at the heart of some popular tools for head electromagnetic modeling [Huang et al., 2019] and our implementation of the forward problem have already been analytically validated by Ziegler et al. [2014].

A.2.3. Electrical conductivity of tissues

As stated in Equation Eq. A.4, electrical conductivity plays a major role in the computation of the electric potential and the other related fields. Unfortunately, determining the exact electrical conductivity σ (Sm^{-1}) of the biological tissues in a non-intrusive manner is an open issue. Multiple methods have been developed to measure it either *in vitro*, *ex vivo* or even *in vivo* but struggle to provide an accurate and reliable value [Burger and Milaan, 1943; Geddes and Baker, 1967; Gabriel, 1996; Gabriel et al., 1996a,b,c; Latikka et al., 2001; Goncalves et al., 2003]. McCann et al. [2019] reviewed the values acquired with different techniques and under specific conditions and derived a realistic underlying probability distribution in the form of a truncated normal distribution for the main tissues composing the head. We use these distributions with the 3 models described in Section A.2.1, which we label Models 1a, 2a and 3a.

In addition, we define a uniform distribution spanning the whole range of the reported conductivity values for all the tissue classes, and refer to it as the extended distribution (EXT). This represents a worst case scenario with no prior information on the conductivity of the different tissues. This uniform distribution is also used

with the 3 FEMs, which we label Models 1b, 2b and 3b. The range and distribution of conductivity values for the tissues considered in each model are summarized in Table A.1.

The goal of the sensitivity analysis, see Section A.2.5, is to determine the parameters that drive the variability in the results. Comparing the sensitivity to the two sets of conductivity values, realistic and extended, will allow us to assess the effect of the prior knowledge added by the truncated normal distributions, especially for the tissues with the narrowest distributions.

For the sake of clarity, we use lowercase letters to indicate a known deterministic value whereas uppercase letters refer to random values. For instance, the tissues conductivities are denoted by the vector $\boldsymbol{\sigma} = [\sigma_1, \sigma_2, \ldots, \sigma_d]$ and $\boldsymbol{\Sigma} = [\Sigma_1, \Sigma_2, \ldots, \Sigma_d]$ corresponds to the vector containing the random parameters modeled by the distributions. Thus for each geometry i, we consider two sets of conductivity distributions: either those introduced in [McCann et al., 2019], giving $\boldsymbol{\Sigma}_a = [\Sigma_{WM}, \Sigma_{GM}, \ldots, \Sigma_{SCP}]$, or the same extended distribution for each of the tissues, i.e.
$\boldsymbol{\Sigma}_b = [\Sigma_{EXT}, \Sigma_{EXT}, \ldots, \Sigma_{EXT}]$ as shown in Table A.1.

A.2.4. EEG and tDCS forward problem

When carrying out EEG source reconstruction analysis, one attempts to recover the underlying brain activity inducing the observed signal at the scalp level. This electrical activity is generally modeled by one or more equivalent current dipoles characterized by their coordinates in space $\boldsymbol{r} = [r_x, r_y, r_z]$ and their dipole moment $\boldsymbol{p} = [p_x, p_y, p_z]$ (Am). In practice, a set of discrete sources is considered rather than the full continuous volume of the gray matter. This set is called a source space and defines potential dipole locations.

The relation between the source space containing n sources and

the electric potential measured on m electrodes at the scalp level is given by the expression

$$[l] \cdot s + \varepsilon = v,$$

Eq. A.5

where $s = [p_1^{(x)}, p_1^{(y)}, p_1^{(z)}, \ldots, p_n^{(x)}, p_n^{(y)}, p_n^{(z)}]^\mathsf{T}$ is the source vector and $p_j^{(k)}$ is the dipole moment of the source located in the j-th site along k-axis,
$\varepsilon = [\varepsilon_1, \ldots, \varepsilon_m]^\mathsf{T}$ and $v = [v_1, \ldots, v_m]^\mathsf{T}$ are respectively the additive noise component vector and the vector of electrode potentials (V), and $[l]$ is equally referred to as the "leadfield" or gain matrix. This matrix looks like this

$$[l] = \begin{bmatrix} l_{1,1}^{(x)} & l_{1,1}^{(y)} & l_{1,1}^{(z)} & \cdots & l_{1,n}^{(x)} & l_{1,n}^{(y)} & l_{1,n}^{(z)} \\ \vdots & \vdots & \vdots & \ddots & \vdots & \vdots & \vdots \\ l_{m,1}^{(x)} & l_{m,1}^{(y)} & l_{m,1}^{(z)} & \cdots & l_{m,n}^{(x)} & l_{m,n}^{(y)} & l_{m,n}^{(z)} \end{bmatrix},$$

Eq. A.6

where each element $l_{i,j}^{(k)}$ corresponds to the electric potential v measured on the i-th electrode due to a current dipole with unitary dipole moment located on the j-th site and oriented along k-axis ($VA^{-1}m^{-1}$). This model encompasses all the geometric information and the physical properties of the head tissues. In the rest of this paper, the notation $[l(\sigma)]$ is used when highlighting the dependencies of the leadfield matrix on the values set for the electrical conductivity.

Following the method described by Weinstein et al. [2000] based on the reciprocity principle, we actually have to solve the tDCS forward problem in order to generate the EEG leadfield. Indeed, to compute $[l]$ on an element basis, the reciprocity principle states that to estimate the voltage difference between two points due to a single current dipole, one needs to compute the electric field e at the coordinates of the dipole resulting from the injection of a 1 A current i between the two points, which is the definition of a tDCS forward problem.

$$v_1 - v_2 = \frac{e \cdot p}{i}$$

Eq. A.7

The technique then consists in setting a reference electrode, iteratively injecting a 1 A current through the m active electrodes, and estimating the electric field on the source space in the i-th row of the matrix $[l]$. This step of the process is achieved in *GetDP* with the generalized minimal residual method (GMRES) configured with a tolerance of 10^{-8} and an incomplete factorization (ILU) preconditioner.

Given that the current sources should only exist in the gray matter, that the mesh for that tissue is made of about 368000 tetrahedra, and that we have a setup of 59 active electrodes, the whole leadfield matrix $[l]_{\text{full}}$ would theoretically have a size of $59 \times (3 \times 368000)$, which is too large for practical use. Therefore we arbitrarily fix the average interval between two sources at 7.5 mm, resulting in 2127 sources and a leadfield matrix $[l] \in \mathbb{R}^{59 \times 6381}$ which is more manageable. This source-to-source distance influences both the the computational resources required to perform the source reconstruction, since it is directly linked to the size of the leadfield matrix, and the number of potentially reconstructed dipoles. In their paper, Michel and Brunet [2019] state that the definition of the spatial resolution is a sensitive problem but that increasing it does not lead to a linear increase of the accuracy. In fact, the accuracy has a limit due to the fact that the amount of information provided to the inverse problem remains constant since the number of electrodes is fixed.

A.2.5. Sensitivity analysis

As defined by Saltelli [2008], sensitivity analysis is the study of how variation in the input parameters of a process influences the variation in the output. In this field, two cases are differentiated. The local sensitivity focuses on the uncertainty at a specific coordinate of the parameters space Ω whereas the global sensitivity captures the variation across the whole space.

One of the most used and studied global sensitivity analysis techniques is the computation of the so called Sobol indices [Sobol, 2001; Saltelli et al., 2010]. Let us consider a model $Y = Y(\boldsymbol{X})$ where Y is the random output variable and $\boldsymbol{X} = [X_1, \ldots, X_{n_\mathrm{p}}]$ is the vector of n_p random input variables. The first and total order Sobol indices for the i-th input variable, s_i and $s_i^{(\mathrm{t})}$ are defined by

$$s_i = \frac{\mathbb{V}_{X_i}(\mathbb{E}_{\boldsymbol{X}_{\backslash i}}(Y \mid X_i))}{\mathbb{V}(Y)}, \qquad \textbf{Eq. A.8}$$

$$s_i^{(\mathrm{t})} = \frac{\mathbb{E}_{\boldsymbol{X}_{\backslash i}}(\mathbb{V}_{X_i}(Y \mid \boldsymbol{X}_{\backslash i}))}{\mathbb{V}(Y)}, \qquad \textbf{Eq. A.9}$$

where $\boldsymbol{X}_{\backslash i}$ is the vector of all the random inputs but X_i, s_i corresponds to the variance in the output explained by X_i alone, $\mathbb{V}_{X_i}(\mathbb{E}_{\boldsymbol{X}_{\backslash i}}(Y \mid X_i))$ is the variance explained by the i-th parameter, also referred to as its main effect, and $s_i^{(\mathrm{t})}$ is the output variance explained by X_i and all its interactions with the other input parameters.

To compute Sobol indices, we follow the method presented by Saltelli et al. [2010] and implemented in the python package *SALib* [Herman and Usher, 2017] that provides a way to compute both s_i and $s_i^{(t)}$ from the same set of evaluations of the model, thus reducing the amount of computation required. This technique relies on n_d observations $\{(y_i^{(\mathrm{d})}, \boldsymbol{x}_i^{(\mathrm{d})}, \ i = 1, \ldots, n_d\}$ where each $y_i^{(\mathrm{d})} = y(\boldsymbol{x}_i^{(\mathrm{d})})$ is the output of the model for a set of inputs $\boldsymbol{x}_i^{(\mathrm{d})} = [x_{i,1}^{(\mathrm{d})}, \ldots, x_{i,n_p}^{(\mathrm{d})}]$. Let us define $\boldsymbol{y}^{(\mathrm{d})} = [y_1^{(\mathrm{d})}, \ldots, y_{n_d}^{(\mathrm{d})}]^{\mathsf{T}}$ the vector of outputs and $[x]^{(\mathrm{d})} = [\boldsymbol{x}_1^{(\mathrm{d})}, \ldots, \boldsymbol{x}_{n_d}^{(\mathrm{d})}]^{\mathsf{T}}$ the matrix of inputs.

The matrix $[x]^{(\mathrm{d})}$ is built of $n_\mathrm{p} + 2$ sub-matrices: $[a]$, $[b]$ and the matrices $[a_b]^{(i)}$ where all the columns are the same as in $[a]$ except the i-th one coming from $[b]$. All these matrices have n_r rows and n_p columns. The input vectors $\boldsymbol{x}_i^{(\mathrm{d})}$ composing the independent matrices $[a]$ and $[b]$ are drawn from the parameters space Ω using the Saltelli extension of Sobol quasi-random sequence [Sobol, 1967, 1976]. Such sequences are described in section A.2.6.

Based on these samples, the numerators of Equations Eq. A.8 and Eq. A.9 are computed with

$$\mathbb{V}_{X_i}(\mathbb{E}_{\boldsymbol{X}_{\setminus i}}(Y \mid X_i))$$
$$= \frac{1}{n_r} \sum_{j=1}^{n_r} \boldsymbol{y}([b])_j \left(\boldsymbol{y}([a_b])_j^{(i)} - \boldsymbol{y}([a])_j \right),$$

<div align="right">Eq. A.10</div>

and

$$\mathbb{E}_{\boldsymbol{X}_{\setminus i}}(\mathbb{V}_{X_i}(Y \mid \boldsymbol{X}_{\setminus i}))$$
$$= \frac{1}{2n_r} \sum_{j=1}^{n_r} \left(\boldsymbol{y}([a])_j - \boldsymbol{y}([a_b])_j^{(i)} \right)^2.$$

<div align="right">Eq. A.11</div>

A.2.6. Surrogate model

The computation of the sensitivity indices described in section A.2.5 requires a large number of model evaluations. When the estimation of the actual model (here the computation of the leadfield matrix) is computationally heavy, a simpler model, referred to as the surrogate model, can be used instead. This simpler version must behave almost like if it were the real one but its evaluation should require less computing power.

Building such a model is the goal of all the supervised learning techniques. Those methods start from a set of n_d observations $\boldsymbol{y}^{(\mathrm{d})} = [y_1^{(\mathrm{d})}, \ldots, y_{n_d}^{(\mathrm{d})}]^\mathsf{T}$ of the actual model at different points of the parameters space $[x]^{(\mathrm{d})} = [\boldsymbol{x}_1^{(\mathrm{d})}, \ldots, \boldsymbol{x}_{n_d}^{(\mathrm{d})}]^\mathsf{T}$ where $y_i^{(\mathrm{d})} = y(\boldsymbol{x}_i^{(\mathrm{d})})$ with $y(\boldsymbol{x})$ the real model. From this relatively small amount of evaluations of the model, the surrogate model $\hat{y}(\boldsymbol{x})$ is built so that $\hat{y} = \hat{y}(\boldsymbol{x}) \approx y(\boldsymbol{x})$ for any vector $\boldsymbol{x} \in \Omega$ that is not in the training set $[x]^{(\mathrm{d})}$.

The first step for building the surrogate model is then to draw n_d vectors $\boldsymbol{x}_i^{(\mathrm{d})}$ to build the matrix $[x]^{(\mathrm{d})}$. This can be performed with various methods but here we consider quasi-random sequences.

Those sequences, compared to real random sequences, take into account the previous points that have been drawn. They are used to cover the space as efficiently as possible. In section A.2.5 the Saltelli extension of Sobol sequence is used to define the coordinates and here, to produce the training set for the surrogate model, we use a Halton sequence [Halton, 1960] as implemented in *chaospy* [Feinberg and Langtangen, 2015].

In *shamo*, the generation of the surrogate model is carried out with "Gaussian Processes Regression" (GPR) [Rasmussen and Williams, 2006]. Let us define the notation for a multivariate normal distribution $\mathcal{N}(\boldsymbol{\mu}, [\gamma])$ where $\boldsymbol{\mu} = [\mu_1, \ldots, \mu_{n_p}]$ is the vector of means along each axis and $[\gamma]$ is the covariance matrix where each $\gamma_{i,i}$ is the variance of the i-th random parameter and the elements $\gamma_{i,j}$ are the correlation between the i-th and the j-th variables.

To predict the n_t values $\boldsymbol{y}^{(t)} = [y_1^{(t)}, \ldots, y_{n_t}^{(t)}]^{\mathsf{T}}$ on the test points $[x]^{(t)}$, GPR handles the problem as Bayesian inference. Under these conditions, the learning samples are treated as random variables following a multivariate normal distribution $P(\boldsymbol{y}^{(\mathrm{d})} \mid [x]^{(\mathrm{d})} = \mathcal{N}(\mu^{(\mathrm{d})}, [\gamma]^{(\mathrm{d})})$. Here, the mean of this distribution is set to the mean of the learning outputs. To consider the test points, this expression becomes

$$P(\boldsymbol{y}^{(\mathrm{d})}, \boldsymbol{y}^{(t)} \mid [x]^{(\mathrm{d})})$$
$$= \mathcal{N}\left(\mu^{(\mathrm{d})}, \begin{bmatrix} [\gamma]^{(t)} & [\gamma]^{(t,d)} \\ [\gamma]^{(d,t)} & [\gamma]^{(\mathrm{d})} + \epsilon[i] \end{bmatrix}\right), \qquad \textbf{Eq. A.12}$$

with ϵ an added noise.

Next, the conditional distribution $P(\boldsymbol{y}^{(t)} \mid \boldsymbol{y}^{(\mathrm{d})}, [x]^{(\mathrm{d})}) = \mathcal{N}(\mu^*, [\gamma]^*)$ is obtained with

$$\mu^* = \mu^{(\mathrm{d})} + [\gamma]^{(t,d)}([\gamma]^{(\mathrm{d})})^{-1}(\boldsymbol{y}^{(\mathrm{d})} - \mu^{(\mathrm{d})}), \qquad \textbf{Eq. A.13}$$

$$[\gamma]^* = [\gamma]^{(t)} - [\gamma]^{(t,d)}([\gamma]^{(\mathrm{d})})^{-1}[\gamma]^{(d,t)}. \qquad \textbf{Eq. A.14}$$

Finally, the mean values μ_i^* and the standard deviation $\gamma_i^* = [\gamma]_{i,i}^*$ are obtained by the marginalisation of each random variable. The values μ_i^* are the predictors corresponding to the test points.

During the training step, the hyper-parameters of the kernel are optimised by maximising the log-marginal likelihood (LML) [Schirru et al., 2011]. When the model outputs more than one scalar, the process can be applied separately to each of the outputs, giving one Gaussian process by output variable. Here, we use the implementation of the GPR from *scikit-learn* [Pedregosa et al., 2011a] and follow the recommendations from Chen et al. [2016]. Thus, the regression part of the GPR is set to the mean of the output variable and the kernel is obtained by the product of a constant kernel and a stationary Matérn kernel with the smoothness parameter $\nu = 2.5$, thus resulting in the covariance function

$$k(\boldsymbol{x}_1, \boldsymbol{x}_2) = \left(1 + \frac{\sqrt{5}}{l} d(\boldsymbol{x}_1, \boldsymbol{x}_2) + \frac{5}{3l} d(\boldsymbol{x}_1, \boldsymbol{x}_2) r \right)$$
$$\cdot \exp\left(-\frac{\sqrt{5}}{l} d(\boldsymbol{x}_1, \boldsymbol{x}_2) \right).$$

Eq. A.15

A.3. Applications

We demonstrate the application of *shamo* on EEG and tDCS forward problems.

A.3.1. EEG forward problem

As described in section A.2.4, the computation of the EEG forward model is of main interest in source reconstruction but is highly dependent on the geometry and the physical properties of the tissues.

To build the surrogate model, we generate a set of leadfield matrices $[l(\boldsymbol{\sigma}^{(i)})]$ for 100 conductivity vectors $\boldsymbol{\sigma}^{(i)}$ drawn from the parameters space Ω using a Halton sequence. This step results in a leadfield matrix where each element is actually a Gaussian process, which gives us the ability to quickly construct any new matrix $[\hat{l}(\boldsymbol{\sigma})]$ for a specific conductivity vector $\boldsymbol{\sigma}$.

The sensitivity indices defined in Equations **Eq. A.8** and **Eq. A.9** are only valid for a model with a single scalar output. Therefore we choose to study the sensitivity of the whole matrix to the values of $\boldsymbol{\sigma}$ with a distance measure $m(\boldsymbol{\sigma})$ relative to a reference leadfield matrix $[l]_{\mathrm{ref}}$, obtained with a fixed $\boldsymbol{\sigma} = \boldsymbol{\sigma}_{\mathrm{ref}}$

$$m(\boldsymbol{\sigma}) = \|[l(\boldsymbol{\sigma})] - [l]_{\mathrm{ref}}\|_{\mathsf{F}}\,, \qquad \text{\textbf{Eq. A.16}}$$

where $\boldsymbol{\sigma}_{\mathrm{ref}}$ is the mean value for each tissue (See Table A.1) and and $\|\ldots\|_{\mathsf{F}}$ is the Frobenius norm.

A surrogate model $\hat{m}(\boldsymbol{\sigma})$ is thus built for this function based on the same training data as the parametric matrix introduced above. Next, the first and total order Sobol indices are computed from two sets of 40000 evaluations of the Gaussian process for the six models of this study, as defined in Section A.2.3. The resulting indices are shown in Figure A.2.

Clearly, for both the truncated distributions and the extended uniform ones, the parameter with the largest influence on the metric is the gray matter conductivity σ_{GM}. Whether one uses the narrow truncated normal (models 2a/3a) or the extended uniform (models 2b/3b) distributions for the compact skull and the outer and inner tables has little influence on the Sobol indices.

Another interesting point is the increasing influence of the CSF conductivity when the uniform distribution is used. While both its first and total order Sobol indices in models 1a to 3a are very small, the value of $s_{\mathrm{CSF}}^{(t)}$ for models 1b to 3b are non negligible meaning there are interactions between parameters.
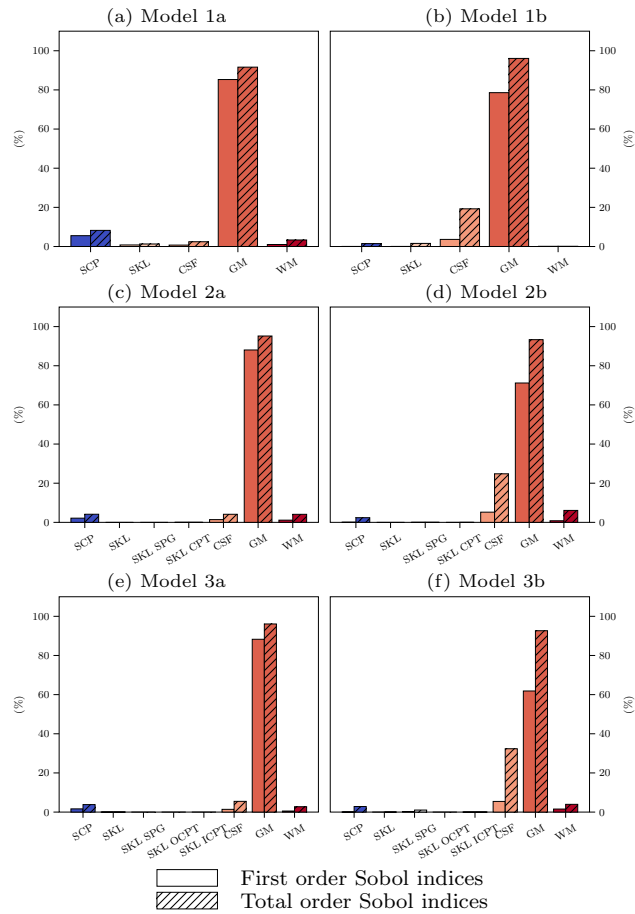
Figure A.2 **First (%) and total order Sobol indices of the metric $m(\sigma)$ for each tissue of each model. In the left column, the values for Σ are the truncated normal distributions from McCann et al. [2019] and int the right column, the extended uniform distribution is used.**

A.3.2. Evaluation of the electrode potential

To illustrate the actual effect of the sensitivity described in the above application, we calculate the electrical potential measured on the scalp due to a single left frontal source located 17.8mm under F3. Model 3 with the σ_{ref} was used as a reference (Figure A.3b) then the conductivity of GM was also set to the minimal and maximal value found in the literature (See Table A.1) leading to slightly modified electrical potential scalp maps (Figure A.3a, c). The scalp map differences of the latter two with the reference one is shown in Figure A.3 d, e.
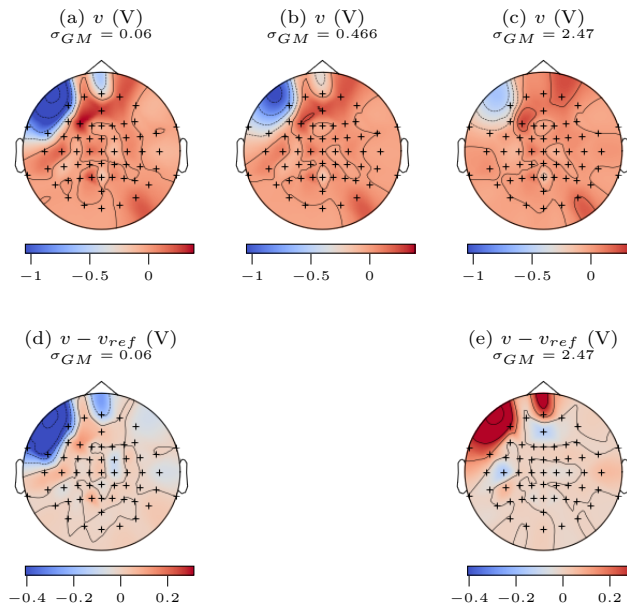
Figure A.3 **(a) the scalp potential (V) computed for** $\sigma_{\mathbf{GM}} = \sigma_{\mathbf{GM,min}} = 0.06$ **(Sm^{-1}), (b) the scalp potential (V) obtained for** $\sigma_{\mathbf{GM}} = \sigma_{\mathbf{GM,ref}} = 0.466$ **(Sm^{-1}) and (c) the scalp potential (V) measured with** $\sigma_{\mathbf{GM}} = \sigma_{\mathbf{GM,max}} = 2.47$**. (d) and (e) show the difference between the computed scalp potential and the reference one (V) respectively for** $\sigma_{\mathbf{GM}} = \sigma_{\mathbf{GM,min}}$ **and** $\sigma_{\mathbf{GM}} = \sigma_{\mathbf{GM,max}}$**.**

A.3.3. Transcranial direct current stimulation (tDCS) simulation

Using the same formulation as for the EEG forward problem, we can model tDCS and obtain the current density, electric potential and electric field accross the whole head.

To illustrate this aspect, we consider a HD-tDCS experiment where electrode P3 was set as a 4 mA injector and electrodes TP9, C3, P1 and O1 were set to ground. We used the mesh from model 3 and the truncated normal conductivity distributions as in model 3a for this simulation. As a metric to assess the sensitivity of the model with regard to the conductivity values, we chose the mean of current density norm in a small region of 368 mm^3 located 22.6 mm under CP3. The results of these simulations are shown in Figure A.4. As an extra feature for researchers in neuroscience, the estimated fields can also be directly exported as a standard multidimensional NifTI image.

As visible in Figure A.4, current density is highest in the scalp tissue between the electrodes, but also spreads diffusely throughout the head volume. The tissues with the highest Sobol index are the scalp, followed by the spongy compartment of the skull. This comes as no surprise, as electrical current follows the path of least resistance.
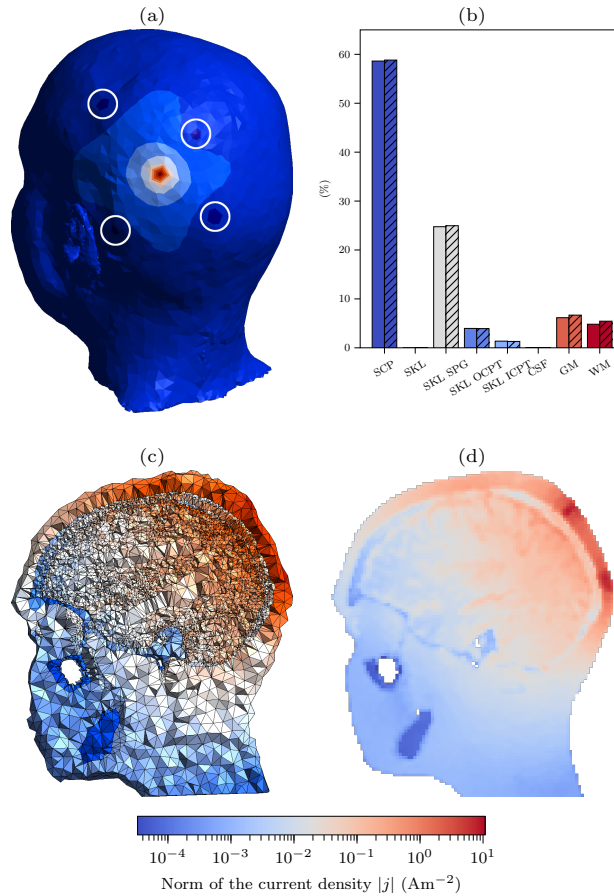
Figure A.4 **(a) A view of the scalp potential induced by the set electrodes surrounded in white, (b) the first (%) and total order Sobol indices of the mean current density in the ROI for each tissue conductivity, (c) a cut of the current density inside the head resulting from the injection of current inside the reference model where $\sigma = \sigma_{\mathbf{ref}}$ and (d) the same information in the form of a NifTI file with a representation of the small mask used to compute the mean of the norm of the current density.**

A.4. Discussion

The pipeline presented in this work uses several well established methods. Here, we discuss the added value of such tool and technical choices and compare it to established solutions such as *SimNIBS* [Thielscher et al., 2015] or *BrainStorm* [Tadel et al., 2011].

First, the generation of a realistic subject specific head model is generally a tedious task involving the segmentation of the head volume, based on MR or CT images, then the delineation of the tissue interfaces. This step often requires further *ad hoc* cleaning to ensure the surfaces are two dimensional manifold, i.e. they are completely closed and thus have an inside and an outside. Then, those surfaces must be integrated into a single mesh and the so defined volumes filled with tetrahedral elements.

Several automated pipelines are now available is the most common toolboxes [Thielscher et al., 2015; Huang et al., 2019; Nielsen et al., 2018] using either *SPM* [Ashburner and Friston, 2005] or *FSL/FreeSurfer* [Smith et al., 2004; Fischl et al., 2004] to segment the structural images. While this greatly simplifies model generation, since it takes care of both the segmentation and meshing steps, it also prevents the user from using non standard segmentations.

Here the FEM mesh is directly built from a 3D image made with labeled voxels. This approach not only provides more control on the refinement of the final mesh but also allows the any number of tissues, even with complex configurations. In practice, this opens the path for more specific cases such as modeling prosthetic, metallic plates or any other unusual head geometry. Moreover one can freely choose the segmentation tool to use or could even proceed manually for difficult cases.

As explained previously, the model presented in this paper does not consider the anisotropy of white matter because no tensor information is provided with the original data. However any kind

of field can be included in the model and handled by the solver, *GetDP*, without extra burden from the point of view of the user. Besides *GetDP* already powers other similar tools like *SimNIBS* [Thielscher et al., 2015] and *ROAST* [Huang et al., 2019] and the forward problem implementation used in *shamo* have been validated by [Ziegler et al., 2014].

Here we only considered two conductivity dependent electrostatic problems, EEG and tDCS. Nevertheless, thanks to *GetDP*'s simple formalism, *shamo* could be directly extended to electromagnetic modeling processes, including MEG and TMS. Indeed this only requires the definition of the equations related to the problem, which are explicitly stored in a problem file for *GetDP*. Nowadays other tools, like *SimNIBS*, also include modules for the quantification of the effect of tissue conductivity uncertainty [Saturnino et al., 2019], showing the importance of such analysis for tDCS applications. Still, beyond electrical conductivity, the sensitivity analysis could also focus on other parameters, e.g. the injected current in HD-tDCS, through python classes available in *shamo* to expose the needed parameters. Importantly, by definition, the Sobol indices rely on a single scalar output function, whose choice is thus critical but also lets the user focus on any feature of interest. Thereby *shamo*'s flexible implementation allows one to define his own processes and sensitivity analysis.

Regarding the surrogate models, we decided to use Gaussian process because they provide information on the confidence over the solution through the standard deviation on each predicted point. This can be used to obtain more in-depth understanding of the model. Such regressor also has the advantage of not requiring huge amounts of training data. Considering the fact that an evaluation of the actual model can take several hours, reducing the number of observations can drastically lower the computation time required. To further reduce this time, the tool provides an easy way to evaluate each sample point separately, thus allowing the use of high-performance computing (HPC) equipment like computer clusters.

In the present work, observations were computed by batches of 100, each on a single core on the CÉCI clusters [5].

Overall, the goal of *shamo* is to provide a single tool to perform three major steps, namely FEM creation, model estimation, and sensitivity analysis. This operated with few dependencies that are all established, in an open source software working out of the box on any major operating system or on HPC platforms.

A.5. Conclusion

In this paper, we presented a python pipeline for accurate electromagnetic modeling of the head which allows for sensitivity analysis and surrogate model building, bringing together similar features as some established software, such as *SimNIBS* [Thielscher et al., 2015] or *ROAST* [Huang et al., 2019] for tDCS and *Brainstorm* [Tadel et al., 2011] or *MNE* [Gramfort et al., 2013] for EEG, unified with a single API. This tool, called *shamo* [Grignard, 2021a], and the full documentation [Grignard, 2021b] are available on Github under GPL-v3 license. A set of examples are also available in the form of jupyter notebooks.

We showed a use-case for the EEG forward problem where a parametric leadfield matrix is computed and can then be used to generate any new matrix for a specific set of tissue conductivity values and another application to tDCS where the current density in a certain region is obtained and can be studied with regard to the electrical sensitivity. Those are only two possible applications but *shamo* could easily be extended to magnetic stimulation or TMS.

Considering the abstraction level of the tool and the outcome that can be obtained from it, one can use our tool to perform finite element analysis and sensitivity analysis without having to dig into

---

5. `http://www.ceci-hpc.be/`

those fields, letting the user employ the toolset of his choice for further analysis. *shamo* could be used in various studies to assess the sensitivity of the results to some parameters or to build parametric models for complex physical fields that, otherwise, should be evaluated every time a new value is needed.

A.6. Data availability

The data that support the findings of this study are available from the IT'IS foundation [6] but restrictions apply to the availability of these data, which were used under licence [7] for the current study, and so are not publicly available. Data are however available from the authors upon reasonable request and with permission of the IT'IS foundation.

A.7. Information sharing

The source code of *shamo* is available on Github [8] under GPLv3 license and is fully documented [9]. It can be installed from PyPI [10]. In addition, *jupyter* notebooks are also available on Github [11] and show how to conduct similar studies.

6. https://itis.swiss/virtual-population/
regional-human-models/mida-model/
7. https://itis.swiss/assets/Downloads/VirtualPopulation/
License_Agreements/LicenseAgreementMIDA.pdf
8. https://github.com/CyclotronResearchCentre/shamo
9. https://cyclotronresearchcentre.github.io/shamo/index.html
10. https://pypi.org/project/shamo/
11. https://github.com/CyclotronResearchCentre/shamo-tutorials

A.8. Acknowledgements

B.
Paper 2

This appendix contains the original text of the second paper written in the context of this thesis, entitled *"Why tDCS models cannot be trusted yet? — A simulation study"* which is still being worked on. All the supplementary materials referenced in this annex are available online with the preprint [1].

---

1. https://hdl.handle.net/2268/294662

Why tDCS models cannot be trusted yet? — A simulation study

Martin Grignard [2], Christophe Geuzaine [3], Michel Hansenne [4], Steve Majerus[4] and Christophe Phillips[2]

Transcranial direct current stimulation (tDCS) has gained increased interest over the past decades due to its affordability, ease of use and wide range of applications. However, its lack of consistency and reproducibility of published results is rising concerns.

A potential solution to improve the method is to tailor the stimulation for each subject based on individual measurements and models. Such model requires accurate information about the geometry of the tissues composing the head of the subjects, about their electric properties and about the electrode montage.

In the present simulation work, we evaluate the effect of an error on the placement of the anode and of the unknown physical properties of the tissues on the induced electric field for 6 experiments on 20 subjects.

In addition to confirming the concerning small tDCS effect size, we show that the uncertainty on the conductivity parameters prevents any other conclusion to be drawn from such models.

2. GIGA CRC In-Vivo Imaging, University of Liège, Belgium
3. Department of Electrical Engineering and Computer Science, University of Liège, Belgium
4. Psychology & Neuroscience of Cognition (PsyNCog) research unit, University of Liège, Belgium

B.1. Introduction

Transcranial direct current stimulation (tDCS) is a non-invasive neuromodulation technique which consists in injecting a small amount of electric current (*i.e.*, usually 1 to 2 mA) through the head of a subject by the mean of two large saline-soaked sponge electrodes (*e.g.*, 5×5 cm^2). The stimulating electrode or anode is placed above the cortical region of interest. The reference electrode, also referred to as cathode, is either located on the same region of the opposite hemisphere in a bipolar electrode montage or on the contralateral orbit region in a unipolar montage. It can also be applied on a silent zone such as the chin, the neck or the deltoid muscle [Nitsche et al., 2008; Kropotov, 2016].

Since the beginning of the century, this tool has received increased interest due to its affordability, simplicity and wide range of application. Indeed, it has been studied in research and clinical applications to help patients recovering from strokes [Boggio et al., 2007], traumatic spinal cord injury [Li et al., 2021] or suffering from refractory epilepsy [Yang et al., 2019], fibromyalgia [Lloyd et al., 2020], depression [Razza et al., 2020], anxiety disorders [Stein et al., 2020] just to name a few. A lot of studies have also tried to use tDCS to improve cognitive functions like working memory or inhibition in normal subjects and patients [Dedoncker et al., 2016; Senkowski et al., 2022; Schroeder et al., 2020].

Whilst more and more papers focusing on tDCS are published every year ($1,088$ papers listed on PubMed in 2021 [5]), two major issues rose up: the high inter-subject variability in the response to the stimulation and the lack of reproducibility of some published results in follow-up studies [Dumont et al., 2021; Jacoby and Lavi-

---

5. `https://pubmed.ncbi.nlm.nih.gov/?term=tDCS&filter=years.`
`2021-2021`

dor, 2018; Westwood, 2018].

With a percentage of expected response generally lower than 50% [Müller-Dahlhaus et al., 2008; Jacobson et al., 2012], the reliability of tDCS is questionable. Wiethoff et al. [2014] concludes that the after-effect of tDCS on corticospinal excitability is highly variable, and the systematic review of Horvath et al. [2015] rose questions about the efficacy of such device and the underlying mechanisms.

One of the proposed solutions to improve the technique is to individualize the intensity of the injected current, referred to as the dose, based on subject specific models [Albizu et al., 2020]. Unfortunately, the recent work by Sallard et al. [2021] indicates that this approach might not improve the efficacy of tDCS over the primary motor cortex. Nevertheless, current modelling is often performed in addition to tDCS to evaluate the current density induced by the stimulation in a given region of interest (ROI).

Such a model relies heavily on the geometry of the subject and on the electrode placement, but also on the electric properties of the tissues composing the head. Those properties have been shown to vary widely between subjects based on numerous factors (*e.g.*, temperature, time of day, health status...). The review from [McCann et al., 2019] provides ranges of low frequency conductivity values for the main biological tissue classes.

The head geometry is usually built based on subject-specific structural images, but electrode positions are not always recorded using virtualization techniques. In this case, they are placed on the model without real world information, inducing a potential error of placement.

On the other hand, the physical properties of the tissues are hard to measure on a subject basis. Hence, constant values across subjects are usually set according to the literature.

In the present simulation work, we study the electric field induced in four different ROIs of the left hemisphere by the injection of $2\,\text{mA}$ with six electrode montages (See Table B.1) and compute

the induced transmembrane potential (ITP) on the 20 subjects from BrainWeb [6]. Previous studies reported ITP values between 0.2 and 0.5 mV [Radman et al., 2009; Opitz et al., 2016].
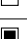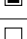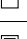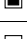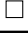
Anode	Cathode	ROI		Bipolar	Unipolar
C3	C4	■	MC	■	☐
C3	Fp2			☐	■
F3	F4	■	dlPFC	■	☐
F3	Fp2			☐	■
F7	F8	■	vmPFC	■	☐
P3	P4	■	IPS	■	☐

Table B.1   **The electrode montages considered with the ROI they target.**

In the process, we account for an error of 1 cm on the anode placement in four directions relative to the reference EEG 10-20 position and for the uncertainty on the electric conductivity of the biological tissues.

B.2. Materials and methods

B.2.1. Dataset

We used the dataset of 20 simulated normal healthy adults (10 females and 10 males) made available by BrainWeb. For each subject, this dataset provides a structural T1-weighted generated based on a SFLASH sequence (TR=22 ms, TE=9.2 ms, flip angle=$30°$ and 1 mm isotropic voxel size), 12 fuzzy tissue probability maps and a discrete segmented volume [Aubert-Broche et al., 2006a,b].

---

6. `https://brainweb.bic.mni.mcgill.ca/`

In the present work, only the T1-weighted images and discrete models were first converted into NIfTI images using *Nibabel* [Brett et al., 2020] and sorted following BIDS specifications [Gorgolewski et al., 2016] to be further processed.

B.2.2. Head geometry

To simulate the electric current in the head of the subjects, we generated finite element models based on the labelled images. These original segmented volumes with $0.5 \times 0.5 \times 0.5$ mm^3 voxels were first cleaned to remove external objects and noise (See Figure B.1a and Figures S1-20a) in four consecutive steps.

First, we created manually binary masks using *itk-SNAP* [Yushkevich et al., 2006] to remove big objects adjacent to the scalp from subjects 18 and 42. The other subjects did not require such manual processing. After this step, an iterative binary opening was performed on the whole head masks until no change between two iterations was measured. This removed the small external clusters. To erase the remaining non-head bodies, we kept only the biggest remaining cluster using *Scipy* [Virtanen et al., 2020]. Finally, we enforced at least one layer of CSF around the gray matter and one layer of soft tissues around the skull.

Next, we merged the original 11 tissues (referred to as SEG-11) into 5 tissues (SEG-05). Indeed, the most common models used to simulate tDCS include only five main tissues classes, namely: white matter (WM), gray matter (GM), cerebrospinal fluid (CSF), skull (SKL) and soft tissues (SFT). This can be attributed to the fact that most of the available automated head segmentation pipelines only output these tissues, even though a recent effort in the community has led to the release of several tools that can produce more accurate models [Puonti et al., 2020; Taberna et al., 2021].

The merging rules are described in Table S1 from the supple-

mentary materials, and the resulting labels are presented in Figure B.1b for subject 41 (See Figures S1-20b for the other subjects).

These final labels were processed with Shamo to generate subject specific finite element models (FEM). The obtained models contained more than 2×10^6 tetrahedra (See Figure B.1c and Figures S1-20c).
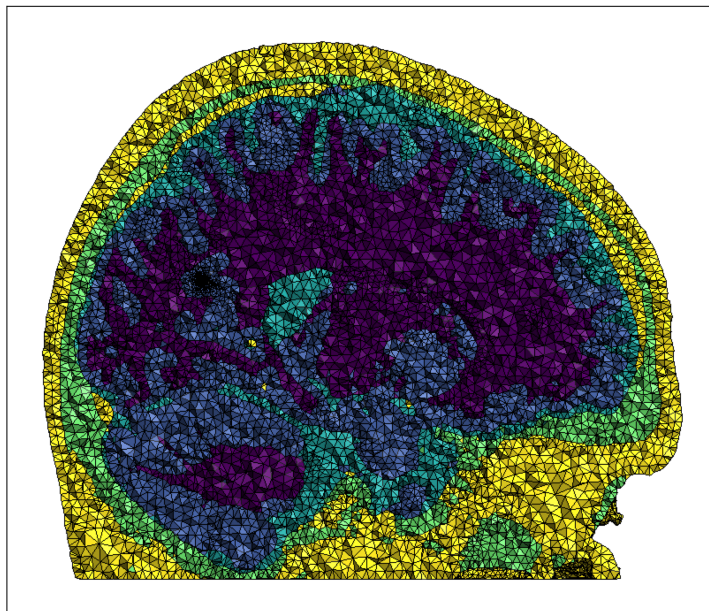
(a) SEG-11
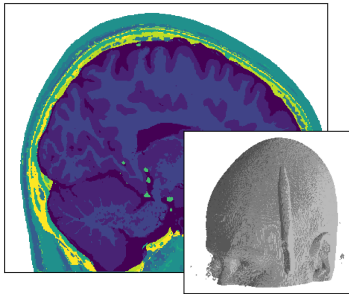
(b) SEG-05
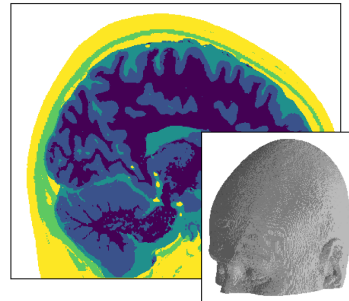
(c) Finite element model

WM   GM   CSF   SKL   SFT

Figure B.1 **(a) The original SEG-11 model, (b) the SEG-05 obtained by first cleaning the labels and then merging tissues following the rules defined in Table S1 and (c) a sagittal cut of the resulting FEM for subject 41.**

B.2.3. Electrode placement

Since one of the goals of this study is to evaluate the effect of the error on the placement of the electrodes, we considered five different positions of the anode for each of the experiments from Table B.1 where the electrode was moved by $1\,$cm relative to the reference EEG 10-20 international system [Jasper, 1958; Klem et al., 1999] position.

We denote the four perturbation directions as central (C)/lateral (L) if the electrode moves toward/away from the symmetry axis of the head and anterior (A)/posterior (P) if the electrode moves towards the front/back of the head. The name of the displaced anode is the concatenation of its base name and the direction (*e.g.*, central P3 is referred to as P3C).

The BrainWeb dataset does not include electrode positions. Consequently, we first located the nasion (NZ), the inion (IZ) and the left and right helix-tragus junction (LHJ and RHJ) in RAS coordinate system manually using *MRIcron* [Rorden et al., 2007]. Then, we generated a high density mesh of the head surface using Shamo [Grignard et al., 2022] and implemented the procedure proposed by Jurcak et al. [2005] to compute the coordinates of both the reference electrodes and their displaced counterparts (See Figure B.2a and Figures S1-20d).

We then produced a finite element model for each electrode montage with each position of the anode by adding the sensors to the base mesh from Section B.2.2. The electrodes were modelled as 5×5 cm^2 square patches, as shown in Figure B.2b for the C3-Fp2 electrode montage on subject 41 (See Figures S1-20e-j for the other montages and subjects). This step resulted in the creation of 30 models per subject (600 models in total).
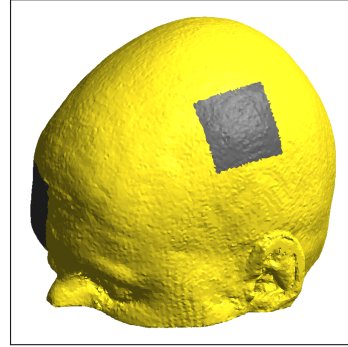
(a) **EEG 10-20**
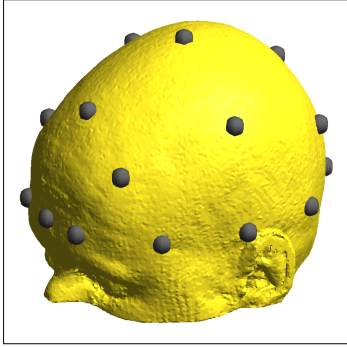
(b) **Montage**

Figure B.2 **(a) The automatically computed EEG 10-20 electrode positions and (b) the resulting model for the C3-Fp2 electrode montage on subject 41.**

B.2.4. Electrical conductivity

In our previous work [Grignard et al., 2022], we showed that the electrical conductivity of the tissues κ (S m^{-1}) influences the results of the simulations by using the conductivity values reported by McCann et al. [2019] (See Table B.2). The mean values in the table are the reported weighted means computed using a weighting method described in their paper. We used the same values in the present study.

The electrical conductivity considered for the soft tissues class (SFT) was set as the one measured for the scalp since its range encompasses those of fat, muscle, and blood which are the three main classes that were merged into it.

We defined 20 different conductivity profiles $\boldsymbol{\kappa} = [\kappa_{\text{WM}}, \kappa_{\text{GM}}, \kappa_{\text{CSF}}, \kappa_{\text{SKL}}, \kappa_{\text{SFT}}]$ by sampling the 5D uniform conductivity space with a quasi-random Halton sequence [Halton, 1960] (See Table S2a in supplementary material). This space, Ω_{uniform},

Tissue	Electrical conductivity ($\mathrm{S\,m^{-1}}$)			
	Min.	Max.	Mean	Std.
■ WM	0.0646	0.8100	0.2167	0.1703
■ GM	0.0600	2.4700	0.4660	0.2392
■ CSF	1.0000	2.5100	1.7100	0.2981
■ SKL	0.0182	1.7180	0.0160	0.0190
■ SFT	0.1370	2.1000	0.4137	0.1760

Table B.2   **The electrical conductivities of the tissues ($\mathrm{S\,m^{-1}}$) as reported by McCann et al. [2019].**

was defined by five uniform distributions ranging from the minimum to the maximum conductivity value for each tissue.

In addition to these profiles, we also determined the reference conductivity profile, as recommended by McCann et al. [2019] (*i.e.* $\boldsymbol{\kappa} = [\bar{\kappa}_{\mathrm{WM}},\ \bar{\kappa}_{\mathrm{GM}},\ \bar{\kappa}_{\mathrm{CSF}},\ \bar{\kappa}_{\mathrm{SKL}},\ \bar{\kappa}_{\mathrm{SFT}}]$).

The uniform distributions used to define $\Omega_{\mathrm{uniform}}$ are considered as the worst case scenario, since some ranges reported by McCann et al. span multiple orders of magnitude (*e.g.*, the conductivity of GM). In order to evaluate the effect of more educated priors on the computed metrics, we also defined a second input parameter space, Ω_{norm}, where we used the truncated normal distributions for each tissue. We drew 20 new conductivity profiles from this new space using the same technique (See Table S2b in supplementary material).

B.2.5. Regions of interest

As explained in Table B.1, each electrode montage targets a specific ROI in the left hemisphere. To extract individual binary masks of these brain areas for each subject, we relied on three different cortical atlases: Brodmann [Fischl et al., 2008], CP-MMP 1.0 [Glasser et al., 2016] and MarsAtlas [Auzias et al., 2016].

Unfortunately, the latter is not available in fsaverage space (*i.e.,* the standard space for *FreeSurfer* defined as a reference cortical surface) [Mills, 2016]. However, it has been published in Colin27 space [Holmes et al., 1998]. To produce the proper labels in fsaverage space from MarsAtlas, we first converted the segmented volume into labels in the native space of the subject. Next, we registered these labels onto fsaverage cortical surface with the surface registration tools from *FreeSurfer* [Dale et al., 1999]. The resulting labels for the four ROIs are displayed on fsaverage in Figure B.3.
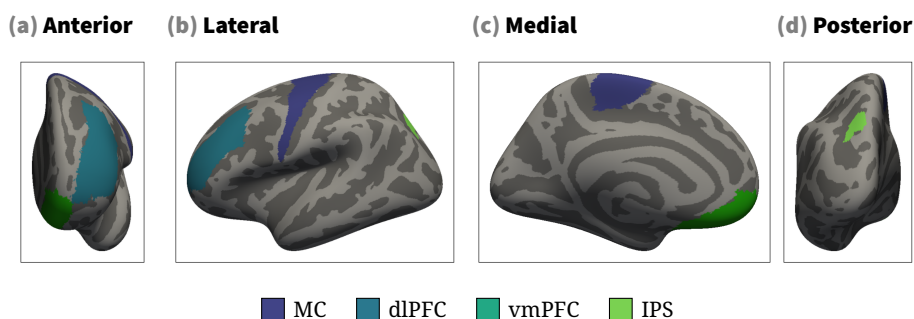

(a) **Anterior** (b) **Lateral** (c) **Medial** (d) **Posterior**

■ MC ■ dlPFC ■ vmPFC ■ IPS

Figure B.3 **The left hemisphere ROIs considered in this study and extracted from Brodmann [Fischl et al., 2008], HCP-MMP 1.0 [Glasser et al., 2016] and MarsAtlas [Auzias et al., 2016] atlases displayed on the inflated surface of fsaverage.**

Once all the labels were extracted and projected on fsaverage, we registered them on the cortical surfaces of each subject and converted them into binary masks coregistered on the SEG-05 images.

We also extracted the surface area (mm^2), the volume (mm^3) and the depth (mm) of these regions for all the subjects (See Table S3).

B.2.6. Simulations

We simulated tDCS with *Shamo* [Grignard et al., 2022] which interfaces with *GetDP* [Geuzaine, 2008] to solve the finite element problems. Each simulation solves the Poisson equation [Hallez et al., 2007; Darbas and Lohrengel, 2018]

$$\nabla \cdot (\kappa \nabla(v)) = -\rho_\mathrm{s}, \qquad \text{Eq. B.1}$$

where v (V) is the electric potential and ρ_s ($\mathrm{A\,m^{-3}}$) is the source volume current density. The boundary conditions were set so that the anode injected $2\,\mathrm{mA}$ and the cathode acted as a reference (i.e. $0\,\mathrm{V}$).

Considering the 20 subjects, their respective 30 finite element models described in Section B.2.2 with the electrode montages from Section B.2.3 and the 21 different conductivity profiles drawn from Ω_uniform defined in Section B.2.4, we ran a total of 12600 simulations (2100 for each experiment).

The simulations calculated the electric potential v (V), the electric field e ($\mathrm{V\,m^{-1}}$) and the current density j ($\mathrm{A\,m^{-2}}$) on the unstructured meshes (See Figure B.4). To make any further processing easier, we converted these fields into NIfTI files by sampling them on a regular $1 \times 1 \times 1\,\mathrm{mm^3}$ grid with the same orientation as the SEG-05 image.

Then, by applying the binary masks built in Section B.2.5, we extracted the values of these fields for all the voxels of the ROIs in each simulation and stored it in a *DuckDB* database [Raasveldt and Mühleisen, 2019]. In addition, we computed both the components normal and tangential to the cortical surface of e and j.

Finally, we computed the average absolute values for all the previously described metrics for each simulation.
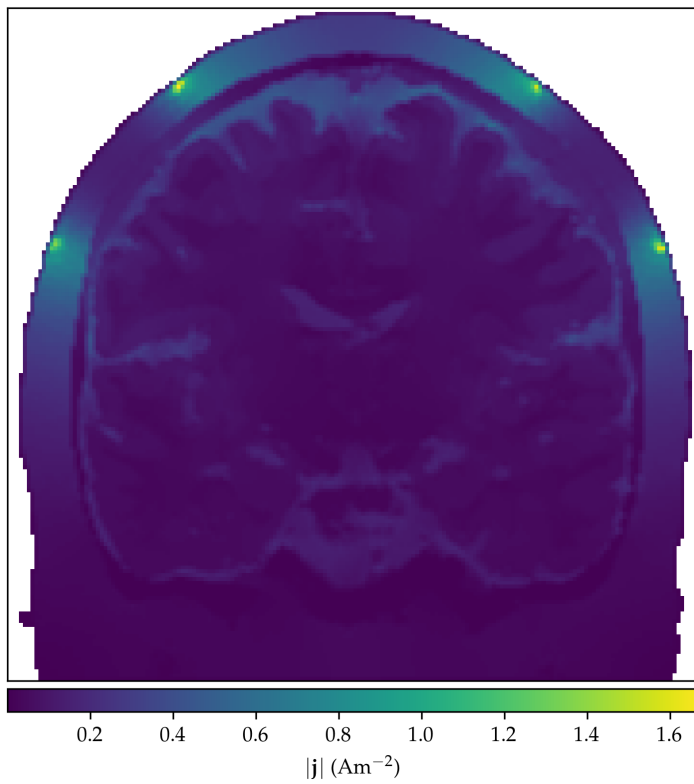
Figure B.4 **A cut of the magnitude of the magnitude of the current density computed in the head of subject 4 resulting from the injection of $2\,\mathrm{mA}$ with the C3-C4 electrode montage.**

B.2.7. **Gaussian process regressors**

As described above, we only performed simulations for the conductivity profiles drawn from Ω_{uniform}, while in Section B.2.4 we stated that we also defined 20 conductivity profiles from Ω_{norm}.

Indeed, running the simulations is computationally expensive. In order to reduce the computation time required, and considering that the points drawn from Ω_{norm} are also included in Ω_{uniform}, we decided to fit multi-output Gaussian process regressors (GPR) [Rasmussen and Williams, 2006] on the results of the simulations described in Section B.2.6 using *scikit-learn* [Pedregosa et al., 2011b]. Following the recommendations from Chen et al. [2016], the regression part of the GPR was set to the mean of the output variable and the kernel was defined as the product of a constant kernel and a stationary Matérn kernel with a smoothness parameter $\nu = 2.5$.

This way, we leveraged the 12600 simulations to interpolate the results corresponding to the conductivity profiles from Ω_{norm}.

B.2.8. **Models**

We focused on the mean absolute magnitude of the electric field $|\bar{e}|$ and of its component normal to the cortical surface $|\bar{e}_r|$. For each experiment, we built different Bayesian models using *Bambi* [Capretto et al., 2020] which is based on *PyMC3* [Salvatier et al., 2016]. The basic expression of all these models is

$$Y \sim \mathcal{N}(\mu, \sigma^2), \qquad \qquad \textbf{Eq. B.2}$$

with Y the dependent variable, μ defined as

$$\mu = \alpha + \boldsymbol{\beta} \cdot \boldsymbol{X} + \varepsilon, \qquad \qquad \textbf{Eq. B.3}$$

where α the intercept, $\boldsymbol{\beta} = [\beta_1, \ldots, \beta_n]$ the slopes, $\boldsymbol{X} = [X_1, \ldots, X_n]^\top$ the vector of independent variables and ε the error term. We also consider the hierarchic counterpart of these pooled models, in which we account for the subject with a random effect. For these models, we have different values of μ, α and $\boldsymbol{\beta}$ for each subject i,

$$\mu_i = \alpha_i + \boldsymbol{\beta}_i \cdot \boldsymbol{X} + \varepsilon,$$
$$\alpha_i = \alpha^{(\text{com})} + \alpha_i^{(\text{sub})}, \qquad \text{Eq. B.4}$$
$$(\beta_j)_i = \beta_j^{(\text{com})} + (\beta_j^{(\text{sub})})_i,$$

where $\alpha^{(\text{com})}$ and $\beta_j^{(\text{com})}$ are respectively the common intercept and slopes and $\alpha_i^{(\text{sub})}$ and $(\beta_j^{(\text{sub})})_i$ are the subject specific contributions to the intercept and slopes.

For all the models described in the next paragraphs, weakly informative priors are set automatically using the method explained in Westfall [2017]. They are then all fitted using the No-U-Turn sampler (NUTS) [Hoffman and Gelman, 2011] with 4 chains of 1000 tune and 1000 draw iterations.

To decide whether a parameter has a significant effect on the dependent variable, we use the 95% highest density interval (HDI) and the region of practical evidence (ROPE) [Kruschke and Liddell, 2018]. This method states that if the 95% HDI lies inside the ROPE for more than 97.5%, the corresponding parameter is null. Conversely, if the 95% HDI intersects with the ROPE for less than 2.5%, the parameter is non-null. Finally, if the intersection between the two intervals is between these two boundaries, we cannot conclude whether the parameter is null or not. The boundaries of the ROPE are set to $\pm 0.1 \cdot \text{std}(Y)$.

Anode placement

To evaluate the effect of a displacement of $1\,\text{cm}$ of the anode with regard to the reference EEG 10-20 position, we define a model

to assess the difference between the measurements computed for each of the 5 anode placements from Section B.2.3 as

$$\mu = \alpha + \sum_{p=1}^{4} \beta_p \cdot X_p + \varepsilon,$$

$$\mu_i = \alpha_i + \sum_{p=1}^{4} (\beta_p)_i \cdot X_p + \varepsilon,$$

where p corresponds to a specific displacement of the anode (anterior, central, lateral or posterior) and X_p is either 0 or 1 based on the anode used to obtain the record.

Conductivity profile

Using the same method, we compare the values of both $|\bar{e}|$ and $|\bar{e}_r|$ calculated for the 20 conductivity profiles described in Section B.2.4 with the values obtained for the reference profile, where the conductivity of each tissue is set to the value recommended by McCann et al. [2019]. Thus, we transform the base models from Equation B.3 and B.4 into

$$\mu = \alpha + \sum_{k=1}^{20} \beta_k \cdot X_k + \varepsilon,$$

$$\mu_i = \alpha_i + \sum_{k=1}^{20} (\beta_k)_i \cdot X_k + \varepsilon.$$

In these expressions, k refers to one of the 20 conductivity profiles established using the quasi-random Halton sequence and X_k is 1 or 0.

Bipolar and unipolar electrode montages

As shown in Table B.1, we simulate a bipolar and an unipolar electrode montage to stimulate both the MC and the dlPFC. In order

to compare the values of $|\bar{e}|$ and $|\bar{e}_r|$ computed for each pairs, we fit the models with the following expected values,

$$\mu = \alpha + \beta_{\text{uni}} \cdot X_{\text{uni}} + \varepsilon,$$
$$\mu_i = \alpha_i + (\beta_{\text{uni}})_i \cdot X_{\text{uni}} + \varepsilon,$$

Eq. B.7

with X_{uni} equal either to 1 if the montage is unipolar or to 0 otherwise.

B.2.9. Induced trans-membrane potential

The steady-state induced trans-membrane potential (ITP), denoted by Δu_{i} (mV), is the potential difference measured between the inside u_{in} and the outside u_{out} of the cell membrane added to the resting state potential Δu_{r} and due to an external stimulation,

$$u_{\text{in}} - u_{\text{out}} = \Delta u_{\text{r}} + \Delta u_{\text{i}}.$$

Eq. B.8

While tDCS is not able to trigger action potentials, it is generally accepted that it generates an induced trans-membrane potential which hyperpolarizes the neuron membranes under the anode and depolarizes it under the cathode [Pelletier and Cicchetti, 2015; Tanaka et al., 2020]. In the present work, we compute the ITP resulting from the different stimulations using analytical expressions for both spherical and spheroidal cells.

Spherical cell

The theoretical steady-state ITP resulting from an external electric field e (V m^{-1}) in a spherical cell of radius r_1 (m) with a non-conductive plasma membrane is described by Schwan's equation [Schwan, 1994]

$$\Delta u_{\text{i}} = \frac{3}{2}|e|r_1\cos(\theta),$$

Eq. B.9

with θ the angle between the electric field and the vector going from the centre of the cell to the point of the membrane where the ITP is calculated.

Consequently, the maximum value of Δu_i is obtained for $\theta = 0$. To avoid using an arbitrary value for r_1, we finally compute

$$\frac{\max(\Delta u_i)}{r_1} = \frac{3}{2}|e|. \qquad \text{Eq. B.10}$$

Spheroidal cell

Pyramidal cortical cells are not spherical, thus we also consider spheroidal cells $r_1 > r_2 = r_3$ with a shape ratio $\gamma = r_1/r_2$ and elongated along the normal of the cortical surface. For such cells, Valic et al. [2003] gives the following expression of the ITP,

$$\Delta u_i = |e|\sin(\varphi)\frac{r_2\sin(\theta)}{1 - l_x} + |e|\cos(\varphi)\frac{r_1\cos(\theta)}{1 - l_z}, \qquad \text{Eq. B.11}$$

where φ is the angle between the electric field and the main axis of the cell and l_x and l_z are the depolarization factors

$$l_z = \frac{1 - \lambda^2}{2\lambda^3}\left(\log\left(\frac{1 + \lambda}{1 - \lambda}\right) - 2\lambda\right), \qquad \text{Eq. B.12}$$

$$l_x = \frac{1}{2}(1 - l_z), \qquad \text{Eq. B.13}$$

with $\lambda = \sqrt{1 - (1/\gamma)^2}$.

Since we already computed the tangential and radial components of the electric field denoted by $|e_t|$ and $|e_r|$, we have

$$\Delta u_i = |e_t|\frac{r_2\sin(\theta)}{1 - l_x} + |e_r|\frac{r_1\cos(\theta)}{1 - l_z}, \qquad \text{Eq. B.14}$$

which is maximized when

$$\theta = \theta_{\max} = \text{atan}\left(\frac{|e_t|(1 - l_z)}{|e_r|\gamma(1 - l_z)}\right). \qquad \text{Eq. B.15}$$

Following what we did for the spherical cell, we derive the size independent expression

$$\frac{\max(\Delta u_{\mathrm{i}})}{r_1} = |e_t|\frac{\sin(\theta_{\max})}{\gamma(1-l_x)} + |e_r|\frac{\cos(\theta_{\max})}{1-l_z}.$$

$$\text{Eq. B.16}$$

B.3. Results

Figure B.5 shows the distributions of the measured values of $|\bar{e}|$ and $|\bar{e}_r|$ (mV m^{-1}) for the different experiments defined in Table B.1 (See also Figures S21-32a-b). Overall, the mean absolute magnitude of the electric field ranges from 47.2 to 644.2 mV m^{-1} and its component normal to the cortical surface from 24.2 to 470.7 mV m^{-1} for the simulations, while for the GPRs, $|\bar{e}|$ ranges from 139.2 to 398.5 mV m^{-1} and $|\bar{e}_r|$ ranges from 69.5 to 223.9 mV m^{-1}.

In order to better picture the results, we show the data obtained for the C3-C4 electrode montage targeting the motor cortex, based on the conductivity profiles drawn from $\Omega_{\mathrm{uniform}}$, all along the following sections. Figure B.6 shows the results for this specific montage, and the outcome of the other experiments are provided in supplementary materials.

B.3.1. Anode placement

Based on the measurements acquired for each anode placements shown in Figure B.7 for the C3-C4 electrode montage (See Figures S22-32e-f for the other experiments), we fitted the model from Equation B.5 and computed the 95 % HDI of β_p and $\beta_p^{(\mathrm{com})}$ which are given in Tables S4/8a-b.

(a) $|\bar{e}|$ (Ω_{uniform})

(b) $|\bar{e_r}|$ (Ω_{uniform})

(c) $|\bar{e}|$ (Ω_{norm})

(d) $|\bar{e_r}|$ (Ω_{norm})

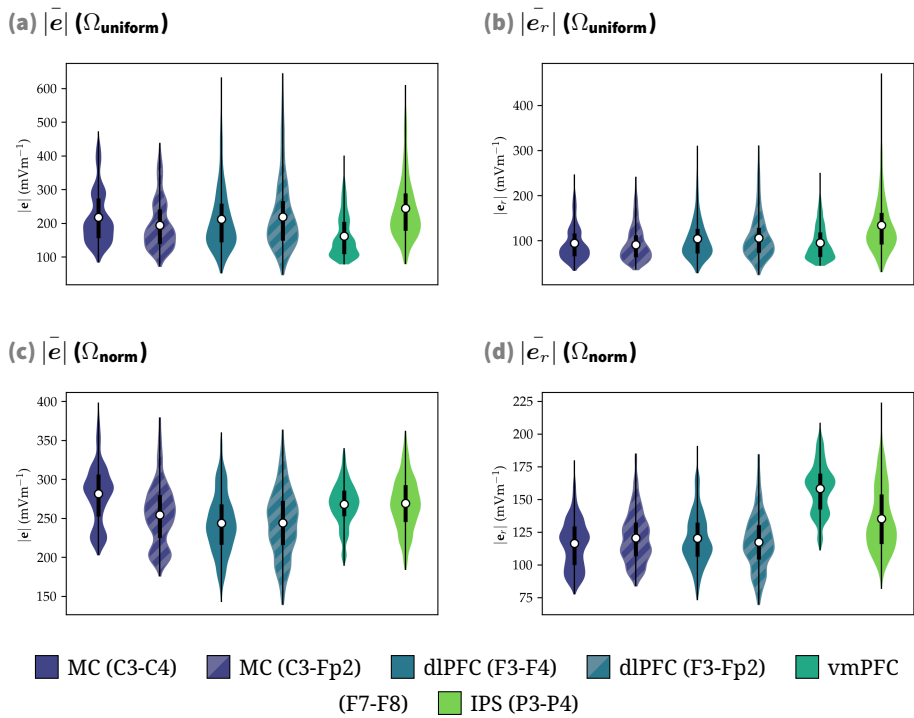MC (C3-C4)   MC (C3-Fp2)   dlPFC (F3-F4)   dlPFC (F3-Fp2)   vmPFC (F7-F8)   IPS (P3-P4)

Figure B.5 **(a/c) The average absolute magnitude of the electric field $|\bar{e}|$ and (b/d) the average absolute magnitude of the normal component of the electric field $|\bar{e_r}|$ recorded for all the simulations for the different ROIs and electrode montages.**

(a) $\left|\overline{e}\right|$

(b) $\left|\overline{e_r}\right|$
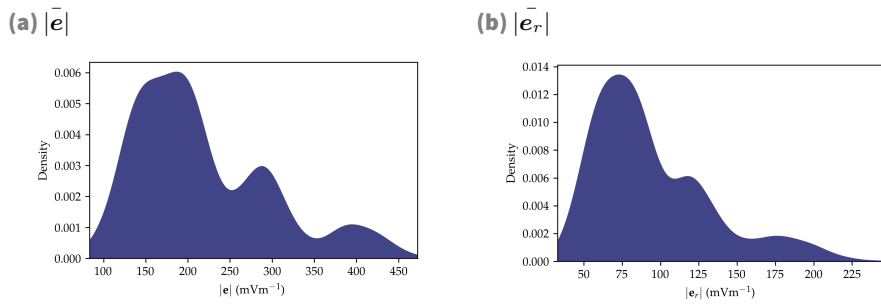
Figure B.6 The average absolute value of (a)the magnitude of the electric field and (b) its radial component for the C3-C4 electrode montage targeting the motor cortex.

(a) $\left|\overline{e}\right|$
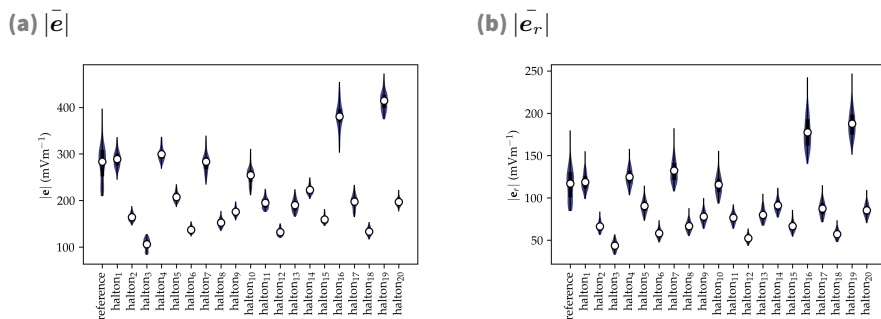
(b) $\left|\overline{e_r}\right|$
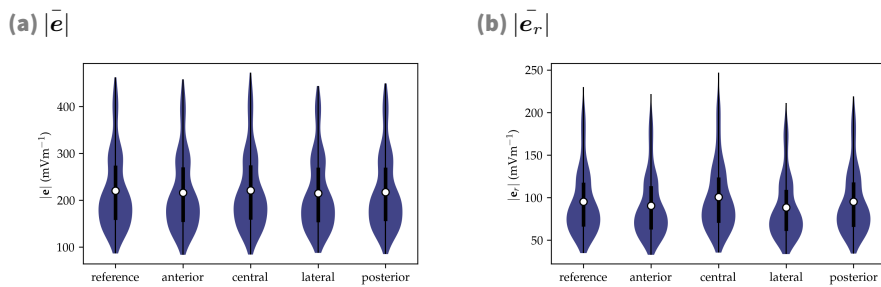
Figure B.7 The average absolute value of (a)the magnitude of the electric field and (b) its radial component for the C3-C4 electrode montage targeting the motor cortex, grouped by anode placements.

Overall, for the results obtained using Ω_{uniform}, most of the $95\,\%$ HDI intercept with the ROPE for more than $2.5\,\%$ but none of them is fully included (*i.e.*, more than $97.5\,\%$) in the ROPE. Consequently, we cannot state that an error of $1\,\text{cm}$ on the placement of the anode plays a significant role or not in the electric field induced in the ROIs.

However, by computing the boundaries of the absolute ratio between the values of β_p and the intercept, we get that such an error on the anode placement yields an absolute relative difference with the reference value up to $27.6\,\%$ for $|\bar{e}|$ and up to $27.1\,\%\,\%$ for $|\bar{e}_r|$.

When moving to Ω_{norm}, the trend is reversed and most of the $95\,\%$ HDI do not intercept with the ROPE, while the maximum absolute ratios between the values of β_p and the intercept drop to $18.5\,\%$ and $17.6\,\%$ for $|\bar{e}|$ and $|\bar{e}_r|$ respectively.

B.3.2. Tissues electrical conductivity

Similarly to the anode placement, Figure B.8 shows the results for the C3-C4 montage (See Figures S22-32c-d for the other experiments).

Following the descriptions of the pooled and hierarchic models from Equation B.6, we determined values for each β_k and $\beta_k^{(\text{com})}$ for both $|\bar{e}|$ and $|\bar{e}_r|$ (See Tables S7/11a-b for the $95\,\%$ HDI).

As opposed to the anode placement, the majority of the $95\,\%$ HDI computed on Ω_{uniform} fall completely outside the ROPE, meaning that the uncertainty on the conductivity of the tissues has a significant influence on the electric field computed in the ROI.

Moreover, by calculating the same absolute ratio between the different β_k and α, we found that some conductivity profiles could induce a difference relative to the reference of up to $112.5\,\%$ and $146.6\,\%$ for $|\bar{e}|$ and $|\bar{e}_r|$ respectively.

Once again, using Ω_{norm} inverses the trend and all the computed

(a) $|\bar{e}|$ **(b)** $|\bar{e}_r|$

Figure B.8   **The average absolute value of (a) the magnitude of the electric field and (b) its radial component for the C3-C4 electrode montage targeting the motor cortex, grouped by conductivity profiles.**

$95\,\%$ HDI intercept for more than $2.5\,\%$ with the ROPE, and some are fully embedded in, meaning that changing the conductivity profile yields easier no significant variation or a variation that cannot be classified as significant or not. The maximum ratios obtained for these results drop considerably when compared to those obtained from $\Omega_{\mathrm{uniform}}$. Indeed, the values are $13.1\,\%$ for $|\bar{e}|$ and $14.2\,\%$ for $|\bar{e}_r|$.

B.3.3. Bipolar and unipolar electrode montages

Figure B.9 provides an overview of the metrics of interest computed for the two electrode montages targeting the motor cortex.

By fitting the model from Equation B.7, we determined the difference between the results computed for the bipolar and unipolar electrode montages targeting both the motor cortex and the dorsolateral prefrontal cortex (See Table S5/9a-b for the $95\,\%$ HDI of $\beta_{\mathrm{uni}}^{(\mathrm{com})}$).

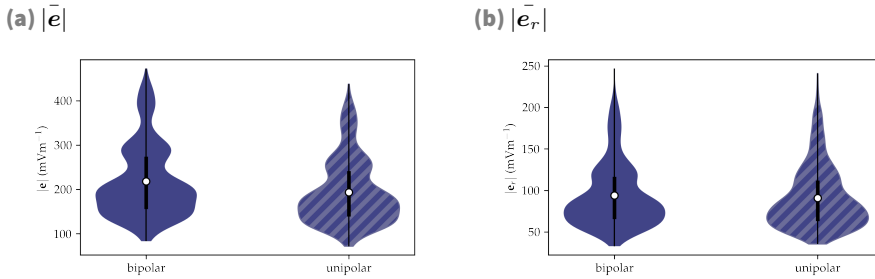**(a)** $|\bar{e}|$

(b) $|\bar{e_r}|$

Figure B.9 **The average absolute value of (a)the magnitude of the electric field and (b) its radial component for the uni- and bi-lateral electrode montages targeting the motor cortex.**

Using the unipolar montage when stimulating the MC yields an electric field of up to $13.7\,\%$ lower than with the bipolar montage for both Ω_{uniform} and Ω_{norm}. However, the effect on the normal component of the electric field is not determined when considering Ω_{uniform} but is significant for Ω_{norm}.

On the other hand, both montages yield equivalent normal components of the electric field when targeting the dlPFC.

B.3.4. Induced transmembrane potential

As described in Section B.2.9, we computed the induced transmembrane potential resulting from the electric field generated in the ROIs for the different electrode montages using analytical expressions for spherical and spheroidal cells. The calculated ranges of $\Delta u_{\text{i}}/r_1$ are shown in Table S6/10.

Across all the experiments, the spherical and spheroidal cell models respectively yield values ranging from 70.9 to $966.3\,\text{mV}\,\text{m}^{-1}$ and from 21.5 to $441.5\,\text{mV}\,\text{m}^{-1}$ when considering Ω_{uniform} and from 208.9 to $597.7\,\text{mV}\,\text{m}^{-1}$ and 62.3 to $209.8\,\text{mV}\,\text{m}^{-1}$ when using Ω_{norm}.

B.4. Discussion

The results of the models assessing the effect of different conductivity profiles in Ω_{uniform} are concerning. As for the anode placement, the F3-Fp2 electrode montage is the most influenced, with a difference of up to 112.5 % on $|\bar{e}|$. Still, it is interesting to note that the direction of the electric field varies the most in the IPS when using the P3-P4 electrode montage. Indeed, the maximum relative difference can be up to 146.6 % on $|\bar{e}_r|$.

Still, for all the experiments, moving from the worst case scenario, where Ω_{uniform} is considered, to more educated priors on the conductivity of the tissues, when Ω_{norm} is used, yields a considerable drop in the variability of the computed metrics, which end up lower than 15 %. This also affects the other Bayesian linear models. Indeed, when the uncertainty lying in the conductivity is reduced, the influence of the other factors grow.

On the other hand, the results we obtained regarding the error on the anode placement are in line with the ones published by Ramaraju et al. [2018]. Indeed, we find that the F3-Fp2 electrode montage is more sensitive to the anode placement than the others. However, the 27.6 % change in the mean absolute electric field in the left dlPFC is comparable with the 38 % they measured in the left frontal lobe. When improving the priors on the conductivity of the tissues, the error on the anode placement becomes significant in most of the cases, but the maximum error decreases to around 18 %.

While such a difference is non-negligible, it results from a displacement of 1 cm of the anode. Considering the work of Rich and Gillick [2019] which showed that the inter- and intra-rater error on the electrode placement is lower than 1 cm, the shift in the anode position we studied can be regarded as an upper bound to the plausible experimental deviation. As a result, the actual variation

of the electric field induced in the ROI due to a misplaced electrode is expected to be smaller than what we calculated here.

These considerable variations obtained with Ω_{uniform} lead us to question the information we can extract from modelling tDCS. Until one cannot feed the models with better priors about the electrical conductivity of the biological tissues, the randomness of the outputs makes it almost impossible to gain insights and draw conclusions about the electric effect of the stimulation. Using Ω_{norm} resulted in a significant improvement of the outcome, but, even thought the electric conductivities of a random subject are more likely to remain closer to the reported mean, nothing prevents them to drift toward the extrema.

Moreover, the conventional way of modelling tDCS, which involves setting almost arbitrary values to the electrical conductivity of the tissues based on the literature, identical for each subject, appears to be an inappropriate assumption.

Techniques such as magnetic resonance electric impedance tomography (MREIT) [Woo and Seo, 2008] and conductivity tensor imaging (CTI) [Marino et al., 2021] could provide a better description of the electric properties of the tissues of each subject.

Finally, tDCS is expected to generate an induced transmembrane potential of around 0.5 mV in the neurons of the target ROI [Radman et al., 2009; Opitz et al., 2016]. The values we obtain analytically, considering $r_1 = 1$ mm, are at most of the same order of magnitude but can be smaller by up to a factor of 20.

Once again, this value relies heavily on the conductivity profile of the models. Still, computing ITP values of 0.02 mV, as compared to a resting potential of -70 mV and a reference action potential threshold of -55 mV, highlights the questionable efficiency of tDCS as a neuromodulation technique. This concern has already been raised by other papers before [Horvath et al., 2015].

Still, it is important to mention that, since the present study only focused on simulations, we cannot draw conclusions on the functional long-lasting effect of the different experiments.

B.5. Conclusion

In the present work, we studied the influence of an error of placement of the anode and of the unknown conductivity profile on the computed electric field resulting from 6 different tDCS experiment targeting 4 ROIs on 20 subjects using a simulation tool. A total of 12600 simulations were performed.

The models used in this paper show that anode displacements of reasonable size yield a negligible to moderate effect on the electric field induced in the ROI. They also highlight that the uncertainty regarding the electrical conductivity of the tissues make it practically impossible to assess the electrical effect of the stimulation in a specific ROI and that using fixed standard values could potentially yield highly biased results. The comparison between Ω_{uniform} and Ω_{norm} clearly shows that using more informative priors reduces the variability of the output.

Improving the conductivity acquisition methods could lead to a better understanding of the factors that underly the variability of the effects of tDCS experiments. Until no new method is proposed to measure tissues electric conductivity on a subject basis, using uncertainty quantification and sensitivity analysis with *Shamo* or other similar tools could allow for more educated conclusions.

We also computed the induced transmembrane potential induced by the stimulation for different simple cell models. The overall size of the computed ITP is concerning.

While we did not perform functional experiments in parallel to the modelling work, the overall results presented here lead us to call for caution when designing, modelling and analysing a tDCS experiment.

B.6. Acknowledgements

Paper 2

C.
Shamo tDCS

This appendix contains all the additional results, figures, and tables from the application of Shamo to tDCS from Chapter 6 and Appendix B.

C.1. Simulation results

C.1.1. MC (C3-C4)
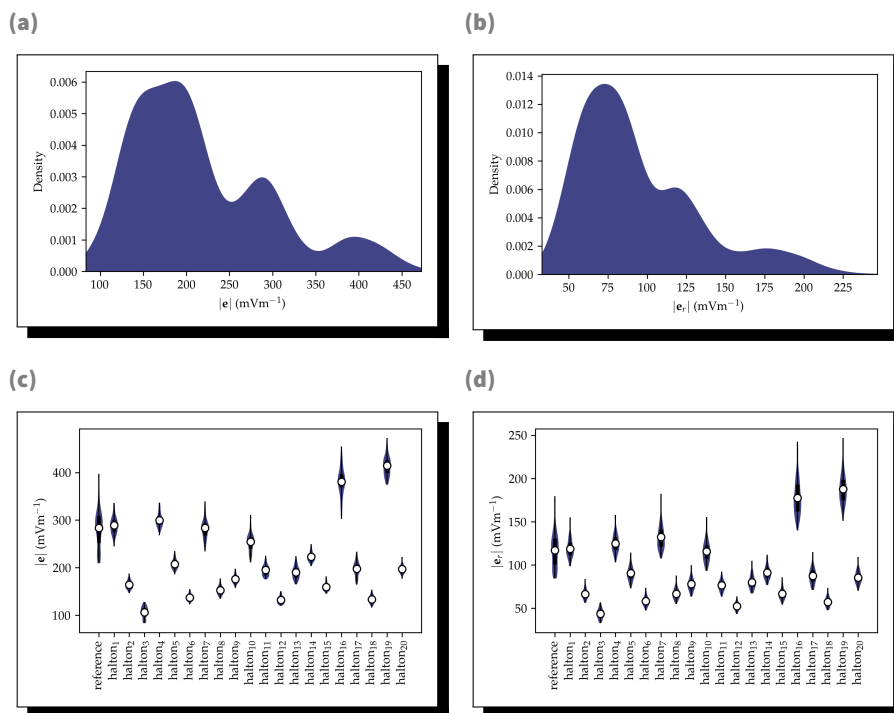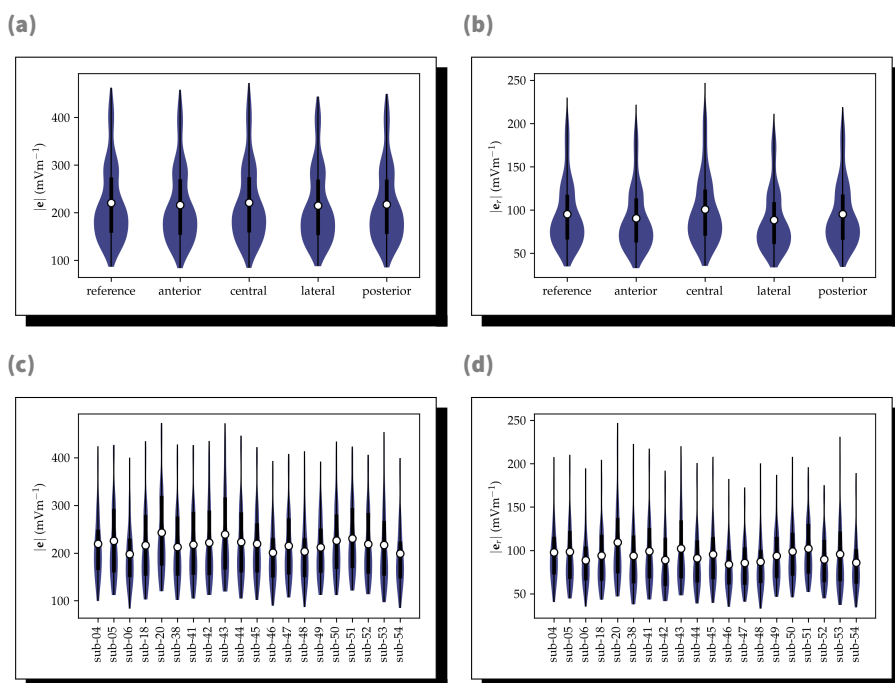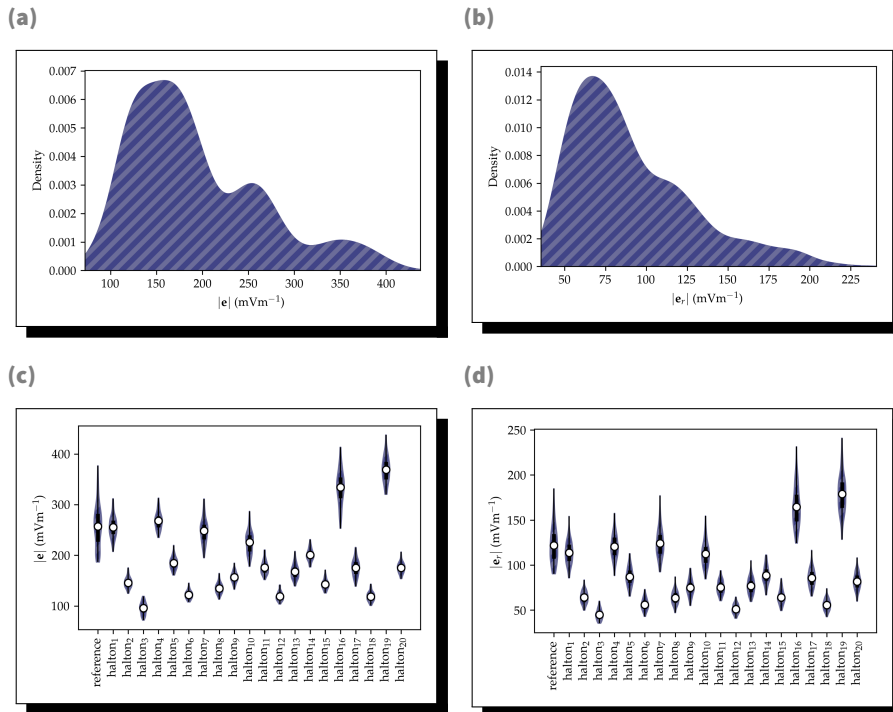
(a)

(b)

(c)

(d)

Figure C.1 **The computed values of the absolute mean magnitude of the electric field (left) and of its radial component (right) (a-b) overall and grouped by (c-d) conductivity profiles for all the simulations of the C3-C4 electrode montage targeting the MC.**
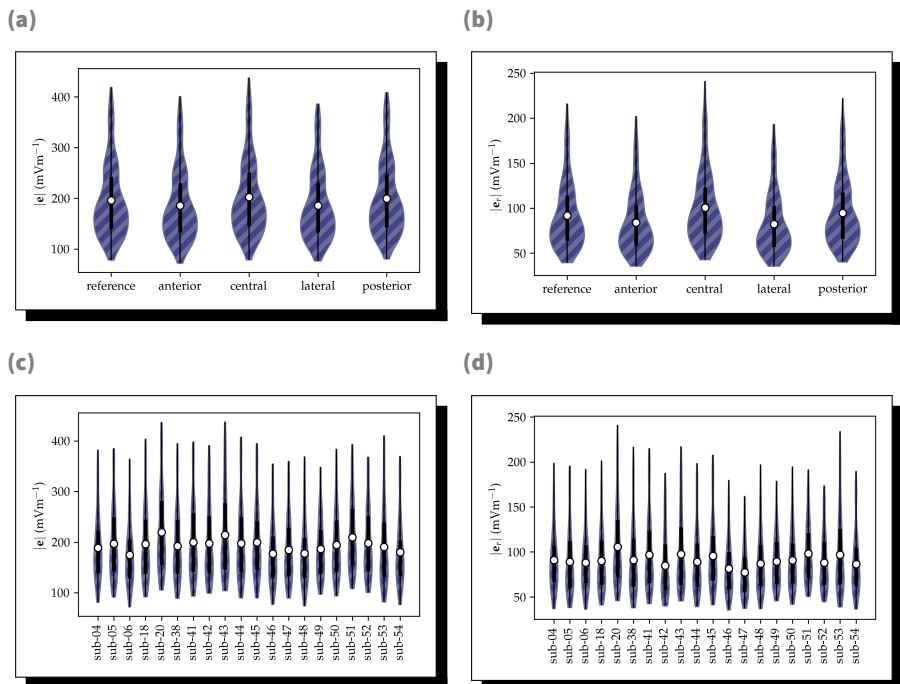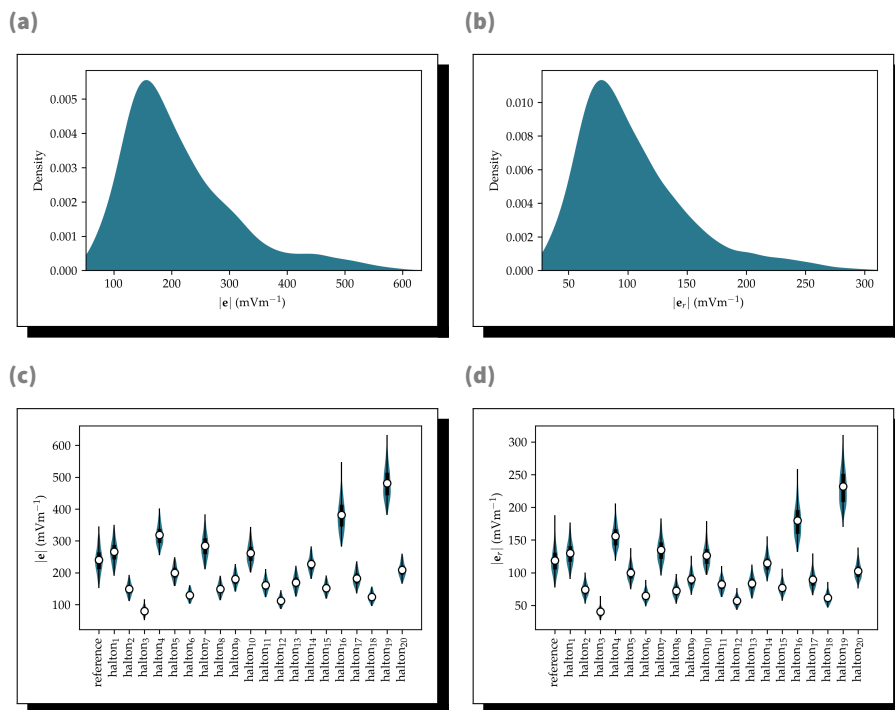
(a)

(b)

(c)

(d)

Figure C.2   **The computed values of the absolute mean magnitude of the electric field (left) and of its radial component (right) grouped by (a-b) anode placement and (c-d) subject for all the simulations of the C3-C4 electrode montage targeting the MC.**

C.1.2. MC (C3-Fp2)

(a)

(b)

(c)

(d)

Figure C.3 **The computed values of the absolute mean magnitude of the electric field (left) and of its radial component (right) (a-b) overall and grouped by (c-d) conductivity profiles for all the simulations of the C3-Fp2 electrode montage targeting the MC.**
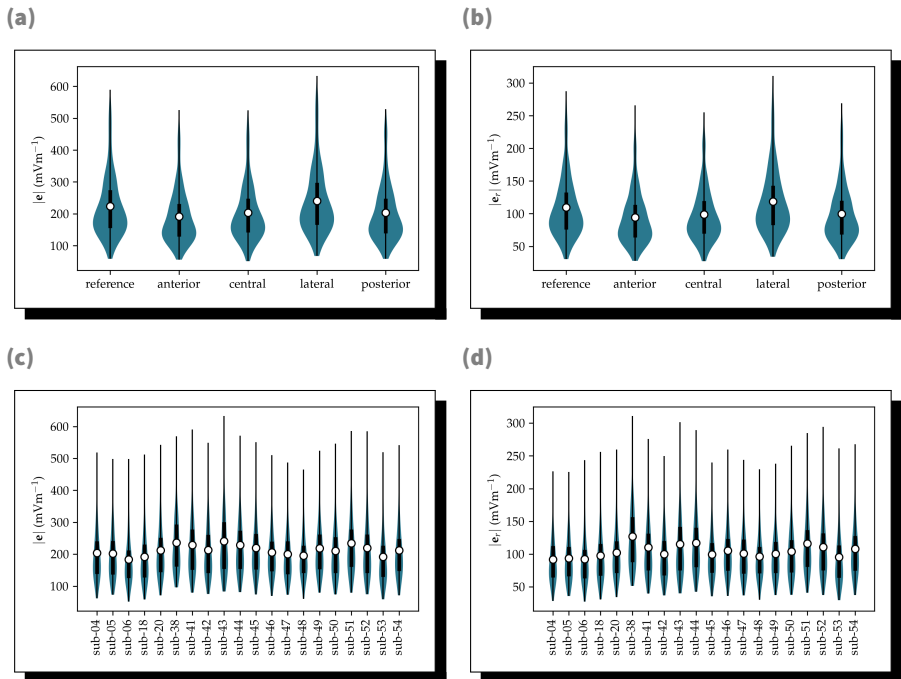
(a)

(b)

(c)

(d)

Figure C.4 **The computed values of the absolute mean magnitude of the electric field (left) and of its radial component (right) grouped by (a-b) anode placement and (c-d) subject for all the simulations of the C3-Fp2 electrode montage targeting the MC.**
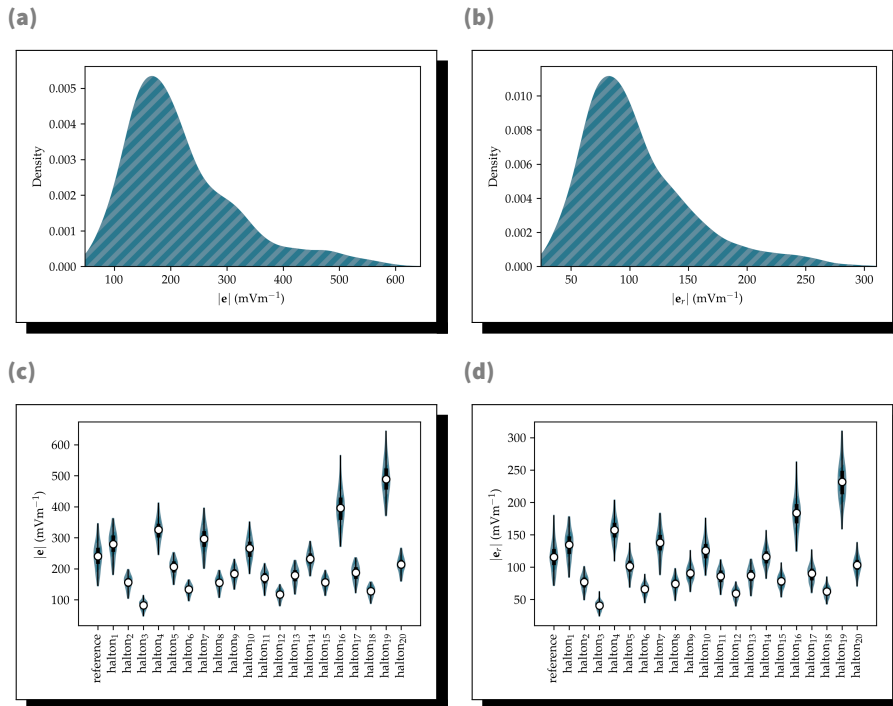
C.1.3. dlPFC (F3-F4)

(a)

(b)

(c)

(d)

Figure C.5   The computed values of the absolute mean magnitude of the electric field (left) and of its radial component (right) (a-b) overall and grouped by (c-d) conductivity profiles for all the simulations of the F3-F4 electrode montage targeting the dlPFC.
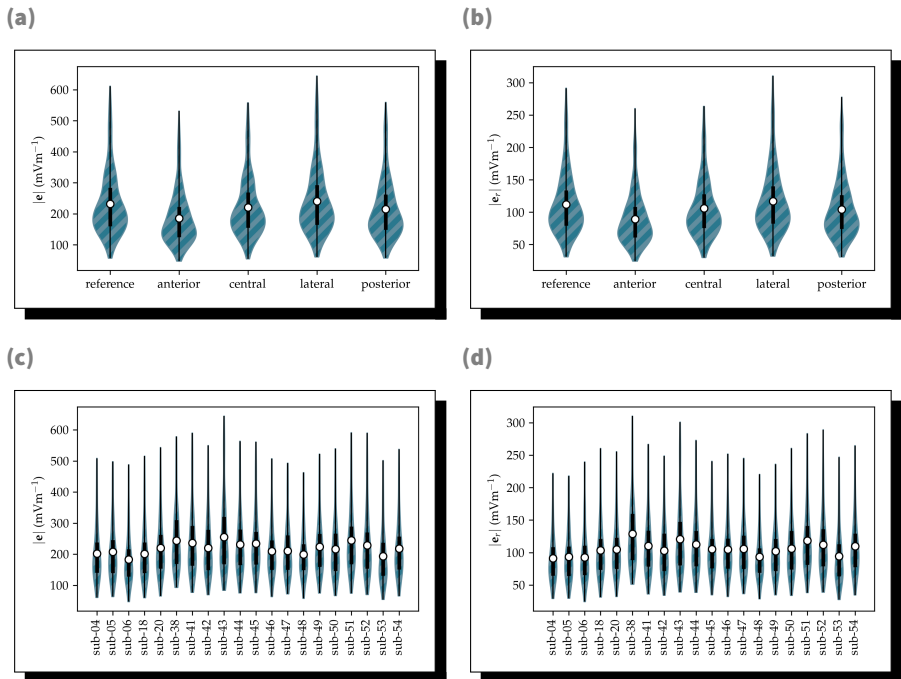
(a)

(b)

(c)

(d)

Figure C.6 **The computed values of the absolute mean magnitude of the electric field (left) and of its radial component (right) grouped by (a-b) anode placement and (c-d) subject for all the simulations of the F3-F4 electrode montage targeting the dlPFC.**

C.1.4. dlPFC (F3-Fp2)

(a)

(b)

(c)

(d)

Figure C.7 **The computed values of the absolute mean magnitude of the electric field (left) and of its radial component (right) (a-b) overall and grouped by (c-d) conductivity profiles for all the simulations of the F3-Fp2 electrode montage targeting the dlPFC.**

(a)

(b)

(c)

(d)

Figure C.8 **The computed values of the absolute mean magnitude of the electric field (left) and of its radial component (right) grouped by (a-b) anode placement and (c-d) subject for all the simulations of the F3-Fp2 electrode montage targeting the dlPFC.**
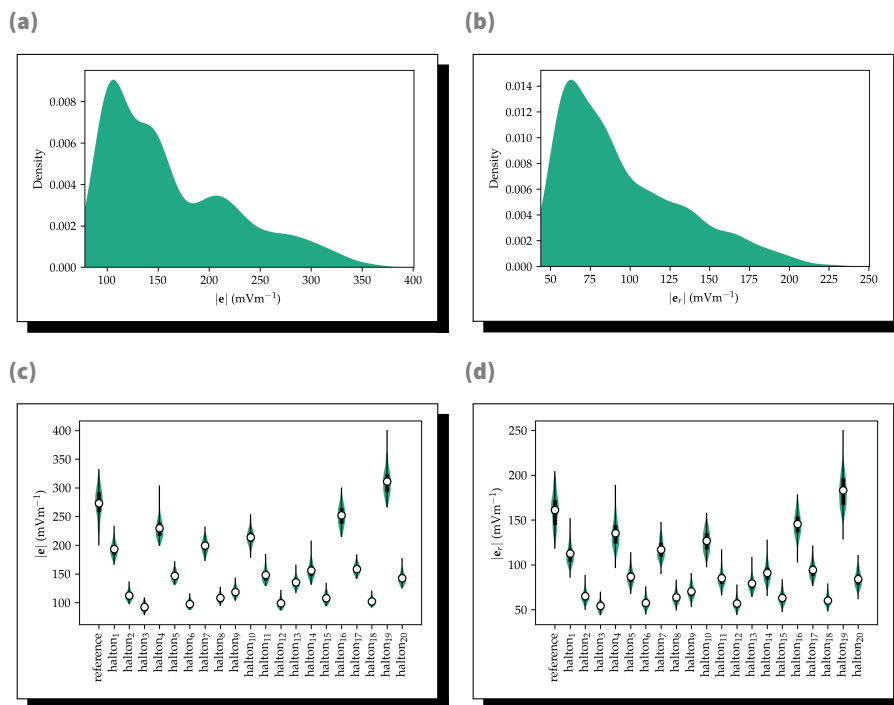
C.1.5. vmPFC (F7-F8)

(a)

(b)

(c)

(d)

Figure C.9 **The computed values of the absolute mean magnitude of the electric field (left) and of its radial component (right) (a-b) overall and grouped by (c-d) conductivity profiles for all the simulations of the F7-F8 electrode montage targeting the vmPFC.**
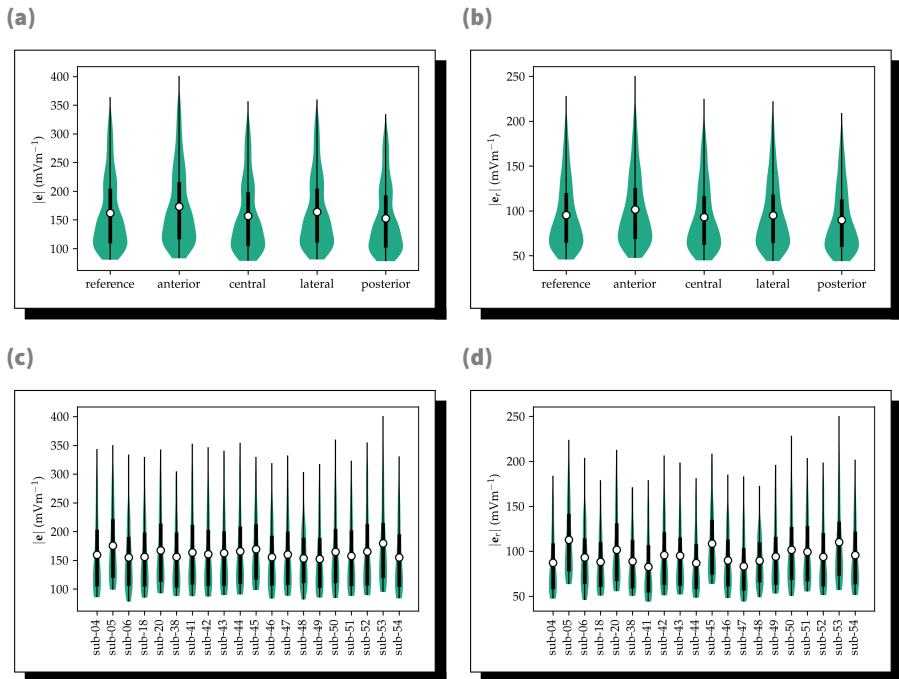
(a)

(b)

(c)

(d)

Figure C.10   **The computed values of the absolute mean magnitude of the electric field (left) and of its radial component (right) grouped by (a-b) anode placement and (c-d) subject for all the simulations of the F7-F8 electrode montage targeting the vmPFC.**

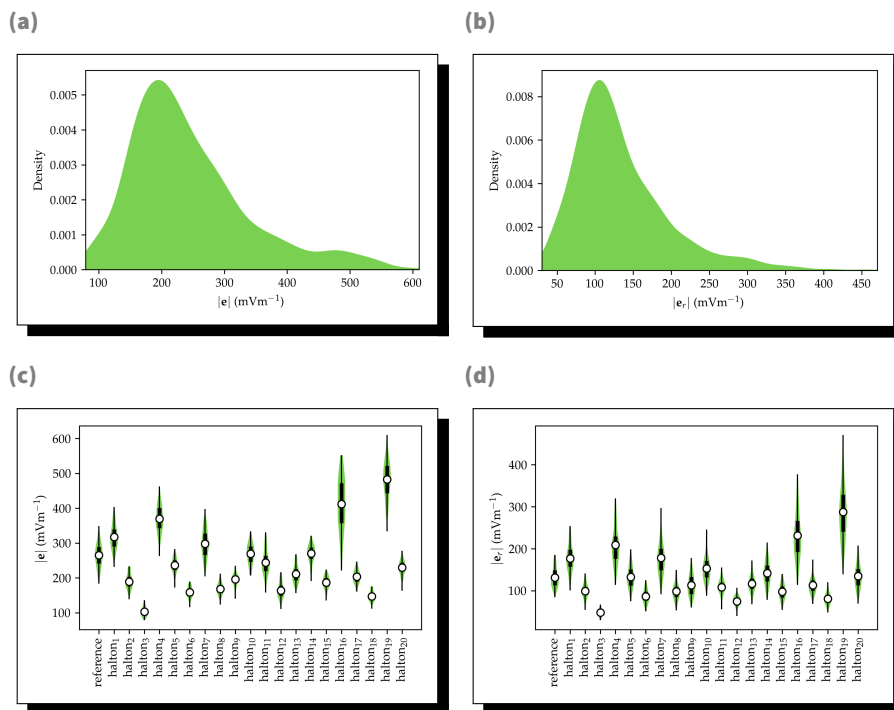# C.1.6. IPS (P3-P4)

(a)

(b)

(c)

(d)

Figure C.11   **The computed values of the absolute mean magnitude of the electric field (left) and of its radial component (right) (a-b) overall and grouped by (c-d) conductivity profiles for all the simulations of the P3-P4 electrode montage targeting the IPS.**
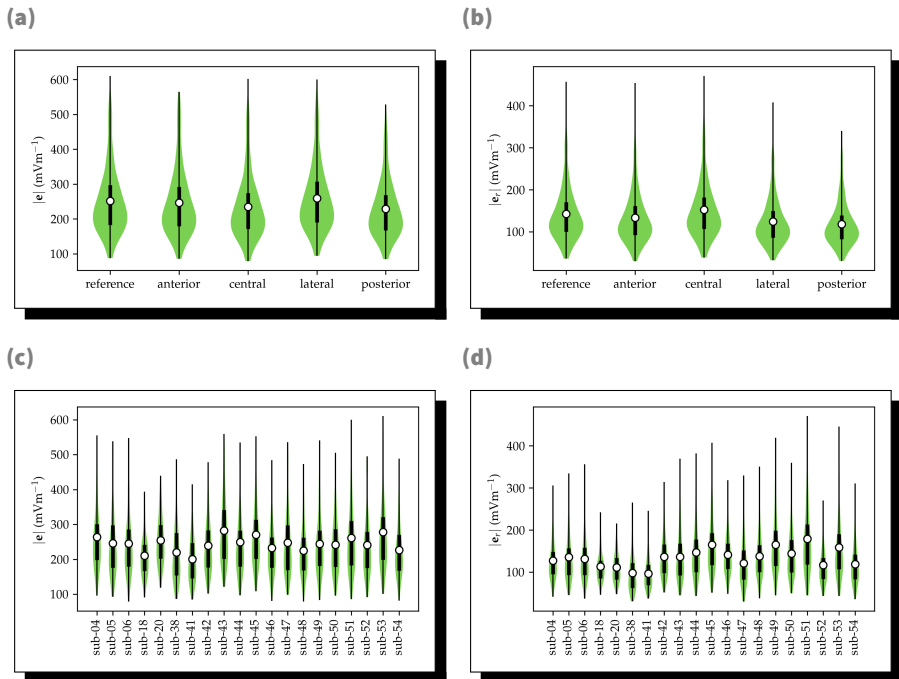
(a)

(b)

(c)

(d)

Figure C.12 **The computed values of the absolute mean magnitude of the electric field (left) and of its radial component (right) grouped by (a-b) anode placement and (c-d) subject for all the simulations of the P3-P4 electrode montage targeting the IPS.**

C.2. Models comparison

C.2.1. Bipolar and unipolar electrode montage

(a)

Coef.	■ MC	■ dlPFC
β_{uni}	$[-29.0,\ -19.2]$	$[\ \ 0.2,\ \ \ 12.5]$

(b)

Coef.	■ MC	■ dlPFC
β_{uni}	$[\ -5.7,\ \ -1.0]$	$[\ -1.7,\ \ \ 4.2]$

Table C.1 **The 95 % HDI computed for the slopes of the hierarchic linear model comparing the unipolar and bipolar experiments for (a) the absolute mean of the magnitude of the electric field and (b) its radial component.**

C.2.2. Anode placement

(a)

Coef.	MC		dlPFC		vmPFC	IPS
	C3-C4	C3-Fp2	F3-F4	F3-Fp2	F7-F8	P3-P4
$\beta_{anterior}$	[−15.5, 6.7]	[−21.0, −0.9]	[−45.3, −19.3]	[−60.6, −33.7]	[2.0, 19.4]	[−17.4, 7.9]
$\beta_{central}$	[−10.6, 11.9]	[−4.2, 15.9]	[−33.3, −7.5]	[−25.4, 2.4]	[−13.5, 3.9]	[−29.9, −3.7]
$\beta_{lateral}$	[−16.9, 6.2]	[−20.4, −0.6]	[4.1, 29.8]	[−4.5, 22.1]	[−6.7, 10.9]	[−5.5, 21.0]
$\beta_{posterior}$	[−14.4, 8.3]	[−6.6, 13.3]	[−33.7, −7.3]	[−30.4, −3.7]	[−18.3, −0.6]	[−36.1, −9.7]
	[−16.9, 11.9]	[−21.0, 15.9]	[−45.3, 29.8]	[−60.6, 22.1]	[−18.3, 19.4]	[−36.1, 21.0]

(b)

Coef.	MC		dlPFC		vmPFC	IPS
	C3-C4	C3-Fp2	F3-F4	F3-Fp2	F7-F8	P3-P4
$\beta_{anterior}$	[−10.0, 0.5]	[−12.9, −3.0]	[−21.9, −9.6]	[−28.7, −16.4]	[1.1, 11.1]	[−17.7, −0.9]
$\beta_{central}$	[0.2, 10.8]	[3.7, 13.5]	[−17.2, −4.3]	[−12.5, 0.1]	[−7.5, 2.9]	[1.4, 17.6]
$\beta_{lateral}$	[−12.0, −1.3]	[−14.8, −4.5]	[2.6, 15.0]	[−1.3, 11.0]	[−5.7, 4.6]	[−26.1, −10.2]
$\beta_{posterior}$	[−5.3, 5.4]	[−2.1, 7.9]	[−16.4, −3.8]	[−14.1, −1.4]	[−10.8, −0.3]	[−33.0, −16.2]
	[−12.0, 10.8]	[−14.8, 13.5]	[−21.9, 15.0]	[−28.7, 11.0]	[−10.8, 11.1]	[−33.0, 17.6]

Table C.2 The 95 % HDI computed for the slopes of the hierarchic linear model comparing the anode placements for (a) the absolute mean of the magnitude of the electric field and (b) its radial component.

C.2.3. Conductivity profile

Coef.	MC		dlPFC		vmPFC	IPS
	C3-C4	C3-Fp2	F3-F4	F3-Fp2	F7-F8	P3-P4
$\beta_{\mathrm{hat01,1}}$	[−8.4, 19.8]	[−5.9, 3.2]	[18.7, 31.5]	[31.6, 46.3]	[−83.0, −76.5]	[43.5, 60.5]
$\beta_{\mathrm{hat01,2}}$	[−136.6, −102.8]	[−114.2, −107.3]	[−98.2, −85.7]	[−91.5, −78.1]	[−163.7, −157.9]	[−81.0, −70.4]
$\beta_{\mathrm{hat01,3}}$	[−191.9, −163.9]	[−164.4, −157.6]	[−166.8, −154.6]	[−165.5, −152.4]	[−183.9, −177.8]	[−167.5, −156.4]
$\beta_{\mathrm{hat01,4}}$	[0.1, 31.9]	[5.7, 16.4]	[71.8, 84.3]	[78.1, 92.0]	[−48.7, −38.2]	[92.9, 117.2]
$\beta_{\mathrm{hat01,5}}$	[−94.6, −58.8]	[−76.2, −68.2]	[−46.6, −34.7]	[−41.4, −27.7]	[−129.5, −123.6]	[−34.1, −23.7]
$\beta_{\mathrm{hat01,6}}$	[−164.2, −128.0]	[−139.3, −130.1]	[−117.5, −105.3]	[−113.8, −100.6]	[−178.7, −172.7]	[−111.7, −101.3]
$\beta_{\mathrm{hat01,7}}$	[−16.0, 15.1]	[−15.5, −0.9]	[36.6, 50.8]	[47.9, 63.7]	[−77.5, −69.9]	[19.9, 46.9]
$\beta_{\mathrm{hat01,8}}$	[−147.3, −113.3]	[−125.5, −118.8]	[−97.6, −85.3]	[−92.7, −79.5]	[−168.0, −162.1]	[−101.6, −91.6]
$\beta_{\mathrm{hat01,9}}$	[−125.5, −89.6]	[−104.5, −95.6]	[−66.9, −54.7]	[−63.4, −50.3]	[−157.5, −151.4]	[−75.6, −62.8]
$\beta_{\mathrm{hat01,10}}$	[−40.5, −18.0]	[−36.8, −25.5]	[14.3, 27.9]	[17.7, 32.4]	[−63.5, −55.1]	[−4.8, 14.4]
$\beta_{\mathrm{hat01,11}}$	[−106.0, −71.6]	[−84.8, −77.3]	[−85.6, −73.3]	[−77.4, −64.0]	[−128.8, −121.3]	[−32.1, −9.7]
$\beta_{\mathrm{hat01,12}}$	[−169.6, −132.9]	[−141.9, −133.8]	[−135.2, −122.7]	[−130.3, −116.6]	[−177.4, −171.3]	[−107.7, −94.3]
$\beta_{\mathrm{hat01,13}}$	[−109.4, −76.8]	[−92.9, −85.7]	[−77.0, −64.9]	[−68.1, −54.8]	[−140.9, −134.6]	[−59.2, −48.9]
$\beta_{\mathrm{hat01,14}}$	[−80.3, −41.8]	[−61.3, −50.4]	[−19.7, −7.6]	[−15.3, −1.8]	[−120.9, −113.6]	[−3.2, 13.4]
$\beta_{\mathrm{hat01,15}}$	[−144.3, −106.0]	[−119.0, −108.9]	[−94.9, −82.6]	[−91.0, −77.5]	[−168.3, −162.1]	[−84.1, −72.5]
$\beta_{\mathrm{hat01,16}}$	[81.9, 111.6]	[65.7, 89.8]	[127.4, 153.9]	[140.4, 170.5]	[−27.6, −13.8]	[114.5, 176.8]
$\beta_{\mathrm{hat01,17}}$	[−100.3, −72.7]	[−84.9, −78.2]	[−64.4, −52.2]	[−60.5, −46.8]	[−117.4, −111.5]	[−67.2, −56.4]
$\beta_{\mathrm{hat01,18}}$	[−167.2, −133.6]	[−141.7, −134.9]	[−122.7, −110.8]	[−119.7, −106.3]	[−174.0, −168.0]	[−123.0, −112.8]
$\beta_{\mathrm{hat01,19}}$	[117.6, 144.5]	[104.7, 120.5]	[228.8, 252.7]	[235.5, 261.3]	[30.6, 45.8]	[196.7, 238.6]
$\beta_{\mathrm{hat01,20}}$	[−104.7, −70.5]	[−85.3, −77.9]	[−37.6, −25.6]	[−33.4, −20.2]	[−133.7, −127.8]	[−40.9, −29.4]
	[−191.9, 144.5]	[−164.4, 120.5]	[−166.8, 252.7]	[−165.5, 261.3]	[−183.9, 45.8]	[−167.5, 238.6]

Table C.3   The 95 % HDI computed for the slopes of the hierarchic linear model comparing the conductivity profiles for the absolute mean of the magnitude of the electric field.

Coef.	MC		dlPFC		vmPFC	IPS
	C3-C4	C3-Fp2	F3-F4	F3-Fp2	F7-F8	P3-P4
β_{halton_1}	[−0.8, 4.1]	[−11.1, −5.6]	[7.7, 14.3]	[15.4, 22.6]	[−51.0, −46.4]	[37.1, 52.7]
β_{halton_2}	[−52.7, −48.6]	[−60.4, −55.5]	[−47.9, −41.5]	[−42.0, −35.3]	[−97.8, −94.4]	[−37.6, −27.2]
β_{halton_3}	[−75.3, −71.2]	[−79.4, −74.3]	[−81.4, −75.1]	[−78.0, −71.4]	[−109.2, −104.9]	[−91.3, −76.2]
β_{halton_4}	[4.5, 10.9]	[−5.0, 2.2]	[33.9, 41.0]	[38.1, 45.3]	[−30.2, −22.0]	[65.0, 89.2]
β_{halton_5}	[−29.0, −24.0]	[−37.6, −32.5]	[−22.1, −16.0]	[−17.4, −10.8]	[−76.2, −72.7]	[−3.9, 6.8]
β_{halton_6}	[−61.0, −56.4]	[−68.3, −63.3]	[−57.1, −50.8]	[−52.9, −46.0]	[−105.7, −102.0]	[−50.3, −39.9]
β_{halton_7}	[10.4, 20.7]	[−3.0, 7.4]	[12.5, 19.7]	[18.6, 26.3]	[−46.8, −42.0]	[35.1, 58.2]
β_{halton_8}	[−52.4, −48.4]	[−60.7, −55.7]	[−49.5, −43.2]	[−44.8, −38.1]	[−99.4, −95.9]	[−38.2, −27.9]
β_{halton_9}	[−41.7, −36.7]	[−49.7, −44.7]	[−32.2, −26.1]	[−28.7, −21.9]	[−92.8, −89.2]	[−24.1, −12.9]
$\beta_{halton_{10}}$	[−5.2, 2.6]	[−13.8, −5.6]	[4.2, 11.0]	[6.5, 13.7]	[−37.4, −31.8]	[13.5, 29.9]
$\beta_{halton_{11}}$	[−42.7, −38.2]	[−49.4, −44.4]	[−39.9, −33.8]	[−33.1, −26.4]	[−78.5, −73.9]	[−32.3, −14.3]
$\beta_{halton_{12}}$	[−66.9, −62.5]	[−73.2, −68.3]	[−65.2, −58.7]	[−59.7, −53.0]	[−106.3, −102.4]	[−63.9, −49.6]
$\beta_{halton_{13}}$	[−39.1, −35.0]	[−47.6, −42.6]	[−38.2, −31.9]	[−31.9, −25.3]	[−83.9, −80.1]	[−20.0, −9.6]
$\beta_{halton_{14}}$	[−28.7, −22.7]	[−36.2, −30.6]	[−7.4, −1.1]	[−2.9, 3.7]	[−72.6, −68.0]	[4.5, 17.1]
$\beta_{halton_{15}}$	[−53.1, −47.6]	[−60.3, −55.1]	[−45.2, −39.0]	[−40.5, −34.0]	[−100.0, −96.1]	[−39.1, −29.0]
$\beta_{halton_{16}}$	[52.2, 68.3]	[34.3, 50.9]	[54.3, 67.6]	[61.2, 75.3]	[−19.9, −12.0]	[78.2, 119.7]
$\beta_{halton_{17}}$	[−31.6, −27.5]	[−38.7, −33.7]	[−32.2, −26.1]	[−28.9, −22.3]	[−68.7, −65.2]	[−23.4, −12.9]
$\beta_{halton_{18}}$	[−61.6, −57.7]	[−68.7, −63.8]	[−60.6, −54.3]	[−56.5, −49.8]	[−102.6, −99.1]	[−55.4, −45.1]
$\beta_{halton_{19}}$	[64.9, 76.8]	[50.4, 63.6]	[105.7, 120.5]	[108.8, 123.4]	[15.7, 28.0]	[133.5, 180.1]
$\beta_{halton_{20}}$	[−33.8, −29.4]	[−42.5, −37.4]	[−19.4, −13.2]	[−15.6, −9.0]	[−79.0, −75.4]	[−3.1, 9.1]
	[−75.3, 76.8]	[−79.4, 63.6]	[−81.4, 120.5]	[−78.0, 123.4]	[−109.2, 28.0]	[−91.3, 180.1]

Table C.4 The 95 % HDI computed for the slopes of the hierarchic linear model comparing the conductivity profiles for the absolute mean of the magnitude of the radial component of the electric field.

C.2.4. Induced transmembrane potential

Cell type	MC		dlPFC		vmPFC	IPS
	C3-C4	C3-Fp2	F3-F4	F3-Fp2	F7-F8	P3-P4
Sphere	[124.9,708.9]	[108.0,656.0]	[76.9,948.8]	[70.9,966.3]	[116.9,601.4]	[117.9,915.3]
Spheroid (γ = 10/8)	[44.0,257.9]	[39.0,241.4]	[27.8,337.2]	[25.3,342.6]	[43.0,228.4]	[44.1,369.5]
Spheroid (γ = 10/5)	[33.1,219.1]	[32.6,210.7]	[24.1,274.7]	[21.5,276.4]	[39.2,213.2]	[32.8,390.0]
Spheroid (γ = 10/2)	[28.9,223.9]	[31.7,219.4]	[24.9,283.1]	[21.9,282.4]	[39.2,230.5]	[26.3,441.5]

Table C.5   The ranges of computed induced transmembrane potential ratios for the spherical and spheroidal models.

List of Figures

List of Tables

Bibliography

S. M. Agarwal, V. Shivakumar, A. Bose, A. Subramaniam, H. Nawani, H. Chhabra, S. V. Kalmady, J. C. Narayanaswamy, and G. Venkatasubramanian. Transcranial Direct Current Stimulation in Schizophrenia. *Clinical Psychopharmacology and Neuroscience*, 11(3):118–125, Dec. 2013. ISSN 1738-1088. doi: 10.9758/cpn.2013.11.3.118. URL https://www.ncbi.nlm.nih.gov/pmc/articles/PMC3897759/.

Z. Akalin Acar and S. Makeig. Effects of Forward Model Errors on EEG Source Localization. *Brain Topography*, 26(3):378–396, July 2013. ISSN 0896-0267, 1573-6792. doi: 10.1007/s10548-012-0274-6. URL http://link.springer.com/10.1007/s10548-012-0274-6.

Z. Akalin Acar, C. E. Acar, and S. Makeig. Simultaneous head tissue conductivity and EEG source location estimation. *NeuroImage*, 124: 168–180, Jan. 2016. ISSN 10959572. doi: 10.1016/j.neuroimage.2015.08.032. URL https://www.sciencedirect.com/science/article/pii/S1053811915007442?via%3Dihub.

M. Akhtari, H. Bryant, A. Mamelak, E. Flynn, L. Heller, J. Shih, M. Mandelkem, A. Matlachov, D. Ranken, E. Best, M. DiMauro, R. Lee, and W. Sutherling. Conductivities of Three-Layer Live Human Skull. *Brain Topography*, 14(3):151–167, Mar. 2002. ISSN 1573-6792. doi: 10.1023/A:1014590923185. URL https://doi.org/10.1023/A:1014590923185.

F. A. Al-Nuaimi, R. J. Al-Nuaimi, S. S. Al-Dhaheri, S. Ouhbi, and A. N. Belkacem. Mind Drone Chasing Using EEG-based Brain Computer Interface. In *2020 16th International Conference on Intelligent Environments (IE)*, pages 74–79, July 2020. doi: 10.1109/IE49459.2020.9154926. ISSN: 2472-7571.

Z. T. Al-qaysi, B. B. Zaidan, A. A. Zaidan, and M. S. Suzani. A review of disability EEG based wheelchair control system: Coherent taxonomy, open challenges and recommendations. *Computer Methods and Programs in Biomedicine*, 164:221–237, Oct. 2018. ISSN 0169-2607. doi: 10.1016/j.cmpb.2018.06.012. URL `https://www.sciencedirect.com/science/article/pii/S0169260718304620`.

A. Albizu, R. Fang, A. Indahlastari, A. O'Shea, S. E. Stolte, K. B. See, E. M. Boutzoukas, J. N. Kraft, N. R. Nissim, and A. J. Woods. Machine learning and individual variability in electric field characteristics predict tDCS treatment response. *Brain Stimulation*, 13(6):1753–1764, Nov. 2020. ISSN 1935-861X. doi: 10.1016/j.brs.2020.10.001. URL `https://www.sciencedirect.com/science/article/pii/S1935861X20302680`.

M. Ando, S. Nobukawa, M. Kikuchi, and T. Takahashi. Identification of Electroencephalogram Signals in Alzheimer's Disease by Multifractal and Multiscale Entropy Analysis. *Frontiers in Neuroscience*, 15, 2021. ISSN 1662-453X. URL `https://www.frontiersin.org/article/10.3389/fnins.2021.667614`.

P. Antonenko, F. Paas, R. Grabner, and T. van Gog. Using Electroencephalography to Measure Cognitive Load. *Educational Psychology Review*, 22(4):425–438, Dec. 2010. ISSN 1573-336X. doi: 10.1007/s10648-010-9130-y. URL `https://doi.org/10.1007/s10648-010-9130-y`.

J. Ashburner. *Computational Neuroanatomy*. PhD thesis, University College London, 2000. URL `/spm/doc/theses/john/`.

J. Ashburner and K. J. Friston. Unified segmentation. *NeuroImage*, 26(3):839–851, July 2005. ISSN 10538119. doi: 10.1016/j.neuroimage.2005.02.018. URL `https://linkinghub.elsevier.com/retrieve/pii/S1053811905001102`.

M. Attene. A lightweight approach to repairing digitized polygon meshes. *The Visual Computer*, 26(11):1393–1406, Nov. 2010. ISSN 1432-2315. doi: 10.1007/s00371-010-0416-3. URL `https://doi.org/10.1007/s00371-010-0416-3`.

B. Aubert-Broche, A. C. Evans, and L. Collins. A new improved version of the realistic digital brain phantom. *NeuroImage*, 32(1):138–145, Aug. 2006a. ISSN 1053-8119. doi: 10.1016/j.neuroimage.2006.03.052.

B. Aubert-Broche, M. Griffin, G. B. Pike, A. C. Evans, and D. L. Collins. Twenty new digital brain phantoms for creation of validation image data bases. *IEEE transactions on medical imaging*, 25(11):1410–1416, Nov. 2006b. ISSN 0278-0062. doi: 10.1109/TMI.2006.883453.

G. Auzias, O. Coulon, and A. Brovelli. MarsAtlas: A cortical parcellation atlas for functional mapping. *Human Brain Mapping*, 37(4): 1573–1592, 2016. ISSN 1097-0193. doi: 10.1002/hbm.23121. URL https://onlinelibrary.wiley.com/doi/abs/10.1002/hbm.23121. _eprint: https://onlinelibrary.wiley.com/doi/pdf/10.1002/hbm.23121.

N. B. Bangera, D. L. Schomer, N. Dehghani, I. Ulbert, S. Cash, S. Papavasiliou, S. R. Eisenberg, A. M. Dale, and E. Halgren. Experimental validation of the influence of white matter anisotropy on the intracranial EEG forward solution. *Journal of Computational Neuroscience*, 29(3):371–387, Dec. 2010. ISSN 0929-5313, 1573-6873. doi: 10.1007/s10827-009-0205-z. URL http://link.springer.com/10.1007/s10827-009-0205-z.

P. D. E. Baniqued, E. C. Stanyer, M. Awais, A. Alazmani, A. E. Jackson, M. A. Mon-Williams, F. Mushtaq, and R. J. Holt. Brain–computer interface robotics for hand rehabilitation after stroke: a systematic review. *Journal of NeuroEngineering and Rehabilitation*, 18(1):15, Dec. 2021. ISSN 1743-0003. doi: 10.1186/s12984-021-00820-8. URL https://jneuroengrehab.biomedcentral.com/articles/10.1186/s12984-021-00820-8.

M. R. Bashar, Y. Li, and P. Wen. Uncertainty and sensitivity analysis for anisotropic inhomogeneous head tissue conductivity in human head modelling. *Australasian Physical & Engineering Sciences in Medicine*, 33(2):145–152, June 2010. ISSN 0158-9938, 1879-5447. doi: 10.1007/s13246-010-0015-7. URL http://link.springer.com/10.1007/s13246-010-0015-7.

M. Bauer, M. van der Wilk, and C. E. Rasmussen. Understanding Probabilistic Sparse Gaussian Process Approximations. In D. Lee, M. Sugiyama, U. Luxburg, I. Guyon, and R. Garnett, editors, *Advances in Neural Information Processing Systems*, volume 29. Curran Associates, Inc., 2016. URL https://proceedings.neurips.cc/paper/2016/file/7250eb93b3c18cc9daa29cf58af7a004-Paper.pdf.

S. Baumann, D. Wozny, S. Kelly, and F. Meno. The electrical conductivity of human cerebrospinal fluid at body temperature. *IEEE Transactions on Biomedical Engineering*, 44(3):220–223, Mar. 1997. ISSN 00189294. doi: 10.1109/10.554770. URL http://ieeexplore.ieee.org/document/554770/.

C. Berthomier, V. Muto, C. Schmidt, G. Vandewalle, M. Jaspar, J. Devillers, G. Gaggioni, S. L. Chellappa, C. Meyer, C. Phillips, E. Salmon, P. Berthomier, J. Prado, O. Benoit, R. Bouet, M. Brandewinder, J. Mattout, and P. Maquet. Exploring scoring methods for research studies: Accuracy and variability of visual and automated sleep scoring. *Journal of Sleep Research*, 2020. doi: 10.1111/jsr.12994. URL https://orbi.uliege.be/handle/2268/244967.

M. Bikson, A. Rahman, and A. Datta. Computational Models of Transcranial Direct Current Stimulation. *Clinical EEG and Neuroscience*, 43(3):176–183, July 2012. ISSN 1550-0594. doi: 10.1177/1550059412445138. URL https://doi.org/10.1177/1550059412445138. Publisher: SAGE Publications Inc.

P. S. Boggio, A. Nunes, S. P. Rigonatti, M. A. Nitsche, A. Pascual-Leone, and F. Fregni. Repeated sessions of noninvasive brain DC stimulation is associated with motor function improvement in stroke patients. *Restorative Neurology and Neuroscience*, 25(2):123–129, 2007. ISSN 0922-6028.

P. S. Boggio, S. P. Rigonatti, R. B. Ribeiro, M. L. Myczkowski, M. A. Nitsche, A. Pascual-Leone, and F. Fregni. A randomized, double-blind clinical trial on the efficacy of cortical direct current stimulation for the treatment of major depression. *The International Journal of Neuropsychopharmacology*, 11(2):249–254, Mar. 2008. ISSN 1461-1457. doi: 10.1017/S1461145707007833.

J. J. Borckardt, M. Bikson, H. Frohman, S. T. Reeves, A. Datta, V. Bansal, A. Madan, K. Barth, and M. S. George. A pilot study of the tolerability and effects of high-definition transcranial direct current stimulation (HD-tDCS) on pain perception. *The Journal of Pain*, 13(2):112–120, Feb. 2012. ISSN 1528-8447. doi: 10.1016/j.jpain.2011.07.001.

M. Brett, C. J. Markiewicz, M. Hanke, M.-A. Côté, B. Cipollini, P. McCarthy, D. Jarecka, C. P. Cheng, Y. O. Halchenko, M. Cottaar, E. Larson, S. Ghosh, D. Wassermann, S. Gerhard, G. R. Lee, H.-T. Wang, E. Kastman, J. Kaczmarzyk, R. Guidotti, O. Duek, J. Daniel, A. Rokem, C. Madison, B. Moloney, F. C. Morency, M. Goncalves, R. Markello, C. Riddell, C. Burns, J. Millman, A. Gramfort, J. Leppäkangas, A. Sólon, J. J. van den Bosch, R. D. Vincent, H. Braun, K. Subramaniam, K. J. Gorgolewski, P. R. Raamana, J. Klug, B. N. Nichols, E. M. Baker, S. Hayashi, B. Pinsard, C. Haselgrove, M. Hymers, O. Esteban, S. Koudoro, F. Pérez-García, N. N. Oosterhof, B. Amirbekian, I. Nimmo-Smith, L. Nguyen, S. Reddigari, S. St-Jean, E. Panfilov, E. Garyfallidis, G. Varoquaux, J. H. Legarreta, K. S. Hahn, O. P. Hinds, B. Fauber, J.-B. Poline, J. Stutters, K. Jordan, M. Cieslak, M. E. Moreno, V. Haenel, Y. Schwartz, Z. Baratz, B. C. Darwin, B. Thirion, C. Gauthier, D. Papadopoulos Orfanos, I. Solovey, I. Gonzalez, J. Palasubramaniam, J. Lecher, K. Leinweber, K. Raktivan, M. Calábková, P. Fischer, P. Gervais, S. Gadde, T. Ballinger, T. Roos, V. R. Reddam, and freec84. nipy/nibabel: 3.2.1, Nov. 2020. URL https://doi.org/10.5281/zenodo.4295521.

J. Bronzino, editor. *The Biomedical Engineering Handbook, Second Edition. 2 Volume Set*, volume 19995277 of *Electrical Engineering Handbook*. CRC Press, Dec. 1999. ISBN 978-0-8493-8594-0 978-1-4200-4951-0. doi: 10.1201/9781420049510. URL http://www.crcnetbase.com/doi/book/10.1201/9781420049510.

A. R. Brunoni, J. Amadera, B. Berbel, M. S. Volz, B. G. Rizzerio, and F. Fregni. A systematic review on reporting and assessment of adverse effects associated with transcranial direct current stimulation. *The International Journal of Neuropsychopharmacology*, 14(8):1133–1145, Sept. 2011. ISSN 1469-5111. doi: 10.1017/S1461145710001690.

D. M. Buchanan, T. Bogdanowicz, N. Khanna, G. Lockman-Dufour, P. Robaey, and A. D'Angiulli. Systematic Review on the Safety and Tolerability of Transcranial Direct Current Stimulation in Children and Adolescents. *Brain Sciences*, 11(2):212, Feb. 2021. ISSN 2076-3425. doi: 10.3390/brainsci11020212. URL `https://www.mdpi.com/2076-3425/11/2/212`. Number: 2 Publisher: Multidisciplinary Digital Publishing Institute.

T. H. Bullock. Neuron Doctrine and Electrophysiology. *Science*, 129(3355): 997–1002, Apr. 1959. doi: 10.1126/science.129.3355.997. URL `https://www.science.org/doi/10.1126/science.129.3355.997`. Publisher: American Association for the Advancement of Science.

H. C. Burger and J. B. v. Milaan. Measurements of the specific Resistance of the human Body to direct Current. *Acta Medica Scandinavica*, 114(6):584–607, 1943. ISSN 0954-6820. doi: 10.1111/j.0954-6820.1943.tb11253.x. URL `https://onlinelibrary.wiley.com/doi/abs/10.1111/j.0954-6820.1943.tb11253.x`. _eprint: https://onlinelibrary.wiley.com/doi/pdf/10.1111/j.0954-6820.1943.tb11253.x.

M. Cambiaghi, S. Velikova, J. J. Gonzalez-Rosa, M. Cursi, G. Comi, and L. Leocani. Brain transcranial direct current stimulation modulates motor excitability in mice. *The European Journal of Neuroscience*, 31(4):704–709, Feb. 2010. ISSN 1460-9568. doi: 10.1111/j.1460-9568.2010.07092.x.

T. Capretto, C. Piho, R. Kumar, J. Westfall, T. Yarkoni, and O. A. Martin. Bambi: A simple interface for fitting bayesian linear models in python, 2020.

R. Cassani, M. Estarellas, R. San-Martin, F. J. Fraga, and T. H. Falk. Systematic Review on Resting-State EEG for Alzheimer's Disease Diagnosis and Progression Assessment. *Disease Markers*, 2018:5174815, 2018. ISSN 1875-8630. doi: 10.1155/2018/5174815.

M. Chauhan, A. Indahlastari, A. K. Kasinadhuni, M. Schar, T. H. Mareci, and R. J. Sadleir. Low-Frequency Conductivity Tensor Imaging of the Human Head In Vivo Using DT-MREIT: First Study. *IEEE transactions on medical imaging*, 37(4): 966–976, Apr. 2018. ISSN 1558-254X. doi: 10.1109/TMI.2017.2783348.

H. Chen and M. Z. Koubeissi. Electroencephalography in Epilepsy Evaluation. *Continuum (Minneapolis, Minn.)*, 25(2):431–453, Apr. 2019. ISSN 1538-6899. doi: 10.1212/CON.0000000000000705.

H. Chen, J. L. Loeppky, J. Sacks, and W. J. Welch. Analysis Methods for Computer Experiments: How to Assess and What Counts? *Statistical Science*, 31 (1):40–60, Feb. 2016. ISSN 0883-4237. doi: 10.1214/15-STS531. URL http://projecteuclid.org/euclid.ss/1455115913.

J. Chen, J. Qin, Q. He, and Z. Zou. A Meta-Analysis of Transcranial Direct Current Stimulation on Substance and Food Craving: What Effect Do Modulators Have? *Frontiers in Psychiatry*, 11, 2020. ISSN 1664-0640. URL https://www.frontiersin.org/article/10.3389/fpsyt.2020.00598.

J.-H. Cho, J. Vorwerk, C. H. Wolters, and T. R. Knösche. Influence of the head model on EEG and MEG source connectivity analyses. *NeuroImage*, 110:60–77, Apr. 2015. ISSN 10538119. doi: 10.1016/j.neuroimage.2015.01.043. URL https://linkinghub.elsevier.com/retrieve/pii/S1053811915000683.

D. Chylinski, F. Rudzik, D. C. 't Wallant, M. Grignard, N. Vandeleene, M. V. Egroo, L. Thiesse, S. Solbach, P. Maquet, C. Phillips, G. Vandewalle, C. Cajochen, and V. Muto. Validation of an automatic arousal detection algorithm for whole-night sleep EEG recordings. *Clocks & Sleep*, 2(3):258–272, jul 2020. doi: 10.3390/clockssleep2030020. URL https://doi.org/10.3390%2Fclockssleep2030020.

J. F. Collard and M. Hinsenkamp. Cellular processes involved in human epidermal cells exposed to extremely low frequency electric fields. *Cellular Signalling*, 27(5):889–898, May 2015. ISSN 0898-6568. doi: 10.1016/j.cellsig.2015.02.007. URL https://www.sciencedirect.com/science/article/pii/S0898656815000418.

D. Coppieters't Wallant, P. Maquet, and C. Phillips. Sleep Spindles as an Electrographic Element: Description and Automatic Detection Methods. *Neural Plasticity*, 2016, 2016a. ISSN 0792-8483. doi: 10.1155/2016/6783812. URL https://orbi.uliege.be/handle/2268/202224. Publisher: Hindawi Publishing Corporation, New York, United States - New York.

D. Coppieters't Wallant, V. Muto, G. Gaggioni, M. Jaspar, S. L. Chellappa, C. Meyer, G. Vandewalle, P. Maquet, and C. Phillips. Automatic artifacts and arousals detection in whole-night sleep EEG recordings. *Journal of Neuroscience Methods*, 258, Jan. 2016b. doi: 10.1016/j.jneumeth.2015.11.005. URL https://orbi.uliege.be/handle/2268/188955. Publisher: Elsevier Science, Amsterdam, Netherlands.

R. Cox and J. Fell. Analyzing human sleep EEG: A methodological primer with code implementation. *Sleep Medicine Reviews*, 54:101353, Dec. 2020. ISSN 1087-0792. doi: 10.1016/j.smrv.2020.101353. URL https://www.sciencedirect.com/science/article/pii/S1087079220300964.

R. W. Cox. AFNI: software for analysis and visualization of functional magnetic resonance neuroimages. *Computers and Biomedical Research, an International Journal*, 29(3):162–173, June 1996. ISSN 0010-4809. doi: 10.1006/cbmr.1996.0014.

A. M. Dale, B. Fischl, and M. I. Sereno. Cortical Surface-Based Analysis: I. Segmentation and Surface Reconstruction. *NeuroImage*, 9(2):179–194, Feb. 1999. ISSN 1053-8119. doi: 10.1006/nimg.1998.0395. URL https://www.sciencedirect.com/science/article/pii/S1053811998903950.

M. Dannhauer, B. Lanfer, C. H. Wolters, and T. R. Knösche. Modeling of the human skull in EEG source analysis. *Human Brain Mapping*, 32(9):1383–1399, Sept. 2011. ISSN 10659471. doi: 10.1002/hbm.21114. URL http://doi.wiley.com/10.1002/hbm.21114.

M. Darbas and S. Lohrengel. Review on Mathematical Modelling of Electroencephalography (EEG). *Jahresbericht der Deutschen Mathematiker-Vereinigung*, July 2018. doi: 10.1365/s13291-018-0183-z.

A. Datta, V. Bansal, J. Diaz, J. Patel, D. Reato, and M. Bikson. Gyri-precise head model of transcranial direct current stimulation: improved spatial focality using a ring electrode versus conventional rectangular pad. *Brain Stimulation*, 2 (4):201–207, 207.e1, Oct. 2009. ISSN 1876-4754. doi: 10.1016/j.brs.2009.03.005.

J. Dedoncker, A. R. Brunoni, C. Baeken, and M.-A. Vanderhasselt. A Systematic Review and Meta-Analysis of the Effects of Transcranial Direct Current Stimulation (tDCS) Over the Dorsolateral Prefrontal Cortex in Healthy and Neuropsychiatric Samples: Influence of Stimulation Parameters. *Brain Stimulation: Basic, Translational, and Clinical Research in Neuromodulation*, 9(4):501–517, July 2016. ISSN 1935-861X, 1876-4754. doi: 10.1016/j.brs.2016.04.006. URL https://www.brainstimjrnl.com/article/S1935-861X(16)30056-0/fulltext. Publisher: Elsevier.

I. Despotović, B. Goossens, and W. Philips. MRI Segmentation of the Human Brain: Challenges, Methods, and Applications. *Computational and Mathematical Methods in Medicine*, 2015, 2015. ISSN 1748-670X. doi: 10.1155/2015/450341. URL https://www.ncbi.nlm.nih.gov/pmc/articles/PMC4402572/.

C. Destrieux, B. Fischl, A. Dale, and E. Halgren. Automatic parcellation of human cortical gyri and sulci using standard anatomical nomenclature. *NeuroImage*, 53(1):1–15, Oct. 2010. ISSN 1053-8119. doi: 10.1016/j.neuroimage.2010.06.010. URL https://www.ncbi.nlm.nih.gov/pmc/articles/PMC2937159/.

J. P. Dmochowski, A. Datta, M. Bikson, Y. Su, and L. C. Parra. Optimized multi-electrode stimulation increases focality and intensity at target. *Journal of Neural Engineering*, 8(4):046011, Aug. 2011. ISSN 1741-2552. doi: 10.1088/1741-2560/8/4/046011.

C. Dondé, N. H. Neufeld, and P. A. Geoffroy. The Impact of Transcranial Direct Current Stimulation (tDCS) on Bipolar Depression, Mania, and Euthymia: a Systematic Review of Preliminary Data. *The Psychiatric Quarterly*, 89(4):855–867, Dec. 2018. ISSN 1573-6709. doi: 10.1007/s11126-018-9584-5.

R. Dumont, S. Majerus, and M. Hansenne. Transcranial Direct Current Stimulation (tDCS) over the Intraparietal Sulcus Does Not Influence Working Memory Performance. *Psychologica Belgica*, 61(1):200–211, July 2021. ISSN 2054-670X. doi: 10.5334/pb.534. URL http://www.psychologicabelgica.com/articles/10.5334/pb.534/. Number: 1 Publisher: Ubiquity Press.

D. Edwards, M. Cortes, A. Datta, P. Minhas, E. M. Wassermann, and M. Bikson. Physiological and modeling evidence for focal transcranial electrical brain stimulation in humans: a basis for high-definition tDCS. *NeuroImage*, 74:266–275, July 2013. ISSN 1095-9572. doi: 10.1016/j.neuroimage.2013.01.042.

A. J. Fagerlund, O. A. Hansen, and P. M. Aslaksen. Transcranial direct current stimulation as a treatment for patients with fibromyalgia: a randomized controlled trial. *Pain*, 156(1):62–71, Jan. 2015. ISSN 1872-6623. doi: 10.1016/j.pain.0000000000000006.

J. Feinberg and H. P. Langtangen. Chaospy: An open source tool for designing methods of uncertainty quantification. *Journal of Computational Science*, 11:46–57, Nov. 2015. ISSN 18777503. doi: 10.1016/j.jocs.2015.08.008. URL https://linkinghub.elsevier.com/retrieve/pii/S1877750315300119.

B. Fischl, D. H. Salat, A. J. W. van der Kouwe, N. Makris, F. Ségonne, B. T. Quinn, and A. M. Dale. Sequence-independent segmentation of magnetic resonance images. *NeuroImage*, 23 Suppl 1:S69–84, 2004. ISSN 1053-8119. doi: 10.1016/j.neuroimage.2004.07.016.

B. Fischl, N. Rajendran, E. Busa, J. Augustinack, O. Hinds, B. T. T. Yeo, H. Mohlberg, K. Amunts, and K. Zilles. Cortical folding patterns and predicting cytoarchitecture. *Cerebral Cortex (New York, N.Y.: 1991)*, 18(8):1973–1980, Aug. 2008. ISSN 1460-2199. doi: 10.1093/cercor/bhm225.

F. Fregni, P. S. Boggio, C. G. Mansur, T. Wagner, M. J. L. Ferreira, M. C. Lima, S. P. Rigonatti, M. A. Marcolin, S. D. Freedman, M. A. Nitsche, and A. Pascual-Leone. Transcranial direct current stimulation of the unaffected hemisphere in stroke patients. *Neuroreport*, 16(14):1551–1555, Sept. 2005. ISSN 0959-4965. doi: 10. 1097/01.wnr.0000177010.44602.5e.

N. Friedman, T. Fekete, K. Gal, and O. Shriki. EEG-Based Prediction of Cognitive Load in Intelligence Tests. *Frontiers in Human Neuroscience*, 13, 2019. ISSN 1662-5161. URL https://www.frontiersin.org/article/10.3389/fnhum.2019.00191.

M. Fuchs, J. Kastner, M. Wagner, S. Hawes, and J. S. Ebersole. A standardized boundary element method volume conductor model. *Clin Neurophysiol*, 113 (5):702–712, 2002.

M. Fuchs, M. Wagner, and J. Kastner. Development of Volume Conductor and Source Models to Localize Epileptic Foci:. *Journal of Clinical Neurophysiology*, 24(2):101–119, Apr. 2007. ISSN 0736-0258. doi: 10.1097/WNP.0b013e318038fb3e. URL http://journals.lww.com/00004691-200704000-00004.

C. Gabriel. Compilation of the Dielectric Properties of Body Tissues at RF and Microwave Frequencies.:. Technical report, Defense Technical Information Center, Fort Belvoir, VA, Jan. 1996. URL http://www.dtic.mil/docs/citations/ADA303903.

C. Gabriel, S. Gabriel, and E. Corthout. The dielectric properties of biological tissues: I. Literature survey. *Physics in Medicine and Biology*, 41(11):2231–2249, Nov. 1996a. ISSN 0031-9155, 1361-6560. doi: 10.1088/0031-9155/41/11/001. URL https://iopscience.iop.org/article/10.1088/0031-9155/41/11/001.

S. Gabriel, R. W. Lau, and C. Gabriel. The dielectric properties of biological tissues: II. Measurements in the frequency range 10 Hz to 20 GHz. *Physics in Medicine and Biology*, 41(11):2251–2269, Nov. 1996b. ISSN 0031-9155, 1361-6560. doi: 10.1088/0031-9155/41/11/002. URL https://iopscience.iop.org/article/10.1088/0031-9155/41/11/002.

S. Gabriel, R. W. Lau, and C. Gabriel. The dielectric properties of biological tissues: III. Parametric models for the dielectric spectrum of tissues. *Physics in Medicine and Biology*, 41(11):2271–2293, Nov. 1996c. ISSN 0031-9155, 1361-6560. doi: 10.1088/0031-9155/41/11/003. URL https://iopscience.iop.org/article/10.1088/0031-9155/41/11/003.

L. A. Geddes and L. E. Baker. The specific resistance of biological material–a compendium of data for the biomedical engineer and physiologist. *Medical & Biological Engineering*, 5(3):271–293, May 1967. ISSN 0025-696X. doi: 10.1007/BF02474537.

V. J. Geraedts, L. I. Boon, J. Marinus, A. A. Gouw, J. J. van Hilten, C. J. Stam, M. R. Tannemaat, and M. F. Contarino. Clinical correlates of quantitative EEG in Parkinson disease: A systematic review. *Neurology*, 91(19):871–883, Nov. 2018. ISSN 1526-632X. doi: 10.1212/WNL.0000000000006473.

C. Geuzaine. GetDP: a general finite-element solver for the de Rham complex. *PAMM Volume 7 Issue 1. Special Issue: Sixth International Congress on Industrial Applied Mathematics (ICIAM07) and GAMM Annual Meeting, Zürich 2007*, 7(1): 1010603–1010604, 2007. doi: 10.1002/pamm.200700750.

C. Geuzaine. GetDP: a general finite-element solver for the de Rham complex. In *PAMM Volume 7 Issue 1. Special Issue: Sixth International Congress on Industrial Applied Mathematics (ICIAM07) and GAMM Annual Meeting, Zürich 2007*, volume 7, pages 1010603–1010604. Wiley, 2008.

C. Geuzaine and J.-F. Remacle. Gmsh: a three-dimensional finite element mesh generator with built-in pre- ad post-processing facilities. *International Journal for Numerical Methods in Engineering*, 79(11):1309–1331, 2009. ISSN 00295981. doi: 10.1002/nme.2579.

M. F. Glasser, T. S. Coalson, E. C. Robinson, C. D. Hacker, J. Harwell, E. Yacoub, K. Ugurbil, J. Andersson, C. F. Beckmann, M. Jenkinson, S. M. Smith, and D. C. Van Essen. A multi-modal parcellation of human cerebral cortex. *Nature*, 536 (7615):171–178, Aug. 2016. ISSN 1476-4687. doi: 10.1038/nature18933.

S. Goncalves, J. de Munck, J. Verbunt, F. Bijma, R. Heethaar, and F. Lopes da Silva. In vivo measurement of the brain and skull resistivities using an EIT-based method and realistic models for the head. *IEEE Transactions on Biomedical Engineering*, 50(6):754–767, June 2003. ISSN 1558-2531. doi: 10.1109/TBME. 2003.812164. Conference Name: IEEE Transactions on Biomedical Engineering.

K. J. Gorgolewski, T. Auer, V. D. Calhoun, R. C. Craddock, S. Das, E. P. Duff, G. Flandin, S. S. Ghosh, T. Glatard, Y. O. Halchenko, D. A. Handwerker, M. Hanke, D. Keator, X. Li, Z. Michael, C. Maumet, B. N. Nichols, T. E. Nichols, J. Pellman, J.-B. Poline, A. Rokem, G. Schaefer, V. Sochat, W. Triplett, J. A. Turner, G. Varoquaux, and R. A. Poldrack. The brain imaging data structure, a format for organizing and describing outputs of neuroimaging experiments. *Scientific Data*, 3(1):160044, June 2016. ISSN 2052-4463. doi: 10.1038/sdata.2016.44. URL https://www.nature.com/articles/sdata201644. Bandiera_abtest:

a Cg_type: Nature Research Journals Number: 1 Primary_atype: Research Publisher: Nature Publishing Group Subject_term: Data publication and archiving;Research data Subject_term_id: data-publication-and-archiving;research-data.

G. Grabner, A. L. Janke, M. M. Budge, D. Smith, J. Pruessner, and D. L. Collins. Symmetric Atlasing and Model Based Segmentation: An Application to the Hippocampus in Older Adults. In R. Larsen, M. Nielsen, and J. Sporring, editors, *Medical Image Computing and Computer-Assisted Intervention – MICCAI 2006*, Lecture Notes in Computer Science, pages 58–66, Berlin, Heidelberg, 2006. Springer. ISBN 978-3-540-44728-3. doi: 10.1007/11866763_8.

A. Gramfort, M. Luessi, E. Larson, D. A. Engemann, D. Strohmeier, C. Brodbeck, R. Goj, M. Jas, T. Brooks, L. Parkkonen, and M. S. Hämäläinen. MEG and EEG data analysis with MNE-Python. *Frontiers in Neuroscience*, 7(267):1–13, 2013. doi: 10.3389/fnins.2013.00267.

S. L. Gratiy, G. Halnes, D. Denman, M. J. Hawrylycz, C. Koch, G. T. Einevoll, and C. A. Anastassiou. From Maxwell's equations to the theory of current-source density analysis. *European Journal of Neuroscience*, 45(8):1013–1023, 2017. ISSN 1460-9568. doi: 10.1111/ejn.13534. URL https://onlinelibrary.wiley.com/doi/abs/10.1111/ejn.13534. _eprint: https://onlinelibrary.wiley.com/doi/pdf/10.1111/ejn.13534.

R. Grech, T. Cassar, J. Muscat, K. P. Camilleri, S. G. Fabri, M. Zervakis, P. Xanthopoulos, V. Sakkalis, and B. Vanrumste. Review on solving the inverse problem in EEG source analysis. *Journal of NeuroEngineering and Rehabilitation*, 5(1):25, Nov. 2008. ISSN 1743-0003. doi: 10.1186/1743-0003-5-25. URL https://doi.org/10.1186/1743-0003-5-25.

D. J. Griffiths. *Introduction to Electrodynamics*. Cambridge University Press, Cambridge, 4 edition, 2017. ISBN 978-1-108-42041-9. doi: 10.1017/9781108333511. URL https://www.cambridge.org/core/books/introduction-to-electrodynamics/3AB220820DBB628E5A43D52C4B011ED4.

M. Grignard. shamo. https://doi.org/10.5281/zenodo.4420811, Jan. 2021a. URL https://doi.org/10.5281/zenodo.4420811.

M. Grignard. shamo documentation. https://cyclotronresearchcentre.github.io/shamo/index.html, Jan. 2021b. URL https://cyclotronresearchcentre.github.io/shamo/index.html.

M. Grignard, C. Geuzaine, and C. Phillips. Shamo: A Tool for Electromagnetic Modeling, Simulation and Sensitivity Analysis of the Head. *Neuroinformatics*, Mar. 2022. ISSN 1559-0089. doi: 10.1007/s12021-022-09574-7. URL `https://doi.org/10.1007/s12021-022-09574-7`.

J. Görtler, R. Kehlbeck, and O. Deussen. A Visual Exploration of Gaussian Processes. *Distill*, 4(4):e17, Apr. 2019. ISSN 2476-0757. doi: 10.23915/distill.00017. URL `https://distill.pub/2019/visual-exploration-gaussian-processes`.

D. Güllmar, J. Haueisen, and J. R. Reichenbach. Influence of anisotropic electrical conductivity in white matter tissue on the EEG/MEG forward and inverse solution. A high-resolution whole head simulation study. *NeuroImage*, 51(1):145–163, May 2010. ISSN 10538119. doi: 10.1016/j.neuroimage.2010.02.014. URL `https://linkinghub.elsevier.com/retrieve/pii/S1053811910001825`.

R. Hajare and S. Kadam. Comparative study analysis of practical EEG sensors in medical diagnoses. *Global Transitions Proceedings*, 2(2):467–475, Nov. 2021. ISSN 2666-285X. doi: 10.1016/j.gltp.2021.08.009. URL `https://www.sciencedirect.com/science/article/pii/S2666285X21000376`.

H. Hallez, B. Vanrumste, R. Grech, J. Muscat, W. De Clercq, A. Vergult, Y. D'Asseler, K. P. Camilleri, S. G. Fabri, S. Van Huffel, and I. Lemahieu. Review on solving the forward problem in EEG source analysis. *Journal of NeuroEngineering and Rehabilitation*, 4(1):46, Nov. 2007. ISSN 1743-0003. doi: 10.1186/1743-0003-4-46. URL `https://doi.org/10.1186/1743-0003-4-46`.

J. H. Halton. On the efficiency of certain quasi-random sequences of points in evaluating multi-dimensional integrals. *Numerische Mathematik*, 2(1):84–90, Dec. 1960. ISSN 0029-599X, 0945-3245. doi: 10.1007/BF01386213. URL `http://link.springer.com/10.1007/BF01386213`.

J. Haueisen, C. Ramon, P. Czapski, and M. Eiselt. On the influence of volume currents and extended sources on neuromagnetic fields: A simulation study. *Annals of Biomedical Engineering*, 23(6):728–739, Nov. 1995. ISSN 0090-6964, 1573-9686. doi: 10.1007/BF02584472. URL `http://link.springer.com/10.1007/BF02584472`.

J. Haueisen, C. Ramon, M. Eiselt, H. Brauer, and H. Nowak. Influence of tissue resistivities on neuromagnetic fields and electric potentials studied with a finite element model of the head. *IEEE Transactions on Biomedical Engineering*, 44(8):727–735, Aug. 1997. ISSN 00189294. doi: 10.1109/10.605429. URL `http://ieeexplore.ieee.org/document/605429/`.

J. Haueisen, D. Tuch, C. Ramon, P. Schimpf, V. Wedeen, J. George, and J. Belliveau. The Influence of Brain Tissue Anisotropy on Human EEG and MEG. *NeuroImage*, 15(1):159–166, Jan. 2002. ISSN 10538119. doi: 10.1006/nimg.2001.0962. URL `https://linkinghub.elsevier.com/retrieve/pii/S1053811901909620`.

J. Herman and W. Usher. SALib: An open-source Python library for Sensitivity Analysis. *Journal of Open Source Software*, 2(9):97, Jan. 2017. ISSN 2475-9066. doi: 10.21105/joss.00097. URL `https://joss.theoj.org/papers/10.21105/joss.00097`.

M. Hetkamp, J. Bender, N. Rheindorf, A. Kowalski, M. Lindner, S. Knispel, M. Beckmann, S. Tagay, and M. Teufel. A Systematic Review of the Effect of Neurofeedback in Cancer Patients. *Integrative Cancer Therapies*, 18:1534735419832361, Mar. 2019. ISSN 1534-7354. doi: 10.1177/1534735419832361. URL `https://www.ncbi.nlm.nih.gov/pmc/articles/PMC6416750/`.

M. D. Hoffman and A. Gelman. The No-U-Turn Sampler: Adaptively Setting Path Lengths in Hamiltonian Monte Carlo. *arXiv:1111.4246 [cs, stat]*, Nov. 2011. URL `http://arxiv.org/abs/1111.4246`. arXiv: 1111.4246.

C. J. Holmes, R. Hoge, L. Collins, R. Woods, A. W. Toga, and A. C. Evans. Enhancement of MR Images Using Registration for Signal Averaging. *Journal of Computer Assisted Tomography*, 22(2):324–333, Apr. 1998. ISSN 0363-8715. URL `https://journals.lww.com/jcat/Abstract/1998/03000/Enhancement_of_MR_Images_Using_Registration_for.32.aspx`.

J. C. Horvath, J. D. Forte, and O. Carter. Evidence that transcranial direct current stimulation (tDCS) generates little-to-no reliable neurophysiologic effect beyond MEP amplitude modulation in healthy human subjects: A systematic review. *Neuropsychologia*, 66:213–236, Jan. 2015. ISSN 00283932. doi: 10.1016/j.neuropsychologia.2014.11.021. URL `https://linkinghub.elsevier.com/retrieve/pii/S0028393214004394`.

Y. Huang and L. C. Parra. Fully Automated Whole-Head Segmentation with Improved Smoothness and Continuity, with Theory Reviewed. *PLOS ONE*, 10(5):e0125477, May 2015. ISSN 1932-6203. doi: 10.1371/journal.pone.0125477. URL `https://dx.plos.org/10.1371/journal.pone.0125477`.

Y. Huang, A. Datta, M. Bikson, and L. C. Parra. Realistic volumetric-approach to simulate transcranial electric stimulation—ROAST—a fully automated open-source pipeline. *Journal of Neural Engineering*, 16(5):056006, July 2019. ISSN 1741-2552. doi: 10.1088/1741-2552/ab208d. URL `https://doi.org/10.1088/1741-2552/ab208d`. Publisher: IOP Publishing.

T. Huisman. Diffusion-weighted and diffusion tensor imaging of the brain, made easy. *Cancer Imaging*, 10(1A):S163–S171, Oct. 2010. ISSN 1740-5025. doi: 10.1102/1470-7330.2010.9023. URL https://www.ncbi.nlm.nih.gov/pmc/articles/PMC2967146/.

F. Hummel, P. Celnik, P. Giraux, A. Floel, W.-H. Wu, C. Gerloff, and L. G. Cohen. Effects of non-invasive cortical stimulation on skilled motor function in chronic stroke. *Brain: A Journal of Neurology*, 128(Pt 3):490–499, Mar. 2005. ISSN 1460-2156. doi: 10.1093/brain/awh369.

M. Hämäläinen, R. Hari, R. J. Ilmoniemi, J. Knuutila, and O. V. Lounasmaa. Magnetoencephalography—theory, instrumentation, and applications to non-invasive studies of the working human brain. *Reviews of Modern Physics*, 65 (2):413–497, Apr. 1993. ISSN 0034-6861, 1539-0756. doi: 10.1103/RevModPhys. 65.413. URL https://link.aps.org/doi/10.1103/RevModPhys.65.413.

M. I. Iacono, E. Neufeld, E. Akinnagbe, K. Bower, J. Wolf, I. Vogiatzis Oikonomidis, D. Sharma, B. Lloyd, B. J. Wilm, M. Wyss, K. P. Pruessmann, A. Jakab, N. Makris, E. D. Cohen, N. Kuster, W. Kainz, and L. M. Angelone. MIDA: A Multimodal Imaging-Based Detailed Anatomical Model of the Human Head and Neck. *PLOS ONE*, 10(4):e0124126, Apr. 2015. ISSN 1932-6203. doi: 10.1371/journal.pone. 0124126. URL https://dx.plos.org/10.1371/journal.pone.0124126.

J. N. Ianof and R. Anghinah. Traumatic brain injury: An EEG point of view. *Dementia & Neuropsychologia*, 11(1):3–5, 2017. ISSN 1980-5764. doi: 10.1590/ 1980-57642016dn11-010002. URL https://www.ncbi.nlm.nih.gov/pmc/articles/PMC5619208/.

J. P. A. Ioannidis. Why Most Published Research Findings Are False. *PLOS Medicine*, 2(8):e124, Aug. 2005. ISSN 1549-1676. doi: 10.1371/journal.pmed. 0020124. URL https://journals.plos.org/plosmedicine/article?id=10.1371/journal.pmed.0020124. Publisher: Public Library of Science.

B. Iooss and P. Lemaître. A Review on Global Sensitivity Analysis Methods. In G. Dellino and C. Meloni, editors, *Uncertainty Management in Simulation-Optimization of Complex Systems*, volume 59, pages 101–122. Springer US, Boston, MA, 2015. ISBN 978-1-4899-7546-1 978-1-4899-7547-8. doi: 10.1007/978-1-4899-7547-8_5. URL http://link.springer.com/10.1007/978-1-4899-7547-8_5. Series Title: Operations Research/Computer Science Interfaces Series.

L. Jacobson, M. Koslowsky, and M. Lavidor. tDCS polarity effects in motor and cognitive domains: a meta-analytical review. *Experimental Brain Research*, 216 (1):1–10, Jan. 2012. ISSN 0014-4819, 1432-1106. doi: 10.1007/s00221-011-2891-9. URL http://link.springer.com/10.1007/s00221-011-2891-9.

N. Jacoby and M. Lavidor. Null tDCS Effects in a Sustained Attention Task: The Modulating Role of Learning. *Frontiers in Psychology*, 9:476, Apr. 2018. ISSN 1664-1078. doi: 10.3389/fpsyg.2018.00476. URL http://journal.frontiersin.org/article/10.3389/fpsyg.2018.00476/full.

G.-H. Jahng, M. B. Lee, H. J. Kim, E. Je Woo, and O.-I. Kwon. Low-frequency dominant electrical conductivity imaging of in vivo human brain using high-frequency conductivity at Larmor-frequency and spherical mean diffusivity without external injection current. *NeuroImage*, 225:117466, Jan. 2021. ISSN 1053-8119. doi: 10.1016/j.neuroimage.2020.117466. URL https://www.sciencedirect.com/science/article/pii/S1053811920309514.

A. Jamil, G. Batsikadze, H.-I. Kuo, L. Labruna, A. Hasan, W. Paulus, and M. A. Nitsche. Systematic evaluation of the impact of stimulation intensity on neuroplastic after-effects induced by transcranial direct current stimulation. *The Journal of Physiology*, 595(4):1273–1288, Feb. 2017. ISSN 1469-7793. doi: 10.1113/JP272738.

M. J. W. Jansen. Analysis of variance designs for model output. *Computer Physics Communications*, 117(1):35–43, Mar. 1999. ISSN 0010-4655. doi: 10.1016/S0010-4655(98)00154-4. URL https://www.sciencedirect.com/science/article/pii/S0010465598001544.

H. Jasper. Report of the committee on methods of clinical examination in electroencephalography: 1957. *Electroencephalography and Clinical Neurophysiology*, 10(2):370–375, May 1958. ISSN 0013-4694. doi: 10.1016/0013-4694(58)90053-1. URL https://www.sciencedirect.com/science/article/pii/0013469458900531.

M. Jenkinson, C. F. Beckmann, T. E. Behrens, M. W. Woolrich, and S. M. Smith. FSL. *NeuroImage*, 62(2):782–790, Aug. 2012. ISSN 10538119. doi: 10.1016/j.neuroimage.2011.09.015. URL https://linkinghub.elsevier.com/retrieve/pii/S1053811911010603.

D. Jing, D. Liu, S. Zhang, and Z. Guo. Fatigue driving detection method based on EEG analysis in low-voltage and hypoxia plateau environment. *International Journal of Transportation Science and Technology*, 9(4):366–376, Dec. 2020. ISSN 2046-0430. doi: 10.1016/j.ijtst.2020.03.008. URL https://www.sciencedirect.com/science/article/pii/S2046043020300253.

T. Jochmann, D. Güllmar, J. Haueisen, and J. R. Reichenbach. Influence of tissue conductivity changes on the EEG signal in the human brain – A simulation study. *Zeitschrift für Medizinische Physik*, 21(2):102–112, May 2011. ISSN 09393889. doi: 10.1016/j.zemedi.2010.07.004. URL https://linkinghub.elsevier.com/retrieve/pii/S0939388910000966.

M. V. Jog, D. J. Wang, and K. L. Narr. A review of transcranial direct current stimulation (tDCS) for the individualized treatment of depressive symptoms. *Personalized medicine in psychiatry*, 17-18:17–22, 2019. ISSN 2468-1725. doi: 10.1016/j.pmip.2019.03.001. URL https://www.ncbi.nlm.nih.gov/pmc/articles/PMC6959848/.

V. Jurcak, M. Okamoto, A. Singh, and I. Dan. Virtual 10-20 measurement on MR images for inter-modal linking of transcranial and tomographic neuroimaging methods. *NeuroImage*, 26(4):1184–1192, July 2005. ISSN 1053-8119. doi: 10.1016/j.neuroimage.2005.03.021.

H. A. S. Kamimura, A. Conti, N. Toschi, and E. E. Konofagou. Ultrasound Neuromodulation: Mechanisms and the Potential of Multimodal Stimulation for Neuronal Function Assessment. *Frontiers in Physics*, 8, 2020. ISSN 2296-424X. URL https://www.frontiersin.org/articles/10.3389/fphy.2020.00150.

N. Katoch, B. K. Choi, S. Z. K. Sajib, E. Lee, H. J. Kim, O. I. Kwon, and E. J. Woo. Conductivity Tensor Imaging of In Vivo Human Brain and Experimental Validation Using Giant Vesicle Suspension. *IEEE Transactions on Medical Imaging*, 38(7):1569–1577, July 2019. ISSN 1558-254X. doi: 10.1109/TMI.2018.2884440. Conference Name: IEEE Transactions on Medical Imaging.

Y. Ke, N. Wang, J. Du, L. Kong, S. Liu, M. Xu, X. An, and D. Ming. The Effects of Transcranial Direct Current Stimulation (tDCS) on Working Memory Training in Healthy Young Adults. *Frontiers in Human Neuroscience*, 13, 2019. ISSN 1662-5161. URL https://www.frontiersin.org/article/10.3389/fnhum.2019.00019.

B. Kerous, F. Skola, and F. Liarokapis. EEG-based BCI and video games: a progress report. *Virtual Reality*, 22(2):119–135, June 2018. ISSN 1434-9957. doi: 10.1007/s10055-017-0328-x. URL https://doi.org/10.1007/s10055-017-0328-x.

M. Khorrampanah, H. Seyedarabi, S. Daneshvar, and M. Farhoudi. Optimization of montages and electric currents in tDCS. *Computers in Biology and Medicine*, 125:103998, Oct. 2020. ISSN 00104825. doi: 10.1016/j.compbiomed.2020.103998. URL https://linkinghub.elsevier.com/retrieve/pii/S0010482520303292.

G. H. Klem, H. O. Lüders, H. H. Jasper, and C. Elger. The ten-twenty electrode system of the International Federation. The International Federation of Clinical Neurophysiology. *Electroencephalography and Clinical Neurophysiology. Supplement*, 52:3–6, 1999. ISSN 0424-8155.

L. Koessler, S. Colnat-Coulbois, T. Cecchin, J. Hofmanis, J. P. Dmochowski, A. M. Norcia, and L. G. Maillard. In-vivo measurements of human brain tissue conductivity using focal electrical current injection through intracerebral multi-contact electrodes. *Human Brain Mapping*, 38(2):974–986, Feb. 2017. ISSN 1097-0193. doi: 10.1002/hbm.23431.

M. Kovacevic, M. Jovanovic, and M. M. Milosevic. On the calculus of Dirac delta function with some applications in classical electrodynamics. *Revista Mexicana de Física E*, 18(2 Jul-Dec), July 2021. ISSN 2683-2216, 1870-3542. doi: 10.31349/RevMexFisE.18.020205. URL https://rmf.smf.mx/ojs/index.php/rmf-e/article/view/5721.

J. D. Kropotov. Chapter 4.4 - Transcranial Direct Current Stimulation. In J. D. Kropotov, editor, *Functional Neuromarkers for Psychiatry*, pages 273–280. Academic Press, San Diego, Jan. 2016. ISBN 978-0-12-410513-3. doi: 10.1016/B978-0-12-410513-3.00018-8.

J. K. Kruschke and T. M. Liddell. The Bayesian New Statistics: Hypothesis testing, estimation, meta-analysis, and power analysis from a Bayesian perspective. *Psychonomic Bulletin & Review*, 25(1):178–206, Feb. 2018. ISSN 1531-5320. doi: 10.3758/s13423-016-1221-4.

I. Laakso, S. Tanaka, S. Koyama, V. De Santis, and A. Hirata. Inter-subject Variability in Electric Fields of Motor Cortical tDCS. *Brain Stimulation*, 8(5):906–913, Oct. 2015. ISSN 1876-4754. doi: 10.1016/j.brs.2015.05.002.

B. Lanfer, M. Scherg, M. Dannhauer, T. Knösche, M. Burger, and C. Wolters. Influences of skull segmentation inaccuracies on EEG source analysis. *NeuroImage*, 62(1):418–431, Aug. 2012. ISSN 10538119. doi: 10.1016/j.neuroimage.2012.05.006. URL https://linkinghub.elsevier.com/retrieve/pii/S1053811912004946.

O. M. Lapenta, L. M. Marques, G. G. Rego, W. E. Comfort, and P. S. Boggio. tDCS in Addiction and Impulse Control Disorders. *The journal of ECT*, 34(3):182–192, Sept. 2018. ISSN 1533-4112. doi: 10.1097/YCT.0000000000000541.

J. Latikka, J. Hyttinen, T. Kuurne, H. Eskola, and J. Malmivuo. The conductivity of brain tissues: comparison of results in vivo and in vitro measurements. In *2001 Conference Proceedings of the 23rd Annual International Conference of the IEEE Engineering in Medicine and Biology Society*, volume 1, pages 910–912, Istanbul, Turkey, 2001. IEEE. ISBN 978-0-7803-7211-5. doi: 10.1109/IEMBS.2001.1019092. URL http://ieeexplore.ieee.org/document/1019092/.

J. S. A. Lee, S. Bestmann, and C. Evans. A Future of Current Flow Modelling for Transcranial Electrical Stimulation? *Current Behavioral Neuroscience Reports*, 8(4):150–159, Dec. 2021. ISSN 2196-2979. doi: 10.1007/s40473-021-00238-5. URL `https://doi.org/10.1007/s40473-021-00238-5`.

C. Li, S. Jirachaipitak, P. Wrigley, H. Xu, and P. Euasobhon. Transcranial direct current stimulation for spinal cord injury-associated neuropathic pain. *The Korean Journal of Pain*, 34(2):156–164, Apr. 2021. ISSN 2005-9159. doi: 10.3344/kjp.2021.34.2.156.

L. M. Li, K. Uehara, and T. Hanakawa. The contribution of interindividual factors to variability of response in transcranial direct current stimulation studies. *Frontiers in Cellular Neuroscience*, 9, 2015. ISSN 1662-5102. URL `https://www.frontiersin.org/article/10.3389/fncel.2015.00181`.

W. Li, N. C. Andreasen, P. Nopoulos, and V. A. Magnotta. Automated parcellation of the brain surface generated from magnetic resonance images. *Frontiers in Neuroinformatics*, 7, Oct. 2013. ISSN 1662-5196. doi: 10.3389/fninf.2013.00023. URL `https://www.ncbi.nlm.nih.gov/pmc/articles/PMC3804771/`.

D. V. Lindley. The Future of Statistics: A Bayesian 21st Century. *Advances in Applied Probability*, 7:106–115, 1975. ISSN 0001-8678. doi: 10.2307/1426315. URL `https://www.jstor.org/stable/1426315`. Publisher: Applied Probability Trust.

H. Liu, Y. Zhang, Y. Li, and X. Kong. Review on Emotion Recognition Based on Electroencephalography. *Frontiers in Computational Neuroscience*, 15, 2021. ISSN 1662-5188. URL `https://www.frontiersin.org/article/10.3389/fncom.2021.758212`.

Y. Liu, S. Zhu, and B. He. Induced current magnetic resonance electrical impedance tomography of brain tissues based on the J-substitution algorithm: a simulation study. *Physics in Medicine and Biology*, 54(14):4561–4573, July 2009. ISSN 0031-9155. doi: 10.1088/0031-9155/54/14/012.

D. M. Lloyd, P. G. Wittkopf, L. J. Arendsen, and A. K. P. Jones. Is Transcranial Direct Current Stimulation (tDCS) Effective for the Treatment of Pain in Fibromyalgia? A Systematic Review and Meta-Analysis. *The Journal of Pain*, 21(11-12):1085–1100, Dec. 2020. ISSN 1528-8447. doi: 10.1016/j.jpain.2020.01.003.

S. Luengo-Sanchez, C. Bielza, R. Benavides-Piccione, I. Fernaud-Espinosa, J. DeFelipe, and P. Larrañaga. A univocal definition of the neuronal soma morphology using Gaussian mixture models. *Frontiers in Neuroanatomy*, 9:137, 2015. ISSN 1662-5129. doi: 10.3389/fnana.2015.00137.

Q. Mahmood, A. Chodorowski, and M. Persson. Automated MRI brain tissue segmentation based on mean shift and fuzzy c -means using a priori tissue probability maps. *IRBM*, 36(3):185–196, June 2015. ISSN 19590318. doi: 10.1016/j.irbm.2015.01.007. URL `https://linkinghub.elsevier.com/retrieve/pii/S1959031815000287`.

J. Malmivuo and R. Plonsey. *Bioelectromagnetism: Principles and Applications of Bioelectric and Biomagnetic Fields*. Oxford University Press, Oct. 1995. ISBN 978-0-19-505823-9. doi: 10.1093/acprof:oso/9780195058239.001.0001. URL `https://oxford.universitypressscholarship.com/view/10.1093/acprof:oso/9780195058239.001.0001/acprof-9780195058239`.

G. Marin, C. Guerin, S. Baillet, L. Garnero, and G. Meunier. Influence of skull anisotropy for the forward and inverse problem in EEG: Simulation studies using FEM on realistic head models. *Human Brain Mapping*, 6(4):250–269, Jan. 1998. ISSN 10659471. doi: 10.1002/(SICI)1097-0193(1998)6:4<250::AID-HBM5>3.0.CO;2-2. URL `http://doi.wiley.com/10.1002/%28SICI%291097-0193%281998%296%3A4%3C250%3A%3AAID-HBM5%3E3.0.CO%3B2-2`.

M. Marino, L. Cordero-Grande, D. Mantini, and G. Ferrazzi. Conductivity Tensor Imaging of the Human Brain Using Water Mapping Techniques. *Frontiers in Neuroscience*, 15, 2021. ISSN 1662-453X. URL `https://www.frontiersin.org/article/10.3389/fnins.2021.694645`.

A. Marrel, B. Iooss, B. Laurent, and O. Roustant. Calculations of Sobol indices for the Gaussian process metamodel. *Reliability Engineering & System Safety*, 94(3):742–751, Mar. 2009. ISSN 09518320. doi: 10.1016/j.ress.2008.07.008. URL `https://linkinghub.elsevier.com/retrieve/pii/S0951832008001981`.

H. McCann, G. Pisano, and L. Beltrachini. Variation in Reported Human Head Tissue Electrical Conductivity Values. *Brain Topography*, 32(5):825–858, Sept. 2019. ISSN 0896-0267, 1573-6792. doi: 10.1007/s10548-019-00710-2. URL `http://link.springer.com/10.1007/s10548-019-00710-2`.

C. M. Michel and D. Brunet. EEG Source Imaging: A Practical Review of the Analysis Steps. *Frontiers in Neurology*, 10:325, Apr. 2019. ISSN 1664-2295. doi: 10.3389/fneur.2019.00325. URL `https://www.ncbi.nlm.nih.gov/pmc/articles/PMC6458265/`.

A. Miladinović, M. Ajčević, P. Busan, J. Jarmolowska, M. Deodato, S. Mezzarobba, P. P. Battaglini, and A. Accardo. EEG changes and motor deficits in Parkinson's disease patients: Correlation of motor scales and EEG power bands. *Procedia Computer Science*, 192:2616–2623, Jan. 2021. ISSN 1877-0509. doi: 10.

1016/j.procs.2021.09.031. URL https://www.sciencedirect.com/science/article/pii/S1877050921017683.

K. Mills. Hcp-mmp1.0 projected on fsaverage, Jul 2016. URL https://figshare.com/articles/dataset/HCP-MMP1_0_projected_on_fsaverage/3498446/2.

V. Montes-Restrepo, P. van Mierlo, G. Strobbe, S. Staelens, S. Vandenberghe, and H. Hallez. Influence of Skull Modeling Approaches on EEG Source Localization. *Brain Topography*, 27(1):95–111, Jan. 2014. ISSN 0896-0267, 1573-6792. doi: 10.1007/s10548-013-0313-y. URL http://link.springer.com/10.1007/s10548-013-0313-y.

J. Mosher, R. Leahy, and P. Lewis. EEG and MEG: forward solutions for inverse methods. *IEEE Transactions on Biomedical Engineering*, 46(3):245–259, Mar. 1999. ISSN 00189294. doi: 10.1109/10.748978. URL http://ieeexplore.ieee.org/document/748978/.

E. Mtui, G. Gruener, P. Dockery, and M. J. T. Fitzgerald. *Fitzgerald's clinical neuroanatomy and neuroscience*. Elsevier, Amsterdam Philadelphia, PA, 8th edition edition, 2021. ISBN 978-0-7020-7909-2.

J. F. M. Müller-Dahlhaus, Y. Orekhov, Y. Liu, and U. Ziemann. Interindividual variability and age-dependency of motor cortical plasticity induced by paired associative stimulation. *Experimental Brain Research*, 187(3):467–475, May 2008. ISSN 1432-1106. doi: 10.1007/s00221-008-1319-7. URL https://doi.org/10.1007/s00221-008-1319-7.

N. Ngernyam, M. P. Jensen, P. Arayawichanon, N. Auvichayapat, S. Tiamkao, S. Janjarasjitt, W. Punjaruk, A. Amatachaya, B. Aree-uea, and P. Auvichayapat. The effects of transcranial direct current stimulation in patients with neuropathic pain from spinal cord injury. *Clinical Neurophysiology: Official Journal of the International Federation of Clinical Neurophysiology*, 126(2):382–390, Feb. 2015. ISSN 1872-8952. doi: 10.1016/j.clinph.2014.05.034.

J. D. Nielsen, K. H. Madsen, O. Puonti, H. R. Siebner, C. Bauer, C. G. Madsen, G. B. Saturnino, and A. Thielscher. Automatic skull segmentation from MR images for realistic volume conductor models of the head: Assessment of the state-of-the-art. *NeuroImage*, 174:587–598, July 2018. ISSN 1095-9572. doi: 10.1016/j.neuroimage.2018.03.001.

M. A. Nitsche and W. Paulus. Excitability changes induced in the human motor cortex by weak transcranial direct current stimulation. *The Journal of Physiology*, 527 Pt 3:633–639, Sept. 2000. ISSN 0022-3751. doi: 10.1111/j.1469-7793.2000.t01-1-00633.x.

M. A. Nitsche and W. Paulus. Sustained excitability elevations induced by transcranial DC motor cortex stimulation in humans. *Neurology*, 57(10), Nov. 2001. ISSN 0028-3878. doi: 10.1212/wnl.57.10.1899.

M. A. Nitsche, D. Liebetanz, N. Lang, A. Antal, F. Tergau, and W. Paulus. Safety criteria for transcranial direct current stimulation (tDCS) in humans. *Clinical Neurophysiology: Official Journal of the International Federation of Clinical Neurophysiology*, 114(11):2220–2222; author reply 2222–2223, Nov. 2003. ISSN 1388-2457. doi: 10.1016/s1388-2457(03)00235-9.

M. A. Nitsche, L. G. Cohen, E. M. Wassermann, A. Priori, N. Lang, A. Antal, W. Paulus, F. Hummel, P. S. Boggio, F. Fregni, and A. Pascual-Leone. Transcranial direct current stimulation: State of the art 2008. *Brain Stimulation*, 1(3): 206–223, July 2008. ISSN 1876-4754. doi: 10.1016/j.brs.2008.06.004.

S. Noachtar and J. Rémi. The role of EEG in epilepsy: a critical review. *Epilepsy & Behavior: E&B*, 15(1):22–33, May 2009. ISSN 1525-5069. doi: 10.1016/j.yebeh.2009.02.035.

M. R. Nuwer. 10-10 electrode system for EEG recording. *Clinical Neurophysiology*, 129(5):1103, May 2018. ISSN 1388-2457. doi: 10.1016/j.clinph.2018.01.065. URL `http://www.sciencedirect.com/science/article/pii/S1388245718300907`.

J. E. Oakley and A. O'Hagan. Probabilistic sensitivity analysis of complex models: a Bayesian approach. *Journal of the Royal Statistical Society: Series B (Statistical Methodology)*, 66(3):751–769, Aug. 2004. ISSN 1369-7412, 1467-9868. doi: 10.1111/j.1467-9868.2004.05304.x. URL `http://doi.wiley.com/10.1111/j.1467-9868.2004.05304.x`.

T. Oostendorp, J. Delbeke, and D. Stegeman. The conductivity of the human skull: results of in vivo and in vitro measurements. *IEEE Transactions on Biomedical Engineering*, 47(11):1487–1492, Nov. 2000. ISSN 0018-9294. doi: 10.1109/TBME.2000.880100. URL `http://ieeexplore.ieee.org/document/880100/`.

R. Oostenveld, P. Fries, E. Maris, and J.-M. Schoffelen. FieldTrip: Open source software for advanced analysis of MEG, EEG, and invasive electrophysiological data. *Computational Intelligence and Neuroscience*, 2011:156869, 2011. ISSN 1687-5273. doi: 10.1155/2011/156869.

A. Opitz, A. Falchier, C.-G. Yan, E. M. Yeagle, G. S. Linn, P. Megevand, A. Thielscher, R. Deborah A., M. P. Milham, A. D. Mehta, and C. E. Schroeder. Spatiotemporal structure of intracranial electric fields induced by transcranial electric stimulation in humans and nonhuman primates. *Scientific Reports*, 6(1):31236, Aug.

2016. ISSN 2045-2322. doi: 10.1038/srep31236. URL `https://www.nature.com/articles/srep31236`. Number: 1 Publisher: Nature Publishing Group.

N. E. Owen, P. Challenor, P. P. Menon, and S. Bennani. Comparison of Surrogate-Based Uncertainty Quantification Methods for Computationally Expensive Simulators. *SIAM/ASA Journal on Uncertainty Quantification*, 5(1):403–435, Jan. 2017. doi: 10.1137/15M1046812. URL `https://epubs.siam.org/doi/abs/10.1137/15M1046812`. Publisher: Society for Industrial and Applied Mathematics.

R. Parlikar, S. Vanteemar S, V. Shivakumar, J. Narayanaswamy C., N. Rao P., and V. Ganesan. High definition transcranial direct current stimulation (HD-tDCS): A systematic review on the treatment of neuropsychiatric disorders. *Asian Journal of Psychiatry*, 56:102542, Feb. 2021. ISSN 1876-2018. doi: 10.1016/j.ajp.2020.102542. URL `https://www.sciencedirect.com/science/article/pii/S1876201820306559`.

F. Pedregosa, G. Varoquaux, A. Gramfort, V. Michel, B. Thirion, O. Grisel, M. Blondel, P. Prettenhofer, R. Weiss, V. Dubourg, J. Vanderplas, A. Passos, D. Cournapeau, M. Brucher, M. Perrot, and E. Duchesnay. Scikit-learn: Machine learning in Python. *Journal of Machine Learning Research*, 12:2825–2830, 2011a.

F. Pedregosa, G. Varoquaux, A. Gramfort, V. Michel, B. Thirion, O. Grisel, M. Blondel, P. Prettenhofer, R. Weiss, V. Dubourg, J. Vanderplas, A. Passos, D. Cournapeau, M. Brucher, M. Perrot, and �. Duchesnay. Scikit-learn: Machine Learning in Python. *Journal of Machine Learning Research*, 12(85):2825–2830, 2011b. URL `http://jmlr.org/papers/v12/pedregosa11a.html`.

S. J. Pelletier and F. Cicchetti. Cellular and Molecular Mechanisms of Action of Transcranial Direct Current Stimulation: Evidence from In Vitro and In Vivo Models. *International Journal of Neuropsychopharmacology*, 18(2):pyu047, Jan. 2015. ISSN 1461-1457. doi: 10.1093/ijnp/pyu047. URL `https://www.ncbi.nlm.nih.gov/pmc/articles/PMC4368894/`.

K. L. Perdue and S. G. Diamond. T1 magnetic resonance imaging head segmentation for diffuse optical tomography and electroencephalography. *Journal of Biomedical Optics*, 19(2), Feb. 2014. ISSN 1083-3668. doi: 10.1117/1.JBO.19.2.026011. URL `https://www.ncbi.nlm.nih.gov/pmc/articles/PMC3924797/`.

A. Perrottelli, G. M. Giordano, F. Brando, L. Giuliani, and A. Mucci. EEG-Based Measures in At-Risk Mental State and Early Stages of Schizophrenia: A Systematic Review. *Frontiers in Psychiatry*, 12, 2021. ISSN 1664-0640. URL `https://www.frontiersin.org/article/10.3389/fpsyt.2021.653642`.

M. C. Piastra, A. Nüßing, J. Vorwerk, H. Bornfleth, R. Oostenveld, C. Engwer, and C. H. Wolters. The Discontinuous Galerkin Finite Element Method for Solving the MEG and the Combined MEG/EEG Forward Problem. *Frontiers in Neuroscience*, 12, 2018. ISSN 1662-453X. URL `https://www.frontiersin.org/articles/10.3389/fnins.2018.00030`.

R. Plonsey and D. B. Heppner. Considerations of quasi-stationarity in electrophysiological systems. *The Bulletin of Mathematical Biophysics*, 29(4):657–664, Dec. 1967. ISSN 0007-4985. doi: 10.1007/BF02476917.

T. C. Project. *CGAL User and Reference Manual*. CGAL Editorial Board, 5.0.3 edition, 2020. URL `https://doc.cgal.org/5.0.3/Manual/packages.html`.

O. Puonti, K. Van Leemput, G. B. Saturnino, H. R. Siebner, K. H. Madsen, and A. Thielscher. Accurate and robust whole-head segmentation from magnetic resonance images for individualized head modeling. *NeuroImage*, 219:117044, Oct. 2020. ISSN 1053-8119. doi: 10.1016/j.neuroimage.2020.117044. URL `https://www.sciencedirect.com/science/article/pii/S1053811920305309`.

D. Purves, editor. *Neuroscience*. Sinauer Associates, Publishers, Sunderland, Mass, 3rd ed edition, 2004. ISBN 978-0-87893-725-7.

M. Raasveldt and H. Mühleisen. DuckDB: an embeddable analytical database. ACM, June 2019. doi: 10.1145/3299869.3320212. URL `https://doi.org/10.1145/3299869.3320212`.

T. Radman, R. L. Ramos, J. C. Brumberg, and M. Bikson. Role of cortical cell type and morphology in subthreshold and suprathreshold uniform electric field stimulation in vitro. *Brain Stimulation*, 2(4):215–228, 228.e1–3, Oct. 2009. ISSN 1876-4754. doi: 10.1016/j.brs.2009.03.007.

M. M. Rahman, A. K. Sarkar, M. A. Hossain, M. S. Hossain, M. R. Islam, M. B. Hossain, J. M. W. Quinn, and M. A. Moni. Recognition of human emotions using EEG signals: A review. *Computers in Biology and Medicine*, 136:104696, Sept. 2021. ISSN 0010-4825. doi: 10.1016/j.compbiomed.2021.104696. URL `https://www.sciencedirect.com/science/article/pii/S001048252100490X`.

S. Ramaraju, M. A. Roula, and P. W. McCarthy. Modelling the effect of electrode displacement on transcranial direct current stimulation (tDCS). *Journal of Neural Engineering*, 15(1):016019, Feb. 2018. ISSN 1741-2552. doi: 10.1088/1741-2552/aa8d8a.

P. E. Rapp, D. O. Keyser, A. Albano, R. Hernandez, D. B. Gibson, R. A. Zambon, W. D. Hairston, J. D. Hughes, A. Krystal, and A. S. Nichols. Traumatic Brain Injury Detection Using Electrophysiological Methods. *Frontiers in Human Neuroscience*,

9, 2015. ISSN 1662-5161. URL `https://www.frontiersin.org/article/10.3389/fnhum.2015.00011`.

C. E. Rasmussen. Gaussian Processes in Machine Learning. In O. Bousquet, U. von Luxburg, and G. Rätsch, editors, *Advanced Lectures on Machine Learning: ML Summer Schools 2003, Canberra, Australia, February 2 - 14, 2003, Tübingen, Germany, August 4 - 16, 2003, Revised Lectures*, Lecture Notes in Computer Science, pages 63–71. Springer, Berlin, Heidelberg, 2004. ISBN 978-3-540-28650-9. doi: 10.1007/978-3-540-28650-9_4. URL `https://doi.org/10.1007/978-3-540-28650-9_4`.

C. E. Rasmussen and C. K. I. Williams. *Gaussian processes for machine learning*. Adaptive computation and machine learning. MIT Press, Cambridge, Mass, 2006. ISBN 978-0-262-18253-9. URL `http://www.gaussianprocess.org/gpml/chapters/RW.pdf`. OCLC: ocm61285753.

S. Razavi, A. Jakeman, A. Saltelli, C. Prieur, B. Iooss, E. Borgonovo, E. Plischke, S. Lo Piano, T. Iwanaga, W. Becker, S. Tarantola, J. H. A. Guillaume, J. Jakeman, H. Gupta, N. Melillo, G. Rabitti, V. Chabridon, Q. Duan, X. Sun, S. Smith, R. Sheikholeslami, N. Hosseini, M. Asadzadeh, A. Puy, S. Kucherenko, and H. R. Maier. The Future of Sensitivity Analysis: An essential discipline for systems modeling and policy support. *Environmental Modelling & Software*, 137:104954, Mar. 2021. ISSN 1364-8152. doi: 10.1016/j.envsoft.2020.104954. URL `https://www.sciencedirect.com/science/article/pii/S1364815220310112`.

L. B. Razza, P. Palumbo, A. H. Moffa, A. F. Carvalho, M. Solmi, C. K. Loo, and A. R. Brunoni. A systematic review and meta-analysis on the effects of transcranial direct current stimulation in depressive episodes. *Depression and Anxiety*, 37(7):594–608, 2020. ISSN 1520-6394. doi: 10.1002/da.23004. URL `https://onlinelibrary.wiley.com/doi/abs/10.1002/da.23004`. _eprint: https://onlinelibrary.wiley.com/doi/pdf/10.1002/da.23004.

J. Reis, H. M. Schambra, L. G. Cohen, E. R. Buch, B. Fritsch, E. Zarahn, P. A. Celnik, and J. W. Krakauer. Noninvasive cortical stimulation enhances motor skill acquisition over multiple days through an effect on consolidation. *Proceedings of the National Academy of Sciences*, 106(5):1590–1595, Feb. 2009. doi: 10.1073/pnas.0805413106. URL `https://www.pnas.org/doi/10.1073/pnas.0805413106`. Publisher: Proceedings of the National Academy of Sciences.

A. Remsik, B. Young, R. Vermilyea, L. Kiekoefer, J. Abrams, S. E. Elmore, P. Schultz, V. Nair, D. Edwards, J. Williams, and V. Prabhakaran. A review of the progression and future implications of brain-computer interface therapies for

restoration of distal upper extremity motor function after stroke. *Expert review of medical devices*, 13(5):445–454, May 2016. ISSN 1743-4440. doi: 10.1080/17434440.2016.1174572. URL https://www.ncbi.nlm.nih.gov/pmc/articles/PMC5131699/.

L. Reuss. Mechanisms of Ion Transport Across Cell Membranes and Epithelia. In *Seldin and Giebisch's The Kidney*, pages 35–56. Elsevier, 2008. ISBN 978-0-12-088488-9. doi: 10.1016/B978-012088488-9.50005-X. URL https://linkinghub.elsevier.com/retrieve/pii/B978012088488950005X.

T. L. Rich and B. T. Gillick. Electrode Placement in Transcranial Direct Current Stimulation—How Reliable Is the Determination of C3/C4? *Brain Sciences*, 9 (3):69, Mar. 2019. ISSN 2076-3425. doi: 10.3390/brainsci9030069. URL https://www.ncbi.nlm.nih.gov/pmc/articles/PMC6468365/.

M. Rojas, D. Ariza, �. Ortega, M. E. Riaño-Garzón, M. Chávez-Castillo, J. L. Pérez, L. Cudris-Torres, M. J. Bautista, O. Medina-Ortiz, J. Rojas-Quintero, and V. Bermúdez. Electroconvulsive Therapy in Psychiatric Disorders: A Narrative Review Exploring Neuroendocrine-Immune Therapeutic Mechanisms and Clinical Implications. *International Journal of Molecular Sciences*, 23(13):6918, June 2022. ISSN 1422-0067. doi: 10.3390/ijms23136918.

C. Rorden, H.-O. Karnath, and L. Bonilha. Improving lesion-symptom mapping. *Journal of Cognitive Neuroscience*, 19(7):1081–1088, July 2007. ISSN 0898-929X. doi: 10.1162/jocn.2007.19.7.1081.

A. Roy, B. Baxter, and B. He. High Definition Transcranial Direct Current Stimulation Induces Both Acute and Persistent Changes in Broadband Cortical Synchronization: a Simultaneous tDCS-EEG Study. *IEEE transactions on bio-medical engineering*, 61(7):1967–1978, July 2014. ISSN 0018-9294. doi: 10.1109/TBME.2014.2311071. URL https://www.ncbi.nlm.nih.gov/pmc/articles/PMC4113724/.

T. Rudroff, C. D. Workman, A. C. Fietsam, and J. Kamholz. Response Variability in Transcranial Direct Current Stimulation: Why Sex Matters. *Frontiers in Psychiatry*, 11, 2020. ISSN 1664-0640. URL https://www.frontiersin.org/article/10.3389/fpsyt.2020.00585.

R. J. Sadleir and A. Argibay. Modeling Skull Electrical Properties. *Annals of Biomedical Engineering*, 35(10):1699–1712, Sept. 2007. ISSN 0090-6964, 1573-9686. doi: 10.1007/s10439-007-9343-5. URL http://link.springer.com/10.1007/s10439-007-9343-5.

R. J. Sadleir, T. D. Vannorsdall, D. J. Schretlen, and B. Gordon. Transcranial direct current stimulation (tDCS) in a realistic head model. *NeuroImage*, 51(4):1310–1318, July 2010. ISSN 10538119. doi: 10.1016/j.neuroimage.2010.03.052. URL `https://linkinghub.elsevier.com/retrieve/pii/S1053811910003393`.

S. Z. K. Sajib, J. E. Kim, W. C. Jeong, H. J. Kim, O. I. Kwon, and E. J. Woo. Reconstruction of apparent orthotropic conductivity tensor image using magnetic resonance electrical impedance tomography. *Journal of Applied Physics*, 117(10):104701, Mar. 2015. ISSN 0021-8979. doi: 10.1063/1.4914904. URL `https://aip.scitation.org/doi/10.1063/1.4914904`. Publisher: American Institute of Physics.

S. Z. K. Sajib, W. C. Jeong, E. J. Kyung, H. B. Kim, T. I. Oh, H. J. Kim, O. I. Kwon, and E. J. Woo. Experimental evaluation of electrical conductivity imaging of anisotropic brain tissues using a combination of diffusion tensor imaging and magnetic resonance electrical impedance tomography. *AIP Advances*, 6(6):065109, June 2016. doi: 10.1063/1.4953893. URL `https://aip.scitation.org/doi/full/10.1063/1.4953893`. Publisher: American Institute of Physics.

E. Sallard, J. L. Rohrbach, C. Brandner, N. Place, and J. Barral. Individualization of tDCS intensity according to corticospinal excitability does not improve stimulation efficacy over the primary motor cortex. *Neuroimage: Reports*, 1(3):100028, Sept. 2021. ISSN 2666-9560. doi: 10.1016/j.ynirp.2021.100028. URL `https://www.sciencedirect.com/science/article/pii/S266695602100026X`.

A. Saltelli, editor. *Global sensitivity analysis: the primer*. John Wiley, Chichester, England ; Hoboken, NJ, 2008. ISBN 978-0-470-05997-5. OCLC: ocn180852094.

A. Saltelli, P. Annoni, I. Azzini, F. Campolongo, M. Ratto, and S. Tarantola. Variance based sensitivity analysis of model output. Design and estimator for the total sensitivity index. *Computer Physics Communications*, 181(2):259–270, Feb. 2010. ISSN 00104655. doi: 10.1016/j.cpc.2009.09.018. URL `https://linkinghub.elsevier.com/retrieve/pii/S0010465509003087`.

J. Salvatier, T. V. Wiecki, and C. Fonnesbeck. Probabilistic programming in Python using PyMC3. *PeerJ Computer Science*, 2:e55, Apr. 2016. ISSN 2376-5992. doi: 10.7717/peerj-cs.55. URL `https://peerj.com/articles/cs-55`. Publisher: PeerJ Inc.

D. San-Juan, L. Morales-Quezada, A. J. Orozco Garduño, M. Alonso-Vanegas, M. F. González-Aragón, D. A. Espinoza López, R. Vázquez Gregorio, D. J. Anschel, and F. Fregni. Transcranial Direct Current Stimulation in Epilepsy. *Brain Stimulation*, 8(3):455–464, June 2015. ISSN 1876-4754. doi: 10.1016/j.brs.2015.01.001.

G. B. Saturnino, A. Thielscher, K. H. Madsen, T. R. Knösche, and K. Weise. A principled approach to conductivity uncertainty analysis in electric field calculations. *NeuroImage*, 188:821–834, Mar. 2019. ISSN 1053-8119. doi: 10.1016/j. neuroimage.2018.12.053. URL http://www.sciencedirect.com/science/article/pii/S1053811918322031.

N. Schaul. The fundamental neural mechanisms of electroencephalography. *Electroencephalography and Clinical Neurophysiology*, 106(2):101–107, Feb. 1998. ISSN 00134694. doi: 10.1016/S0013-4694(97)00111-9. URL https://linkinghub.elsevier.com/retrieve/pii/S0013469497001119.

M. Scher. Ontogeny of Eeg Sleep from Neonatal through Infancy Periods. *Handbook of clinical neurology / edited by P.J. Vinken and G.W. Bruyn*, 98:111–29, Dec. 2011. doi: 10.1016/B978-0-444-52006-7.00008-3.

P. H. Schimpf. Application of Quasi-Static Magnetic Reciprocity to Finite Element Models of the MEG Lead-Field. *IEEE Transactions on Biomedical Engineering*, 54(11):2082–2088, Nov. 2007. ISSN 1558-2531. doi: 10.1109/TBME.2007.895112. Conference Name: IEEE Transactions on Biomedical Engineering.

A. Schirru, S. Pampuri, G. De Nicolao, and S. McLoone. Efficient Marginal Likelihood Computation for Gaussian Process Regression. *arXiv:1110.6546 [stat]*, Oct. 2011. URL http://arxiv.org/abs/1110.6546. arXiv: 1110.6546.

C. Schmidt, S. Wagner, M. Burger, U. v. Rienen, and C. H. Wolters. Impact of uncertain head tissue conductivity in the optimization of transcranial direct current stimulation for an auditory target. *Journal of Neural Engineering*, 12(4):046028, Aug. 2015. ISSN 1741-2560, 1741-2552. doi: 10.1088/1741-2560/12/4/046028. URL https://iopscience.iop.org/article/10.1088/1741-2560/12/4/046028.

R. Schobi, B. Sudret, and J. Wiart. POLYNOMIAL-CHAOS-BASED KRIGING. *International Journal for Uncertainty Quantification*, 5(2), 2015. ISSN 2152-5080, 2152-5099. doi: 10.1615/Int.J.UncertaintyQuantification.2015012467. URL https://www.dl.begellhouse.com/journals/52034eb04b657aea,65319583582efa6d,26fcd479064bfbc7.html. Publisher: Begel House Inc.

D. L. Schomer and F. H. Lopes da Silva. *Niedermeyer's Electroencephalography: Basic Principles, Clinical Applications, and Related Fields*. Lippincott Williams & Wilkins, Philadelphia, 2011. ISBN 978-0-7817-8942-4.

P. A. Schroeder, T. Schwippel, I. Wolz, and J. Svaldi. Meta-analysis of the effects of transcranial direct current stimulation on inhibitory control. *Brain Stimulation: Basic, Translational, and Clinical Research in Neuromodulation*, 13(5):

1159–1167, Sept. 2020. ISSN 1935-861X, 1876-4754. doi: 10.1016/j.brs.2020. 05.006. URL `https://www.brainstimjrnl.com/article/S1935-861X(20) 30105-4/fulltext`. Publisher: Elsevier.

H. Schwan. Electrical properties of tissues and cell suspensions: mechanisms and models. In *Proceedings of 16th Annual International Conference of the IEEE Engineering in Medicine and Biology Society*, volume 1, pages A70–A71 vol.1, Nov. 1994. doi: 10.1109/IEMBS.1994.412155.

D. Senkowski, R. Sobirey, D. Haslacher, and S. R. Soekadar. Boosting working memory: uncovering the differential effects of tDCS and tACS. *Cerebral Cortex Communications*, 3(2):tgac018, Apr. 2022. ISSN 2632-7376. doi: 10.1093/texcom/ tgac018. URL `https://doi.org/10.1093/texcom/tgac018`.

L. Shreve, A. Kaur, C. Vo, J. Wu, J. M. Cassidy, A. Nguyen, R. J. Zhou, T. B. Tran, D. Z. Yang, A. I. Medizade, B. Chakravarthy, W. Hoonpongsimanont, E. Barton, W. Yu, R. Srinivasan, and S. C. Cramer. Electroencephalography measures are useful for identifying large acute ischemic stroke in the Emergency Department. *Journal of stroke and cerebrovascular diseases : the official journal of National Stroke Association*, 28(8):2280–2286, Aug. 2019. ISSN 1052-3057. doi: 10.1016/j.jstrokecerebrovasdis.2019.05.019. URL `https://www.ncbi.nlm.nih.gov/pmc/articles/PMC6790298/`.

S. M. Smith, M. Jenkinson, M. W. Woolrich, C. F. Beckmann, T. E. J. Behrens, H. Johansen-Berg, P. R. Bannister, M. De Luca, I. Drobnjak, D. E. Flitney, R. K. Niazy, J. Saunders, J. Vickers, Y. Zhang, N. De Stefano, J. M. Brady, and P. M. Matthews. Advances in functional and structural MR image analysis and implementation as FSL. *NeuroImage*, 23 Suppl 1:S208–219, 2004. ISSN 1053-8119. doi: 10.1016/j.neuroimage.2004.07.051.

R. S. Snell. *Clinical neuroanatomy*. Wolters Kluwer Health/Lippincott Williams & Wilkins, Philadelphia, 7th ed edition, 2010. ISBN 978-0-7817-9427-5. OCLC: ocn253189573.

I. Sobol. On the distribution of points in a cube and the approximate evaluation of integrals. *USSR Computational Mathematics and Mathematical Physics*, 7(4): 86–112, Jan. 1967. ISSN 00415553. doi: 10.1016/0041-5553(67)90144-9. URL `https://linkinghub.elsevier.com/retrieve/pii/0041555367901449`.

I. Sobol. Uniformly distributed sequences with an additional uniform property. *USSR Computational Mathematics and Mathematical Physics*, 16(5):236–242, Jan. 1976. ISSN 00415553. doi: 10.1016/0041-5553(76)90154-3. URL `https://linkinghub.elsevier.com/retrieve/pii/0041555376901543`.

I. Sobol. Global sensitivity indices for nonlinear mathematical models and their Monte Carlo estimates. *Mathematics and Computers in Simulation*, 55(1-3):271–280, Feb. 2001. ISSN 03784754. doi: 10.1016/S0378-4754(00)00270-6. URL `https://linkinghub.elsevier.com/retrieve/pii/S0378475400002706`.

P. Soullié, A. Missoffe, K. Ambarki, J. Felblinger, and F. Odille. MR electrical properties imaging using a generalized image-based method. *Magnetic Resonance in Medicine*, 85(2):762–776, 2021. ISSN 1522-2594. doi: 10.1002/mrm.28458. URL `https://onlinelibrary.wiley.com/doi/abs/10.1002/mrm.28458`. _eprint: https://onlinelibrary.wiley.com/doi/pdf/10.1002/mrm.28458.

G. F. Spitoni, R. L. Cimmino, C. Bozzacchi, L. Pizzamiglio, and F. Di Russo. Modulation of spontaneous alpha brain rhythms using low-intensity transcranial direct-current stimulation. *Frontiers in Human Neuroscience*, 7:529, 2013. ISSN 1662-5161. doi: 10.3389/fnhum.2013.00529.

C. J. Stagg and M. A. Nitsche. Physiological basis of transcranial direct current stimulation. *The Neuroscientist: A Review Journal Bringing Neurobiology, Neurology and Psychiatry*, 17(1):37–53, Feb. 2011. ISSN 1089-4098. doi: 10.1177/1073858410386614.

C. J. Stagg, A. Antal, and M. A. Nitsche. Physiology of Transcranial Direct Current Stimulation. *The Journal of ECT*, 34(3):144–152, Sept. 2018. ISSN 1095-0680. doi: 10.1097/YCT.0000000000000510. URL `https://journals.lww.com/ectjournal/Abstract/2018/09000/Physiology_of_Transcranial_Direct_Current.3.aspx`.

D. J. Stein, L. Fernandes Medeiros, W. Caumo, and I. L. Torres. Transcranial Direct Current Stimulation in Patients with Anxiety: Current Perspectives. *Neuropsychiatric Disease and Treatment*, 16:161–169, Jan. 2020. ISSN 1176-6328. doi: 10.2147/NDT.S195840. URL `https://www.ncbi.nlm.nih.gov/pmc/articles/PMC6969693/`.

S. R. Synigal, E. S. Teoh, and E. C. Lalor. Including Measures of High Gamma Power Can Improve the Decoding of Natural Speech From EEG. *Frontiers in Human Neuroscience*, 14, 2020. ISSN 1662-5161. URL `https://www.frontiersin.org/article/10.3389/fnhum.2020.00130`.

G. A. Taberna, J. Samogin, and D. Mantini. Automated Head Tissue Modelling Based on Structural Magnetic Resonance Images for Electroencephalographic Source Reconstruction. *Neuroinformatics*, Jan. 2021. ISSN 1539-2791, 1559-0089. doi: 10.1007/s12021-020-09504-5. URL `http://link.springer.com/10.1007/s12021-020-09504-5`.

F. Tadel, S. Baillet, J. C. Mosher, D. Pantazis, and R. M. Leahy. Brainstorm: A User-Friendly Application for MEG/EEG Analysis. *Computational Intelligence and Neuroscience*, 2011:e879716, Apr. 2011. ISSN 1687-5265. doi: 10.1155/2011/879716. URL https://www.hindawi.com/journals/cin/2011/879716/. Publisher: Hindawi.

T. Tamanna and M. Z. Parvez. *Cognitive Load Measurement Based on EEG Signals*. IntechOpen, Feb. 2021. ISBN 978-1-83968-636-8. doi: 10.5772/intechopen.96388. URL https://www.intechopen.com/chapters/undefined/state.item.id. Publication Title: The Science of Emotional Intelligence.

T. Tanaka, Y. Isomura, K. Kobayashi, T. Hanakawa, S. Tanaka, and M. Honda. Electrophysiological Effects of Transcranial Direct Current Stimulation on Neural Activity in the Rat Motor Cortex. *Frontiers in Neuroscience*, 14, 2020. ISSN 1662-453X. URL https://www.frontiersin.org/article/10.3389/fnins.2020.00495.

H. Thair, A. L. Holloway, R. Newport, and A. D. Smith. Transcranial Direct Current Stimulation (tDCS): A Beginner's Guide for Design and Implementation. *Frontiers in Neuroscience*, 11, 2017. ISSN 1662-453X. URL https://www.frontiersin.org/article/10.3389/fnins.2017.00641.

A. Thielscher, A. Antunes, and G. B. Saturnino. Field modeling for transcranial magnetic stimulation: A useful tool to understand the physiological effects of TMS? In *2015 37th Annual International Conference of the IEEE Engineering in Medicine and Biology Society (EMBC)*, pages 222–225, Milan, Aug. 2015. IEEE. ISBN 978-1-4244-9271-8. doi: 10.1109/EMBC.2015.7318340. URL http://ieeexplore.ieee.org/document/7318340/.

T. E. Thompson and T. W. Tillack. Organization of glycosphingolipids in bilayers and plasma membranes of mammalian cells. *Annual Review of Biophysics and Biophysical Chemistry*, 14:361–386, 1985. ISSN 0883-9182. doi: 10.1146/annurev.bb.14.060185.002045.

A. P. Tran, S. Yan, and Q. Fang. Improving model-based functional near-infrared spectroscopy analysis using mesh-based anatomical and light-transport models. *Neurophotonics*, 7(1):015008, Feb. 2020a. ISSN 2329-423X, 2329-4248. doi: 10.1117/1.NPh.7.1.015008. URL https://www.spiedigitallibrary.org/journals/neurophotonics/volume-7/issue-1/015008/Improving-model-based-functional-near-infrared-spectroscopy-analysis-using-mesh/10.1117/1.NPh.7.1.015008.full. Publisher: SPIE.

Y. Tran, A. Craig, R. Craig, R. Chai, and H. Nguyen. The influence of mental fatigue on brain activity: Evidence from a systematic review with meta-

analyses. *Psychophysiology*, 57(5):e13554, May 2020b. ISSN 1540-5958. doi: 10.1111/psyp.13554.

D. S. Tuch, V. J. Wedeen, A. M. Dale, J. S. George, and J. W. Belliveau. Conductivity tensor mapping of the human brain using diffusion tensor MRI. *Proceedings of the National Academy of Sciences*, 98(20):11697–11701, Sept. 2001. ISSN 0027-8424, 1091-6490. doi: 10.1073/pnas.171473898. URL http://www.pnas.org/cgi/doi/10.1073/pnas.171473898.

M. Tudor, L. Tudor, and K. I. Tudor. [Hans Berger (1873-1941)–the history of electroencephalography]. *Acta medica Croatica : casopis Hrvatske akademije medicinskih znanosti*, 59(4), 2005. ISSN 1330-0164. URL https://pubmed.ncbi.nlm.nih.gov/16334737/. Publisher: Acta Med Croatica.

B. Valic, M. Golzio, M. Pavlin, A. Schatz, C. Faurie, B. Gabriel, J. Teissié, M.-P. Rols, and D. Miklavcic. Effect of electric field induced transmembrane potential on spheroidal cells: theory and experiment. *European biophysics journal: EBJ*, 32 (6):519–528, Sept. 2003. ISSN 0175-7571. doi: 10.1007/s00249-003-0296-9.

S. Vallaghe and M. Clerc. A Global Sensitivity Analysis of Three- and Four-Layer EEG Conductivity Models. *IEEE Transactions on Biomedical Engineering*, 56(4): 988–995, Apr. 2009. ISSN 1558-2531. doi: 10.1109/TBME.2008.2009315. Conference Name: IEEE Transactions on Biomedical Engineering.

R. Van Uitert, C. Johnson, and L. Zhukov. Influence of Head Tissue Conductivity in Forward and Inverse Magnetoencephalographic Simulations Using Realistic Head Models. *IEEE Transactions on Biomedical Engineering*, 51(12):2129–2137, Dec. 2004. ISSN 0018-9294. doi: 10.1109/TBME.2004.836490. URL http://ieeexplore.ieee.org/document/1360032/.

B. Vanrumste. *EEG dipole source analysis in a realistic head model*. dissertation, Ghent University, 2002. URL http://hdl.handle.net/1854/LU-522108.

A. A. Vatinno, A. Simpson, V. Ramakrishnan, H. S. Bonilha, L. Bonilha, and N. J. Seo. The Prognostic Utility of Electroencephalography in Stroke Recovery: A Systematic Review and Meta-Analysis. *Neurorehabilitation and Neural Repair*, 36(4-5):255–268, Apr. 2022. ISSN 1552-6844. doi: 10.1177/15459683221078294.

M. F. Villamar, M. S. Volz, M. Bikson, A. Datta, A. F. Dasilva, and F. Fregni. Technique and considerations in the use of 4x1 ring high-definition transcranial direct current stimulation (HD-tDCS). *Journal of Visualized Experiments: JoVE*, 50309 (77):e50309, July 2013. ISSN 1940-087X. doi: 10.3791/50309.

I. D. Villegas, J. R. Camargo, and C. A. Perdomo Ch. Recognition and Characteristics EEG Signals for Flight Control of a Drone. *IFAC-PapersOnLine*, 54(4):50–55, Jan. 2021. ISSN 2405-8963. doi: 10.1016/j.ifacol.2021.10.009. URL `https://www.sciencedirect.com/science/article/pii/S2405896321014117`.

P. Virtanen, R. Gommers, T. E. Oliphant, M. Haberland, T. Reddy, D. Cournapeau, E. Burovski, P. Peterson, W. Weckesser, J. Bright, S. J. van der Walt, M. Brett, J. Wilson, K. J. Millman, N. Mayorov, A. R. J. Nelson, E. Jones, R. Kern, E. Larson, C. J. Carey, İ. Polat, Y. Feng, E. W. Moore, J. VanderPlas, D. Laxalde, J. Perktold, R. Cimrman, I. Henriksen, E. A. Quintero, C. R. Harris, A. M. Archibald, A. H. Ribeiro, F. Pedregosa, P. van Mulbregt, and SciPy 1.0 Contributors. SciPy 1.0: Fundamental Algorithms for Scientific Computing in Python. *Nature Methods*, 17:261–272, 2020. doi: 10.1038/s41592-019-0686-2.

J. Vorwerk, J.-H. Cho, S. Rampp, H. Hamer, T. R. Knösche, and C. H. Wolters. A guideline for head volume conductor modeling in EEG and MEG. *NeuroImage*, 100:590–607, Oct. 2014. ISSN 10538119. doi: 10.1016/j.neuroimage.2014.06.040. URL `https://linkinghub.elsevier.com/retrieve/pii/S1053811914005175`.

J. Vorwerk, R. Oostenveld, M. C. Piastra, L. Magyari, and C. H. Wolters. The FieldTrip-SimBio pipeline for EEG forward solutions. *BioMedical Engineering OnLine*, 17(1):37, Mar. 2018. ISSN 1475-925X. doi: 10.1186/s12938-018-0463-y. URL `https://doi.org/10.1186/s12938-018-0463-y`.

J. Vorwerk, U. Aydin, C. Wolters, and C. Butson. Influence of Head Tissue Conductivity Uncertainties on EEG Dipole Reconstruction. *Frontiers in Neuroscience*, 13, June 2019a. doi: 10.3389/fnins.2019.00531.

J. Vorwerk, A. Hanrath, C. H. Wolters, and L. Grasedyck. The multipole approach for EEG forward modeling using the finite element method. *NeuroImage*, 201:116039, Nov. 2019b. ISSN 10538119. doi: 10.1016/j.neuroimage.2019.116039. URL `https://linkinghub.elsevier.com/retrieve/pii/S1053811919306202`.

H. Wang, F. Yan, T. Xu, H. Yin, P. Chen, H. Yue, C. Chen, H. Zhang, L. Xu, Y. He, and A. Bezerianos. Brain-Controlled Wheelchair Review: From Wet Electrode to Dry Electrode, From Single Modal to Hybrid Modal, From Synchronous to Asynchronous. *IEEE Access*, 9:55920–55938, 2021a. ISSN 2169-3536. doi: 10.1109/ACCESS.2021.3071599. Conference Name: IEEE Access.

X. Wang, C. Xia, L. Lu, H. Qi, and J. Zhang. Electromagnetic Exposure Dosimetry Study on Two Free Rats at 1.8 GHz via Numerical Simulation. *Frontiers in Public Health*, 9, 2021b. ISSN 2296-2565. URL `https://www.frontiersin.org/articles/10.3389/fpubh.2021.721166`.

Y. Wang, D. R. Haynor, and Y. Kim. An investigation of the importance of my-ocardial anisotropy in finite-element modeling of the heart: methodology and application to the estimation of defibrillation efficacy. *IEEE transactions on bio-medical engineering*, 48(12):1377–1389, Dec. 2001. ISSN 0018-9294. doi: 10.1109/10.966597.

D. Weinstein, L. Zhukov, and C. Johnson. Lead Field Basis for FEM Source Lo-calization. *Annals of Biomedical Engineering*, 28(9):1059–1065, 2000. doi: 10.1114/1.1310220.

S. Weller, M. A. Nitsche, and C. Plewnia. Enhancing cognitive control training with transcranial direct current stimulation: a systematic parameter study. *Brain Stimulation*, 13(5):1358–1369, Sept. 2020. ISSN 1935-861X. doi: 10.1016/j.brs. 2020.07.006. URL https://www.sciencedirect.com/science/article/pii/S1935861X20302047.

K. Wendel, O. Väisänen, J. Malmivuo, N. G. Gencer, B. Vanrumste, P. Durka, R. Magjarević, S. Supek, M. L. Pascu, H. Fontenelle, and R. Grave De Peralta Menendez. EEG/MEG source imaging: Methods, challenges, and open issues. *Computational Intelligence and Neuro-science*, 2009:12, 2009. ISSN 16875265. doi: 10.1155/2009/656092. URL https://com-mendeley-prod-publicsharing-pdfstore.s3.eu-west-1.amazonaws.com/c880-PUBMED/10.1155/2009/656092/CIN2009_656092_pdf.pdf?X-Amz-Security-Token=FQoGZXIvYXdzEIL%2F%2F%2F%2F%2F%2F%2F%2F%2F%2FwEaDIQNRX5%2B1wioW%2F6kZiKfBKQFXLst36hT5pegKTM22X6RRZS1gYe.

J. Westfall. Statistical details of the default priors in the Bambi library. *arXiv:1702.01201 [stat]*, Feb. 2017. URL http://arxiv.org/abs/1702.01201. arXiv: 1702.01201.

S. J. Westwood. Null Effects on Working Memory and Verbal Fluency Tasks When Applying Anodal tDCS to the Inferior Frontal Gyrus of Healthy Participants. *Frontiers in Neuroscience*, 12:19, 2018.

S. Wiethoff, M. Hamada, and J. C. Rothwell. Variability in response to transcranial direct current stimulation of the motor cortex. *Brain Stimulation*, 7(3):468–475, June 2014. ISSN 1876-4754. doi: 10.1016/j.brs.2014.02.003.

M. Windhoff, A. Opitz, and A. Thielscher. Electric field calculations in brain stim-ulation based on finite elements: An optimized processing pipeline for the generation and usage of accurate individual head models. *Human Brain Map-ping*, 34(4):923–935, 2013. ISSN 1097-0193. doi: https://doi.org/10.1002/hbm. 21479. URL https://onlinelibrary.wiley.com/doi/abs/10.1002/hbm. 21479. _eprint: https://onlinelibrary.wiley.com/doi/pdf/10.1002/hbm.21479.

C. Wolters, A. Anwander, X. Tricoche, D. Weinstein, M. Koch, and R. MacLeod. Influence of tissue conductivity anisotropy on EEG/MEG field and return current computation in a realistic head model: A simulation and visualization study using high-resolution finite element modeling. *NeuroImage*, 30(3):813–826, Apr. 2006. ISSN 10538119. doi: 10.1016/j.neuroimage.2005.10.014. URL `https://linkinghub.elsevier.com/retrieve/pii/S1053811905007871`.

E. J. Woo and J. K. Seo. Magnetic resonance electrical impedance tomography (MREIT) for high-resolution conductivity imaging. *Physiological Measurement*, 29(10):R1–26, Oct. 2008. ISSN 0967-3334. doi: 10.1088/0967-3334/29/10/R01.

A. J. Woods, A. Antal, M. Bikson, P. S. Boggio, A. R. Brunoni, P. Celnik, L. G. Cohen, F. Fregni, C. S. Herrmann, E. S. Kappenman, H. Knotkova, D. Liebetanz, C. Miniussi, P. C. Miranda, W. Paulus, A. Priori, D. Reato, C. Stagg, N. Wenderoth, and M. A. Nitsche. A technical guide to tDCS, and related non-invasive brain stimulation tools. *Clinical Neurophysiology: Official Journal of the International Federation of Clinical Neurophysiology*, 127(2):1031–1048, Feb. 2016. ISSN 1872-8952. doi: 10.1016/j.clinph.2015.11.012.

Z. Wu, Y. Liu, M. Hong, and X. Yu. A review of anisotropic conductivity models of brain white matter based on diffusion tensor imaging. *Medical & Biological Engineering & Computing*, 56(8):1325–1332, Aug. 2018. ISSN 0140-0118, 1741-0444. doi: 10.1007/s11517-018-1845-9. URL `http://link.springer.com/10.1007/s11517-018-1845-9`.

D. Yang, Q. Du, Z. Huang, L. Li, Z. Zhang, L. Zhang, X. Zhao, X. Zhao, T. Li, Y. Lin, and Y. Wang. Transcranial Direct Current Stimulation for Patients With Pharmacoresistant Epileptic Spasms: A Pilot Study. *Frontiers in Neurology*, 10, 2019. ISSN 1664-2295. URL `https://www.frontiersin.org/article/10.3389/fneur.2019.00050`.

M. Ye and M. C. Hill. Chapter 10 - Global Sensitivity Analysis for Uncertain Parameters, Models, and Scenarios. In G. P. Petropoulos and P. K. Srivastava, editors, *Sensitivity Analysis in Earth Observation Modelling*, pages 177–210. Elsevier, Jan. 2017. ISBN 978-0-12-803011-0. doi: 10.1016/B978-0-12-803011-0.00010-0. URL `https://www.sciencedirect.com/science/article/pii/B9780128030110000100`.

P. A. Yushkevich, J. Piven, H. C. Hazlett, R. G. Smith, S. Ho, J. C. Gee, and G. Gerig. User-guided 3D active contour segmentation of anatomical structures: significantly improved efficiency and reliability. *NeuroImage*, 31(3):1116–1128, July 2006. ISSN 1053-8119. doi: 10.1016/j.neuroimage.2006.01.015.

S. Zaghi, M. Acar, B. Hultgren, P. S. Boggio, and F. Fregni. Noninvasive brain stimulation with low-intensity electrical currents: putative mechanisms of action for direct and alternating current stimulation. *The Neuroscientist: A Review Journal Bringing Neurobiology, Neurology and Psychiatry*, 16(3):285–307, June 2010. ISSN 1089-4098. doi: 10.1177/1073858409336227.

W. Zhao, E. J. W. Van Someren, C. Li, X. Chen, W. Gui, Y. Tian, Y. Liu, and X. Lei. EEG spectral analysis in insomnia disorder: A systematic review and meta-analysis. *Sleep Medicine Reviews*, 59:101457, Oct. 2021. ISSN 1532-2955. doi: 10.1016/j.smrv.2021.101457.

E. Ziegler, S. L. Chellappa, G. Gaggioni, J. Q. Ly, G. Vandewalle, E. André, C. Geuzaine, and C. Phillips. A finite-element reciprocity solution for EEG forward modeling with realistic individual head models. *NeuroImage*, 103:542–551, Dec. 2014. ISSN 10538119. doi: 10.1016/j.neuroimage. 2014.08.056. URL `https://linkinghub.elsevier.com/retrieve/pii/ S1053811914007307`.

I. Zorzos, I. Kakkos, E. M. Ventouras, and G. K. Matsopoulos. Advances in Electrical Source Imaging: A Review of the Current Approaches, Applications and Challenges. *Signals*, 2(3):378–391, June 2021. ISSN 2624-6120. doi: 10.3390/ signals2030024. URL `https://www.mdpi.com/2624-6120/2/3/24`.